



A flexible transceiver array employing transmission line resonators for cardiac MRI at 7 T

Sajad Hossein Nezhadian

► To cite this version:

Sajad Hossein Nezhadian. A flexible transceiver array employing transmission line resonators for cardiac MRI at 7 T. Medical Physics [physics.med-ph]. Université Paris Saclay (COMUE), 2017. English. NNT : 2017SACLS492 . tel-01756163

HAL Id: tel-01756163

<https://theses.hal.science/tel-01756163>

Submitted on 1 Apr 2018

HAL is a multi-disciplinary open access archive for the deposit and dissemination of scientific research documents, whether they are published or not. The documents may come from teaching and research institutions in France or abroad, or from public or private research centers.

L'archive ouverte pluridisciplinaire **HAL**, est destinée au dépôt et à la diffusion de documents scientifiques de niveau recherche, publiés ou non, émanant des établissements d'enseignement et de recherche français ou étrangers, des laboratoires publics ou privés.

Réseau flexible de résonateurs à ligne de transmissions pour l'émission et la réception en IRM cardiaque à 7T

Thèse de doctorat de l'Université Paris-Saclay
préparée à l'Université Paris-Sud

École doctorale n°575
Electrical, optical, bio-physics and engineering (EOBE)
Spécialité de doctorat: Imagerie et Physique Médicale

Thèse présentée et soutenue à Orsay, le 19 décembre 2017 par

Sajad Hossein Nezhadian

Composition du Jury:

M. Joël MISPELTER Directeur de Recherche, Institut Curie	Président
M. Jacques FELBLINGER Professeur, Université de Lorraine	Rapporteur
M. Martin MEYERSPEER Professeur associé, Medical University of Vienna	Rapporteur
M. Olivier GIRARD Ingénieur de recherche, Université d'Aix-Marseille	Examineur
M. Jean-Christophe GINEFRI Maître de Conférences, Université Paris-Sud	Directeur de thèse
M. Elmar LAISTLER Assistant Professeur, Medical University of Vienna	Co-encadrant de thèse

Table of Contents

Table of Contents	i
Preface	i
Symbols and Abbreviations.....	ii
Abstract.....	iv
Résumé	vi
Acknowledgments.....	viii
Résumé de Thèse	ix
Chapitre 1: Introduction	x
Chapitre 2: Théorie et contexte scientifiques.....	xiii
Chapitre 3: Conception, développement et test d'un réseau de TLRs flexible à 12 éléments pour l'IRM à 7T.	xvii
Chapitre 4: Discussion, Conclusion et Perspectives.....	xxviii
1 Introduction	2
1.1 Thesis Outline.....	3
1.2 General Introduction.....	4
1.3 Motivation.....	5
2 Theory and Background	10
2.1 Basic Principles of Magnetic Resonance	11
2.1.1 Nuclear Spin	11
2.1.2 Spin Energy Levels and Magnetization	12
2.1.3 Larmor Precession.....	15
2.1.4 Relaxation	18
2.1.5 Free Induction Decay (FID).....	21
2.2 Signal and Noise in MR Experiments	22
2.2.1 The Reciprocity Principle.....	22
2.2.2 Noise Contributions	25
2.3 Magnetic Resonance Signal Acquisition	28
2.3.1 Spin-Echo.....	28
2.3.2 Gradient-Echo (GRE)	29
2.3.3 Magnetic Field Gradients: Spatial Encoding	30
2.3.4 Slice Selection	31
2.3.5 Phase Encoding	33
2.3.6 k-Space	34
2.3.7 Parallel Imaging (PI)	35

2.3.8	Parallel Transmission (pTx)	37
2.4	Radio Frequency Coils	38
2.4.1	Basic Principles.....	38
2.4.2	RF Coil Design.....	45
2.4.3	Connecting the RF Coil to the MR Scanner	58
2.4.4	Experimental Characterization of RF Coils	67
2.5	Specific Absorption Rate (SAR)	71
2.6	Numerical Electromagnetic Simulations	72
2.6.1	Full-wave electromagnetic (EM) simulation	72
2.6.2	Finite Difference Time Domain (FDTD) Method	73
2.6.3	Combining FDTD and Circuit Co-Simulation.....	75
2.6.4	3D EM Simulation of TLRs	76
2.7	Current State of Cardiac MRI	77
2.7.1	UHF CMR	81
3	Development of a 12-Element Flexible TLR Array for ^1H 7T Cardiac MRI.....	86
3.1	Tools and Materials.....	87
3.1.1	EM Simulation	87
3.1.2	Phantoms	89
3.2	Individual Array Elements	91
3.2.1	Single TLR Design	91
3.2.2	Inter-TLR Decoupling.....	93
3.2.3	Decoupling Ring Effects on TLR Performance.....	97
3.2.4	Single Element TLR vs. Conventional loop	103
3.3	Array Development and Implementation.....	106
3.3.1	Coil Fabrication on Flexible PCB.....	106
3.3.2	Static B_1^+ Shimming.....	107
3.3.3	Cabling, Interfacing, and Housing	110
3.4	Performance Evaluation of the Array	114
3.4.1	Decoupling Performance	114
3.4.2	Power Loss Evaluation	116
3.4.3	Transmit Efficiency ($B_1^+ / \sqrt{P_{\text{input}}}$) Profiles.....	119
3.4.4	Array Performance in Terms of SAR.....	123
3.4.5	Noise Correlation and Parallel Imaging Performance.....	124
3.5	Conclusion and Summary	131
4	Discussion, Conclusions and Perspectives	134

4.1	Discussion.....	135
4.2	Conclusions	137
4.3	Future Work	137
4.3.1	Integration of an additional ³¹ P array	137
4.3.2	Compatibility with parallel transmission systems	138
4.3.3	Improvement of coverage.....	139
4.3.4	EM Simulation Methods for bent TLRs	140
4.3.5	MR Thermometry.....	142
4.3.6	Certification for In Vivo Usage	142
A.	Appendix	144
A.1	Analytical model of TLRs	145
A.1.1	Description of the Resonator	145
A.1.2	Differential mode	146
A.1.3	Common mode	149
A.1.4	Resonance Condition	151
A.1.5	Inductance equations.....	152
A.1.6	Characteristic Impedance	153
A.2	Analytical Model for Decoupling Optimization of Decoupling Rings	154
	List of Figures	160
	List of Tables	166
	Bibliography	168
	Publication List.....	182
	Journal articles	183
	Conference proceedings	183
	Curriculum Vitae	184

Preface

Symbols and Abbreviations

γ	Gyromagnetic Ratio (MHz/T)
\hbar	Reduced Planck Constant $\hbar/2\pi = 1.054571726(47) \times 10^{-34}$ Js)
k_B	Boltzmann constant = 1.4×10^{-23} (J/K)
c	Vacuum speed of light = 299793458 (m/s)
λ	Wavelength (m)
B	Magnetic flux density (T)
B_0	Static magnetic flux density (T)
B_1	RF magnetic flux density (T)
B_1^+	Positively rotating RF field : Transmit field (T)
B_1^-	Negatively rotating RF field : Receive field (T)
H	Magnetic field (A/m)
E	Electric field (V/m)
μ_0	Permeability of free space = $4\pi \times 10^{-7}$ (H/m)
μ_r	Relative permeability
ϵ_0	Permittivity of free space $8.854187817 \dots \times 10^{-12}$ (F/m)
ϵ_r	Relative permittivity
σ	Electrical conductivity
^1H	Hydrogen-1 isotope
^{31}P	Phosphor-31 isotope
I	Spin quantum number
m_I	Magnetic quantum number
ω_L	Larmor Frequency $\omega_L = \gamma B_0$
ω_0	RF Coil Resonance Frequency $\omega_0 = 1/\sqrt{LC}$
NMR	Nuclear Magnetic Resonance
MRI	Magnetic Resonance Imaging
MRS	Magnetic Resonance Spectroscopy

SNR	Signal to Noise Ratio
SAR	Specific Absorption Rate
UHF	Ultra High Field
RF	Radio Frequency
FDTD	Finite Difference Time Domain
FOV	Field of View
MoM	Methods of Moments
FEM	Finite Element Method
ROI	Region of Interest
VOI	Volume of Interest
PI	Parallel Imaging
pTx	Parallel Transmission
EMS	Electromagnetic Simulation
TLR	Transmission Line Resonator
MTMG	Multi-Turn Multi-Gap
FID	Free Induction Decay
emf	electromotive force
SMASH	SiMultaneous Acquisitions of Spatial Harmonics
SENSE	SENSitivity Encoding
GRAPPA	GeneRalized Autocalibrating Partially Parallel Acquisitions
IEC	Electro-technical Commission
HTS	High Temperature Superconductor
WPD	Wilkinson Power Divider
TC	Thin Conductive
DUT	Device Under the Test
VNA	Vector Network Analyser
DAM	Double Angle Method
PD	Proton Density
PEC	Perfect Electric Conductor
PRF	Proton Resonance Frequency

Abstract

Magnetic resonance imaging (MRI) is a non-invasive imaging methodology which uses the magnetic properties of an atomic nucleus and its interaction with a static magnetic field B_0 together with a time varying magnetic field B_1 which is produced by a radio frequency coil.

Spatial and/or temporal resolution in MRI is limited by the available signal to noise ratio (SNR). The SNR can be enhanced by working at ultra-high field (UHF) ($B_0 \geq 7$ T) and employing coil arrays. Receive arrays combine the high SNR of surface coils with an extended field of view and give access to faster signal acquisition by parallel imaging. Transmit arrays enable parallel transmission techniques that can be used to accelerate excitation pulses and produce a more homogeneous transmit field. Receive and transmit arrays can be combined as a single physical entity to transceiver arrays.

Mechanical flexibility of the coil arrays enables improved geometrical conformity of the coil to the sample yielding a significant SNR gain in the receive mode, and improved transmit efficiency. Among available coil technologies, transmission line resonators (TLRs) are self-resonant structures which can be monolithically fabricated on a flexible substrate, thus, enabling the TLR array to be form-fitted to the target anatomy, e.g. the human torso.

One of the major technical challenges in coil array design is the mutual coupling between the individual elements. Conventional decoupling techniques such as partial overlap, L/C decoupling circuits, and preamplifier decoupling may impose limitations on the design of flexible arrays and are not well suited for monolithic, double-sided coil designs. In previous work, efficient decoupling for an array of TLRs was demonstrated using coil annexes with the limitations of interfering with the coil geometry, being inefficient for large coils, and higher minimum substrate thickness.

In this thesis, a flexible 12-channel transceiver TLR array for 7 T cardiac ^1H MRI was developed. This new hardware was successfully designed, constructed, tested, and used in MRI experiments. The size of the array is 38 cm \times 28.5 cm with TLRs of 84 mm diameter as the individual elements. A decoupling ring-based technique was used where the basic TLR geometry is surrounded by a conducting ring. In array configuration, decoupling rings of nearest neighbours are deposited on opposite sides of the substrate for overlapping. A capacitive matching scheme was developed using circuit co-simulation resulting in symmetric current distribution along the TLR conductors. The effect of the decoupling ring on the TLR

performance was evaluated by 3D electromagnetic simulation, bench tests, and MR measurements. It was demonstrated that the presence of the decoupling ring degrades neither transmit nor receive performance of the TLR.

The overall performance of the developed array was also evaluated by 3D electromagnetic simulation, bench tests, and MR measurements. Efficient inter-element decoupling was demonstrated in flat configuration on a box-shaped phantom ($S_{ij} < -19$ dB), bent ($S_{ij} < -16$ dB) on a human torso phantom, and bent on a subject in vivo ($S_{ij} < -16$ dB). Investigation of the parallel imaging performance of the array demonstrated that acceleration factors up to 3 in bent configuration can be employed without significant SNR degradation (g-factor < 1.6).

In conclusion, this thesis presents a flexible TLR array to be used for 7 T cardiac MRI. The array enables geometrical conformity to bodies within a large range of size and shape. Furthermore, the fabricated array is compatible with parallel imaging and pTx techniques. Future work aims at combining the developed ^1H array with a ^{31}P array for cardiac ^{31}P MR spectroscopy at 7 T.

Résumé

L'imagerie par résonance magnétique (IRM) est une modalité non-invasive qui est devenue un outil d'investigation clinique majeur. L'IRM utilise les propriétés magnétiques des noyaux en présence d'un champ statique B_0 et d'un champ alternatif B_1 produit par une antenne radiofréquence. La résolution spatiale et/ou temporelle en IRM est limitée par le rapport signal-sur-bruit (RSB). Celui-ci peut être amélioré en travaillant à ultra haut champ ($B_0 \geq 7$ T) et en utilisant des réseaux d'antennes en émission/réception. Ces réseaux combinent la sensibilité élevée des antennes de surface avec un champ de vue élargi et permettent d'utiliser des techniques d'imagerie parallèle pour accélérer l'acquisition et homogénéiser le champ B_1 d'excitation. La flexibilité mécanique des antennes autorise une meilleure conformation de celles-ci à la surface de l'échantillon, conduisant à un gain de sensibilité en réception et une efficacité de transmission accrue. Parmi les technologies disponibles pour la fabrication d'antennes, les résonateurs à ligne de transmission (TLR), qui sont des structures auto-résonantes monolithiques pouvant être fabriquées sur substrats souples, sont particulièrement bien adaptés pour la réalisation de réseaux flexibles pouvant être conformés à la surface de régions anatomiques de tailles variables d'un sujet à l'autre, comme le torse par exemple. L'une des principales difficultés dans la conception de réseaux d'antennes concerne l'annulation du couplage magnétique entre les éléments du réseau. Les techniques de découplage conventionnelles, telles que le chevauchement des antennes, l'ajout de circuits R-L-C, ou le découplage par préamplificateur ne sont pas adaptées pour les antennes monolithiques double-face et peuvent compromettre leur flexibilité. Au cours de précédents travaux, une technique utilisant des annexes de courant a permis de découpler les éléments d'un réseau de TLR mais s'est avérée d'une efficacité limitée pour les antennes de grandes tailles et/ou déposées sur des substrats épais.

Au cours de cette thèse, nous avons développé un réseau de TLR flexible de 12 éléments pour l'IRM cardiaque à 7T. Ce nouveaux systèmes a été conçu, développé, testé et utilisé avec succès dans une expérience d'IRM. La taille du réseau développé est de 38 cm \times 28,5 cm, avec des TLR de 8,4 cm de diamètre. Nous avons étudié et optimisé une technique de découplage basée sur l'ajout d'anneaux conducteurs autour de chaque TLR, les anneaux de TLR adjacents étant déposés sur des faces opposées du substrat pour permettre leur chevauchement. Un circuit capacitif pour l'accord et l'adaptation, développé par co-simulation, a été utilisé afin de préserver la distribution de courant intrinsèque dans le TLR. Les effets des anneaux de

découplages ont été évalués par simulation électromagnétique, mesure sur table et en imagerie, et nous avons montré que la présence des anneaux de découplage ne dégradait pas les performances des TLR. Les performances du réseau développé ont elles aussi été évaluées par simulation électromagnétique, mesure sur table et en imagerie. Un découplage efficace a été obtenu lorsque le réseau est en configuration plane ($S_{ij} < -19$ dB) et courbé sur un fantôme de torse ($S_{ij} < -16$ dB). L'utilisation du réseau en imagerie parallèle a permis d'accélérer l'acquisition d'un facteur 3 sans dégradation significative du RSB (g-factor < 1.6).

En conclusion, nous avons développé un réseau de TLR flexible pour l'IRM cardiaque à 7T. Ce réseau peut être conformé à la surface d'échantillons de tailles variables permettant ainsi d'augmenter la sensibilité de détection. Ce réseau peut fonctionner en réception et transmission parallèle permettant de réduire le temps de l'expérience et d'homogénéiser le champ d'excitation. Les perspectives de ce travail visent la combinaison de ce réseau avec un réseau pour la spectroscopie du phosphore à 7T.

Acknowledgments

Along the bumpy way of my PhD studies, many people helped me and this is the moment to express my sincere gratitude to the following in particular.

Foremost, I would like to thank my supervisors Jean-Christophe Ginefri and Elmar Laistler for their continuous support throughout my PhD studies, as well as their patience, motivation and immense knowledge. I would also like to express my gratitude for their help with the preparation of the thesis manuscript. Besides my supervisors, my sincere thanks also go to Roberta Frass-Kriegl for all of her support during my PhD studies and helping me a lot to gain a deeper understanding in RF coil engineering.

I thank Luc Darrasse and Ewald Moser for welcoming me in IR4M in Orsay and Division MR Physics in Vienna and for their useful scientific comments and discussions. I thank the administrative management assistant of IR4M, Albine Pinseel for providing me with lots of support in French administration system and handling my work-related trips. I would like to thank all of my colleagues in IR4M for their useful discussions, interesting comments and creating a nice working ambiance, especially, Geneviève, Zoé, Marie, Ludovic, George, Khaoula, Zhoujian and all of the PhD student colleagues. I thank all members of the Division MR Physics and Radiology departments in Vienna for their support during my PhD studies, especially my colleagues in the RF lab, Michael, Jürgen, Sigrun, Lucia, Lena and Ehsan for helping me gain my experience and knowledge in the RF coil engineering and providing me a pleasant working environment.

Finally, I thank my parents, family and friends who were always there for me and supported me to continue my studies. Without them, I would not have imagined myself here, towards the end of my PhD studies.

I acknowledge financial support from Austrian/French FWF/ANR programme Blanc grant, Nr. I1371-B24, “FLEXAR7” and Austrian/French OeAD/MAEE projects WTZ/PHC Amadée FR10/2015.

تا بدانجا رسيد دانش من تا بدانم همی كه نادانم

ابوشكور بلخي

Résumé de Thèse

Chapitre 1: Introduction

L'imagerie par résonance magnétique (IRM) est une modalité non-invasive qui est devenue un outil d'investigation clinique majeur qui donne accès à de nombreuses informations anatomiques et fonctionnelles. La qualité des images en IRM est fixée par le rapport-signal-sur-bruit (RSB) accessible. Celui-ci peut être amélioré en augmentant l'intensité du champ statique B_0 , en optimisant la sensibilité de détection des antennes radiofréquences ou en utilisant des séquences d'acquisition avancées.

Les imageurs cliniques actuels ont des gammes de champ statique de 1,5 à 3 T et sont équipés de canaux d'émission, associés à une antenne d'émission dite « corps-entier » et de canaux de réception associés à des réseaux d'antennes de réception. En émission, l'antenne corps entier permet de produire un champ radiofréquence de forte intensité et homogène sur la région d'intérêt. En réception, les réseaux d'antennes permettent d'obtenir une forte sensibilité sur un champ de vue élargi. En IRM à ultra haut champ ($\geq 7T$) les phénomènes de propagation dus à la longueur d'onde réduite ne permettent pas de produire un champ homogène sur la région d'intérêt avec une antenne corps entier pour. De plus, à très haut champ statique des problématiques importantes liées au dépôt d'énergie dans les tissus et pouvant compromettre la sécurité des patients apparaissent. L'utilisation d'antenne corps entier à haut champ n'est de ce fait pas possible. La solution actuelle permettant de contourner ces difficultés consiste à utiliser les réseaux d'antennes à la fois pour la réception du signal RMN mais également pour la production du champ radiofréquence pendant les phases d'émission.

Ces réseaux combinent la haute sensibilité des antennes de surface et le champ de vue élargi des antennes de volume. Ils permettent de plus d'utiliser des techniques d'imagerie parallèle, permettant ainsi d'accélérer l'acquisition et d'ajuster individuellement le profil de champ de chaque antenne afin de compenser l'inhomogénéité du champ RF en haute fréquence.

Cependant, le développement de réseau d'antennes pour l'IRM haut champ est particulièrement difficile en raison de l'interaction complexe entre le champ électromagnétique haute fréquence et les tissus et de nombreux aspects cruciaux, tels que le découplage, l'efficacité de transmission, ou encore le TAS, doivent être attentivement évalués et optimisés. Dans ce contexte l'utilisation de logiciels de simulation électromagnétique 3D est devenue incontournable dans le processus de développement de réseaux d'antennes haut champ et de l'optimisation de leurs performances.

Les réseaux d'antennes sont en très grande majorité conçus pour être fabriqués sur des supports rigides et ne sont de fait pas flexibles. La non-flexibilité des réseaux se traduit par une conformation imparfaite à la surface d'échantillons de tailles et de formes différentes et entraîne une réduction significative du RSB. Au cours de la dernière décennie, quelques travaux ont concerné le développement de réseaux flexibles pour l'IRM et il a été montré que l'amélioration du couplage magnétique entre le réseau et l'échantillon rendue possible par la flexibilité améliorerait significativement la qualité des images. Le développement de réseaux flexibles impose plusieurs restrictions au regard des principes et des technologies pouvant être utilisées.

La technologie standard de fabrication d'antenne RF, basée sur l'utilisation de composants R-L-C discrets, impose des limites fortes en termes de flexibilité, dues principalement à la rigidité des conducteurs et à la fragilité mécanique des soudures. Ces problèmes sont particulièrement forts à très haut champ car l'enroulement des antennes doit être segmenté pour homogénéiser la distribution de courant et de nombreuses capacités doivent être soudées. Afin de contourner ces limitations, il est possible de développer des antennes basées sur le principe des résonateurs à ligne de transmission (TLR).

Les TLRs sont des structures monolithiques auto-résonantes qui peuvent être fabriquées sur des substrats très fins et souples. La fréquence de résonance d'un TLR est fixée par sa géométrie (diamètre, nombre de tours, nombre de gap, largeur des pistes, épaisseur du substrat) et par la permittivité du substrat. Ce type de structure est particulièrement avantageux pour le développement de réseaux d'antennes flexibles pour l'IRM à très haut champ car il permet de s'affranchir de l'utilisation de composants discrets, favorisant ainsi la flexibilité, la compacité et la légèreté du réseau. Dans la plus part des travaux relatifs à l'utilisation de TLR, la transmission du signal entre le TLR et la chaîne électronique de l'imageur a été réalisée par couplage inductif à l'aide d'une boucle de couplage placée à proximité du TLR. Il a été récemment rapporté que l'utilisation d'une boucle de couplage pouvait dégrader le RSB et distordre le champ radiofréquence. Dans le cas d'un réseau de TLRs, les boucles de couplage peuvent également dégrader le découplage mutuel entre les TLRs du réseau. Ces inconvénients peuvent être éliminés en utilisant un couplage capacitif qui consiste à connecter directement les TLRs à la chaîne d'acquisition à l'aide de capacités discrètes qui permettent de réaliser l'adaptation en puissance pour la transmission du signal. Il a été montré que le couplage capacitif était particulièrement intéressant pour les TLRs car il peut être mis en œuvre sans perturber la distribution de courant, préservant ainsi la cartographie du champ radiofréquence.

Cette technique peut toutefois compromettre la flexibilité et des solutions adaptées, utilisant par exemple des substrats hybrides composés de parties flexibles et de parties rigides, doivent être développées.

Un aspect critique lors de la conception d'un réseau concerne l'élimination du couplage magnétique mutuel entre les éléments du réseau. Le découplage entre antenne peut être réalisé de plusieurs façons, comme par le chevauchement partiel des antennes, l'insertion de composants L-C entre les antennes ou encore l'utilisation de préamplificateurs. Ces techniques ne sont toutefois pas adaptées aux réseaux de TLRs monolithiques et flexibles et de nouvelles solutions ont dûes être explorées. Récemment, le découplage d'un réseau de TLRs a été réalisé grâce à l'utilisation d'annexes de courant, petites boucles placées en série sur l'enroulement principal du TLR. Bien que cette technique préserve l'aspect monolithique des TLRs et n'altère pas la flexibilité du réseau, elle s'est révélée d'une efficacité limitée dans le cas où le couplage magnétique initial entre TLRs est trop fort. Une solution alternative pour annuler le couplage magnétique entre les éléments d'un réseau de TLRs est d'utiliser une technique basée sur l'ajout d'anneaux de découplage. Cette technique consiste à entourer chaque TLR par un anneau conducteur dans le but de créer un flux magnétique compensant le flux de couplage initial. Les anneaux de deux TLR adjacents sont déposés sur des faces opposées du substrat afin de permettre leur chevauchement et ainsi ajuster l'amplitude du flux de découplage.

Dans le contexte spécifique de l'IRM cardiaque à haut champ, l'utilisation de réseaux flexibles de TLRs est particulièrement intéressante car elle permet de développer des réseaux avec un poids réduit, assurant une couverture suffisante de la région cardiovasculaire et présentant une bonne adaptabilité aux différentes tailles et formes des torsos humains tout en garantissant la sécurité du patient et une facilité d'utilisation.

L'objectif de cette thèse était de développer un réseau flexible de TLR fonctionnant en émission et en réception pour l'IRM cardiaque à 7 T. Pour atteindre cet objectif, nous avons choisi d'utiliser la technique de couplage capacitif pour la transmission du signal et la technique d'anneau de découplage pour annuler le couplage mutuel entre les TLRs du réseau. Ce travail s'est déroulé dans le cadre d'une collaboration entre le Laboratoire d'Imagerie par Résonance Magnétique Médicale et Multi-Modalités (IR4M) at Université Paris-Sud (Orsay, France) et le Division MR Physics of the Center for Medical Physics and Biomedical Engineering of the Medical (CMPBME) de l'Université de Vienne (Autriche).

Chapitre 2: Théorie et contexte scientifiques

L'imagerie par résonance magnétique (IRM) est une modalité non-invasive qui est devenue un outil d'investigation clinique majeur et qui est basée sur le phénomène de résonance magnétique nucléaire (RMN). La RMN manipule les moments magnétiques des atomes dont le spin est différent de un. En l'absence de champ magnétique externe, les moments magnétiques sont orientés aléatoirement. L'application d'un champ magnétique, B_0 , se traduit par l'alignement de ces moments, soit dans le même sens que le champ appliqué (spins parallèles, niveau de plus basse énergie), soit dans le sens opposé (spins anti-parallèles, niveau de plus haute énergie). La résultante de cet alignement forme une aimantation (M_0) dont l'axe de précession est aligné selon B_0 et la fréquence angulaire notée fréquence de Larmor.

Au cours d'une expérience standard de RMN, une antenne radiofréquence (RF) est utilisée pour créer un champ magnétique alternatif, B_1 (dénommé champ RF), perpendiculaire au champ statique B_0 et qui produit le basculement de l'aimantation dans le plan transverse. Après l'arrêt du champ RF, l'aimantation retourne à sa position initiale, induisant une force électromotrice (fem) dans l'antenne RF. Cette fem, appelée signal de précession libre, décroît exponentiellement avec une constante de temps T_2^* . Le retour à l'équilibre de l'aimantation se décompose en deux décroissances, celle de la composante longitudinale (\vec{M}_z) et celle de la composante transversale (\vec{M}_{xy}), avec des constantes de temps respectives T_1 et T_2 , dont les valeurs différentes permettent d'obtenir des contrastes spécifiques.

Pour réaliser l'image 2D ou 3D d'un échantillon, le signal RMN capté par l'antenne RF doit être localisé spatialement. Cela se fait à l'aide de gradients de champ magnétique, permettant d'exciter des tranches de l'échantillon et ainsi coder le signal dans l'espace. Après avoir sélectionné une tranche par l'application d'un premier gradient, deux autres gradients sont utilisés pour réaliser un codage en fréquence et un codage en phase, discriminant ainsi le signal dans les trois directions de l'espace.

L'imagerie parallèle (PI) utilise des réseaux d'antennes RF pour détecter le signal RMN en provenance de l'échantillon et consiste à n'acquérir qu'une partie des composantes de ce signal. Cela permet, en plus d'une augmentation du rapport signal sur bruit (RSB), de réduire le temps de l'expérience d'IRM. La transmission parallèle (pTx) utilise également des réseaux d'antennes RF mais cette fois pour générer le champ RF produisant le basculement de

l'aimantation. Combinée à des impulsions RF sélectives, cela permet d'accélérer l'expérience d'IRM et de produire un champ RF plus homogène dans l'échantillon.

Dans une expérience d'IRM, le RSB de l'image obtenue dépend, d'un point de vue instrumental, de l'efficacité magnétique de l'antenne, qui traduit son aptitude à détecter un champ magnétique, et du niveau de bruits présents fixé principalement par les pertes propres de l'antenne et les pertes induites dans l'antenne par l'échantillon. Les pertes induites par l'échantillon résultent principalement du couplage magnétique entre l'antenne et l'échantillon et sont en général dominantes par rapport aux pertes propres de l'antenne, en particulier à haut champ. Dans le cas où les pertes de l'antenne sont dominantes, le RSB est alors limité par le bruit propre de l'antenne et peut être augmenté en réduisant la résistance de l'antenne, par l'utilisation d'antennes en cuivre refroidies ou d'antennes en matériaux supraconducteurs.

Les antennes radiofréquence (RF) permettent de faire le lien entre l'échantillon à imager et l'appareil d'IRM en réalisant l'émission et la détection des signaux RF pendant l'expérience d'IRM. Afin d'assurer le transfert d'énergie avec le système de spins, l'antenne doit être accordée à la fréquence de Larmor. Un champ magnétique linéairement polarisé peut être décomposé en deux composantes polarisées circulairement et tournant en sens inverse. Ces composantes sont le champ B_1^+ , tournant dans le sens horaire, et le champ B_1^- , tournant dans le sens anti-horaire par rapport au champ statique B_0 . Seule la composante tournant dans le même sens que la précession des spins, c'est-à-dire B_1^+ , est à considérer pour la génération du champ à l'émission. La composante B_1^- est quant à elle impliquée dans la détection du signal RMN produit par les spins pendant la phase de relaxation. En général, les antennes RF sont optimisées pour obtenir un RSB élevé et produire un champ RF homogène dans l'échantillon. Les antennes de volume (solénoïde, cage d'oiseau, selle de cheval) entourent complètement la zone à imager et sont avantageuses pour les applications en IRM requérant un champ RF homogène sur une grande région d'intérêt. Les antennes de surface (boucle conductrice) sont placées à la surface de la zone à imager. Elles permettent d'obtenir un RSB supérieur à celui des antennes de volume, grâce à un meilleur couplage magnétique avec l'échantillon et une diminution du bruit induit par celui-ci, mais donnent accès à un champ de vue plus réduit que les antennes de volumes. Les antennes de surfaces conventionnelles sont réalisées à l'aide d'un enroulement conducteur aux bornes duquel sont soudées des capacités pour réaliser l'accord et l'adaptation en puissance. Une alternative à la technologie conventionnelle pour le développement d'antenne d'IRM est l'utilisation de résonateurs à ligne de transmission (TLR). Ces structures monolithiques auto résonantes permettent de s'affranchir de l'utilisation de composants

discrets et autorisent de fait une forte réduction de la taille de l'antenne et la réalisation d'antennes très fines et flexibles.

Les réseaux d'antenne permettent de bénéficier de la très haute sensibilité des antennes de surface de petites tailles tout en accédant à un champ de vue élargi, comparable à celui des antennes de volumes. Les réseaux d'antennes sont utilisés en réception en imagerie parallèle pour accélérer la formation de l'image ainsi d'en émission en transmission parallèle pour optimiser l'homogénéité du champ d'excitation. Ce dernier point étant particulièrement critique à haut champ. La principale difficulté dans le développement de réseaux d'antenne concerne l'annulation du couplage magnétique entre les antennes constituant le réseau. Plusieurs techniques sont utilisées classiquement pour découpler les antennes d'un réseau. Il est possible de chevaucher les antennes entre elles, afin de créer un flux magnétique opposé au flux de couplage initial, mais cette technique entraîne un recouvrement des profils de sensibilité des antennes et limite les possibilités d'accélération en imagerie parallèle. Une technique courante est de souder des condensateurs et/ou des inductances entre chaque antenne afin de réaliser une transformation d'impédance et ainsi bloquer le courant induit entre antenne. Cette technique utilise des composants soudés sur l'enroulement et est peu compatible avec le caractère monolithique des TLRs et limite fortement la flexibilité accessible. Une solution comparable dans le principe consiste à connecter des préamplificateurs et des capacités aux bornes de l'antenne afin de bloquer le courant induit. Cette technique n'est toutefois pas utilisable en émission et n'est pas adaptées aux TLRs et aux réseaux flexibles. Une solution originale utilisant des annexes de courant placées en série sur l'enroulement de l'antenne a été proposée et mise en œuvre avec succès pour découpler les TLRs d'un réseau. Cette solution préserve le caractère monolithique des TLR et n'altère pas la flexibilité mais s'est révélés d'une efficacité limitée dans le cas de TLR de grand diamètre ou déposer sur des substrats épais. Très récemment, une technique de découplage utilisant des anneaux de découplage a été spécifiquement développée pour un réseau de TLR. Cette technique consiste à entourer chaque TLR du réseau par un anneau conducteur, les anneaux voisins étant déposés sur des faces opposées du substrat afin de permettre leur chevauchement en vue d'optimiser le découplage mutuel. Cette technique de découplage ne dépend pas de la fréquence de travail et n'impose pas de restriction quant à la taille des TLRs pouvant être découplés.

En marge du développement du réseau proprement dit, il est nécessaire de développer l'ensemble des blocs fonctionnels requis pour une utilisation en IRM. Ces blocs permettent d'effectuer la commutation émission/réception du réseau, de distribuer la puissance d'émission

aux différents éléments du réseau, de réduire le mode commun dans les câbles, de pré-amplifier le signal détecté, et d'accorder et adapter en puissance chaque antenne à la réception.

Pour évaluer les performances d'une antenne, ou d'un réseau d'antennes, plusieurs outils et techniques sont utilisées à différentes étapes du développement. En premier lieu, des logiciels de simulation électromagnétiques 3 D sont utilisés pour la conception des antennes et l'optimisation des circuits électroniques associés. La simulation électromagnétique permet d'estimer le découplage entre éléments d'un réseau, l'efficacité de transmission, l'énergie déposée dans les tissus, ainsi que le profil de sensibilité en détection. Après fabrication, il est nécessaire de qualifier l'antenne par des mesures électromagnétiques réalisées sur banc de mesure. Cela permet de déterminer la fréquence de résonance effective de l'antenne, son facteur de qualité à vide et en charge, renseignant sur les différents mécanismes de pertes présents, ainsi que le facteur de sensibilité de l'antenne, correspondant au champ radiofréquence créé par unité de courant dans l'antenne. Enfin, avant de pouvoir utiliser une antenne dans le cadre d'une application donnée, il est nécessaire de valider son bon fonctionnement par des expériences d'IRM réalisées sur fantômes, reproduisant au mieux les conditions réelles d'imagerie sur l'homme.

Outre une forte sensibilité et homogénéité de détection, les antennes utilisées en IRM cardiaque doivent vérifier plusieurs critères, tels qu'un poids réduit, un champ de vue latéral couvrant la région cardiovasculaire et une profondeur de sensibilité incluant l'ensemble du cœur, une adaptabilité à l'anatomie du patient, et le respect des normes de sécurité. Les différents travaux menés dans ce domaine ont montré l'intérêt d'utiliser des réseaux 2D à grand nombre d'éléments car ils permettent une meilleure optimisation du champ B_1 , améliorent la sensibilité de détection en imagerie parallèle et l'efficacité de transmission quand ils sont utilisés avec un système de transmission multi-canaux. La plus part des réseaux développés pour l'IRM cardiaque utilise deux parties, l'une placée au-dessus du torse et l'autre sous le dos afin d'augmenter la zone de sensibilité. Certains travaux ont concerné l'amélioration de l'adaptabilité du réseau à l'anatomie du torse en utilisant des circuits imprimés flexibles ou en combinant plusieurs sous-réseaux modulaires pour ajuster spécifiquement la forme de la zone observée. Malgré les avancées réalisées au cours de ces travaux, de nombreux enjeux persistent pour améliorer les performances spécifiques des réseaux en IRM cardiaque à haut champ, tant sur les aspects de flexibilité que de sensibilité de détection et homogénéité du champ d'excitation.

Chapitre 3: Conception, développement et test d'un réseau de TLRs flexible à 12 éléments pour l'IRM à 7T.

L'objectif de ce projet doctoral était de développer un réseau de TLRs flexible pour l'IRM du proton à 7T. Nous avons pour cela effectué des simulations électromagnétiques 3D à l'aide du logiciel XFDTD couplées à des co-simulations électriques avec le logiciel ADS, des mesures électromagnétiques sur table avec un analyseur de réseaux, et des caractérisations en IRM sur un appareil clinique de 7T.

L'utilisation de TLRs comme élément individuel du réseau a été retenue en raison de la nature intrinsèquement monolithique de ces structures et de leur grande flexibilité lorsqu'ils sont fabriqués sur substrat souple. Pour valider le choix d'utiliser des antennes basées sur le principe des TLRs au lieu d'utiliser des antennes standards en technologie R-L-C, nous avons comparé par simulation électromagnétique les performances d'un TLR avec celles d'une antenne de surface simple boucle standard de même dimension. Aucune différence notable n'a été observée. Le diamètre initial des TLRs constituant le réseau a été choisi au regard du champ de vue nécessaire pour une application en imagerie cardiaque ainsi que des mécanismes de pertes à 7T. L'optimisation de la géométrie (largeur des pistes, diamètre final, nombre de tour, nombre de gap) a ensuite été réalisée par simulation électromagnétique. Les caractéristiques géométriques des TLRs utilisés sont indiquées sur la figure 1.

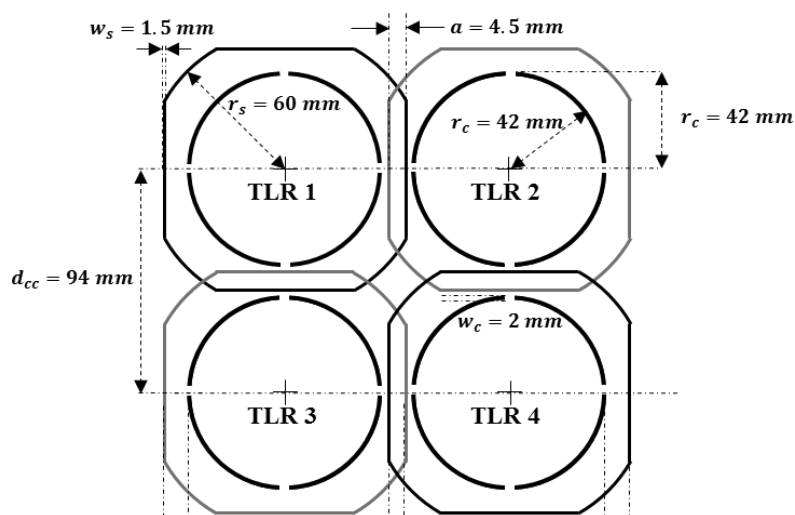


Figure 1: Réseau de TLRs à 4 éléments avec anneau de découplage

Au cours de cette thèse, nous avons étudié une technique de découplage basée sur l'utilisation d'anneaux conducteurs afin d'éliminer le flux magnétique partagé entre les éléments du réseau.

L'efficacité de cette technique a été évaluée et optimisée par étape, d'abord dans le cas d'un seul TLR puis dans le cas d'un réseau de TLR. Afin de ne pas altérer la distribution de courant intrinsèque dans l'enroulement d'un TLR, nous avons utilisé une technique de couplage capacitive pour réaliser l'adaptation en puissance et l'accord individuel des TLRs.

L'optimisation du découplage mutuel entre éléments voisins du réseau, consistant à déterminer la configuration optimale des anneaux (taille et niveau de chevauchement) a été réalisée à la fois par modélisation analytique du flux magnétique et par simulation électromagnétique dans le cas d'un réseau de 4 TLRs comme représenté sur la figure 1. Les caractéristiques géométriques des anneaux de découplage indiquées sur cette figure correspondent à un découplage optimal.

Les résultats de cette optimisation sont présentés ci-dessous, pour le calcul analytique (figure 2) et pour la simulation électromagnétique (figure 3).

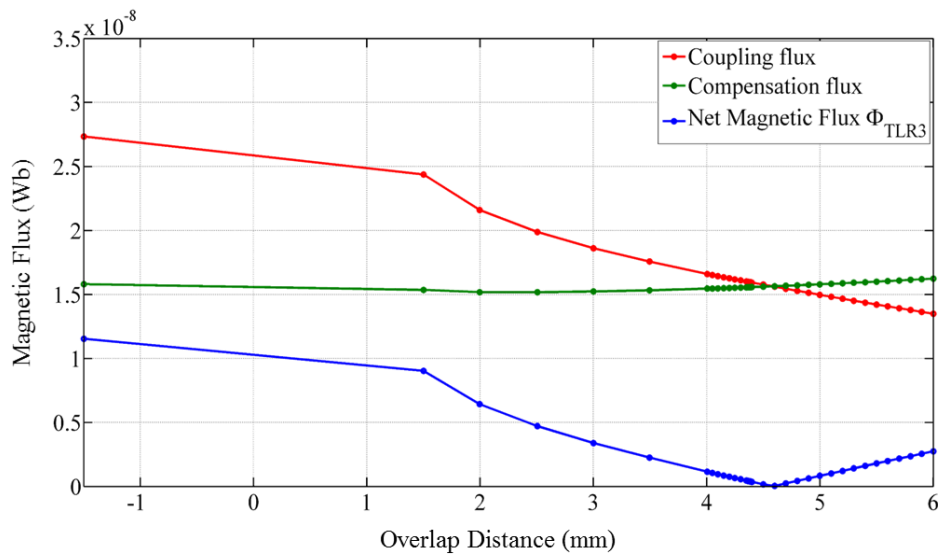


Figure 2: Variation des flux de couplage et de découplage entre les éléments 3 et 4 du réseau, calculés analytiquement en fonction du niveau de chevauchement des anneaux.

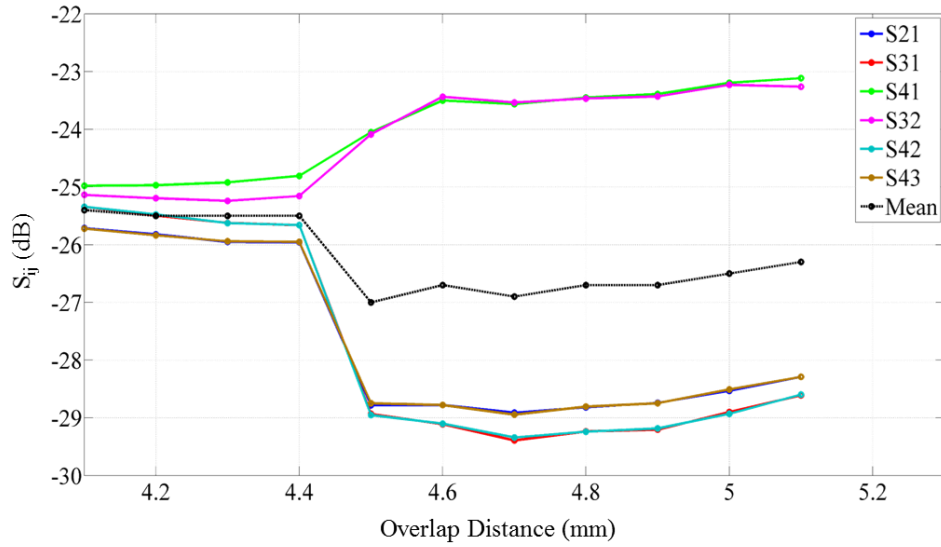


Figure 3. Variation des paramètres S des éléments du réseau déterminées par simulation électromagnétique en fonction du niveau de chevauchement des anneaux.

A l'issue de cette optimisation, nous avons retenu une distance de chevauchement entre anneau de 4, 5 mm, valeur pour laquelle la moyenne des paramètres S est la plus faible (- 27 dB)

En parallèle de l'optimisation du découplage, l'effet de l'anneau de découplage sur les performances d'un TLR a été évalué, à la fois par simulation électromagnétique 3D et par expérience d'IRM, en analysant l'efficacité de transmission, $(B_1^+ / \sqrt{P_{\text{input}}})$, le TAS, et la qualité de l'image obtenue. A titre représentatif, les cartes de $(B_1^+ / \sqrt{P_{\text{input}}})$ sont représentées ci-dessous.

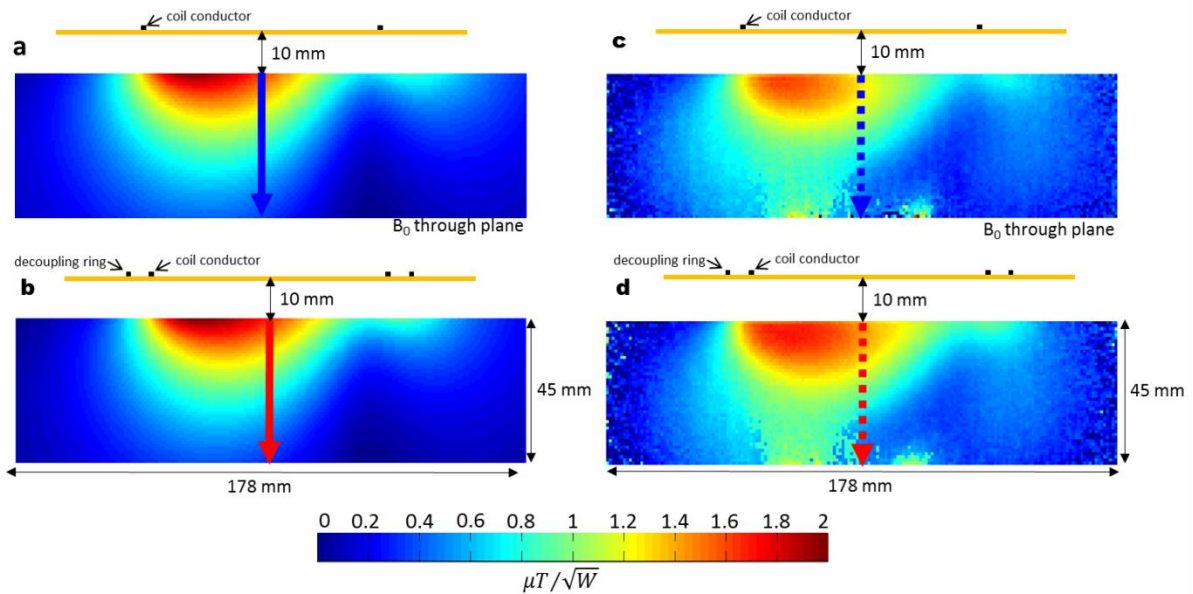


Figure 4. Cartes d'efficacité de transmission $(B_1^+ / \sqrt{P_{\text{input}}})$ simulées pour un TLR sans (a) et avec (b) un anneau de découplage et mesurées pour un TLR sans (c) et avec (d) un anneau de découplage.

Suite à l'optimisation de la géométrie des éléments individuels et des anneaux de découplage, nous avons conçu un réseau de 12 éléments (4 colonnes, 3 lignes) comme représenté sur la figure 5.

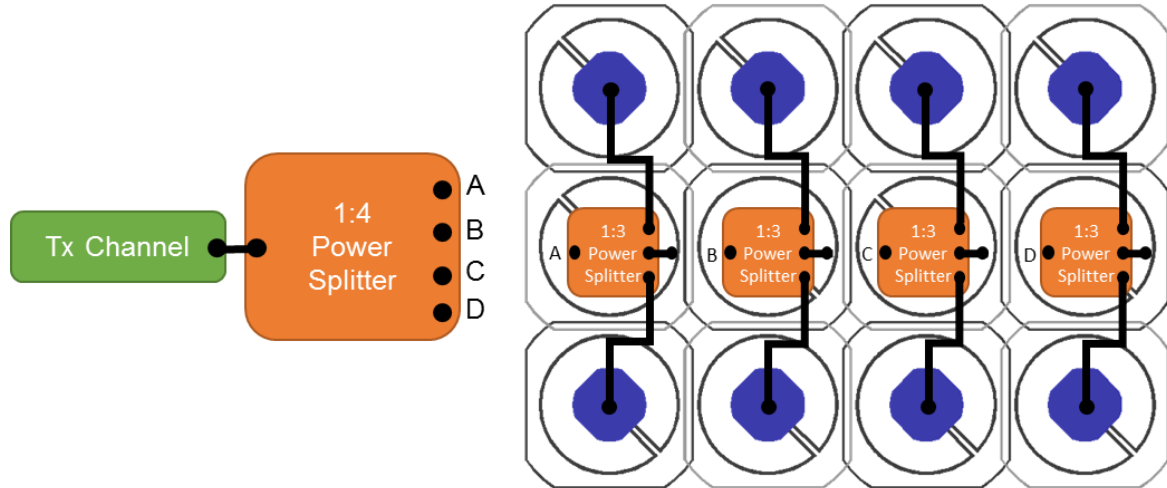


Figure 5: Schéma de principe du réseau à 12 éléments.

Pour ajuster la phase du signal d'entrée des éléments du réseau, nous avons considéré l'homogénéité du champ RF B_1^+ , l'efficacité de transmission ($B_1^+ / \sqrt{P_{\text{input}}}$), ainsi que le TAS afin d'assurer la sécurité du patient et l'efficacité du réseau dans un contexte d'IRM clinique. Au cours de cette procédure d'ajustement, nous avons fait varier les phases entre chaque colonne du réseau et maintenu identiques les phases des éléments d'une même colonne.

Afin de pouvoir utiliser les 12 éléments du réseau en mode émission/réception, nous avons conçu, fabriqué et intégré à chaque élément une carte électronique d'interfaçage contenant un commutateur émission/réception, un diviseur de puissance, un préamplificateur faible bruit et un réseau capacitif d'accord et d'adaptation en puissance.

La figure ci-dessous présente une photo de la carte d'interfaçage et du boîtier dans laquelle elle est enfermée.

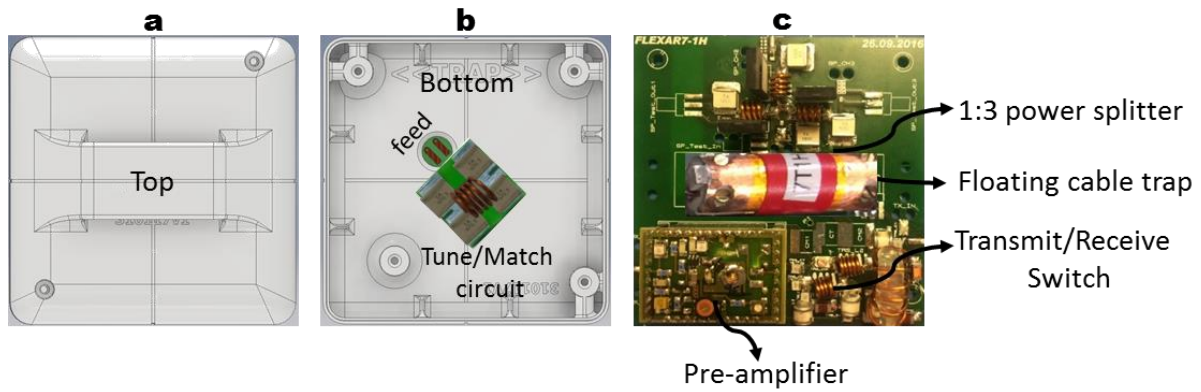


Figure 6: Capot supérieur (a) et socle (b) du boîtier contenant la carte d'interface (c).

Le réseau complet fabriqué est représenté ci-dessous :

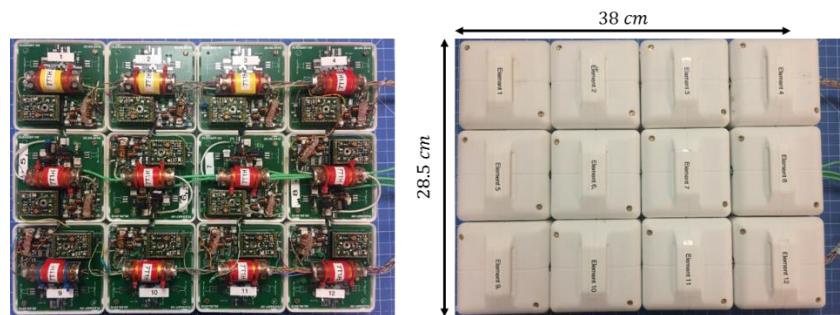


Figure 7: Photo du réseau final sans capot (gauche) et avec capot (droite).

Les performances (découplage mutuel, efficacité de transmission, corrélation de bruit, SNR) du réseau développé ont ensuite été évaluées en configuration plane par simulation électromagnétique 3D, mesure sur table et en IRM, ainsi qu'en configuration courbée par mesure sur table et en IRM.

Les paramètres S du réseau en configuration plane simulées et mesurées sur table, traduisant l'efficacité de découplage, sont présentées dans le tableau ci-dessous.

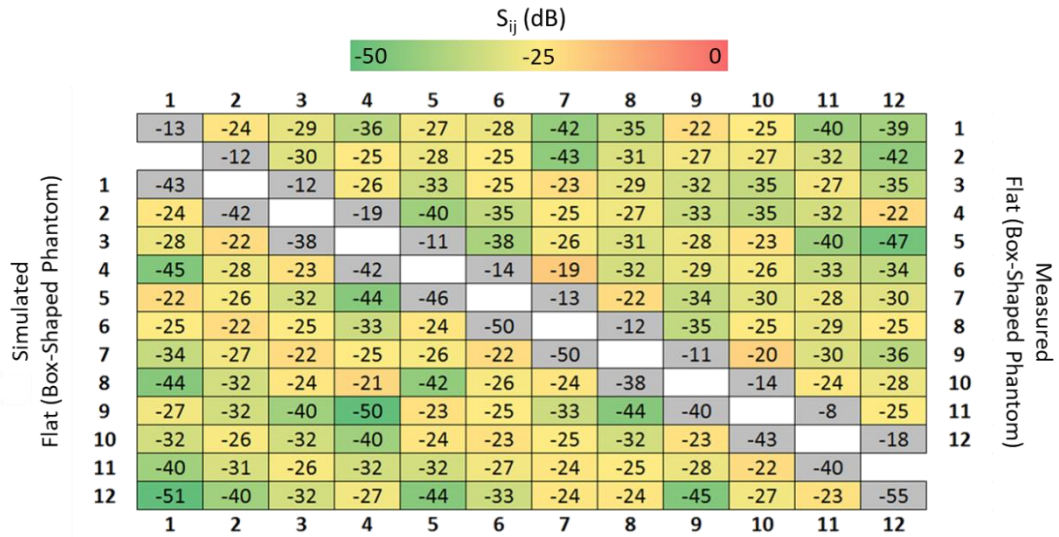


Figure 8: Paramètres S simulées et mesurées avec le réseau de 12 éléments placé en configuration plane sur un fantôme rectangulaire.

Les paramètres S ont aussi été déterminées par mesure sur table en configuration courbée lorsque le réseau était conformé à un fantôme de torse et conformé sur le torse d'un volontaire. Les résultats sont présentés dans le tableau ci-dessous.

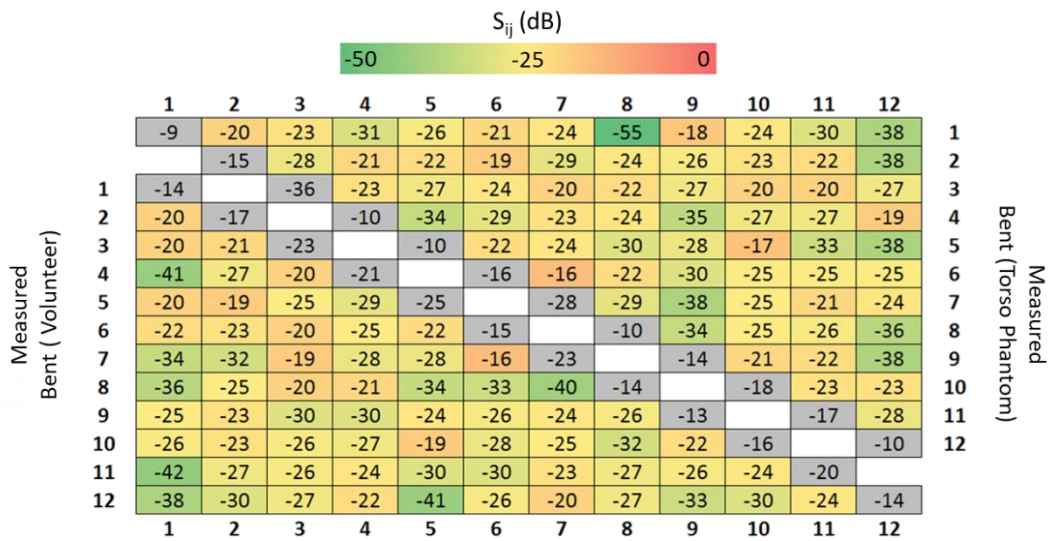


Figure 9: Paramètres S mesurées avec le réseau de 12 éléments placé en configuration courbée sur un fantôme de torse et sur le torse d'un volontaire.

Afin de déterminer la puissance effectivement transmise depuis l'imageur jusqu'aux éléments du réseau, les pertes présentes dans l'ensemble de la chaîne électronique (câbles, carte d'interfaçage) ainsi que les déphasages entre chaque colonne du réseau ont été calculés à partir des paramètres S mesurées sur table. La détermination de ces pertes a ensuite été utilisée pour

normaliser les cartes d'efficacité de transmission ($B_1^+ / \sqrt{P_{input}}$) obtenues par simulation et celles obtenues expérimentalement en IRM. Les résultats sont présentés figure 10.

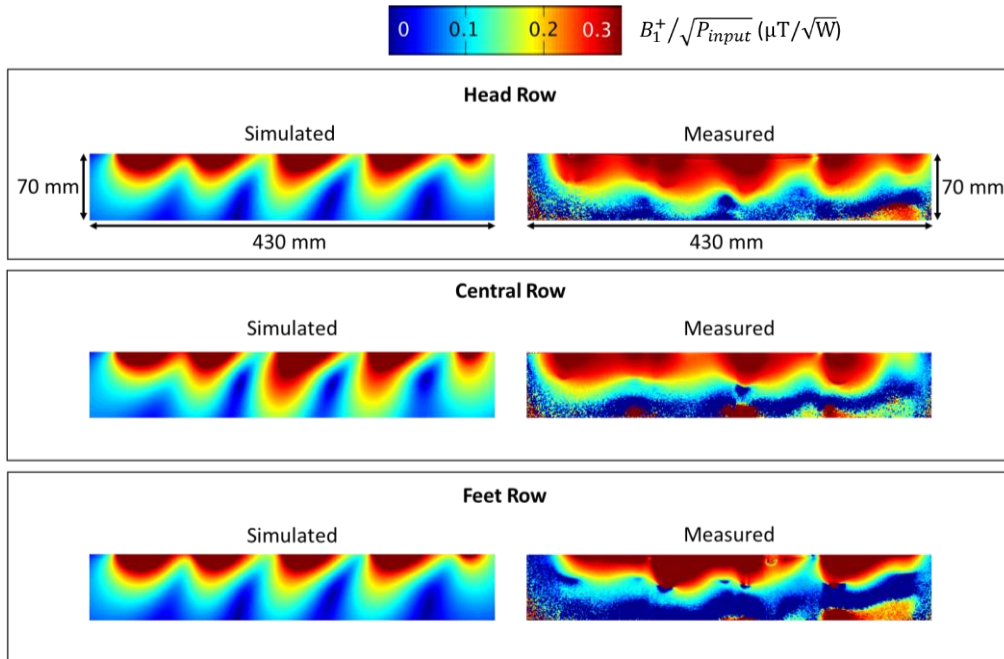


Figure 10: Cartes d'efficacité de transmission dans le plan transverse simulées et mesurées pour les trois colonnes du réseau lorsque le réseau est positionné à plat sur un fantôme rectangulaire.

L'efficacité de transmission a également été déterminée expérimentalement en IRM lorsque le réseau était conformé au fantôme de torse. Les cartes correspondantes sont présentées ci-dessous.

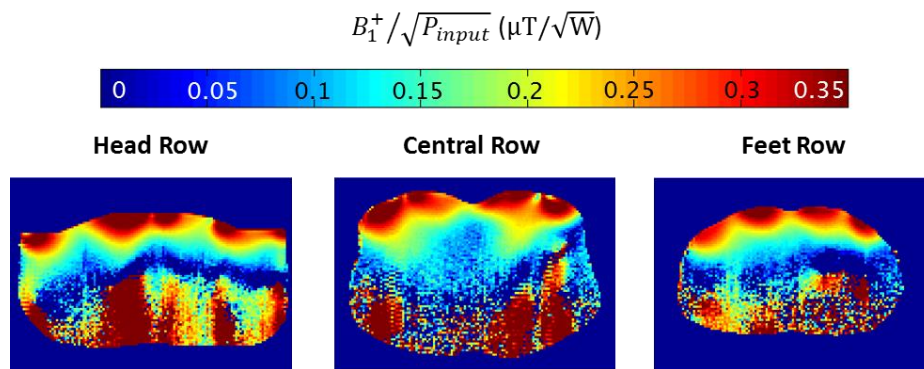


Figure11: Cartes d'efficacité de transmission mesurées en IRM pour les 3 colonnes du réseau lorsqu'il est conformé à un fantôme de torse.

Afin d'évaluer la conformité du réseau développé au regard de la sécurité du patient, nous avons utilisé le logiciel SimOptx afin de calculer le taux spécifique d'absorption (TAS) à partir des données de simulation électromagnétiques issues de XFDTD. Pour des raisons de capacité

de calculs, cela n'a été fait qu'en configuration plane. Pour estimer le dépôt d'énergie effectivement déposé lors d'une expérience d'IRM, nous avons utilisé les valeurs mesurées de la phase et de l'amplitude de la puissance délivrée à chaque élément du réseau ainsi que la mesure des pertes de la chaîne de transmission. Les cartes de TAS ainsi obtenues sont présentées figure 12.

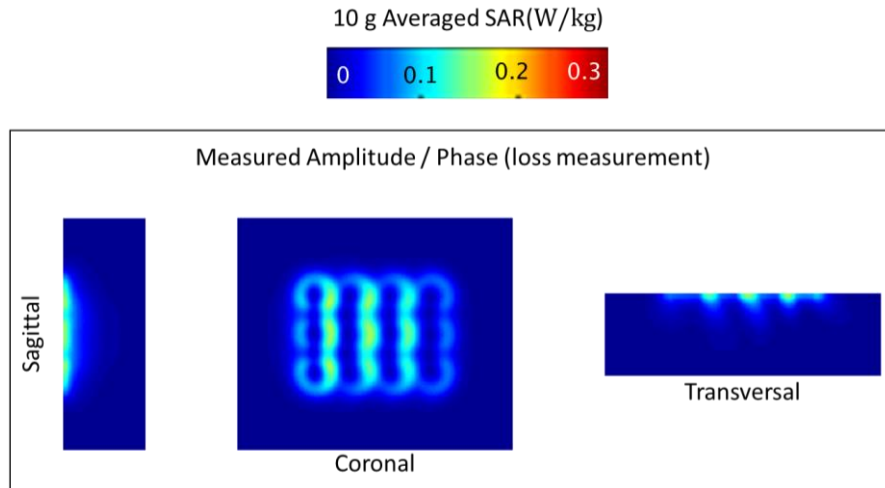


Figure 12: TAS moyen pour 10g en configuration plane.

Nous avons évalué les performances en imagerie parallèle à l'aide d'une technique de réplica pseudo-multiple et la méthode de reconstruction grappa. Nous avons déterminé la matrice de corrélation de bruit du réseau (figure 13) en configuration plane et courbée à partir de cartes de bruit acquises sur fantôme. Les valeurs obtenues sont satisfaisantes au regard des performances usuelles rapportées dans la littérature.

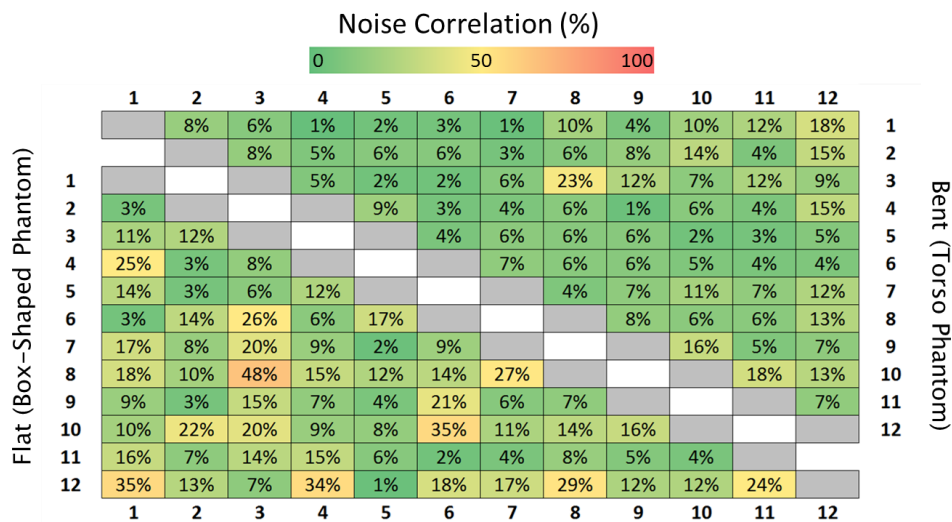


Figure 13: Matrice de corrélation de bruit du réseau en configuration plane et courbée acquise sur fantôme.

Nous avons utilisé une séquence 2D d'écho de gradient pour acquérir des images de fantôme en configuration plane et courbée (figure 14) avec des facteurs d'accélération de 1, 2, 3 et 4 et nous avons déterminé les cartes de RSB (figure 15) et de g-facteur (figure 16) correspondantes.

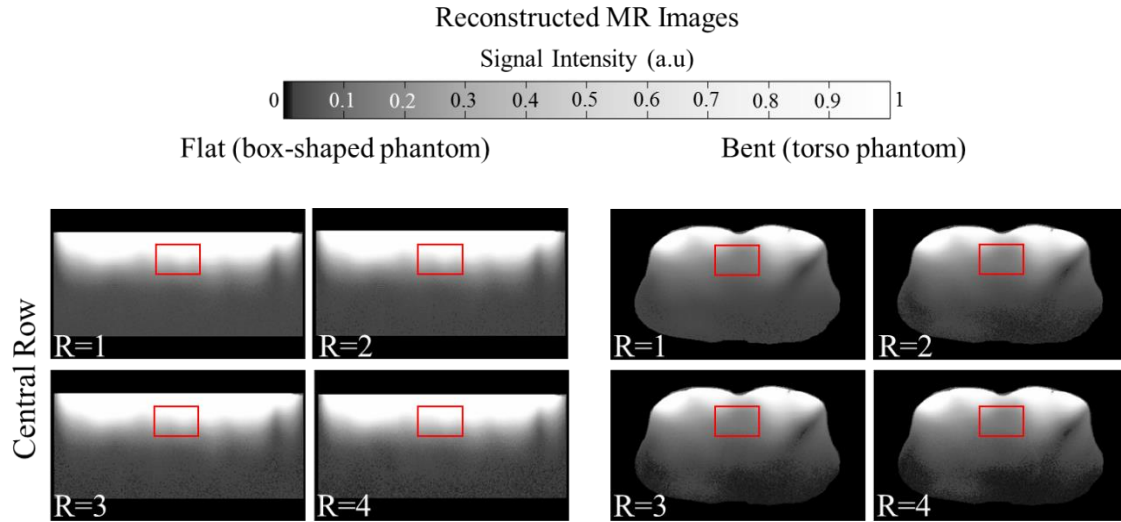


Figure 14. Coupes d'IRM transverses acquises par la colonne centrale du réseau en configuration plane sur le fantôme rectangulaire et courbée sur le fantôme de torse pour différentes valeurs du facteur d'accélération.

Aucune dégradation des performances du réseau n'a été observée en configuration courbée, démontrant ainsi la robustesse du réseau vis à vis de la flexibilité.

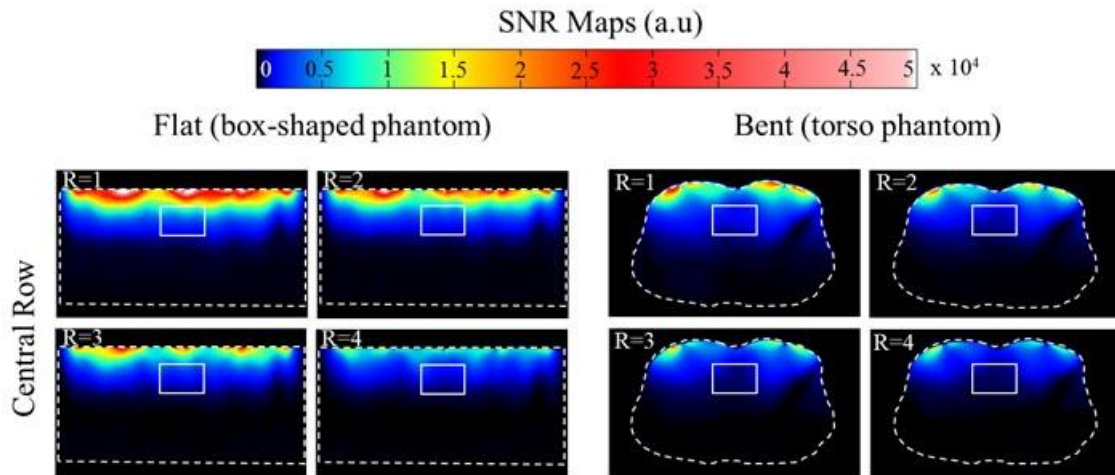


Figure 15: Cartes de RSB mesurées sur fantômes avec le réseau en configuration plane et courbée pour différents facteurs d'accélération.

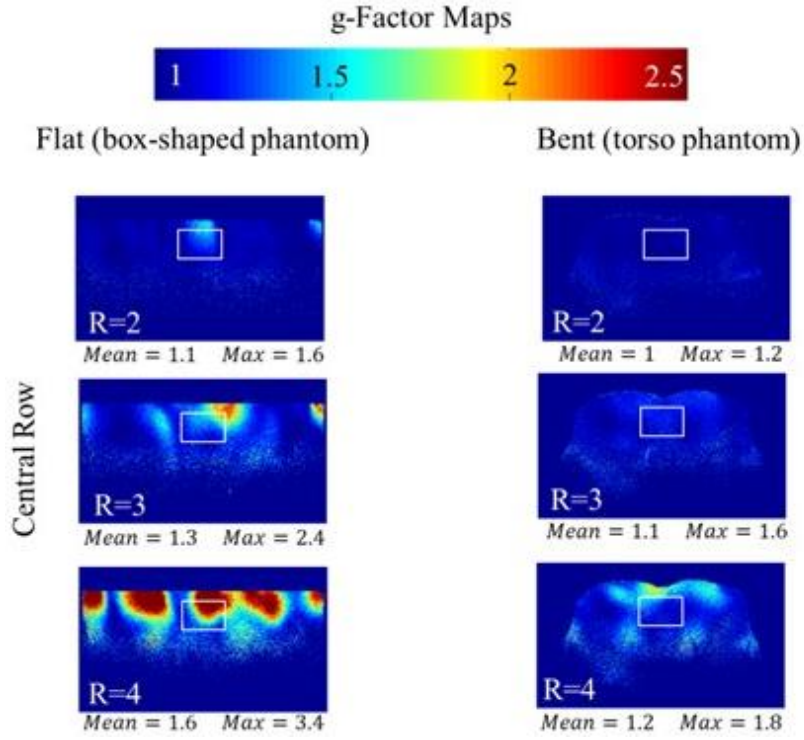


Figure 16: Cartes de g-facteur mesurées sur fantômes avec le réseau en configuration plane et courbée pour différents facteurs d'accélération.

Des facteurs d'accélération jusqu'à trois peuvent être utilisés sans dégrader significativement les performances en imagerie.

Nous avons également réalisé des images dans le plan coronal avec le réseau en configuration plane (figure 17) et déterminé les cartes de RSB et g-facteurs associées (figure 18). Les résultats obtenus pour deux coupes situées respectivement 2 cm et 4 cm au-dessus du plan du réseau sont présentés ci-après.

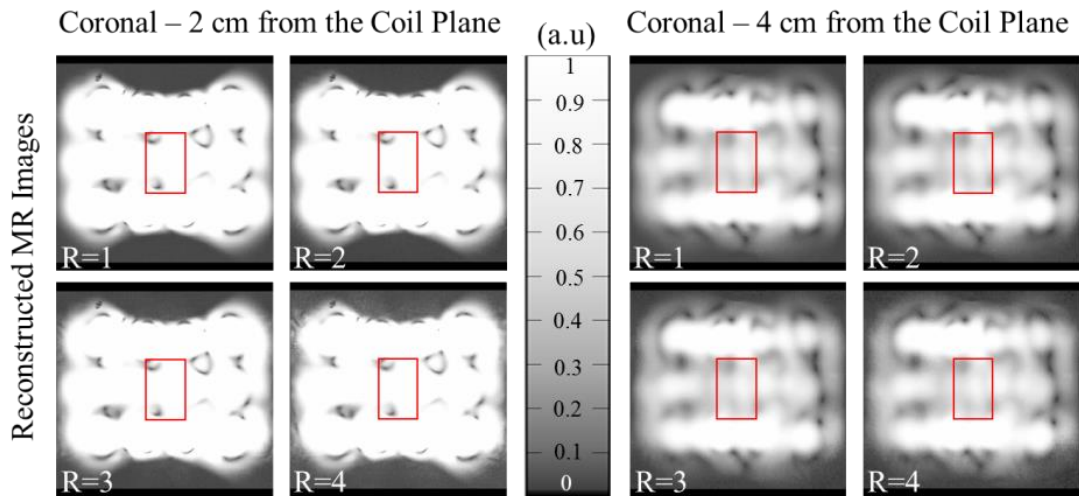


Figure17. Coupes d'IRM coronales de fantôme, situées 2 et 4 cm au-dessus du plan du réseau acquises par la colonne centrale du réseau en configuration plane pour différentes valeurs du facteur d'accélération.

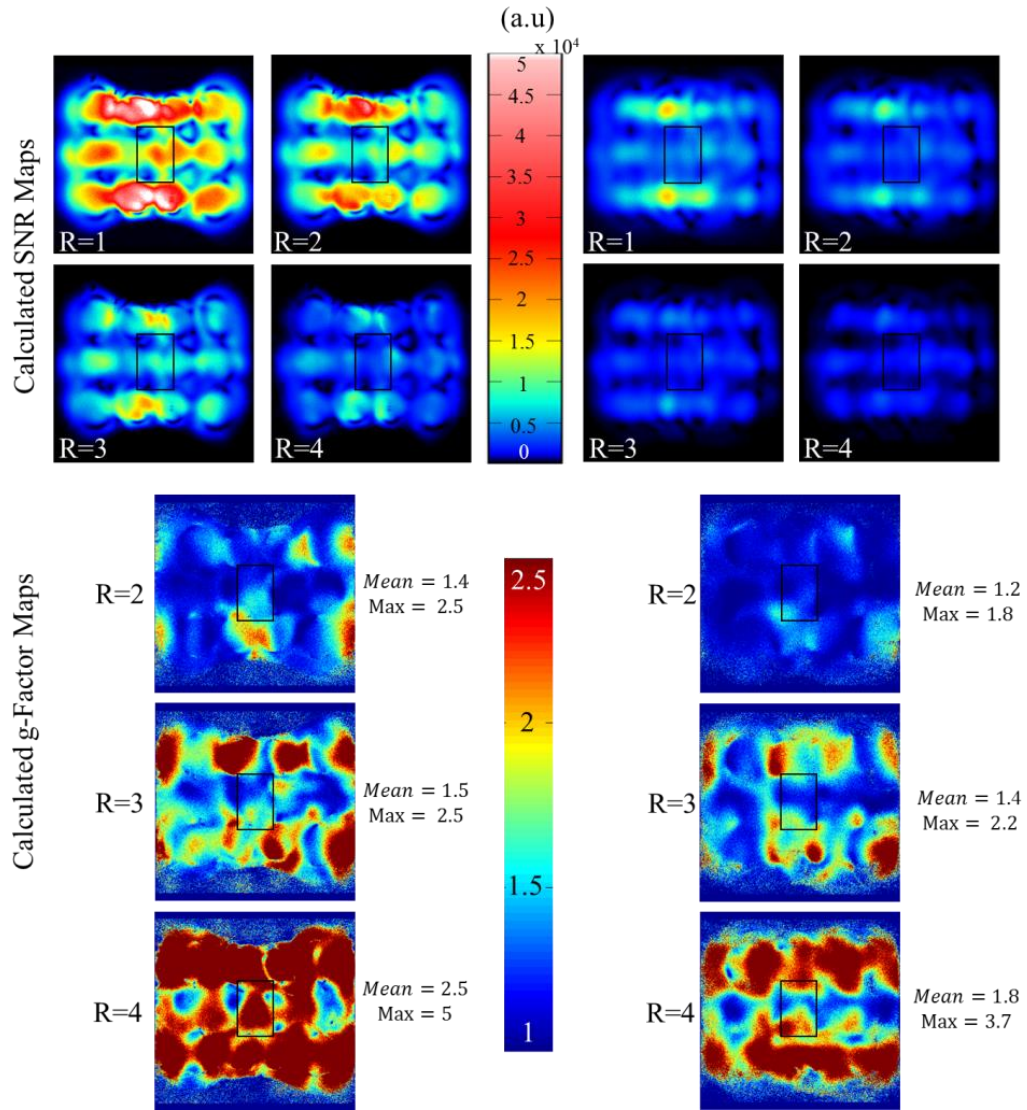


Figure 18: Cartes de RSB et g-facteur mesuré sur fantôme avec le réseau en configuration plane pour différents facteurs d'accélération. Et pour des coupes situées à 2 cm et 4 cm au-dessus de plan du réseau.

Chapitre 4: Discussion, Conclusion et Perspectives

Au cours de ce travail, nous avons développé avec succès un réseau flexible à 12 éléments basé sur le principe des TLRs utilisant des anneaux de découplage et fonctionnant en émission/réception pour l'IRM à 7T. La flexibilité du réseau permet une conformation à la surface d'échantillons de tailles et formes variables, optimisant ainsi la sensibilité de détection en IRM. Par ailleurs, ce réseau est compatible avec les techniques d'imagerie parallèle et de transmission parallèle, autorisant l'accélération de l'acquisition du signal et l'homogénéisation du champ RF d'excitation.

Nous avons pu établir, par simulation électromagnétique 3D et expérimentalement en IRM que l'utilisation d'anneaux de découplage ne dégradait pas les performances en transmission des TLRs. De plus, nous avons montré en IRM que la qualité des images n'était pas affectée par la présence d'anneau de découplage. En parallèle, la comparaison d'un TLR avec une simple boucle segmentée a révélé qu'aucune différence notable n'était observée sur les performances électromagnétiques.

Les performances du réseau ont été évaluées sur table et en IRM lorsque celui-ci était conformé à la surface d'un fantôme de torse. Les paramètres S, la matrice de corrélation, le RSB ainsi que les cartes de g-facteurs se sont avérées robuste au regard de la déformation mécanique du réseau. Nous avons pu acquérir des images de fantôme de torse avec un facteur d'accélération de 3 sans observer de dégradation significative du RSB.

Dans cette thèse, une technologie hybride combinant des circuits imprimés rigides et des matériaux souples a été utilisée rendant possible l'intégration de l'ensemble des composants électroniques nécessaires au conditionnement du signal tout en préservant la flexibilité du réseau. Nous avons également conçu un boîtier spécifique maintenant la flexibilité du réseau et garantissant l'isolation entre les composants et le patient. Le réseau ainsi obtenu est particulièrement avantageux pour l'IRM cardiaque, application dans laquelle la taille et la forme du torse présentent une grande variabilité inter-patient.

L'une des perspectives de ce travail est de combiner le réseau développé au cours de cette thèse avec un réseau pour la spectroscopie du phosphore. Il faudra alors surmonter les verrous liés au découplage des éléments du réseau ^{31}P , aux interférences entre les deux réseaux et à la préservation de la flexibilité de l'ensemble. Il est aussi envisagé de développer un second réseau pour l'IRM du proton afin de le placer à l'arrière du torse et augmenter ainsi le champ

de vue accessible et l'homogénéité du champ d'excitation. Dans le but d'utiliser le réseau développé avec un système de transmission multi-canaux, il sera nécessaire de modifier les circuits électroniques pour permettre une utilisation en transmission parallèle, tel que la suppression des distributeurs de puissance entre éléments centraux du réseau.

Il n'a pas été possible d'effectuer de simulation électromagnétique du réseau en configuration courbée en raison de la complexité et de la densité du maillage nécessaire ainsi que du temps de calcul rédhibitoire que cela entraîne. Cette étape est toutefois indispensable pour certifier le réseau et permettre son utilisation in-vivo. Une stratégie possible consiste à simuler séparément les éléments latéraux du réseau et les éléments centraux. Afin de prendre en compte la courbure du réseau et la position inclinée des éléments latéraux tout en maintenant le maillage utilisé pour la configuration plane, l'ensemble de l'espace de simulation pourrait être tourné selon l'axe du champ statique pour placer horizontalement les éléments latéraux du réseau. A l'issue des simulations en configuration courbée, la procédure de certification au regard des critères dictés par les trois directives européennes standardisées pour les dispositifs médicaux pourra être réalisée. Son obtention permettra à terme d'utiliser ce réseau en protocole de recherche clinique et d'envisager sa commercialisation.

1 Introduction

1.1 Thesis Outline

This PhD thesis was conducted in the frame of a bilateral project between the Laboratoire d'Imagerie par Résonance Magnétique Médicale et Multi-Modalités (IR4M) at Université Paris-Sud (Orsay, France) and the Division MR Physics at the Center for Medical Physics and Biomedical Engineering of the Medical (CMPBME) University of Vienna (Austria). The main objective of this work was to develop a flexible transceiver RF coil array for 7 T cardiac MRI.

This thesis contains four chapters organized as follows:

Chapter 1 provides a general introduction of MRI followed by a motivation section discussing the available methodologies to design coil arrays tailored for cardiac MRI at UHF justifying the work performed in the scope of this thesis.

The theory and background of MRI and RF coils are presented in chapter 2, starting with the fundamentals of NMR to image formation in MRI experiments explaining principles of NMR, signal and noise in MRI experiments, and MR signal generation and acquisition techniques. The chapter is continued by an overview of the principles of RF coils and numerical electromagnetic simulation methods. Finally, this chapter is summed up by giving an overview of the current state of the art in methodology and hardware for cardiac MRI and the associated challenges at UHF.

Chapter 3 is the main part of this thesis where the design, implementation and performance evaluation of the developed flexible transceiver TLR array are described. The methodology used to design a 12-element flexible TLR array is presented step by step from the single coil element to the final array.

Chapter 4 contains a detailed discussion about the achievements and limitations of the work performed, followed by the conclusions of the thesis, leading to perspectives concerning related future work and follow-up projects.

The Appendix describes the derivation of the resonance condition for TLRs and the analytical model for decoupling optimization based on decoupling rings.

The references and lists of figures and tables together with a publication list and CV of the author are presented at the end of this manuscript.

1.2 General Introduction

Magnetic resonance imaging (MRI) is a non-invasive imaging method which is widely used to obtain high resolution in-vivo images. MRI is based on the principle of nuclear magnetic resonance (NMR), i.e. it uses the atomic nuclei magnetic properties in the presence of a strong static magnetic field (B_0) and a time varying magnetic field (B_1) produced by a radio frequency (RF) coil to acquire in-vivo images.

The image quality in MRI depends on the achievable signal to noise ratio (SNR). The SNR can be improved by increasing the strength of B_0 field, optimizing the RF coil detection sensitivity and developing optimized imaging sequences in terms of image reconstruction techniques and parameters. In addition, contrast agents such as gadolinium can be used to improve the visibility of the structures in MRI.

Clinically available MR systems (1.5 - 3 T) are typically equipped with a single transmit channel and an RF volume coil referred to as body coil which is integrated inside the magnet bore and several receive channels associated with receive coil arrays. Receiver arrays combine the advantages of the intrinsically high SNR of surface coils (1) with an extended field of view (FOV) and give access to parallel imaging techniques allowing for accelerated imaging (2,3). Modern clinical MRI scanners are equipped with multi-channel transmit systems which give access to the parallel transmission (pTx) technique. Transmit body coils aim to produce a high and homogeneous B_1 over the region of interest and are very efficient and widely used at clinical strength. However, they are not suited for UHF systems due to propagation effects associated with the reduced wave length leading to strong B_1 inhomogeneity. Another issue in UHF MRI is the amount of power deposited in the body referred to as specific absorbed rate (SAR), which increases with frequency. High SAR leads tissue heating and should therefore be avoided. For these reasons, dedicated local transmit coil have to be used at UHF MRI. A common strategy is to employ the coil, or coil array, as transceiver, i.e. for both transmissions and reception purposes.

The development of transceiver arrays for UHF MRI is however challenging due to the complex interactions between coil and human body at high frequency and makes the use of advanced numerical full-wave 3D electromagnetic simulation (EMS) mandatory to correctly evaluate the EM field produced inside the sample and investigate safety issues in terms of SAR.

1.3 Motivation

Applying a high static magnetic field in MRI yields an inherent increase of the signal-to-noise ratio (SNR)(4,5). The issues encountered at UHF MRI can be overcome by using transceiver arrays that achieve high sensitivity in the receive mode and enable dynamic B_1^+ shimming in the transmit mode providing a way to compensate for the transmit field inhomogeneity at UHF (6–8).

Most of the designed coil arrays use rigid support and have an inflexible configuration. Such rigid coil arrays do not allow for efficient coil to sample conformity resulting in SNR degradation and may increase inter-element mutual coupling and losses due to mismatch because of the load variation from one subject to another. Flexibility of coil arrays is therefore of utmost importance to ensure close proximity of the coil to the surface of the patient and maximize the detection sensitivity. In the past decade, several approaches to design flexible coil arrays have been published: Hardy et al designed a 128-channel coil array based on etching copper on a thin flexible substrate (9). Adjustable semi-flexible transmission lines were used by Adriany et al. to design a 16-channel transceiver coil (10). Goenze et al. used interchangeable small surface loops placed on a strip of plastic (11). Braided thin wires mounted on an elastic textile were designed by Nordmeyer-Massner et al (12). Wu et al. employed primary and secondary harmonic rigid micro-strip coil to build a transceiver array (13). Most recently, Corea et al. demonstrated another technology by printing based on conductive silver micro-flake solution (14). In all of these works, an increase in SNR, transmit efficiency, and improved parallel imaging performance were demonstrated due to better conformity of the array coil to the subject. Some of the above mentioned techniques have used semi-rigid designs (9–11,13) and capacitive decoupling which may limit their efficiency in terms of mechanical flexibility in case of strong patient size variation. Other designs offer more freedom in mechanical flexibility while they are designed as receive-only arrays employing overlap decoupling which may impact the parallel imaging efficiency (12,14). Therefore, a transceiver flexible coil array is desirable for UHF MRI.

The use of standard RLC coil technology is widely spread but may impose restrictions on the development of flexible coils due to the minimum space required for placing discrete components and the use of many rigid solder joints that strongly reduce the flexibility of the coil. This is mostly important at UHF where multiple discrete capacitors are needed for coil segmentation to create a more symmetric current distribution in the winding (15,16). These

issues can be reduced by employing the TLR technology (17). TLRs are self-resonant structures that can be fabricated on a substrate which may be thin and flexible (18–20). The resonance frequency of TLRs is fixed by the geometry of the design (i.e. loop diameter, line width and substrate thickness, number of turns and gaps) and substrate permittivity. Previous studies demonstrated an improvement in RF homogeneity for a multi-turn TLR in comparison with conventional surface coil with the same mean radius (21). Furthermore, a dedicated study comparing multi-turn multi-gap (MTMG) TLRs with conventional surface coils of the same mean radius was done, reporting additional degrees of freedom for tuning using MTMG TLRs (22). TLRs have been shown to enable a mechanically flexible array for UHF MRI combining the advantages of parallel imaging with the possibility of form-fitting (17). For the above mentioned reasons, TLR technology appears well suited to develop flexible coils at UHF MRI.

In previous work, an inductive tuning and matching technique for TLRs using a pickup loop was employed (17). It was reported that inductive coupling technique may reduce the SNR due to the pickup loop noise factor, introduce additional magnetic coupling between neighbouring pickup loops, and distort B_1^+ pattern due to the presence of the pickup loops (13,23). Such drawbacks do not exist when using capacitive tuning and matching technique. Furthermore, in case of a receive-only array, the introduction of additional circuitry by the capacitive scheme facilitates pre-amplifier decoupling (see section 2.4.2.3.1.3). Placing the feed port of the capacitive network in the middle of a TLR section ensures that the current in the network is maximum, thus improving the tuning and matching efficiency. This is based on the fact that the maximum voltage along the transmission line i.e. between the top and bottom conductors is obtained in the middle of each conductor section (18,19). Due to the symmetry of the design, the feed port can be placed in the middle of any conductor section on either side of a TLR, preserving the symmetry of the current distribution. Therefore, capacitive coupling technique appears advantageous for TLR coils as compared to inductive one.

Mutual decoupling between individual elements of an array is one of the major technical challenges in designing TLR arrays as they are monolithic structures fabricated using standard photolithographic process without additional solder joints (17). Conventional decoupling techniques such as partial overlap of the coils or using electronic circuits are not well suited for TLR technology and may limit the design flexibility. In a previous work, efficient decoupling for an array of TLRs was demonstrated using coil annexes (17) with the limitations of interfering with the coil geometry, being inefficient for large coils, high number of turns or thick substrates (24). Another possibility to cancel the mutual flux shared by individual

elements within an array of TLRs, is to use a decoupling ring-based technique (25,26), where each TLR element is surrounded by a conducting ring, the rings of nearest neighbours being deposited on opposite sides of the substrate for overlapping. Decoupling ring based-technique is of interest as it preserves the advantage of distinct coil profiles and the flexible compatibility of annexes decoupling while overcoming the efficiency limitations encountered for some coil geometry or size.

It has been shown that UHF can be beneficial for cardiac magnetic resonance (CMR) due the inherent increase in SNR (27). However, the problems associated with UHF such as off-resonance artefacts, transmit field inhomogeneity, dielectric effects and tissue heating are still of concern. Such limitations are critical for CMRI since electrical conductivity and permittivity variation within the heart makes it particularly susceptible to the field inhomogeneity. Local transceiver coil arrays are widely designed to tackle the above mentioned issues at UHF. Different coil configurations based on strip lines, loop coils and dipole antennas with a rigid or semi-flexible housings containing 4 to 32 channels have been developed and their performances have been demonstrated for CMR at 7 T (28–33). Snyder et al developed a 1D 8-channel array of strip line resonators including separable 4-element arrays for the anterior and posterior parts of the human thorax (28). Dieringer et al designed a 4-element array of rectangular loops placing each 2-element in anterior and posterior parts of the human chest (29). However, this design was limited to the specific patient size. A comparison between 3 different loop arrays with 4, 8 and 16 elements was done by Winter et al demonstrating an increase in parallel imaging efficiency and freedom in B_1^+ uniformity by increasing the number of elements and using multi-dimensional designs (30). Graessel et al developed a modular 32-channel loop array in the form of 8 independent blocks demonstrating the high resolution and accelerated cardiac MRI with the compatibility to the pTx system (32). The use of radiative elements such as dipole antenna tailored for cardiac MRI at 7 T has been shown in a recent design by Oezerdem et al demonstrating a 16-channel bow-tie antenna supporting high resolution and accelerated imaging (33). Most of the existing designs employed anterior and posterior parts to increase the transmit depth and field coverage due to the deep position of the heart in the thorax. A typical UHF CMR array is required to have the following requirements (27):

- Light weight
- Cover the cardiovascular region
- Mechanical flexibility

- Multi dimensional array
- Patient comfort
- Ease of use

TLR arrays meet most of the abovementioned requirements and therefore have the potential and capabilities to be used for UHF CMR. The challenge in designing TLR arrays is to optimize the coil geometry with respect to the desired penetration depth while achieving efficient inter-element decoupling and ensuring a SAR below the authorized limit.

The aim of this thesis was to develop a flexible transceiver TLR array combining the advantages of coil arrays with the possibility of form-fitting which is interesting for cardiac MRI applications where the shape and size of human torsos could vary considerably from one patient to another (27). In this work, we combined a capacitive technique for tuning and matching the individual elements with the decoupling ring-based technique to cancel mutual coupling between elements in view of developing a flexible 12-element TLR array targeting CMRI at 7 T.

2 Theory and Background

2.1 Basic Principles of Magnetic Resonance

The formulas and conclusions discussed in this chapter are mainly based on the book given in (34).

2.1.1 Nuclear Spin

The intrinsic angular momentum of nuclear particles, i.e. protons and neutrons, is referred to as spin. Because moving electric charges produce a magnetic field based on Maxwell's equations, this leads to a magnetic moment. The spin angular momentum vector \vec{J} and its associated magnetic moment $\vec{\mu}$ are related to each other via a constant called gyromagnetic ratio γ , which depends on the nuclear particle.

$$\vec{\mu} = \gamma \cdot \vec{J} \quad (2.1)$$

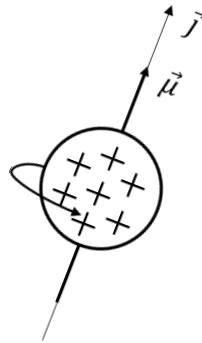


Figure 2.1: Proton magnetic moment and spin.

The nuclear spin is a quantum mechanical property that can have positive or negative sign corresponding to its clockwise and counter-clockwise rotational directions. The spin angular momentum component J_z parallel to an external magnetic field and its magnitude are both quantized

$$J_z = m_I \cdot \hbar \quad (2.2)$$

where $\hbar = h/2\pi$ and h is the Planck's constant (6.626×10^{-34} Js). m_I is the magnetic quantum number where it has $2I + 1$ possibilities as,

$$m_I = -I, -I + 1, \dots, I - 1, I \quad (2.3)$$

I is the spin quantum number and its relation with the total angular momentum $|J|$ is

$$|J| = \hbar\sqrt{I(I+1)} \text{ where } I = 0, 1/2, 1, 3/2, \dots \quad (2.4)$$

Equation (2.4) demonstrates that atomic nuclei with $I \neq 0$ produce a magnetic moment that is necessary for NMR experiments. Both protons and neutrons have spin quantum number $I = 1/2$ resulting in two possibilities for the magnetic quantum number $m_I = \pm 1/2$. Depending on the atomic number Z and mass number A of a nucleus, spin quantum number can be either integer or half-integer. For example, for 'even-even' nuclei (even numbers of Z and A) spin quantum number is zero and, therefore, the magnetic moment is also zero. For other combinations the situation is complicated, for example for atomic nuclei with large number of protons the orbital motions of nucleons should be taken into account in addition to spins of all nucleons. Thus, in this case the spin quantum number often has to be determined by experimental methods.

2.1.2 Spin Energy Levels and Magnetization

In the absence of an external magnetic field spins (e.g. proton spins) are randomly oriented. Applying a magnetic field B_0 (typically along the z -direction, w.l.o.g.) causes the spins to align either parallel or anti-parallel with respect to the applied field, this is called the Zeeman effect. The parallel or anti-parallel orientation of spins are dependent on the energy levels they have in the presence of the external magnetic field B_0 . The energy of a magnetic moment in an external magnetic field B_0 along z -direction is given by

$$E = -\mu_z B_0 \quad (2.5)$$

where μ_z is the component of magnetic moment along B_0 which can be written as

$$\mu_z = \gamma m_I \hbar \quad (2.6)$$

For the proton, which has $I = 1/2$, there are two possible orientations for μ_z based on the magnetic quantum number as

$$f(x) = \begin{cases} \mu_z = 1/2 \gamma \hbar, & m_I = 1/2 \\ \mu_z = -1/2 \gamma \hbar, & m_I = -1/2 \end{cases} \quad (2.7)$$

Combining equations (2.5) and (2.6) yields

$$E = -\gamma m_I \hbar B_0 \quad (2.8)$$

Equation (2.8) demonstrates that spins aligned parallel to the external magnetic field have lower energy than spins which are oriented anti-parallel to the field. As an example, proton spin energy levels are presented in Figure 2.2.

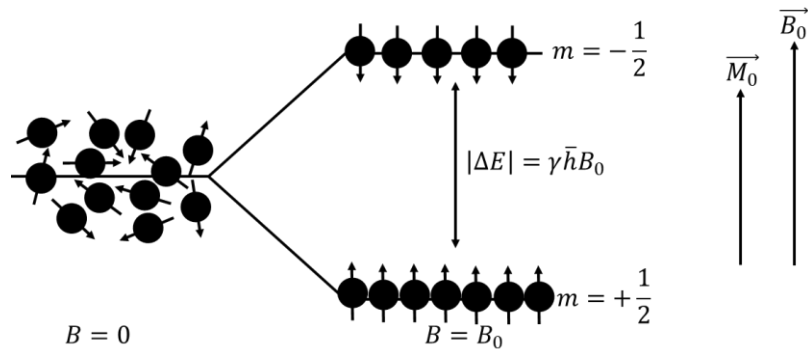


Figure 2.2: Energy difference between proton spin states as a function of the external magnetic field B_0 .

Proton spins can either absorb energy and move to the higher energy level or emit their energy and return to the lower energy level. The amount of the energy needed for transmission between two energy levels increases with the magnetic field strength

$$\Delta E = \gamma \hbar B_0 \quad (2.9)$$

The energy of a photon is $E = \hbar\omega$, therefore the frequency of the photons associated with emission or absorption of this energy difference ω_L , called the Larmor frequency, which is proportional to the applied external magnetic field strength

$$\omega_L = \gamma B_0 \quad (2.10)$$

Population of spins in lower ($N_{+1/2}$) and higher ($N_{-1/2}$) energy levels can be described by Boltzmann statistics

$$\frac{N_{-1/2}}{N_{+1/2}} = \exp\left(\frac{-\gamma \hbar B_0}{k_B T}\right) \quad (2.11)$$

k_B is the Boltzmann constant (1.4×10^{-23} J/K) and T is the temperature. At room temperature and a given field strength, the thermal energy $k_B T$ is much larger than magnetic energy $\gamma \hbar B_0$. Therefore using Taylor series expansion equation (2.11) can be written as

$$k_B T \gg \gamma \hbar B_0 \xrightarrow{\text{yields}} \frac{N_{-1/2}}{N_{+1/2}} = 1 - \frac{-\gamma \hbar B_0}{k_B T} \quad (2.12)$$

Equation (2.11) indicates that the population of spins in the lower energy level is higher than that of the higher energy level. The higher population of spins in the low energy state gives rise to a net magnetization M_0 of the whole spin system. Since spins in the lower energy state have the same direction as B_0 , M_0 points in the direction of B_0 as well. For arbitrary spins, the strength of M_0 can be calculated as

$$M_0 \cong \rho_0 \frac{I(I+1)\gamma^2 \hbar^2}{3k_B T} B_0 \quad (\hbar\omega_L \ll k_B T) \quad (2.13)$$

$\rho_0 = N/V$ is the density of spins per unit of volume. For the proton, i.e. $I = 1/2$, equation (2.13) becomes

$$M_0 \cong \frac{1}{4} \rho_0 \frac{\gamma^2 \hbar^2}{3k_B T} B_0 \quad (\hbar\omega_L \ll k_B T) \quad (2.14)$$

Equation (2.14) shows that the strength of the net magnetization is linearly related to the spin density and the strength of the applied external magnetic field.

2.1.3 Larmor Precession

When an external magnetic \vec{B}_0 is applied, the magnetic moment of the atomic nuclei encounters a torque which forces it to be parallel to \vec{B}_0

$$\vec{T} = \vec{\mu} \times \vec{B}_0 \quad (2.15)$$

The total angular momentum \vec{J} interacts with the torque \vec{T} as

$$\vec{T} = \frac{d\vec{J}}{dt} \quad (2.16)$$

Combining equations (2.15) and (2.16) yield to the motion equation for the magnetic moment $\vec{\mu}$

$$\frac{d\vec{\mu}}{dt} = \gamma \cdot \vec{\mu} \times \vec{B}_0 \quad (2.17)$$

The sum of all magnetic moments in a sample yields the total magnetization \vec{M} , thus equation (2.17) can be extended to equation (2.18) referred to as the Bloch equation (35)

$$d\vec{M}/dt = \gamma \cdot \vec{M} \times \vec{B}_0 \quad (2.18)$$

Considering the external magnetic field \vec{B}_0 along z-direction, the Bloch equations for the individual components of \vec{M} are

$$\frac{dM_x}{dt} = \gamma M_y B_0, \quad \frac{dM_y}{dt} = \gamma M_x B_0, \quad \frac{dM_z}{dt} = 0 \quad (2.19)$$

The solutions to this set of differential equations is a precession of the total magnetization (\vec{M}) about the Z-axis with the so called Larmor frequency ω_L (see equation (2.10)).

$$M_x(t) = M_{x0} \cdot \cos(\omega_L t) + M_{y0} \cdot \sin(\omega_L t) \quad (2.20)$$

$$M_y(t) = -M_{x0} \cdot \sin(\omega_L t) + M_{y0} \cdot \cos(\omega_L t) \quad (2.21)$$

$$M_z(t) = M_{z0} \quad (2.22)$$

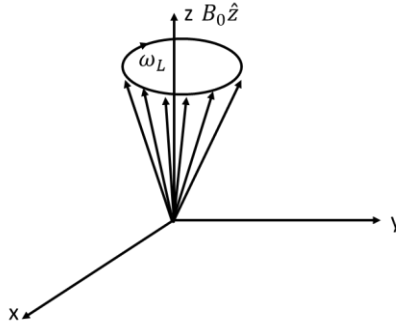


Figure 2.3: Spin precession movement of spin around the external magnetic field B_0 .

Rotating and laboratory frame of reference are used to describe magnetization and precession analysis in MRI.

In the rotating frame of reference we consider that the coordinate system for observation of the magnetization rotates about the Z-axis in the same direction that \vec{M} rotates about \vec{B}_0 . This way the magnetization precessing at ω_L (equation (2.10)) appears to be stationary in the rotating frame of reference. In this frame, the z-coordinate does not change and coordinates are represented as (x', y', z') . The frame of reference that is stationary with respect to the laboratory has coordinates (x, y, z) .

Applying a radio frequency (RF) field \vec{B}_1 , perpendicular to the external magnetic field \vec{B}_0 , one can re-write Bloch equations in the laboratory frame in the absence of relaxation.

$$\frac{dM_x}{dt} = \gamma \cdot (M_y B_0 - M_z B_{1y}) \quad (2.23)$$

$$\frac{dM_y}{dt} = \gamma \cdot (-M_x B_0 + M_z B_{1x}) \quad (2.24)$$

$$\frac{dM_z}{dt} = \gamma \cdot (M_x B_{1y} - M_y B_{1x}) \quad (2.25)$$

Solutions for equations above are given by

$$M_x(t) = M_0 \cdot \sin(\omega_1 t) \cdot \sin(\omega_L t) \quad (2.26)$$

$$M_y(t) = M_0 \cdot \sin(\omega_1 t) \cdot \cos(\omega_L t) \quad (2.27)$$

$$M_z(t) = M_0 \cdot \cos(\omega_1 t) \quad (2.28)$$

where $\omega_1 = \gamma B_1$ and M_0 is the magnitude of the net magnetization vector \vec{M} .

Once an RF field is applied in addition to B_0 , the net magnetization vector precesses about the sum of the two fields $\vec{B} = \vec{B}_0 + \vec{B}_1$. Based on equations (2.26), (2.27) and (2.28) at $t = 0$ the net magnetization vector is parallel to the z-axis; this state is referred to as the equilibrium state.

In a typical MRI experiment, additional B_1 field is created by applying an RF pulse for a short time. In the rotating frame, applying an RF pulse (B_1 field) causes the net magnetization to be rotated an axis in the xy plane by an angle called “flip angle”. The flip angle produced by an RF pulse of shape $f(t)$ and duration τ is given by

$$\alpha = \gamma B_1(t) \int_0^\tau f(t) dt \quad (2.29)$$

For a rectangular pulse shape, equation (2.29) can be simplified to

$$\alpha = \gamma B_1 \tau \quad (2.30)$$

Flip angle depends on the amplitude of the applied B_1 field and the pulse length τ for a rectangular pulse shape. For example in order to obtain a flip angle of $\pi/2$, a rectangular pulse with the length $\tau = \pi/2\gamma B_1$ is needed to be applied.

2.1.4 Relaxation

The net magnetization vector \vec{M}_0 can be divided into a longitudinal component \vec{M}_z and a transversal component \vec{M}_{xy} . Both magnetization components tend to come back to their equilibrium state, as it is the lowest energy state with $M_z = M_0$ and $M_{xy} = 0$. This process is called relaxation. The return to equilibrium for longitudinal magnetization is in the form of a recovery and for transversal magnetization it is a decay. The longitudinal recovery is based on energy is released to the surrounding lattice. In other words, spins in the higher energy level release their energy to the surrounding lattice and return to their lower energy state. This process is called longitudinal or spin-lattice relaxation. The rate of change in longitudinal magnetization is given by

$$\frac{dM_z}{dt} = \frac{1}{T_1} \cdot (M_0 - M_z) \quad (2.31)$$

T_1 is a time constant referred to as t (Figure 2.4).

The solution to equation (2.31) is given by

$$M_z(t) = M_z(0) \cdot e^{-\frac{t}{T_1}} + M_0 \cdot \left(1 - e^{-\frac{t}{T_1}}\right) \text{ when } (B_0 || z) \quad (2.32)$$

$$M_z(t) = M_0 + (M_z(0) - M_0) \cdot e^{-\frac{t}{T_1}} \quad (2.33)$$

$M_z(0)$ is the z-component of the magnetization immediately after excitation.

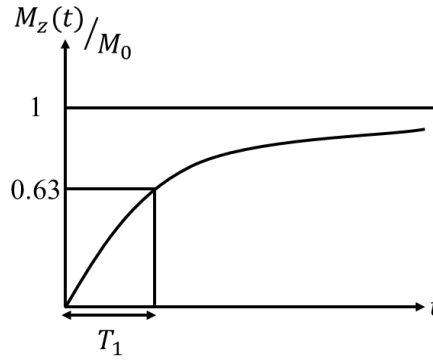


Figure 2.4: T_1 relaxation

Based on the equation (2.33), after time T_1 , longitudinal magnetization has recovered $1/e = 63\%$ of its value (M_0) in the equilibrium state (see Figure 2.4).

Simultaneously to the longitudinal relaxation, the transversal magnetization decays due to interactions of the spins with other spins (Figure 2.5). This phenomenon is called spin-spin relaxation resulting in a decrease in their phase coherence, due to local deviations from the Larmor frequency. The transversal magnetization M_{xy} decays with time constant T_2 , which is described by the differential equations below

$$\frac{dM_x(t)}{dt} = -\frac{M_x(t)}{T_2} \quad (2.34)$$

$$\frac{dM_y(t)}{dt} = -\frac{M_y(t)}{T_2} \quad (2.35)$$

Solution to the equations above is given by

$$M_{xy}(t) = M_{xy}(0) \cdot e^{-\frac{t}{T_2}} \quad (2.36)$$

T_1 and T_2 are independent parameters. T_1 reflects energy exchange between spins and the system while T_2 is an entropy process as there is no net energy transfer between spins and the surrounding lattice. The variation of T_1 and T_2 relaxation time for different tissues is exploited to obtain image contrast in MRI (Table 2.1).

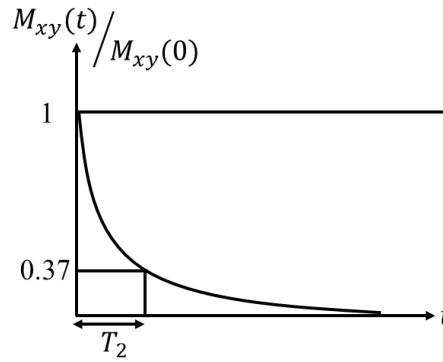


Figure 2.5: T_2 relaxation

Table 2.1: T_1 and T_2 values of various tissues at 1.5 T (34)

Tissue	T_1 (ms)	T_2 (ms)
Grey Matter	950	100
White Matter	600	80
Blood	1200	100-200
Muscle	900	50
Fat	250	60

Based on the equation (2.36), after the time T_2 , transversal magnetization has lost $1/e = 63\%$ of its initial value (Figure 2.5). In practice, there is an additional dephasing contribution introduced by local magnetic field inhomogeneities, which cause the transversal magnetization to decay faster than the predicted T_2 time. The associated time constant is called T_2^* .

$$\frac{1}{T_2^*} = \frac{1}{T_2} + \frac{1}{T_2'} \quad (2.37)$$

T_2' denotes B_0 inhomogeneity which is mainly due to the susceptibility difference between different sample tissues as well as technical imperfections. Using spin-echo sequences (section 2.3.1), the signal loss due to the T_2' can be recovered.

By including relaxation times into the equation of motion, for $\vec{B}_{\text{ext}} = B_0 \hat{z}$, the Bloch equations can be written as

$$\frac{dM_x}{dt} = \omega_L M_y - \frac{M_x}{T_2} \quad (2.38)$$

$$\frac{dM_y}{dt} = -\omega_L M_x - \frac{M_y}{T_2} \quad (2.39)$$

$$\frac{dM_z}{dt} = \frac{M_0 - M_z}{T_1} \quad (2.40)$$

Solutions to the equations above are given in equations (2.33) and (2.36).

2.1.5 Free Induction Decay (FID)

In the equilibrium state, the net magnetization (M_0) of the sample is aligned parallel to the external field. Assuming a sample placed in a static magnetic field where an RF coil (simple conductor loop) is positioned perpendicularly to the static field direction in vicinity of the sample, an RF pulse oscillating at the Larmor frequency is used to tip down the magnetization to the transversal plane. The rotating transversal magnetization induces an electromotive force (emf) in the RF coil that decays exponentially with the time constant T_2^* . This is called free induction decay (FID) and is shown in Figure 2.6.

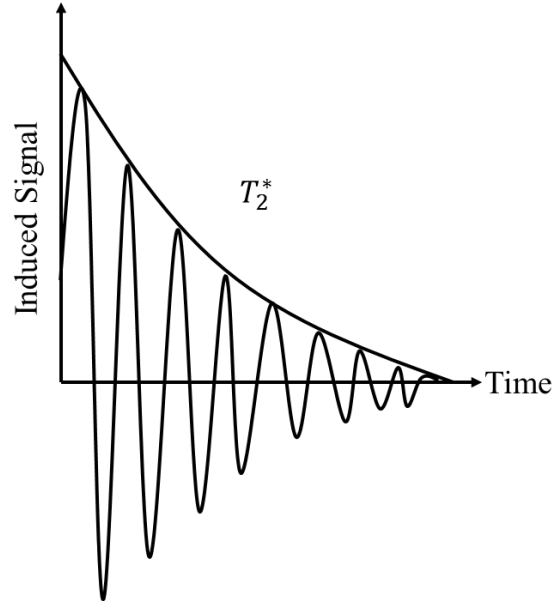


Figure 2.6: Free Induction Decay (FID).

2.2 Signal and Noise in MR Experiments

2.2.1 The Reciprocity Principle

The principle of reciprocity is the link between transmit and receive field of an RF coil. It states that the emf induced by a rotating magnetization \vec{M} in an RF coil at a given point in the space is proportional to the magnetic field \vec{B}_1 created at the same point by circulating current I in the RF coil (36,37). In the following, we will derive an expression for the emf produced by the change of magnetic flux through the coil by the spin magnetization and show the relationship to the created magnetic field per unit of current by the coil.

The magnetization of a sample \vec{M} at time t and position \vec{r} arisen from the current density \vec{J}_M is given by

$$\vec{J}_M(\vec{r}, t) = \vec{\nabla} \times \vec{M}(\vec{r}, t) \quad (2.41)$$

The magnetic field produced in the coil can be defined as

$$\vec{B}_1 = \vec{\nabla} \times \vec{A} \quad (2.42)$$

where \vec{A} is the vector potential at position \vec{r} arisen from a source current such that

$$\vec{A}(\vec{r}) = \frac{\mu_0}{4\pi} \int d^3\vec{r}' \frac{\vec{J}(\vec{r}')}{|\vec{r} - \vec{r}'|} \quad (2.43)$$

The flux through a coil in terms of vector potential using equation (2.42) and Stokes's theorem can be written as

$$\Phi = \int_S \vec{B}_1 \cdot d\vec{S} = \int_S (\vec{\nabla} \times \vec{A}) \cdot d\vec{S} = \oint d\vec{l} \cdot \vec{A} \quad (2.44)$$

Using equations (2.41), (2.42) and (2.44) and the vector identity, $\vec{A} \cdot (\vec{B} \times \vec{C}) = -(\vec{A} \times \vec{C}) \cdot \vec{B}$, the magnetic flux through the coil Φ_M due to the spin magnetization can be calculated as

$$\begin{aligned} \Phi_M &= \oint d\vec{l} \cdot \left[\frac{\mu_0}{4\pi} \int d^3\vec{r}' \frac{\vec{\nabla}' \times \vec{M}(\vec{r}')}{|\vec{r} - \vec{r}'|} \right] \\ &= \frac{\mu_0}{4\pi} \int d^3\vec{r}' \vec{M}(\vec{r}') \cdot \left[\vec{\nabla}' \times \left(\oint \frac{d\vec{l}}{|\vec{r} - \vec{r}'|} \right) \right] \end{aligned} \quad (2.45)$$

The vector potential \vec{A} for a loop with circulating current I at position \vec{r} can be evaluated as

$$\vec{A}(\vec{r}) = \frac{\mu_0}{4\pi} \oint \frac{I d\vec{l}}{|\vec{r} - \vec{r}'|} \quad (2.46)$$

Based on equation (2.46) it can be demonstrated that the curl of the linear integral over the current pass in equation (2.45) is the same as the magnetic field per unit current that would be produced by the coil at position \vec{r}

$$\frac{\vec{B}_1(\vec{r}')}{I} = \vec{\nabla}' \times \left(\frac{\mu_0}{4\pi} \oint \frac{d\vec{l}}{|\vec{r} - \vec{r}'|} \right) \quad (2.47)$$

Finally, the flux through the coil can be written as

$$\Phi_M(t) = \int_{\text{sample}} d^3\vec{r} \vec{B}_1(\vec{r}) \cdot \vec{M}(\vec{r}, t) \quad (2.48)$$

After excitation, the resulting rotating magnetization in the x-y plane, induces an emf in the receiver RF coil which can be calculated by Faraday's law of induction

$$\text{emf} = -\frac{d\phi}{dt} \quad (2.49)$$

By combining equations (2.48) and (2.49)

$$\text{emf} = -\frac{d\Phi_M(t)}{dt} = -\frac{d}{dt} \int_{\text{sample}} d^3\vec{r} \vec{M}(\vec{r}, t) \cdot \vec{B}_1(\vec{r}) \quad (2.50)$$

Equation (2.50) states that the emf induced in the RF coil by the spin magnetization is proportional to the magnetic field per unit of current that would be created by the coil when used as a transmitter demonstrating the reciprocity principle (34).

Considering B_1 to be homogeneous over the sample volume V (37),

$$\text{emf} = \frac{\omega_0 B_{1xy} M_{xy} V}{I} \cos(\omega_0 t) \quad (2.51)$$

where B_{1xy} is the transverse component of the B_1 magnetic field and M_{xy} is the magnetization in the x-y plane.

2.2.2 Noise Contributions

The signal measured in MRI contains different noise sources arising from thermal agitation of electric charges in electrical conductors. The noise voltage associated to thermal noise was demonstrated by Nyquist in 1928 (38)

$$V_{\text{noise}} = \sqrt{4k_B \Delta f T_{\text{eq}} R_{\text{eq}}} \quad (2.52)$$

where k_B is the Boltzmann constant, Δf is the receiver bandwidth, $T_{\text{eq}} R_{\text{eq}}$ denotes the total equivalent temperature-weighted sum of resistance based on the respective contribution rates and local temperatures in different media. Main noise sources in MRI experiment are originated from the RF coil resistance (R_c) and the sample resistance (R_s)

$$R_{\text{eq}} T_{\text{eq}} = R_c T_c + R_s T_s \quad (2.53)$$

where T_c and T_s are the coil and the sample temperatures, respectively.

The coil resistance (R_c) arises from the ohmic losses within the conducting material. This resistance is increased at higher frequency due to the tendency of the alternating current to have larger current density close to the conductor surface referred to as skin effect.

$$R_c \propto \sqrt{\omega_0} \propto \sqrt{B_0} \quad (2.54)$$

Coil losses can be minimized by choosing optimized wires in terms of geometry and conductivity (e.g. copper) and careful soldering.

Sample noise can be classified into three different contributions, magnetically coupled noise, capacitively coupled noise, and spin noise. Sample noise depends on the conductivity (e.g. 0.7 S/m for biological tissues at 300 MHz (39)) and the temperature of the sample.

Induced eddy currents in the sample together with thermally agitated electric charges create a voltage in the receiver that cannot be distinguished from the original NMR signal. This leads to random fluctuations of the MR signal. The magnetic coupling between coil and sample increases linearly with frequency, thus sample noise increases at higher field strength (40)

$$R_s \propto \omega_0^2 \propto B_0^2 \quad (2.55)$$

Potential differences between different parts of the coil during RF transmission, result in virtually formed capacitors between the RF coil and the conductive sample (Figure 2.7). These stray electric fields penetrate the sample and induce dielectric losses.

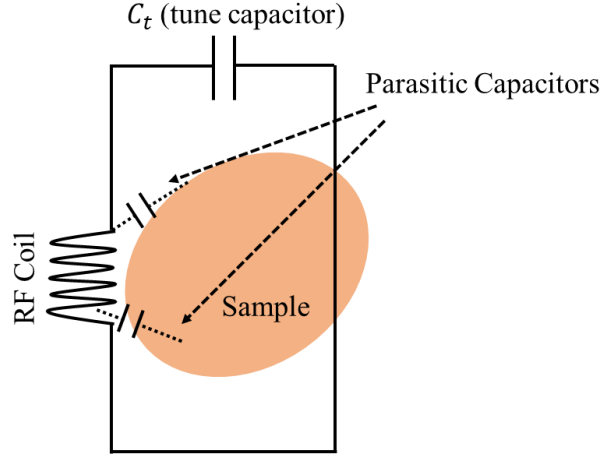


Figure 2.7: Parasitic capacitors between RF coil and conductive sample due to the potential differences.

Dielectric losses are caused by thermal fluctuations of the electric dipoles at the surface of the sample and are coupled to the coil by the inverse pathway. Since this noise is not coupled to the coil via the magnetic induction pathway which is necessary for the signal detection, it can be reduced by proper coil design such as segmented coils by distributed series capacitors (41).

Spin noise originates from the fluctuations of the transverse magnetic moment of the nuclear spin system (42). Spin noise contribution in MRI is negligible as readout gradients spread the resonance over several kHz. However, spin noise can be problematic for high resolution spectroscopy (bandwidth of 1 kHz).

Losses due to magnetic coupling are the dominant loss mechanism for the sample resistance contribution (R_s).

Combining equations (2.51) and (2.52) yields the signal to noise ratio (SNR) formula

$$\text{SNR} = \frac{\text{emf}}{V_{\text{noise}}} = \frac{\omega_0 B_{1xy} M_0 V \cos(\omega_0 t)}{I \sqrt{4K_B \Delta f T_{\text{eq}} R_{\text{eq}}}} \propto \frac{B_0^2}{\sqrt{B_0^2 + \alpha \sqrt{B_0}}} \quad (2.56)$$

α depends on R_c/R_s which demonstrates the dominant noise source, i.e. coil resistance or sample resistance.

At low frequencies or when the sample or coil size is small, coil noise is dominant, resulting in an SNR dependency of $\sqrt[4]{B_0^7}$ (see equation (2.53)). The SNR is proportional to B_0 when the sample noise is the dominant loss contribution i.e. at high frequencies or with large coils.

The RF sensitivity factor (S_{RF}) characterizes the contribution of the RF coil to the SNR and is defined as

$$S_{\text{RF}} = \frac{\omega_0 B_1/I}{\sqrt{4K_B \Delta f T_{\text{eq}} R_{\text{eq}}}} \quad (2.57)$$

where B_1/I is the magnetic coupling coefficient. Using Biot-Savart's law at low frequency, the B_1 field per unit current created by a circular loop at distance a along its axis can be determined as

$$B_1/I = \frac{\mu_0 r^2}{2(r^2 + a^2)^{3/2}} \quad (2.58)$$

where μ_0 is the vacuum permeability. It demonstrates that the coupling factor decreases with increasing coil radius r . Thus, based on equation (2.58), it can be stated that smaller coils have higher sensitivity in the vicinity of the coil in comparison to larger coils.

Ideally, an NMR experiment should be carried out in the sample noise dominated regime. If, on the other hand, RF coil noise is dominant, the achievable SNR is limited by internal coil noise. In that case the SNR can be improved by reducing the coil's internal resistance e.g. by cooling or using superconducting materials. For a given field strength, sample size and conductivity, and coil resistance, the coil size determines whether coil or sample noise is dominant (43).

2.3 Magnetic Resonance Signal Acquisition

Usually the sampled signal in MRI is not the FID (see Figure 2.6) but rather an echo. As stated in the previous section, FID decays exponentially with T_2^* due to the spin dephasing. An echo signal can be generated by refocusing spins using spin-echo or gradient-echo sequences.

2.3.1 Spin-Echo

In the spin-echo sequence (44), initially the magnetization is tipped down to the transverse plane by a 90° RF pulse. In the beginning all spins are in phase thus add together to form the maximum signal. But due to the spin-spin interactions and external magnetic field inhomogeneity (T_2^* effects), spins start to steadily dephase, leading to a decrease in the amplitude of the detectable signal. Applying a 180° pulse at time point τ after the excitation, flips the magnetization about the y-axis which reverts the sign of spin phase. Therefore, the spins now start to rephase, reaching a maximum of phase coherence after another time interval τ . This results in reformation of the measured signal referred to as “echo”. A step-by-step explanation of the echo formation in a spin-echo sequence is shown in Figure 2.8.

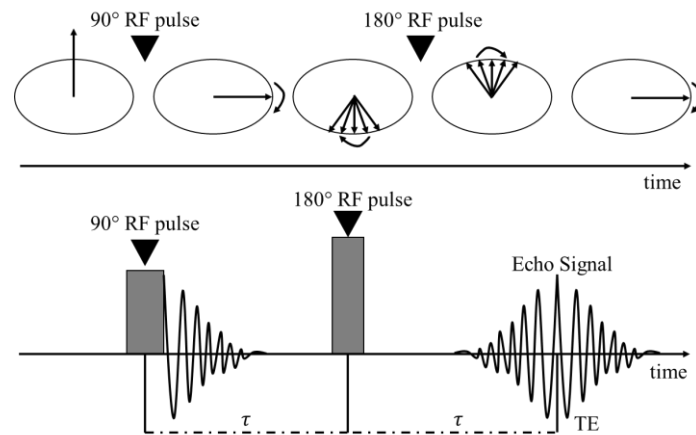


Figure 2.8: Spin echo sequence : Formation of an echo by a 180° pulse after excitation pulse (90°) shown by spins (top) and sequence diagram (bottom).

Considering the 180° pulse to be applied after the time τ following the 90° pulse, the echo is generated after $TE = 2\tau$, called echo time. In the multi-spin echo sequence, several 180° pulses are applied after the 90° excitation pulse resulting in several echoes (Figure 2.9). Applying 180° pulses after the time τ , compensate for the spin dephasing due to the local field inhomogeneities (T_2' effects). Therefore, the generated echo amplitudes decrease with T_2 time (45).

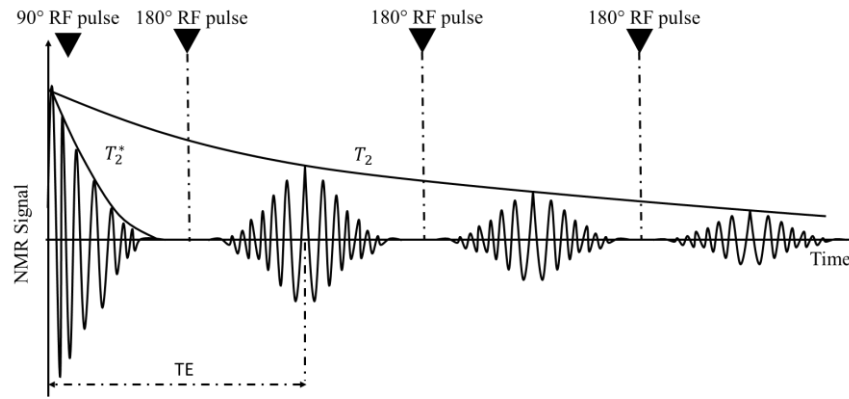


Figure 2.9: Multi-spin echo sequence.

2.3.2 Gradient-Echo (GRE)

Refocusing of spins can be also done by using a gradient coil. In such a sequence, after the 90° excitation pulse, a linear magnetic gradient field is switched on across the sample, causing the spins to precess at different angular velocity based on their location within the sample. This yields a much faster T_2^* decay and causes spins to dephase much faster. In other words, the gradient artificially spoils the transverse magnetization. By reversing the gradient field, spins are rephased (see Figure 2.10) resulting in an echo generation. Since in this sequence a gradient is used to generate an echo instead of the 180° pulse, it is called gradient-echo sequence (46).

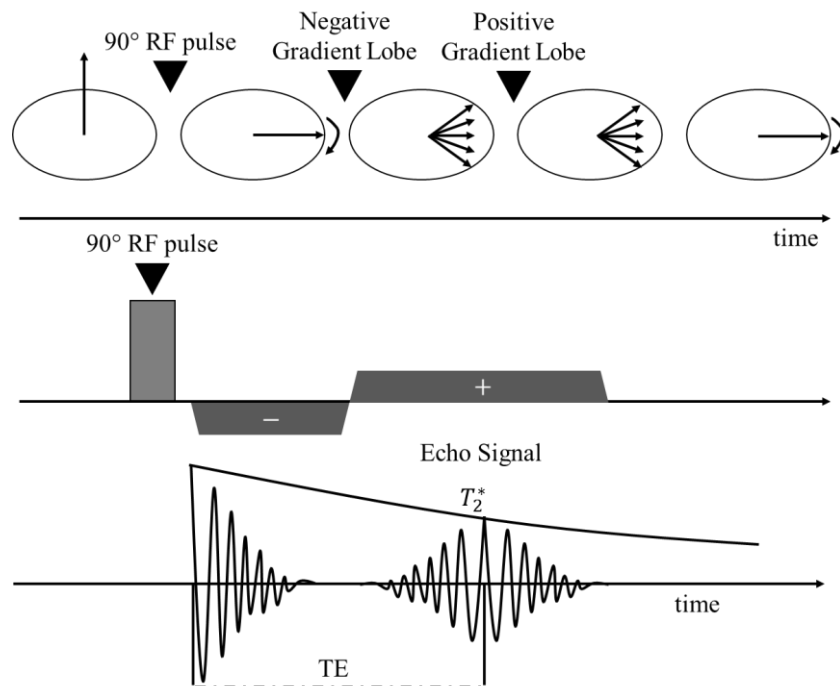


Figure 2.10 Gradient echo sequence diagram.

Spin-echo sequences account for dephasing of the spins due to the susceptibility effects of field inhomogeneity and can be used for imaging with T_2 contrast. On the other hand a gradient-echo refocuses spins much faster than a 180° pulse resulting in shorter echo times and faster multi-echo sequences in comparison with spin-echo sequence.

2.3.3 Magnetic Field Gradients: Spatial Encoding

To create an image of a sample in the MRI experiment, the measured NMR signal needs to be spatially encoded. Magnetic field gradients are responsible for creating an additional small spatially varying magnetic field along different axes (x,y,z) in addition to the main magnetic field B_0 . This causes the resonance frequency to be a function of position on the axis along which the gradient is applied.

A typical MR scanner is equipped with three orthogonal gradient coils which are designed to generate linear magnetic field gradients G_x, G_y, G_z .

$$G = G_x \hat{x} + G_y \hat{y} + G_z \hat{z} \quad (2.59)$$

The total magnetic field at position \vec{r} considering $\vec{B}_0 = B_0 \hat{z}$ is given by

$$\vec{B}(\vec{r}) = B_0 \hat{z} + \vec{G} \cdot \vec{r} \quad (2.60)$$

Thus, the Larmor frequency becomes a function of position \vec{r} as

$$\omega_L(\vec{r}) = \gamma(B_0 \hat{z} + \vec{G} \cdot \vec{r}) \quad (2.61)$$

where $\omega_L = \gamma B_0$ is the Larmor frequency for $\vec{r} = (0,0,0)$, which is at the centre of the corresponding axes, or when gradients are off, i.e. vector $\vec{G} = (0,0,0)$. To localize the signal in MRI, three methods employing magnetic field gradients are discussed in the following sections.

2.3.4 Slice Selection

A magnetic field gradient can be used to excite only spins within a selected slice (47). Slice selection can be achieved in any direction by applying the gradient field in the corresponding direction. (Figure 2.11)

For example, in order to excite a transversal slice (x-y plane), the gradient field along z-direction has to be applied

$$\omega_L(z) = \gamma(B_0 + G_z z) \hat{z} \quad (2.62)$$

This leads to a position dependency of the spins' Larmor frequency within the excited slice. By applying an RF pulse simultaneously together with a slice selective gradient, only spins with $\omega_L = \omega_0$ can be excited. Since the Larmor frequency is a function of spatial position, spins within the selected slice are excited. Location and thickness of the selected slice are determined by the strength of the slice selective gradient and the applied RF pulse profile, i.e. its frequency bandwidth.

Slice position z and thickness Δz can be determined by

$$z = \frac{\omega_c - \gamma B_0}{\gamma G_z} \quad (2.63)$$

$$\Delta z = \frac{\Delta \omega}{\gamma G_z} \quad (2.64)$$

where ω_c denotes the centre frequency of the applied RF pulse and its bandwidth $\Delta \omega$.

The selected slice profile in the frequency domain is determined by the shape of the applied RF pulse in the time domain using the Fourier Transform. As an example, an infinitely long sinc-shape excitation pulse results in a rectangular slice profile selection (Figure 2.11a). A graphical representation of the slice selective gradient is demonstrated in Figure 2.11b.

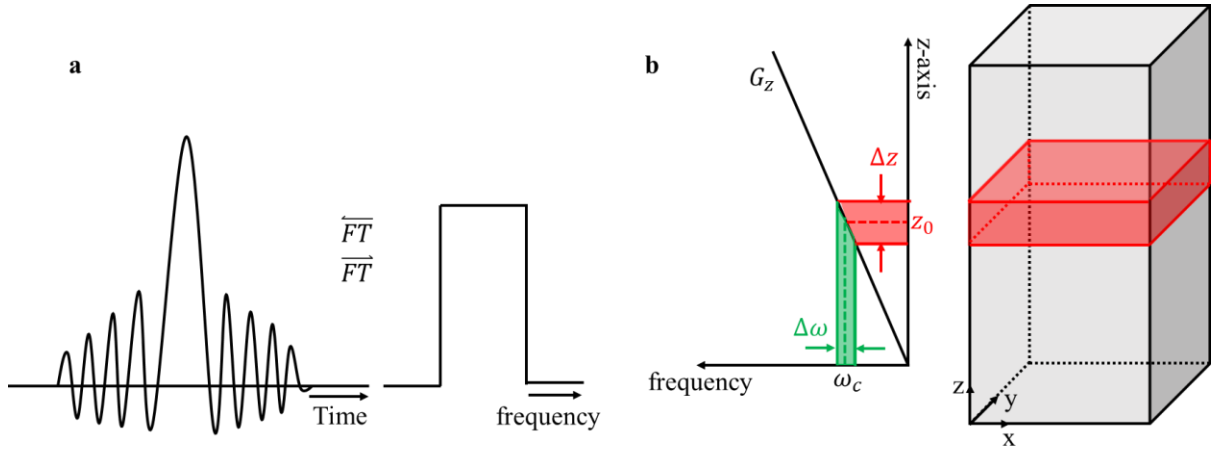


Figure 2.11: (a) Fourier Transform of a sinc shaped RF pulse results in rectangular slice profile and vice versa. (b) Slice selection in z-direction.

Once a slice is selected, measured signal from different points should be spatially encoded. Spatial encoding of the selected slice can be done in two processes: frequency and phase encoding.

In the case of frequency encoding, the magnetic field gradient is applied during signal readout and not during excitation. By applying, for example, a gradient G_x along x-direction during the signal readout, the Larmor frequency becomes a function of position along x-direction (see Figure 2.12).

This causes the MR signal to be a mixture of frequencies along the x-axis. Using discrete Fourier transform, the signal contribution of each frequency can be determined. Thus, the contributed signal with a certain bandwidth for each pixel is mapped to its corresponding spatial location and used to reconstruct an image. The readout bandwidth depends on the gradient strength (G_x), number of sampled voxels, and the field of view (FOV).

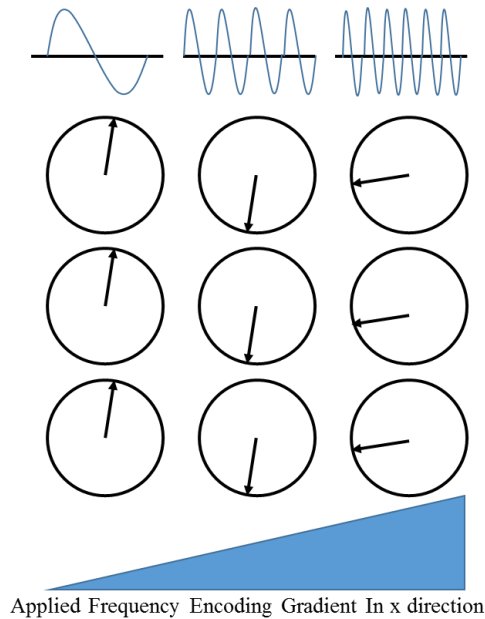


Figure 2.12: Frequency-encoding applied in x direction resulting in shift in Larmor frequency of spins within each column.

2.3.5 Phase Encoding

In order to construct a 2D image, after slice selection, spatial encoding needs to be done in two directions. Frequency encoding was discussed to be done in x-direction, applying another frequency encoding gradient at the same time would result in an ambiguity of the signal localization. Therefore, a third gradient is applied in the y-direction, a so-called phase-encoding gradient, is applied after the slice selection and before the signal readout (see Figure 2.14) (48). This again results in different precession frequencies depending on the position of the spins along y-axis, causing spatially dependent phase information for the signal localization. During the signal readout (frequency readout), the phase encoding gradient is switched off, all spins in each column shown in Figure 2.13, again precess with the same frequency but different phase depending on their position along y-axis. Phase-encoding is used to map the position of the spins along y-axis. To fully encode a 2D image, the phase-encoding process has to be done for each data point along the frequency-encoding direction. For acquiring a 3D image in MRI, the whole volume of interest is excited at once instead of using the slice selection. In addition to the existing frequency and phase encodings, another phase encoding gradient is applied along the third dimension.

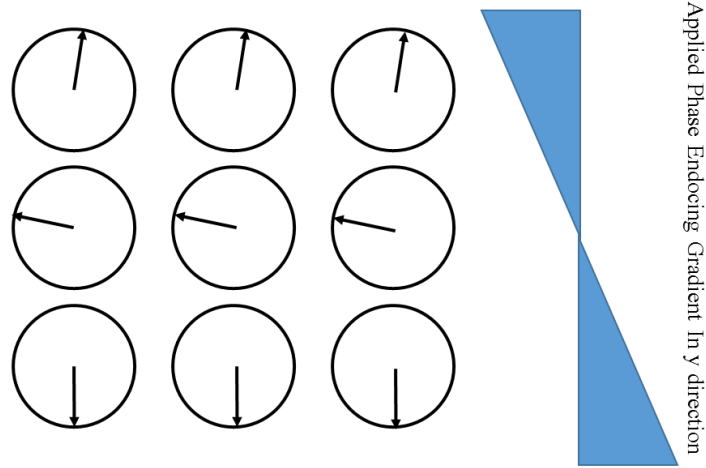


Figure 2.13: Phase-encoding gradient is applied in y direction resulting in phase difference between spins with in each row.

2.3.6 k-Space

k-space contains the acquired signal in the spatial frequency domain, this means that image space and k-space are related to each other via the Fourier transformation. The raw data acquired during signal readout are stored line by line in a matrix which is called k-space (49,50). After applying the excitation pulse, the image readout is determined by the applied gradient waveforms. The readout trajectory through k-space is defined by

$$\vec{k}(t) = \gamma \int_0^t \vec{G}(t') dt' \quad (2.65)$$

where $\vec{G} = (G_x, G_y, G_z)$ is the applied gradient and t denotes the time after the excitation pulse. The resulting signal time-course is given by (50)

$$S(t) = \gamma \int_{\text{sample}} \rho(\vec{r}) e^{-i\vec{k}(t) \cdot \vec{r}} d\vec{r} \quad (2.66)$$

where $\rho(\vec{r})$ is the effective spin density at point \vec{r} . k-space coordinates contain the spatial frequencies corresponding to the image features. The frequency-encoding gradient is

commonly used to store the data points along the k-space lines (k_x axis) while phase-encoding is usually applied to switch between the lines in k-space.

To sample a full image, all points in k-space need to be covered by the trajectory. However, in practice only a discrete subset of the k-space points can be sampled depending on bandwidth, FOV, and desired resolution. The centre of k-space contains low spatial frequencies representing large image structures and image contrast, while higher spatial frequencies represent edges and fine details in an image. The higher spatial frequencies are located further away from the centre in k-space.

The spin warp sequence (gradient echo sequence) (46) is one of the basic MR imaging sequences which employs the Fourier transform formalism shown in Figure 2.14. In this sequence, a slice selection gradient is applied simultaneously with the 90° excitation pulse. This gradient dephases the spins (positive lobe) and then its polarity is inverted (negative lobe) to refocus the spins again. Applying the negative lobe of G_{fr} and G_{pe} move the starting point of the k-space trajectory to the upper-left corner in k-space. Then the phase-encoding gradient is switched off and the G_{fr} polarity is reversed to sample the data. This causes a sweep over the data points along k_x (from left to right). This procedure has to be repeated for different G_{pe} steps after each excitation until all k-space lines are filled. Inverse Fourier transform is used to reconstruct a 2D image from this k-space data.

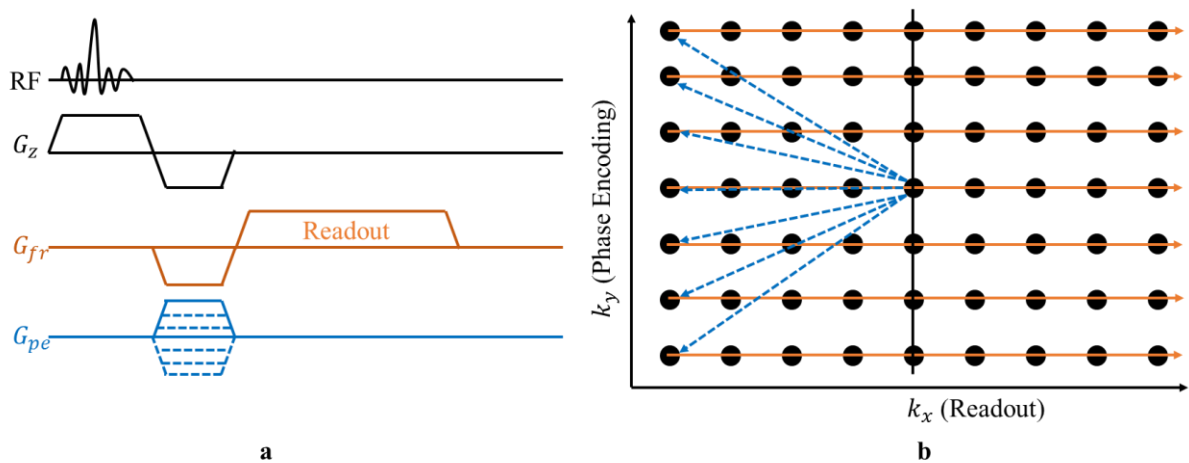


Figure 2.14: Spin-wrap sequence. Sequence diagram (a) and corresponding k-space trajectory (b).

2.3.7 Parallel Imaging (PI)

As discussed in the previous section, the duration of image acquisition is directly related to the number of phase-encoding steps. Therefore, reducing the number of phase encoding steps can

results in faster scan times in MRI. Parallel Imaging (PI) (51–54) is used to acquire a reduced amount of k-space data employing an array of RF coils, i.e. phased array coils. PI uses different algorithms to find the missing data points in k-space making use of the spatial information contained in sensitivity profiles of the individual coil elements. In 1997, the first algorithm for PI was presented by Sodickson and Manning (2). The presented reconstruction technique was dubbed SMASH (SiMultaneous Acquisitions of Spatial Harmonics) and uses individual coil sensitivities to find omitted phase-encoding steps. In this algorithm, a sinusoidal phase modulation is applied across the whole object during each phase-encoding step (52). This sinusoidal modulation causes a shift in the measured k-space data. Therefore, individual coil sensitivities are combined to form the phase-encode shift functions which are used to find missing lines in the k-space (52). Despite of reducing the scan time using SMASH, this approach requires a good approximation of these phase-encode shift functions, which is often difficult to achieve (52).

Another reconstruction algorithm is SENSE (SENSitivity Encoding) which was introduced by Pruessmann et al (3) in 1999. In this algorithm, individual coil sensitivities are acquired during a pre-scan MRI measurement in order to reconstruct the aliased images due to the undersampling. The SNR in PI reconstruction techniques is defined as (3)

$$\text{SNR}_{\text{acc}} = \frac{\text{SNR}_{\text{full}}}{g\sqrt{R}} \text{ with } R = \frac{n_{k^{\text{full}}}}{n_{k^{\text{acc}}}} \quad (2.67)$$

where R is the acceleration factor defined as the ratio of the number of data points of a full k-space over the number of points for the accelerated k-space. For example, if every other line in k-space is acquired, the acceleration factor $R = 2$. g is the coil geometry factor, which is always equal or greater than 1, indicating an additional geometry-dependent loss in SNR by non-orthogonal coil sensitivity profiles. Ideally, $g = 1$, this would be the case, where the coil sensitivities are completely uncorrelated to each other. Coils having very similar sensitivities, result in higher g -factors and this lowers the SNR.

Although SMASH and SENSE can be used for arbitrary coil configurations, however, the robustness of these methods is strongly dependent on the knowledge of the individual coil sensitivities. While SMASH-based methods perform reconstruction in k-space, SENSE works on the aliased images in image space. Another k-space-based reconstruction technique is GRAPPA (GeneRalized Autocalibrating Partially Parallel Acquisitions) (55). In this algorithm,

k-space lines which were left out due to undersampling are found using Auto-Calibration Signals (ACS). ACS is known as acquiring a portion of the k-space (usually the centre) with the desired line spacing and image FOV of the final reconstructed image but with lower resolution. The acquired portion is used as a kernel to sweep over the under-sampled data for determining the necessary weights needed to reconstruct omitted k-space lines during undersampling. This results in a complete k-space for each coil in the array. After applying the Fourier transform to obtain an image for each coil, one method to obtain the final combined image is based on the root-sum-of-squares (RSS) combination (1). Unlike SENSE, GRAPPA does not rely on the sensitivity profiles, which makes this algorithm robust to image areas with low signal such as the lungs or regions with motion where obtaining coil sensitivities might be difficult (53). SENSE and GRAPPA are widely used nowadays in MRI clinical routine resulting in faster scan time and increasing the temporal resolution.

2.3.8 Parallel Transmission (pTx)

All of the mentioned reconstructions techniques for PI are used for receiver coils. The idea of transferring PI from the receiver chain to the transmit case was initially proposed by Katscher et al. in 2003 employing a technique called Transmit SENSE (56). In this method, each transmit element within a transmit coil array is driven with different excitation waveform used to excite portions of k-space in parallel. This gives additional degrees of freedom to shorten spatially selective RF pulse and generate more homogeneous excitation profiles. In general, pTx approaches can be divided in two groups, static and dynamic pTx. In static pTx, the transmit setting is optimized before the experiment and remains the same throughout the experiment. While in dynamic pTx, each channel transmit setting can be manipulated individually during the experiment (57).

In pTx, the key component is the transmit coil array. Considering an array of RF coils with N elements, based on the principle of superposition, the total B_1^+ produced in the sample is the sum of the B_1^+ fields created by each of the individual elements of the array (equation (2.68)).

$$B_1^+ (\vec{r}, t) = \sum_{i=1}^N B_{1,i}^+ (\vec{r}, t) \quad (2.68)$$

Static pTx is described by equation (2.69). In this approach, the same RF pulse waveform $p(t)$ is transmitted to each channel each scaled by a complex channel-specific weight w_i defining a set amplitude and phase for each channel (57).

$$B_1^+ (\vec{r}, t) = p(t) \sum_{i=1}^N w_i S_i(\vec{r}) \quad (2.69)$$

where $S_i(\vec{r})$ is the transmit sensitivity of coil element i and \vec{r} is the location in space.

In dynamic pTx, each element has its own RF waveform $p_i(t)$ weighted by each element's transmit efficiency $S_i(\vec{r})$ which is described by equation (2.70):

$$B_1^+ (\vec{r}, t) = \sum_{i=1}^N p_i(t) S_i(\vec{r}) \quad (2.70)$$

The sum of the local electric fields produced by the individual elements of the array yields a total spatially variable electric field. This can results in ‘SAR hot spots’ in unexpected regions (57,58). Therefore, the SAR distribution needs to be accurately simulated before in vivo experiments to prevent patient harming.

2.4 Radio Frequency Coils

2.4.1 Basic Principles

2.4.1.1 RLC Circuits

Radio frequency (RF) coils enable the connection between the sample and MRI system by transmission and detection of the RF signals during an MRI experiment. The coil itself is an inductor with inductance L forming a basic loop (Figure 2.15a) which stores EM energy. Furthermore, the loop wire has inherent resistive losses R as shown in Figure 2.15a.

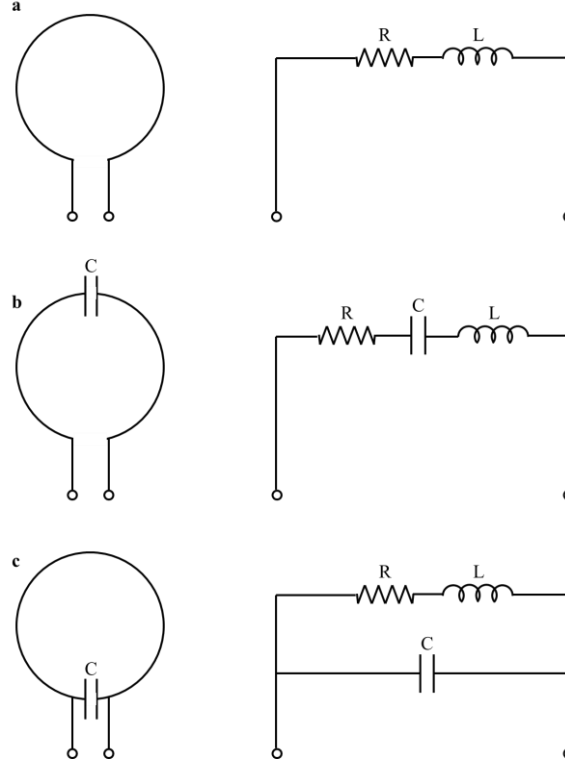


Figure 2.15: (a) Simple conductor loop and its equivalent circuit. (b) Basic geometry of an RF coil with series RLC configuration. (c) Basic geometry of an RF coil with parallel RLC configuration.

Therefore, the energy is not only stored in the coil but also dissipated through ohmic losses. By placing a capacitor with capacitance C either in series (Figure 2.15b) or parallel (Figure 2.15c) to the coil inductor an RLC circuit is composed. The total equivalent impedance seen from the circuit's ports for the series RLC circuit can be written as

$$Z_{\text{tot}} = R + (j\omega L + \frac{1}{j\omega C}) \quad (2.71)$$

The resonance happens when the imaginary part of Z_{tot} is zero (59),

$$j\omega_{\text{series}}L + \frac{1}{j\omega C} = 0 \rightarrow \omega_{\text{series}} = \frac{1}{\sqrt{LC}} \quad (2.72)$$

Equation (2.72) demonstrates that the angular frequency of the series RLC circuit is the same as the natural frequency of LC circuits which is given by

$$\omega_0 = \frac{1}{\sqrt{LC}} \quad (2.73)$$

In case of a parallel RLC circuits (Figure 2.15c), the total equivalent impedance using Thévenin's theorem, is given by,

$$Z_{\text{tot}} = \frac{R \cdot (L\omega)^2}{R^2 + \left(L\omega - \frac{1}{C\omega}\right)^2} - \frac{j}{C\omega} \cdot \frac{R^2 + \left(L\omega - \frac{1}{C\omega}\right)}{R^2 + \left(L\omega - \frac{1}{C\omega}\right)^2} \quad (2.74)$$

The imaginary part of equation (2.74) cancels at

$$\omega_{\text{parallel}} = \sqrt{\frac{1}{LC} - \frac{R^2}{L^2}} \quad (2.75)$$

The angular frequency of the parallel RLC circuit ω_{parallel} is close to the natural frequency ω_0 since usually $L \gg R$.

As stated in the previous chapter to flip the magnetization to the x-y plane, the frequency of the excitation pulse (ω_0) should be the same as the Larmor frequency ω_L . Based on the equations (2.72) and (2.75), L and C are selected in a way that the RF coil resonance frequency ω_0 matches the Larmor frequency ω_L .

The quality factor (Q -factor) is defined as the ratio of the stored energy in the coil inductance L over the dissipated power per cycle

$$Q = 2\pi \frac{\text{stored energy}}{\text{dissipated energy per cycle}} = \frac{\omega_0 L}{R} \quad (2.76)$$

where ω_0 is the angular frequency and R is the coil's ohmic resistance.

The Q -factor can be measured by

$$Q = \frac{f_0}{\Delta f} \quad (2.77)$$

where $f_0 = \omega_0/2\pi$ is the resonance frequency and Δf is -3 dB bandwidth of the resonance peak. Based on equation (2.77), RF coils act as a bandpass filter. Therefore, RF coils with lower losses result in larger Q -factors which correspond to a narrow bandwidth and thus, a more efficient filtering.

As an example, for a simple loop coil (8 cm diameter, 1.5 mm wire thickness at 297.2 MHz the measured Q -factor is 276 when the coil is not loaded (22). When the coil is loaded by a conductive sample, the sample resistance R_s is added to the coil resistance (see equation (2.53)), thus loaded Q -factor can be calculated as

$$Q_{\text{loaded}} = \frac{\omega_0 L}{R_c + R_s} \quad (2.78)$$

The increase in resistance due to the conductive sample may results in Q -factor reduction by a factor of two or more (60–64). For example, for a simple loop coil (8 cm diameter, 1.5 mm wire thickness at 297.2 MHz) the measured Q -factor is 14.5 when the coil is loaded (22). The large Q -factor drop indicates that sample losses are strongly dominant over coil losses. In this case sensitivity of the NMR probe cannot be enhanced by reducing the coil noise (43).

2.4.1.2 Transmit and Receive Fields of an RF Coil

Ampere's law states that a current density passing through a conductor loop generates a magnetic field \vec{B}_1

$$\int \vec{J} \cdot d\vec{s} = \frac{1}{\mu_0} \oint \vec{B}_1 \cdot d\vec{l} \quad (2.79)$$

The generated \vec{B}_1 field inside the sample causes the magnetization (M_0) to be tilted into the transverse plane. Furthermore, based on the principle of reciprocity, the coil sensitivity in a particular location can be determined by its transmit \vec{B}_1 field.

A linearly polarized magnetic field can be decomposed in two counter-rotating circularly polarized components as shown in Figure 2.16 (65).

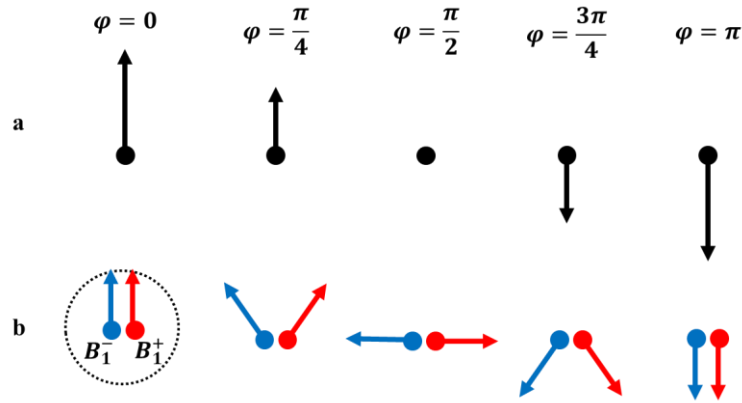


Figure 2.16: A linearly polarized \vec{B}_1 field (a) and its corresponding circularly polarized components.

Decomposed components are rotating clockwise (B_1^+) and counterclockwise (B_1^-) around the direction of the static magnetic field \vec{B}_0 .

$$B_1^+ = \frac{B_{1x} + iB_{1y}}{2} \quad (2.80)$$

$$B_1^- = \frac{B_{1x}^* - iB_{1y}^*}{2} \quad (2.81)$$

Only the magnetic field component rotating in the same direction as the spins' precession is pertinent in nuclear excitation. Therefore, the B_1^+ component of the total \vec{B}_1 field causes the magnetization to be rotated in the transverse plane (x-y plane) during RF excitation (36). Contrarily, the received signal depends on B_1^- .

The B_1^+ and B_1^- fields are not necessarily equal, especially at ultra-high frequencies (66). The time varying magnetic and electric field generated by an RF coil can be written as (65)

$$\vec{B}_1(\vec{r}, t) = \vec{B}_1(\vec{r})e^{i\omega t} \quad (2.82)$$

$$\vec{E}(\vec{r}, t) = \vec{E}(\vec{r})e^{i\omega t} \quad (2.83)$$

Using the phasor notation, \vec{B}_1 can be decomposed into complex components along the orthogonal x, y, z axes of a laboratory frame of reference: B_{1x} , B_{1y} and B_{1z} . The total amplitude of the \vec{B}_1 is expressed as

$$|B_1| = \sqrt{B_{1x}B_{1x}^* + B_{1y}B_{1y}^* + B_{1z}B_{1z}^*} \quad (2.84)$$

Assuming \vec{B}_0 to be parallel to the z -axis

$$|B_{1xy}| = \sqrt{B_{1x}B_{1x}^* + B_{1y}B_{1y}^*} \quad (2.85)$$

Equation (2.82) and equation (2.83) obey the Faraday's law of induction and the modified Ampere's law as (65)

$$\vec{\nabla} \times \vec{E} = -i\omega\vec{B}_1 \quad (2.86)$$

$$\vec{\nabla} \times \vec{B}_1 = \mu_0(\sigma + i\omega\epsilon_r\epsilon_0)\vec{E} \quad (2.87)$$

where μ_0 and ϵ_0 are the permeability and permittivity of free space, respectively. σ and ϵ_r are the electrical conductivity and permittivity of the biological sample, respectively.

Equation (2.86) indicates that generated magnetic field \vec{B}_1 of the coil induces an electric field perpendicular to \vec{B}_0 (indicated by factor i). Equation (2.87) denotes that both displacement currents ($i\omega\epsilon_r\epsilon_0\vec{E}$) and conduction currents ($\sigma\vec{E}$) contribute to the overall magnetic field in the sample (65). The B_{1x} and B_{1y} relations for a single surface loop is given by (36)

$$B_{1x} = kC_{0x}I_0e^{i(\varphi+\alpha)} \quad (2.88)$$

$$B_{1y} = kC_{0y}I_0e^{i(\varphi+\beta)} \quad (2.89)$$

where I_0 and φ are current amplitude and phase in the coil. k is a coil-geometry dependent scaling factor, C_{0x} and C_{0y} are position dependent scaling factors. α and β are position and frequency dependent phase changes due to the displacement and conduction currents.

Amplitudes of B_1^+ and B_1^- are obtained by combining equations (2.85), (2.88) and (2.89)

$$|B_1^\pm| = \frac{kI_0}{2} \sqrt{C_{0x}^2 + C_{0y}^2 \mp 2C_{0x}C_{0y} \cos(\varphi + \alpha) \sin(\varphi + \beta) \pm 2C_{0x}C_{0y} \sin(\varphi + \alpha) \cos(\varphi + \beta)} \quad (2.90)$$

At sufficiently low fields, phases α and β tend to be zero (36) and equation (2.90) can be written as

$$|B_{1xy}| = 2|B_1^+| = 2|B_1^-| = kI_0\sqrt{C_{0x}^2 + C_{0y}^2} \quad (2.91)$$

This indicates that if $\alpha = \beta = 0$, the B_1 field of the surface coil is linearly polarized and can be decomposed into two equally counter-rotating components (Figure 2.16).

At high fields, the behaviour of the magnetic field is strongly dependent on the biological properties of the sample, i.e. relative permittivity and electrical conductivity. Larger B_0 (higher frequency) requires a larger B_1 field in order to rotate the magnetization into the transverse plane. Therefore the E -field induced in the sample, based on Faraday's induction law (equation (2.86)), becomes larger, resulting in higher SAR (equation (2.120)). Furthermore, based on equation (2.87) conduction currents induced in the sample produce a magnetic field which adds to the overall \vec{B}_1 field and is 90° out of phase. This is due to the fact that the induced \vec{E} -field and the generated \vec{B}_1 field of the coil are 90° out of phase. However, displacement currents produce a field inside the sample back in phase with the original \vec{B}_1 field. This adds in-phase contributions to the overall \vec{B}_1 within the sample, but it cannot change the polarization of the

original \vec{B}_1 field (65). With increasing frequency, conduction currents become larger, therefore, they produce a larger out-of-phase magnetic field in the sample resulting in an inhomogeneity of the \vec{B}_1 field. B_1^+ and B_1^- at high field are not identical due to the mentioned effect. They are basically mirrored inhomogeneous maps along the coil axis of each other where the overall \vec{B}_1 is symmetrical relative to the coil central axis.

The wavelength (λ) for a plane wave propagating inside a medium is given by

$$\lambda_{\text{tissue}} = \frac{1}{\sqrt{\epsilon\mu}} \lambda_{\text{freespace}} \quad (2.92)$$

$\epsilon = \epsilon_0\epsilon_r$ and $\mu = \mu_0\mu_r$ are the permittivity and permeability of the medium.

At ultra-high frequencies (i.e. $f_0 \geq \sim 300$ MHz) (UHF), the wavelength becomes comparable to the size of human organs, resulting in interactions of the propagating field with the dielectric sample. E.g., at 300 MHz, the wavelength in tissue is reduced to 10-15 cm. The field inhomogeneity and local SAR “hotspots” are attributed to propagation effects at high fields (15). Equation (2.92) denotes that dielectric permittivity causes the wavelength to be decreased in dielectric samples e.g. the human body.

2.4.2 RF Coil Design

Ever since the field of magnetic resonance has grown rapidly as a tool for various biomedical applications, numerous RF coil designs have been introduced. In general, RF coils are optimized to obtain high SNR and a homogeneous \vec{B}_1 field. Furthermore special care should be taken during construction of an RF coil such as using materials that do not disturb \vec{B}_0 and ensuring mechanical stability of the coil (67). RF coils are designed for optimality with respect to the target application, however, there is no unique optimal RF coil suitable for each and every application.

2.4.2.1 Volume Coils

Volume coils are advantageous for MR applications which require a homogeneous \vec{B}_1 field over a large volume of interest (VOI). With volume coils, the sample is physically inserted into the coil. Thus, the size of the designed coil should ensure fitting of samples with various sizes.

A volume coil in its simplest form is a simple loop coil wrapped around the sample. This concept was later extended to solenoid (37) and saddle coil designs (68).

The solenoid design is frequently used for microscopic coil development. It produces a \vec{B}_1 field along its axis as shown in Figure 2.17a. Therefore, in order to create the required B_1 field in the transverse plane, the coil axis should be placed perpendicular to the static magnetic field \vec{B}_0 . In most clinical scanners, the patient is positioned along the \vec{B}_0 field inside the scanner, therefore, placing a solenoidal coil perpendicular to the sample is problematic, except for small anatomical structures such as the finger (69), which can be positioned accordingly. The high inductance and parasitic capacitance across the windings of the solenoid design result in a low self-resonance frequency making the design less applicable at higher frequency. Solenoid coils are easy to build and can be optimized by varying the diameter, number of turns and the distance between turns as explained by Hoult et al. (37) in order to create a homogeneous \vec{B}_1 field.

The saddle coil is composed of two series loops covering the whole sample (Figure 2.17b) yielding a homogeneous \vec{B}_1 field and providing a good filling factor (67). In comparison with a saddle coil, a solenoid coil of the same dimensions leads to approximately three times better sensitivity (37). This can be explained by the assumption made for the derivation of the SNR formula by Hoult et al. (37) demonstrating that half of the energy is stored via the field \vec{B}_1 within the confines of the coil and the field is homogeneous within those confines. This assumption is true for the solenoid coil due to the closed form and continuity of the windings while for the saddle coil it is not true as its open design demonstrates that most of the magnetic energy is stored in the flux lying close to the wires which does not pass through the sample (37).

The birdcage coil (70,71) is the most commonly used type of volume coil in MRI. A birdcage coil consists of several rods (legs) of wire placed circularly around the sample. The rods are terminated from both sides by two closed rings, referred to as end-rings (Figure 2.17c). Birdcage coils are divided into three designs based on the configuration and placement of capacitors: high-pass, low-pass, and band-pass designs. In high-pass designs, capacitors are distributed along the end-rings while in low-pass designs capacitors are placed along the legs. Placing the capacitors in both, the end-rings and the legs, result in a band-pass birdcage design. The reason for this nomenclature is that the equivalent electrical circuit of a low-pass bird cage consists of series inductors with parallel shunt capacitors, and for the high-pass design it

consists of series capacitors with parallel shunt inductors. These circuits act as low-pass and high-pass filters, respectively. The length-to-diameter ratio of the birdcage is a crucial factor for the achievable \vec{B}_1 homogeneity. Practical considerations for designing birdcage resonators have been published (67).

The \vec{B}_1 field created by a birdcage coil is oriented orthogonally to the coil axis, which stands in contrast to the solenoid coil. Therefore, the axis of the birdcage coil can be placed along the static magnetic field \vec{B}_0 .

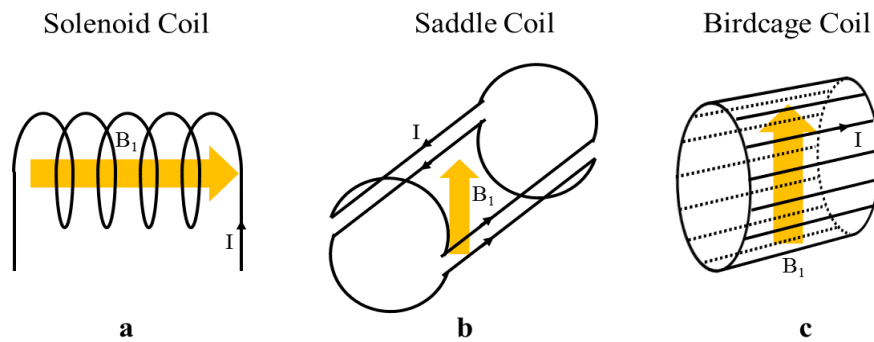


Figure 2.17: Common volume coils: Solenoid design (a), Saddle coil design (b) and birdcage coil (c). The yellow arrows depict the orientation of the produced B_1 field.

2.4.2.2 Surface Coils

Surface coils are designed for applications in anatomical regions with restricted ROI (72). Surface coils are placed directly on the investigated anatomical structures yielding an improvement in sensitivity. The signal amplitude received by surface coils with smaller size is higher close to the coil in comparison with volume coils or surface coils with larger size. Since the FOV for surface coils is reduced, less noise from the sample is coupled to the coil in comparison with volume coils (see equations (2.93) and (2.94)), resulting in higher SNR. However, the \vec{B}_1 field created by surface coils is intrinsically inhomogeneous and diminishes with increasing distance from the coil. The sample resistance in case of a homogeneous spherical sample of radius b with a volume coil of uniform coupling coefficient B_1/I can be determined by (43):

$$R_s = \frac{2\pi}{15} \sigma \omega^2 (B_1/I)^2 b^5 \quad (2.93)$$

The sample resistance for a simple surface loop based on the model given in (43) can be calculated by

$$R_s \approx \frac{2}{3\pi} \sigma \mu_0^2 \omega^2 n^2 a^3 \arctan\left[\frac{\pi a}{8d}\right] \quad (2.94)$$

where a is the coil radius, n is the number of turns, d is the coil to sample distance and ω is the angular resonance frequency. μ_0 is the magnetic permeability of free space and σ is the electrical conductivity of the sample.

As long as sample noise dominates over coil noise, coil miniaturization is a way to improve sensitivity. In the coil noise domain, SNR can be improved by reducing the internal coil noise (43). This can be achieved by using cryogenic RF coils (43,73–75), superconducting RF coils (43,75,76), and/or coil miniaturization (77,78).

2.4.2.2.1 Conventional Surface Coils

A conventional surface coil consists of a conductor loop with a tuning capacitor (Figure 2.15c). The coil size is chosen based on the MR application. In practice, several distributed (segmented) capacitors are often used in order to produce a more even current distribution in each segmented part, thus a more uniform \vec{B}_1 field (16). Furthermore, loop segmentation by distributed capacitors minimizes the conservative electric fields caused by electric potentials along the conductor. This is advantageous especially at high-field MRI in order to reduce the electric field induced in the sample, thus, minimizing the SAR (see section 2.5), and reducing electrically coupled noise from the sample.

As a rule of thumb, the segmented sections should not be longer than one twentieth of the respective wavelength.

2.4.2.2.2 Transmission Line Resonators (TLRs)

TLRs are composed of two circular conducting layers deposited on both sides of a dielectric substrate as shown in Figure 2.18 (18–20). The concept of TLRs as MRI surface coils has been

demonstrated long ago (18,19). The current flow along the transmission line is altered by the gaps. On each side of the substrate, the gaps are placed at the center of a conductor segment on the opposite side of the substrate. The \vec{B}_1 field of the TLR is created by the common mode current given by the half of the sum of the currents flowing in the two conductors (19), while the differential current, i.e. half of the difference of the currents flowing in the two conductors, does not create a magnetic field outside the transmission line (19). The differential mode current depends on the position and the intrinsic properties of the transmission line, e.g. its inductance, capacitance, characteristic impedance (Z_c), and propagation constant (β). The geometry of the windings sets the equivalent inductance, and the capacitive effect is distributed between the two conductor layers within the dielectric substrate. This way, TLR can be imagined as two loops strongly coupled to each other, and are also referred to as parallel-plate split ring resonators. A detailed analysis to derive the resonance condition for TLRs based on the transmission line theory is given in annex A.1.

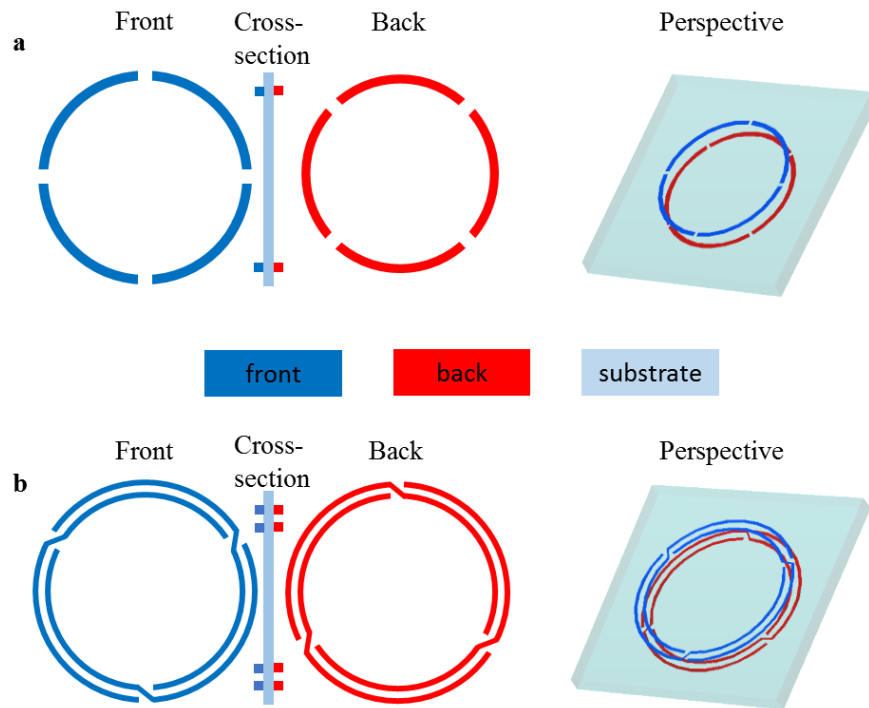


Figure 2.18: Basic design of Transmission Line Resonators (TLRs). (a) Single turn with four gaps on each side. The gaps on each side, are placed at the center of a conductor segment on the opposite side of the substrate. (b) two turn TLR with three gaps.

TLRs are typically fabricated by standard photolithographic etching techniques. TLRs can be printed on flexible substrates such as Teflon or Polyamide which makes their application

interesting for building flexible coils that can be better conformed for various sample sizes and shapes. TLRs are also interesting for high temperature superconducting (HTS) coils, as they are monolithic and, therefore, do not require lossy solder joints. The chosen substrate should fulfil the following requirements:

- Electrical conductivity σ very close to zero
- High break-down voltage
- Low dielectric loss which is characterized by the loss tangent i.e. $\tan(\delta)$

In this work, polyamide (Kapton) was used as the substrate material for all of the investigated simulations and fabricated RF coils. Polyamide has a relative permittivity of about 3.5 and a loss tangent of 0.001 at 300 MHz (79). Materials such as FR4, Teflon are frequently used as substrates for TLRs. Sapphire can be used for superconducting TLRs which can be fine-tuned and matched contact less via a moveable inductive loop and dielectric material (80).

An analytical model for resonance frequency of TLRs based on transmission line theory was initially “proposed” by Gonord et al for single structures (19) and was extended to multiple turns designs by Serfaty et al (81) using the following equation

$$\frac{L_{\text{tot}}\omega_0}{4N_g Z_0} \tan\left(\frac{\omega_0 \sqrt{\epsilon} l_f}{4N_g c}\right) = 1 \quad (2.95)$$

where ω_0 is the angular resonance frequency, L_{tot} is TLR’s equivalent inductance, l_f is the length of one conducting band and Z_0 is the parallel-plate transmission line characteristic impedance and ϵ is the permittivity of the substrate, N_g denotes the number of gaps per conductor and c is the vacuum speed of light. The derivation of equation (2.95) based on the transmission line theory together with the corresponding formulas for L_{tot} and Z_0 are given in the appendix. The accuracy of the analytical model for TLRs to predict resonance frequency in comparison with experiments is within 10 % range (82). Possible reasons for such a deviation could be inaccuracy in the estimation of the characteristic transmission line impedance and/or inductance and substrate dielectric properties. Therefore, accurate modelling of TLRs using 3D EMS is desirable.

2.4.2.3 Array Coils (Phased-Array Coils)

RF coil arrays were introduced to take advantage of high SNR of small surface coil over an extended field of view (FOV) (1). The local signal collected by the individual coils within the

array is then combined to obtain an overall signal over the imaged FOV. Early MRI scanners generally had only one single receiver channel, therefore, array segments needed to be electronically switched to fully cover the sample. These coils are referred to as switched coils which offered SNR advantages over the single coils when the slices are widely separated (1). This is because of the fact that coils are switched during each excitation, therefore, only one coil can be associated with a particular slice (1). The design and configuration of RF coil array has evolved during the past decades. In general, arrays exist either in a planar combination of surface coils applied to a plane such a human torso or a combination of surface coils surrounding the sample, e.g. human head (1). Initially, arrays were designed in an inflexible configuration with rigid housings resulting in an inefficient conformity for different sample sizes causing a significant SNR reduction (11). Flexible arrays were introduced to the MRI in the past decade (9,11–13,17,82–87) to ensure the proximity and conformity of the coil for samples with various sizes. Also array coils can be used in the transmit mode in order to achieve a more homogeneous B_1^+ pattern by adjusting the phases of individual elements referred to as static phase shimming (88). RF coil array employs PI (2,3) and Parallel transmission (56) which are advantageous to speed up MRI experiment and creating more uniform transmit B_1^+ field. Transmit SENSE permits choosing arbitrary excitation patterns by supplying each element with different amplitude and phase referred to as dynamic phase shimming (57). Additionally, parallel transmission techniques provide a solution to shorten the spatially selective RF pulse by using transmit phased-array coils (56,88).

2.4.2.3.1 Mutual Decoupling in the Array Designs

Placing two resonators in close vicinity results in strong magnetic coupling and peak splitting in resonance frequency response as shown in Figure 2.20. One of the major technical challenges in array coil designs is to eliminate the mutual coupling between individual elements. Considering the circuit's model of two RF coils close to each other, the mutual impedance Z_{21} is defined as the ratio of the induced voltage in coil 2 due to current flowing in coil 1

$$Z_{21} = \frac{V_2}{I_1} = R_{21} + iX_{21} \quad (2.96)$$

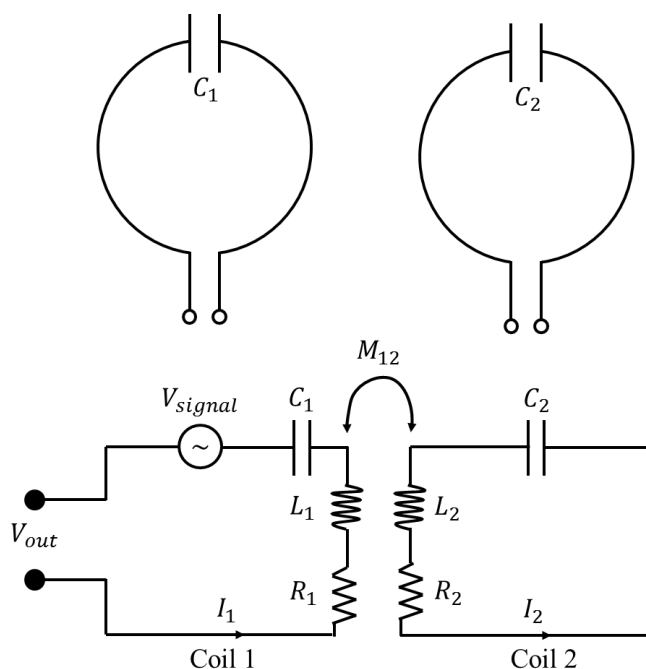


Figure 2.19: Two resonators placed in close vicinity to each other (top) and their corresponding electrical circuit coupled to each other via mutual coupling between them.

Like self-impedance, mutual impedance has a resistive (R_{21}) and reactive (X_{21}) part, where the latter is usually inductive for NMR coils. The inductive mutual coupling between the two coils yields peak-splitting in the resonance frequency of the individual coils as shown in Figure 2.20.

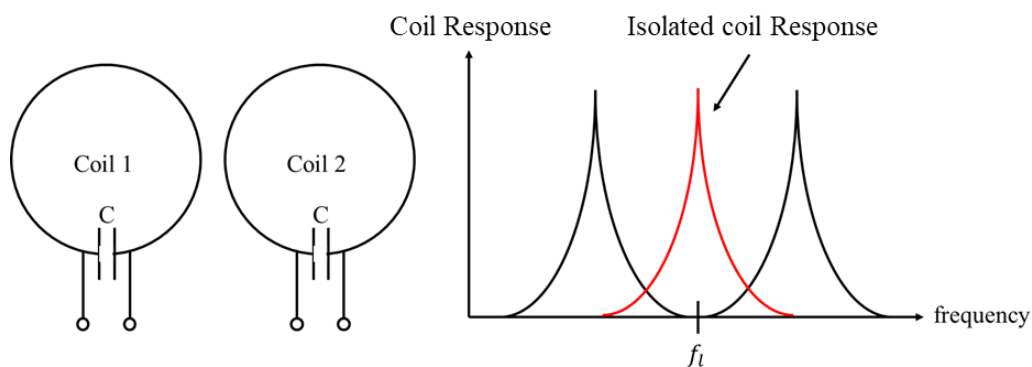


Figure 2.20: Peak splitting in resonance frequency response due to the mutual coupling of two adjacent RF coils.

The coupling strength referred to as the coupling coefficient can be calculated as

$$k = \frac{M_{12}}{\sqrt{L_1 L_2}} \quad (2.97)$$

where M_{12} is the mutual inductance between the two coils and L_1 and L_2 are self-inductances of each coil. Depending on the distance between the two coils and the Q -factor of the two coils, three situations (see equation (2.97)) are defined

- Under coupling: The two coils are placed far away from each other yielding to a small M .
- Critical coupling: Critical coupling coefficient k_c depends on the Q -factors of the two RF coils,

$$k_c = \frac{1}{\sqrt{Q_{\text{coil1}} \cdot Q_{\text{coil2}}}} \quad (2.98)$$

- Over coupling: Further decreasing the distance between the two coils results in coupling coefficients higher than k_c .

The voltage at the output of the coil (see Figure 2.19) can be calculated by (89)

$$V_{\text{out}} = V_{\text{signal}} + \overbrace{\left(R_1 + i \left(\omega L_1 - \frac{1}{\omega C_1} \right) \right)}^{N_{\text{coil}}} I_1 + \overbrace{i \omega M_{12} I_2}^{N_{\text{coupling}}} \quad (2.99)$$

Based on equation (2.99), a noise associated with coil 1 i.e. N_{coil} and another noise associated with mutual coupling is added to the received signal. Here, N_{coil} can be minimized by tuning coil 1 to the Larmor frequency, thereby $\omega L_1 = 1/\omega C_1$ which is the resonance condition. Thus only intrinsic resistance R_1 remains. Then, N_{coupling} can be minimized by eliminating mutual coupling and flowing current in coil 2 (I_2). Various techniques to eliminate the mutual flux shared between the individual elements of an array (minimizing N_{coupling} in equation (2.99)) are briefly discussed in the following sections.

2.4.2.3.1.1 Overlap decoupling

One of the common ways to cancel mutual coupling (see equation (2.99)) between coil elements in an array is by finding the correct overlap distance so that the net magnetic flux shared by the coils is zero (Figure 2.21) (1). This method is simple and frequency independent,

however, the overlap is possible only for neighbour coils and not the next-nearest neighbour coil. Therefore, the mutual coupling of next-nearest neighbours might still be significant.

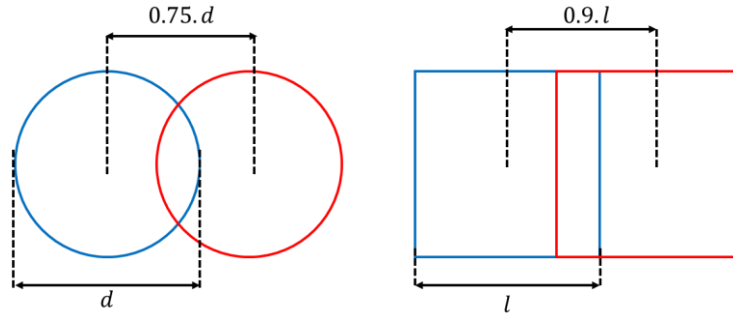


Figure 2.21: Overlap distance necessary for mutual decoupling of circular (left) and square (right) loops.

2.4.2.3.1.2 L-C Network

The mutual coupling between coil elements can be eliminated using interconnecting L-C networks (25). Figure 2.22 represents the circuit model for capacitive and inductive decoupling schemes.

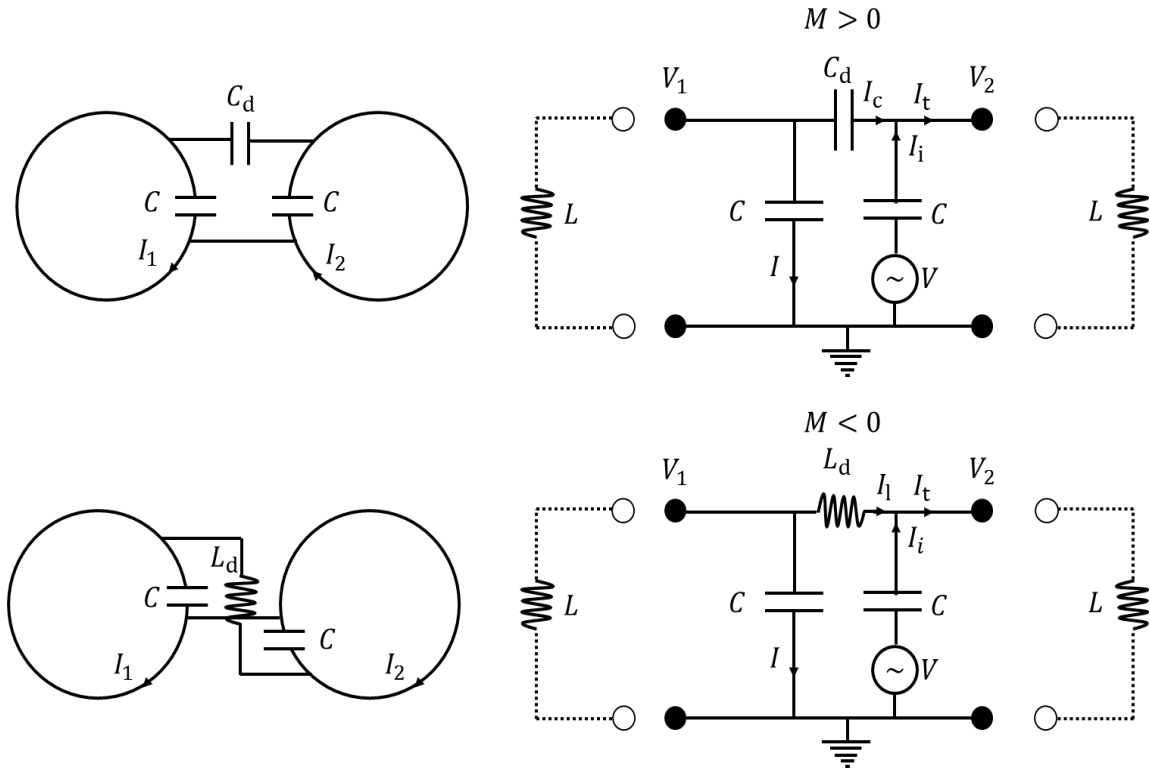


Figure 2.22: Capacitive decoupling scheme for $M > 0$ and its equivalent two-port circuit model (top). Inductive decoupling scheme for $M < 0$ and its equivalent two-port circuit model (bottom.)

I_1 and I_2 are the currents flowing in coils 1 and 2, respectively, and L and C are the self-inductance and capacitance of each coil, respectively. The sign of M can be defined based on the direction of the currents flowing in the two coils, i.e. if I_1 and I_2 flow in opposite directions such that the mutual coupling causes an increase of the induced voltage (see the second term in the right-hand-side of equation (2.99)) the sign of M is positive, otherwise the sign of M is negative (25). For simplicity the resistance of the wires is ignored. V_1 and V_2 are the voltages at the terminals of coils 1 and 2 and V is the induced voltage in coil 2 by the current flowing in coil 1. Assuming that current I has zero phase and by setting V_2 to zero (25), the voltage V_1 is given by

$$V_1 = I \cdot \frac{1}{j\omega C_1} = \left| \frac{1}{j\omega C} \right| \angle -90^\circ \quad (2.100)$$

since $M > 0$, the induced voltage is given by

$$V_1 = j\omega M \cdot I = |\omega M \cdot I| \angle 90^\circ \quad (2.101)$$

and the induced current in the second coil can be determined by

$$I_i = \frac{V}{1/j\omega C_1} = \left| \frac{V}{1/j\omega C_1} \right| \angle 180^\circ \quad (2.102)$$

The current passing through the decoupling capacitor is given by

$$I_c = \frac{V_1 - V_2}{1/j\omega C_d} = \left| \frac{V_1}{1/j\omega C_d} \right| \angle 0^\circ \quad (2.103)$$

This way, the total cross-talk current $I_t = I_c + I_i$ can be reduced to zero by adjusting C_d . Similarly for the inductive decoupling scheme (see Figure 2.22) where $M < 0$, the induced voltage on the second coil is given by

$$V_1 = j\omega M \cdot I = |\omega M \cdot I| \angle -90^\circ \quad (2.104)$$

The induced current in the second coil and the current passing through the decoupling inductor are given by the following equations

$$I_i = \frac{V}{1/j\omega C_1} = \left| \frac{V}{1/j\omega C_1} \right| \angle 0^\circ \quad (2.105)$$

$$I_l = \frac{V_1 - V_2}{j\omega L_d} = \left| \frac{V_1}{1/j\omega C_d} \right| \angle -180^\circ \quad (2.106)$$

The total cross-talk current $I_t = I_l + I_i$ can then be reduced to zero by adjusting L_d . L-C decoupling method strongly depends on the load and in the case of using only capacitors it is frequency dependent. Nevertheless, L-C decoupling is applicable in both transmit and receive modes with restriction of element placement.

2.4.2.3.1.3 Preamplifier Decoupling

Another alternative approach to decouple the coil elements is to reduce the induced current in coil 2 due to flowing current in coil 1, thus reducing the shared magnetic flux. Preamplifier decoupling implementation is shown in Figure 2.23. Here, L_2 and C_2 are used to match coil 2 to 50Ω while they act as a parallel resonant circuit when the input impedance of the preamplifier is zero. In this case, the coil sees a very high impedance that acts like an open-circuit i.e. $I_2 = 0$. This way, the term N_{coupling} in equation (2.99) becomes zero resulting in the decoupling of coil 1 from coil 2. Since preamplifiers are very sensitive to the higher voltages in the transmit mode, this decoupling technique is only feasible for receive only arrays.

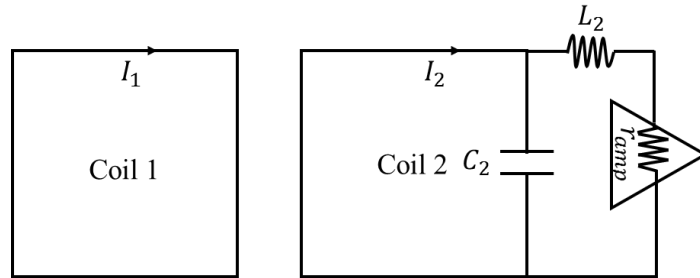


Figure 2.23: Preamplifier decoupling: Minimizing the induced current I_2 by transforming a high impedance using the preamplifier.

2.4.2.3.1.4 Overlapping Annexes

Decoupling using overlapped annexes was introduced by Kriegl et al (17) to decouple an array of TLRs. In this method, the coil elements are decoupled via the mutual flux shared between the overlapped annexes shown in Figure 2.24. With this method, efficient decoupling can be obtained and it is frequency independent. However it is limited by coil geometry and there is no analytical modelling for decoupling optimization. This technique is especially advantageous for double sided monolithic flexible designs e.g. TLRs, while using conventional decoupling techniques discussed in previous sections are not well suited for them. Conventional decoupling techniques are rather restricted to the single layer designs with lumped elements or they require several layers which implies a more complex design (17).

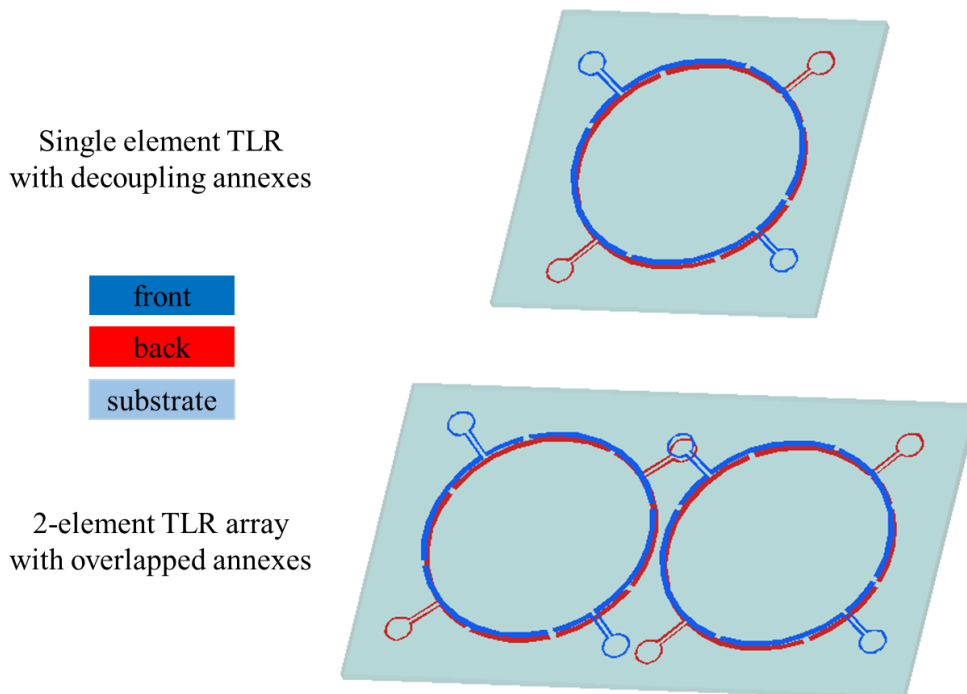


Figure 2.24: single turn TLR with 4 gaps: Single element TLR with decoupling annexes (top), each conductor side contains two annexes. 2-element TLR array with overlapped annexes (bottom), two annex from opposite conductor sides are overlapped.

2.4.2.3.1.5 Decoupling Rings

Another strategy to decouple individual elements of an array is to place a concentric loop around the elements (26). In this method, decoupling is done via the shared magnetic flux of the overlapped decoupling rings. In contrast to conventional decoupling techniques discussed

in previous sections, decoupling rings are compatible for flexible monolithic arrays, e.g. TLR arrays. The original FOV of non-overlapped arrays is preserved using decoupling rings, which is not the case for overlapped decoupling technique. For TLR arrays, decoupling rings of the nearest neighbours are deposited on the both sides of the substrate for overlapping as shown in Figure 2.25. Decoupling optimization is done by analytical calculation of the shared magnetic flux as a function of the decoupling overlap distance (90). An analytical model for decoupling optimization is given in A.2. In the present work, we used the decoupling ring technique to develop the 12-element flexible TLR array. This method is further discussed in section 3.3.2.

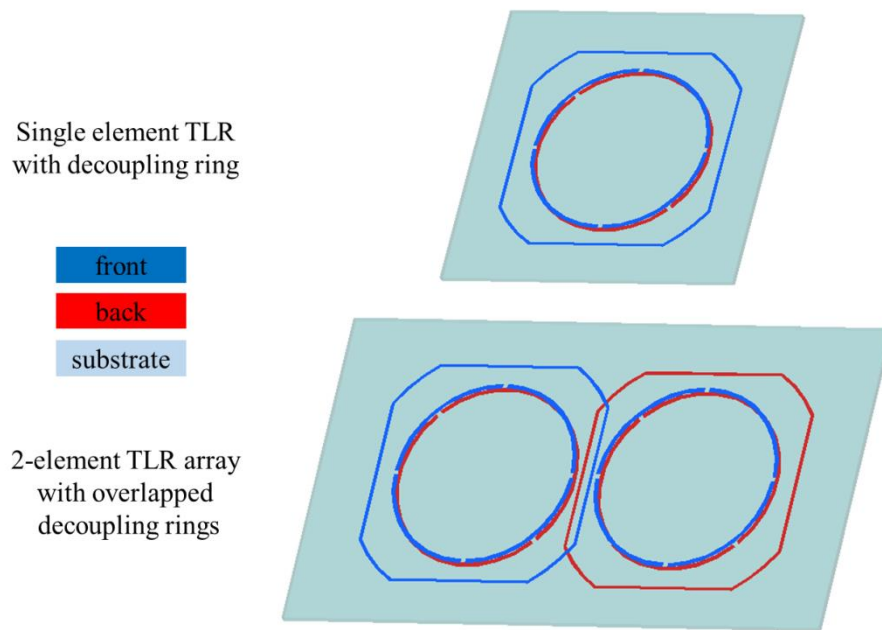


Figure 2.25: single turn TLR with 4 gaps: Single element TLR with the decoupling ring (top). 2-element TLR array with overlapped decoupling rings (bottom): decoupling rings of the two elements are deposited on both sides of the substrate for overlapping.

2.4.3 Connecting the RF Coil to the MR Scanner

In general an RF coil has a dual role; transmitting the RF signal which rotates the spin magnetization and detecting the magnetic flux created by the precession of spin magnetization in the transverse plane. Therefore, it is necessary to connect the RF coil to the transmit and receive chains. The necessary compartments in the transmit and receive chains are explained in the following section.

2.4.3.1 Power/Noise Matching

Connections between the RF probe and the MR scanner is usually made by coaxial cables having a characteristic impedance of $50\ \Omega$. It is important to transfer the maximum available power to the RF probe during RF transmission. To this end, the coil and the cable should have the same impedance Z_0 (typically $50\ \Omega$). This condition is called power matching. A mismatch in impedance makes the transmit and receive chain less efficient.

On the other hand, preamplifiers are used in order to amplify the induced signal (in the order of mV (89) to a higher voltage. In the receive chain a noise may be added to the induced signal by the preamplifier. Preamplifiers are usually characterized by their noise figure(91)

$$NF(dB) = 20\log\left(\frac{SNR_{input}}{SNR_{output}}\right) \quad (2.107)$$

Noise figure reflects SNR degradation during signal amplification. The Noise figure (NF) depends on the frequency and the impedance that the coil presents to the preamplifier referred to as source impedance. The noise figure is minimized for a unique source impedance called Z_{opt} (typically $50\ \Omega$). Most of the MRI preamplifiers are calibrated for Z_{opt} of $50\ \Omega$. To ensure optimal SNR performance of the preamplifier, the coil impedance should be transformed to Z_{opt} . Typically, the impedance of a loaded RF probe is presented as $Z = R + iX$, where R is a resistive part ranging from a few Ω to less than $0.01\ \Omega$ and X is the reactive part in the range of 20 - $200\ \Omega$. Modern preamplifiers can achieve a noise figure (NF) of $0.3\ dB$. Since the signal induced in the RF coil is very small (in order of mV) the preamplifier has to be placed in close vicinity of the coil in order to minimize insertion losses arisen from connecting cables.

The two common ways used in practice to transform the complex impedance of a loaded RF coil to the required purely resistive $50\ \Omega$ are capacitive and inductive matching techniques which are discussed in the following sections.

2.4.3.2 Capacitive Tuning and Matching

A basic tuning and matching network is composed of two variable capacitors, one in parallel with the RF probe and the other in series with the RF coaxial cable shown in Figure 2.26.

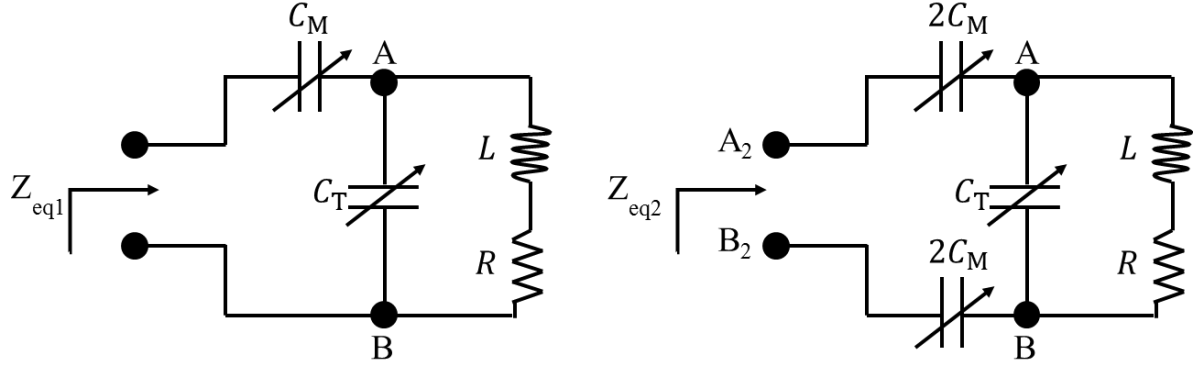


Figure 2.26: Basic tuning and capacitive circuitry: unbalanced (left) and balanced (right) network.

Capacitive components introduce less noise to the circuit due to the higher Q -factors in comparison with inductive components (16). Ceramic capacitors with fixed capacitance have a Q -factor around 1000 at 300 MHz, while real inductors have a Q -factor of 50 at the same frequency. As discussed in section 2.2.2, the alternating electric field associated with time varying magnetic field is responsible for both dielectric and radiation losses. Both dielectric and radiation losses can be minimized by a proper design of tuning and matching network (16). The total impedance seen from port AB (see Figure 2.26) can be calculated by

$$Z_{AB} = \frac{R(XC_T)^2}{R^2 + (XL - (XC_T)^2)} - j \left(XC_T \frac{R^2 + XL(XL - XC_T)}{R^2 + (XL - (XC_T)^2)} \right) \quad (2.108)$$

where $XL = L\omega$ and $XC_T = 1/C_T\omega$.

The total equivalent input impedances of the electrical circuits shown in Figure 2.26 can be written as

$$Z_{eq1} = Z_{AB} + XC_M \quad (2.109)$$

$$Z_{eq2} = Z_{AB} + \frac{XC_M}{4} \quad (2.110)$$

where $XC_M = 1/C_M\omega$.

Balancing the probe i.e. symmetry with respect to the ground, reduces the common unwanted current that may induce dielectric and radiation losses. As such, the same current flows in both capacitors resulting in the same voltage with respect to the ground but with opposite phases. The voltage is cut in half in comparison with the asymmetric design providing a reduction of electrical losses. Coil segmentation is another approach to minimize radiation losses, as already discussed in section 2.2.2. The Q -factor measured at 200 MHz for the designs shown in Figure 2.27 are listed in Table 2.2 (16).

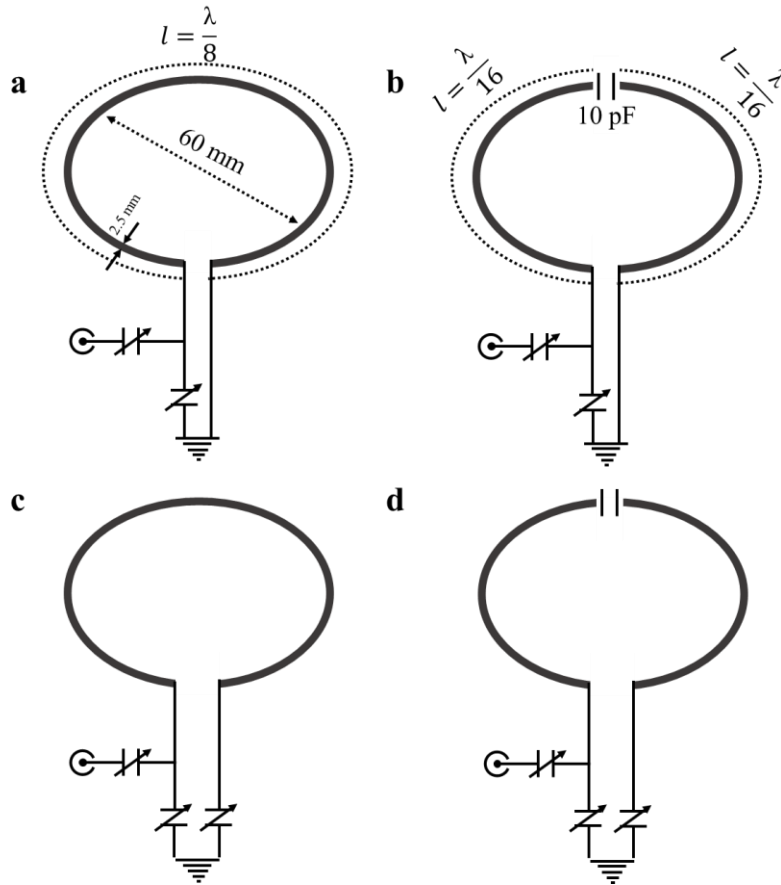


Figure 2.27: Experimental setup used to demonstrate radiation loss effect: non segmented (a) and segmented (b) loops with unbalanced tune and match network. Non segmented (c) and segmented (d) loops with balanced tune and match network.

Table 2.2: Measured Q -factor at 200 MHz for the loop coil designs demonstrated in Figure 2.27(16).

Loop coil	Unbalanced network	Balanced network
Non segmented	80 (Figure 2.27a)	260 (Figure 2.27c)
segmented	200 (Figure 2.27b)	400 (Figure 2.27d)

2.4.3.3 Inductive Tuning and Matching

Another way to tune and match an RF probe at the desired frequency is inductive matching. Automatic balancing with respect to the electric field, no need for direct electrical connections and independent adjustments of tuning and matching are among the advantages of this procedure (16,23,91).

Inductive matching is usually done by an inductive loop referred to as pickup loop. Using the inductive matching approach, the coil impedance has to be transformed to $Z_0=50\ \Omega$ at the terminals of the pick-up loop.

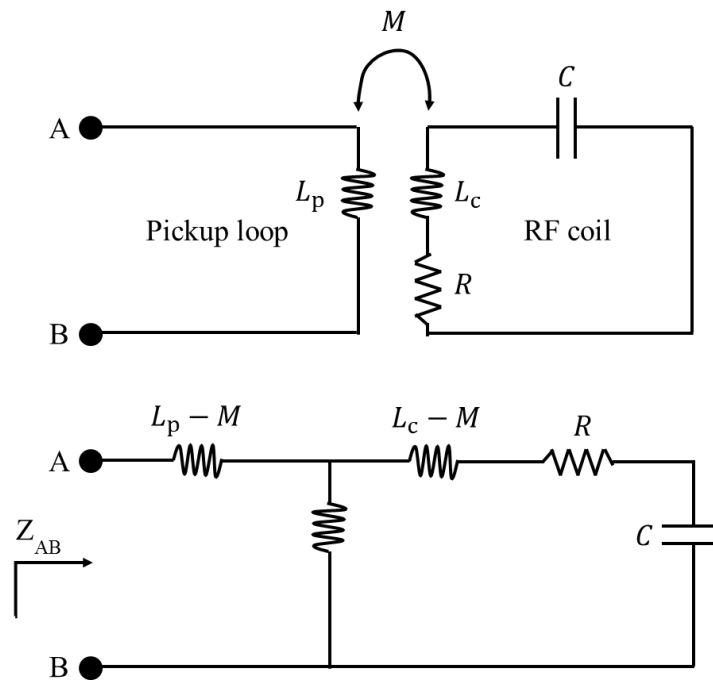


Figure 2.28: Inductively matched circuit diagram (top) and its equivalent T-circuit (bottom). The ohmic losses in the pick-up loops are considered to be negligible.

The RF coil is coupled to the pick-up loop (here assumed to be a lossless pick-up loop) by the shared magnetic flux via the mutual inductance between them (Figure 2.28). The total impedance seen from port AB can be written as

$$Z_{AB} = \frac{(\omega M)^2}{R^2 + (X_r)^2} R_r - j \left(\frac{(\omega M)^2}{R^2 + (X_r)^2} X_r + L_p \omega \right) \quad (2.111)$$

where $X_r = L_c \omega - 1/C\omega$.

Impedance matching is achieved by changing the distance between the pick-up loop and the coil so as to make $Z_{ab}=50\ \Omega$. Depending on the three coupling conditions defined in section 2.4.2.3.1, the following impedance matching situations are obtained:

- Under coupling: a small resistive impedance is transferred at the terminals of the coupling loop which is much smaller than Z_0 and impedance matching is impossible.
- Critical coupling: The transformed impedance is exactly $Z_0=50\ \Omega$ at the resonance frequency.
- Over coupling: The resistive part of the transformed impedance is higher than Z_0 . In this situation, impedance matching can be achieved at two different frequencies slightly below and above the original resonance frequency.

Special care in designing inductive matching steps has to be taken into account for resistive losses in the pickup loop, which are characterized by coupling loop noise factor and current flowing in it. This may perturb the main magnetic field created by the RF coil (92).

2.4.3.4 Common Mode Current Blocking

A coaxial cable itself is an unbalanced structure i.e. a single signal working against ground. Connecting one end of a balanced circuit like RF coil to the shield of the coaxial cable yields an unbalanced circuit. This results in a current flowing on the shield of the coaxial cable referred to as common mode current. The common mode current affects coil tuning, coupling between coils in a phased array coil, image inhomogeneity and may cause severe patient burns (16,92). Baluns and cable traps are used to prevent common mode currents. A balun is a network that converts an unbalanced circuit into a balanced one. Figure 2.29 shows various types of baluns. Furthermore, baluns can act as impedance transformers such as $\lambda/2$ balun which is a 4:1 impedance transformer, i.e. the impedance of the balanced side is four times the impedance at the unbalanced side (16). Using cable traps is another possibility to reduce common mode currents. Figure 2.29.d shows a typical cable trap without any need of soldering to the coaxial cable called floating cable trap (93).

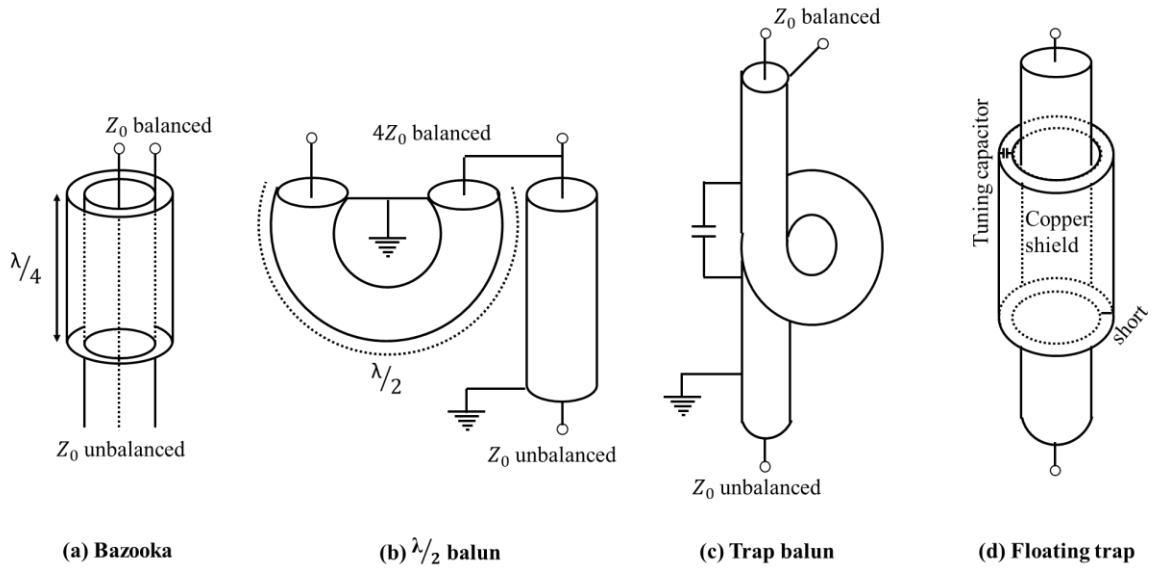


Figure 2.29: Typical baluns and cable traps designed to eliminate common mode currents.

2.4.3.5 Receiver, Transmitter, Transceiver probes

Generally, NMR probes are divided into three different groups based on their functionality: Transmit-only coils which produce the excitation field, Receive-only coils which detect the signal from the body after the excitation and the so called transceiver coils. An RF probe which is used in both transmit and receive modes is called a transceiver coil. Often at low field, a single receive-only coil or phased-array coil is used in combination with a separate volume coil as a transmit-only coil in order to provide a more homogeneous B_1^+ distribution. While in the UHF MRI due to the lack of a commercially available whole body transmit coil, most of the RF coils are designed as transceiver RF coils. In both transceiver and receive-only coils, the transmit chain should be isolated from the receive chain. For receive only coils, the coupling to the transmit coil has to be avoided. The transmit coil induces high current in the receive coil during transmission which may pose a potential risk for the patient. Additionally, coil sensitivity might be degraded during reception due to the mutual coupling between two coils. One way to avoid coupling between separate transmit and receive coils is to detune one coil while using the other by using a trap circuit and a PIN diode switch (93–95). The simplest form of a trap is an inductance connected in parallel with one of the coil capacitors which forms a resonance frequency when diodes are activated. The formed resonance introduces a high impedance at the resonance frequency which blocks the current flow in the RF coil. PIN diodes are triggered by an actively DC signal provided by the MR scanner (active detuning) or they

can be replaced by fast RF diodes which are triggered by the induced transmit signal (passive detuning).

2.4.3.6 Transmit/Receive Switch

In the case of transceiver coils, if the transmit power passes in the receive channel the preamplifier can be permanently damaged. To isolate transmit path (Tx) from the receive path (Rx), transmit and receive switches (T/R switch) are used. T/R switches are mainly based on PIN diodes and quarter-wavelength transmission lines which act as impedance transformers (16). A simple T/R switch diagram is shown in Figure 2.30.

During RF transmission both PIN diodes (D_1 , D_2) are active. Closing D_1 allows the transmit signal to pass through the coil while closing D_2 connects the preamplifier input to the ground. The quarter-wavelength transmission line transforms the short circuit impedance (ideally 0) to a very high impedance (ideally ∞) at the other end of transmission line. This high impedance prevents the transmit current to pass through the preamplifier. During reception, both PIN diodes (D_1 , D_2) are opened, and therefore the signal received by the coil can directly reach the preamplifier.

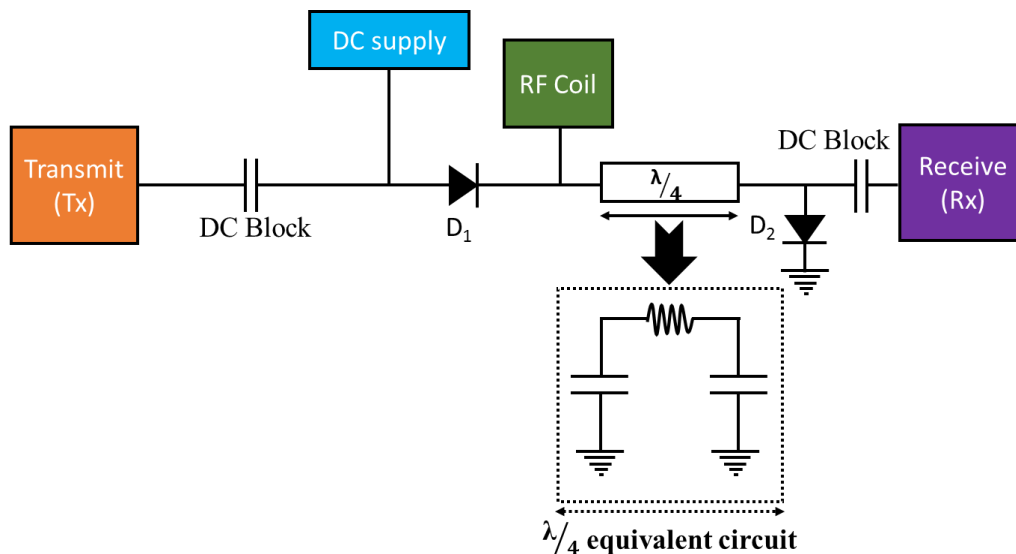


Figure 2.30: Transmit and Receive (T/R) switch based on quarter-wavelength transmission line.

2.4.3.7 Power Splitter

Typically, MR scanners are equipped with only one transmit channel (Tx). In order to use an array, the power delivered from the single Tx channel has to be split between individual elements within the array. One simple method to achieve low loss power splitting is to use a

Wilkinson Power Divider (WPD) (96). The WPD is based on quarter-wavelength transmission lines and it can be used to split the transmit power into equal or unequal parts. A three-way WPD which splits the power equally with the same amplitude and phase is shown in Figure 2.31.

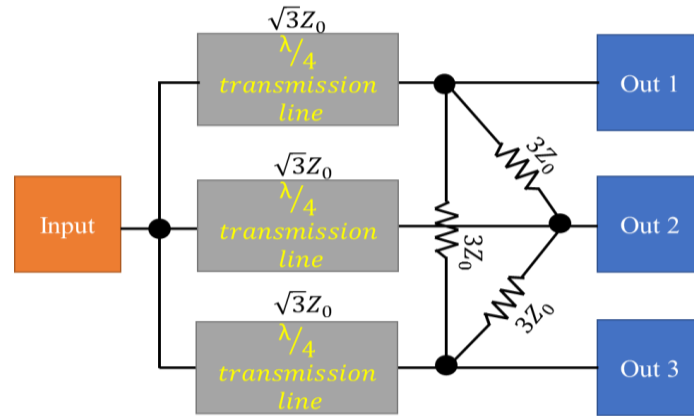


Figure 2.31: three-way Wilkinson power splitter.

Z_0 is the characteristic impedance of the transmission line e.g. 50Ω . The lumped element model for the quarter wavelength transmission line is given in Figure 2.32.

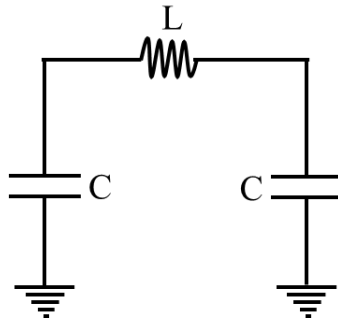


Figure 2.32: lumped element model of the quarter wavelength transmission line.

In the electrical circuit given in Figure 2.32, $L = Z_0/\omega$ and $C = 1/\omega Z_0$.

2.4.4 Experimental Characterization of RF Coils

2.4.4.1 Bench Measurement

2.4.4.1.1 Network Analyzer

An RF network is classically analyzed by a vector network analyzer (VNA). Using VNA, the amplitude and phase information of the electrical networks as a function of frequency can be measured. Typically, a VNA consists of a power generator that generates a test signal routed to the device under the test (DUT) by a signal separation device. The altered signal is then routed to the VNA receiver (typically two receivers) also by the signal separation device. The measured signal in the VNA receiver can be displayed in various formats e.g. linear logarithmic scale or in the form of smith chart. Additionally, VNA is widely used to measure scattering parameters (S-parameters) which are described in section 2.4.4.1.2. In this work, bench measurements were performed using a two-and four-port VNA (E50601B and EB071C, Agilent, Santa Clara, USA).

2.4.4.1.2 S-Parameters

Scattering parameters establish the relationship between incident, reflected and transmitted waves with voltage V of the electrical network under the test. The S-parameters of a two-port network are defined as,

$$\begin{aligned} S_{11} &= \frac{V_{1b}}{V_{1f}} \Big|_{V_{2f}=0} & S_{21} &= \frac{V_{2b}}{V_{1f}} \Big|_{V_{2f}=0} \\ S_{12} &= \frac{V_{1b}}{V_{2f}} \Big|_{V_{1f}=0} & S_{22} &= \frac{V_{2b}}{V_{2f}} \Big|_{V_{1f}=0} \end{aligned} \quad (2.112)$$

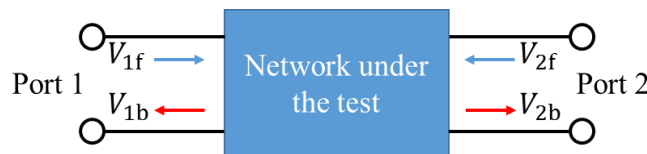


Figure 2.33: A two-port network S-parameters analysis.

The indices f and b denote the forward and backward voltages as shown in Figure 2.33. In S_{ij} , the first subscripts (i) refers to the receiving port and the second one (j) denotes the transmitting port.

$$S_{ij} = \begin{bmatrix} S_{ii} & S_{ij} \\ S_{ji} & S_{jj} \end{bmatrix} \quad (2.113)$$

The diagonal elements of the S_{ij} matrix are reflected measurement corresponding to the respective voltage reflection coefficients ρ while off-diagonal elements are transmitted measurements. Often, S-parameters are expressed in dB scale.

2.4.4.1.3 Resonance Frequency and Q -Factor Determination

Typical characteristics of an RF coil such as Q -factor and resonance frequency can be extracted from S-parameters measurements as a function of the frequency using sniffer loops (pickup loop). Sniffer loops are commonly fabricated in the form of single-loop or double-loop probes as shown in Figure 2.34.

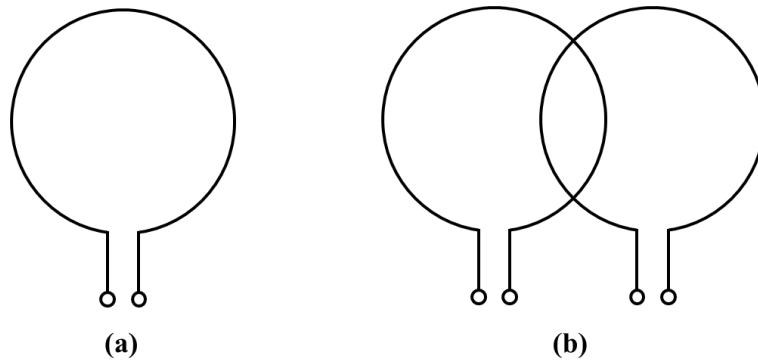


Figure 2.34: Sniffer loop designs: single loop (a) and double-loop design (b) which the two loops are decoupled via overlapping.

The double-loop probe (67) consists of two identical loops which are decoupled via partial overlapping. By connecting the double-loop probe to the VNA, a transmission measurement (S_{ij}) can be performed. The incident signal transmitted through one of the loops induces a current in the RF coil; then the voltage induced in the second loop by the current flowing in the RF coil is recorded by VNA. The resonance frequency and Q -factor can be calculated from S_{21} curve by determining the curve maximum and respective -3 dB bandwidth. Additionally, the coupling between the probe and the RF coil should not be strong, else an equivalent resistance

is added to the coil which leads to an error in measured Q -factor. This error can be neglected for $S_{21} \leq -40$ dB. During measurement with a two-loop probe, one should ensure that the loops are efficiently decoupled from each other ($S_{21} \leq -80$ dB). At resonance frequency, the S_{21} value should exceed the reference level by approximately +20 dB (97).

Another common sniffer loop is the single-loop probe (98) which performs reflection measurements. This measurement typically consists of two steps with the first performed with sniffer loop in free space (ρ_0) and the second in the presence of the RF coil (ρ_c). Subtracting the first measurement from the second yields a compensated reflection coefficient

$$\rho_{\text{comp}} = \rho_c - \rho_0 \quad (2.114)$$

Like the double-gap loop probe method, the influence of the single-loop on the Q -factor measurement can be minimized if the dip in S_{ii} curve is below -40 dB, else one can correct the initially determined Q -value using (98) using the following formula

$$Q = \frac{Q_{\text{initial}}}{1 - \rho_{\text{comp}}} \quad (2.115)$$

In this work, single-loop probe method was mostly used to measure the RF coil characteristics on bench.

2.4.4.2 MRI Experiments

2.4.4.2.1 MRI Scanner

The most important part of an MRI scanner is the main magnet that should provide a homogenous static field with good temporal stability. Nowadays, modern magnets are built using superconducting technology to achieve field strengths ≥ 1.5 T. The shim coils are placed in the bore of the magnet to homogenize the static magnetic field in the presence of the sample. In addition to shim coils, gradient coils are placed in the magnet bore for signal localization (see section 2.3.3).

In this work, MRI experiments were carried out on a 7 T whole-body scanner (Magnetom, 7 T MRI, Siemens Medical Solutions, Erlangen, Germany). The 7 T scanner is equipped with a SC72d gradient coil with a maximum gradient strength of 70 mT/m and slew rate of 200 T/m/s.

The scanner is equipped with one transmit channel for ^1H nuclei, another transmit channel for x-nuclei and 32 receive channels.

2.1.1 Imaging Sequences (MR Performance)

Before in vivo imaging with RF coil, its functionality has to be tested inside the scanner. In order to simulate the realistic environment, a tissue-like phantom has to be constructed for MR experiments. Special care must be taken to obtain correct tissue dielectric properties such as relative permittivity and electrical conductivity. In this work, three different phantoms were used for MRI experiment which are described in 3.1.2.

A basic test for the RF coil performance is to acquire an MR image of a homogenous phantom. Gradient echo (GRE) sequences are widely used for the RF coil characterization (99,100). A more advanced imaging test for flexible coils is to perform MRI experiment of the coil form-fitted to the phantom with non-planar surface.

One of the most important characteristics of the RF coils is B_1^+ field distribution especially at UHF. B_1^+ field distribution is determined from the acquired flip angle maps during MRI experiments. Numerous techniques enabling B_1^+ field mapping have been established (101). Available methods are based on the image or phase information acquired during experiments. Equation (2.116) defines flip angle map achieved by an RF pulse as a function of pulse duration τ , gyromagnetic ratio γ and the B_1^+ field

$$\alpha(x) = \gamma B_1^+(x) \int_0^\tau f(t) dt \quad (2.116)$$

$f(t)$ is the shape of the RF pulse. Among the established techniques for flip angle mapping, the so called double-angle method (DAM) (102) is widely used in MRS experiments.

DAM is an image-based strategy which uses the ratio of two images with two different flip angle maps. Using GRE sequence, the signal amplitudes of the first and second images are proportional to $\sin(\alpha)$ and $\sin(2\alpha)$, respectively. The flip angle is then calculated by taking the ratio of the two acquisitions

$$r = \frac{\sin(\alpha)}{\sin(2\alpha)} = \frac{1}{2\cos(\alpha)} \quad (2.117)$$

DAM leads to robust results and can be implemented straight forward. DAM is inherently inefficient, because it takes rather long to acquire flip angle maps since a $TR \geq 5 T_1$ is needed to allow for full recovery of the longitudinal magnetization before each excitation. Furthermore, using DAM, flip angles between 90° - 180° give the same magnitude ratios as those obtained for flip angle maps between 0° and 90° . Therefore, this method is only valid for flip angle maps between 0° and 90° . The DAM method has been extended to take into account phase information from two acquisitions in order to map flip angles from 0° to 180° (103). Taking into account the phase information, for flip angles from 0° to 90° , the two acquisitions have the same phase, while for flip angles between 90° and 180° the phase of the two acquisitions differs by 180° (103). This way flip angles ranging from 0° to 180° can be mapped by determining the relative phase difference between the two acquisitions.

In this work, we used a magnitude-based method called Saturated Turbo FLASH (satTFL) (104) to acquire flip angle maps. This method relies on the acquisition of two images, a proton density (PD) weighted image and a preconditioned image following a slice-selective saturation RF pulse. A turbo fast low-angle shot (Turbo FLASH) sequence is used for image readout. The flip angle can be determined from the intensity ratios of the two acquisitions

$$\alpha = \arccos\left(\frac{S_{\text{sat}}}{S_0}\right) \quad (2.118)$$

where S_0 is the signal intensity of the proton-weighted image and S_{sat} is that of the preconditioned image.

2.5 Specific Absorption Rate (SAR)

During RF transmission, an oscillating magnetic field passes along with an oscillating electric field through the body resulting in induced conduction currents within the body. Therefore, a significant amount of the transmitted power is absorbed by the body where it is dissipated in form of heat. The specific absorption rate (SAR) is defined as the total energy deposited in the

body and is used as a proxy measure to estimate the actual safety-relevant entity, namely temperature change of the body during an MRI experiment (105).

The deposited power in the sample is given by Poynting's theorem as (106)

$$P_{\text{diss}} = \int \frac{\sigma(x) |\vec{E}(x)|^2}{2} dx \quad (2.119)$$

where σ denotes the sample electrical conductivity and $\vec{E}(x)$ is the spatially varying electric field. Taking the sample weight into account, the SAR can be defined as

$$\text{SAR} = \frac{1}{2} \int \frac{\sigma(x) |\vec{E}(x)|^2}{\rho(x)} dx \quad (2.120)$$

where ρ is the sample density.

Dissipated power in the sample can be estimated using the loaded to unloaded Q -ratio (107)

$$P_{\text{diss}} = P_{\text{in}} \left(1 - \frac{Q_{\text{lo}}}{Q_{\text{un}}}\right) \quad (2.121)$$

where P_{in} is the input power delivered to the coil terminals.

Tissue heating due to RF exposure is legally constraint for safety reasons. The International Electro-technical Commission (IEC) guideline (REF IEC 60601-2-33) (105) sets the limits for the allowable global and local SAR for the whole body, head, extremities, and in any 1 g and 10 g tissue volume. Therefore, to prevent harming the patient, it is necessary to accurately calculate the possible SAR values, especially at ultra-high fields. The maximum SAR directly limits the input power and sets a limit for the applicable RF pulses.

2.6 Numerical Electromagnetic Simulations

2.6.1 Full-wave electromagnetic (EM) simulation

Due to the complex interactions between electromagnetic field and the human body, full-wave electromagnetic (EM) simulation of RF probes is widely used to characterize the performance

of the RF coil before fabrication. In the early days of NMR probe simulations, electromagnetic field could be reliably derived assuming spatially uniform current distribution in the coil conductors based on the Biot-Savart law(70). Due to the weak interaction of the EM- field with biological tissues, Biot-Savart law is still valid even in the presence of the load. However as the quasi-static approximation is no longer valid for high frequencies where the wavelength is comparable to the size of human tissues (see section 2.4.1.2), full-wave 3D EM simulation is demanded to assess the RF coil characteristics at high fields. A 3D EM simulation provides electric and magnetic field distributions of the MRI probe inside the human body or dedicated phantoms by solving Maxwell equations. Simulated electric and magnetic fields can be used to calculate SNR and SAR profiles. Different methods such as methods of moments (MoM), finite difference time domain (FDTD) method and finite element method (FEM) have been established yielding to a satisfactory approximation to Maxwell equations (108).

One of the most widely used techniques in 3D EMS is FDTD (109) which is described in details in the following section. All of the 3D EMS performed in this work are based on the FDTD method.

2.6.2 Finite Difference Time Domain (FDTD) Method

FDTD method was introduced by Kane Yee in 1966 (109). This method demonstrates a numerical technique that solves Maxwell curl equations (equations (2.122) and (2.123)) directly in the time domain on discretised space grid using central difference approximations.

$$\vec{\nabla} \times \vec{E} = -\mu_0 \frac{\partial \vec{H}}{\partial t} \quad (2.122)$$

$$\vec{\nabla} \times \vec{H} = \sigma \vec{E} + \varepsilon \frac{\partial \vec{E}}{\partial t} \quad (2.123)$$

FDTD discretizes the problem space into cubes called “Yee Cells” (Figure 2.35) using the three dimensional Cartesian coordinate system. The respective material properties i.e. relative permeability μ , relative permittivity ε and electrical conductivity σ are assigned to each cell. For each cell, the electric field components are assigned to the centre of each edge along the edge while the magnetic field components are assigned to the centre of each face perpendicular

to it as shown in Figure 2.35. This way, equations (2.122) and (2.123) can be replaced by finite difference equations which are discretized in the space and time ($\Delta x, \Delta y, \Delta z$) by central different approximations (108). Depending on the simulation, an excitation source has to be specified. Excitation can be a plane wave, current or a voltage source placed on the conductive part of the simulated RF coil. FDTD calculates the E -field and H -field for the individual Yee cells at any position iteratively from their previous values at the adjacent grid position until the desired numerical stability is achieved. FDTD can pose problems in modelling structures with curved surfaces, irregular geometries, and/or detailed boundaries, because the simulation mesh is composed of cuboid cells on a uniform Cartesian grid.

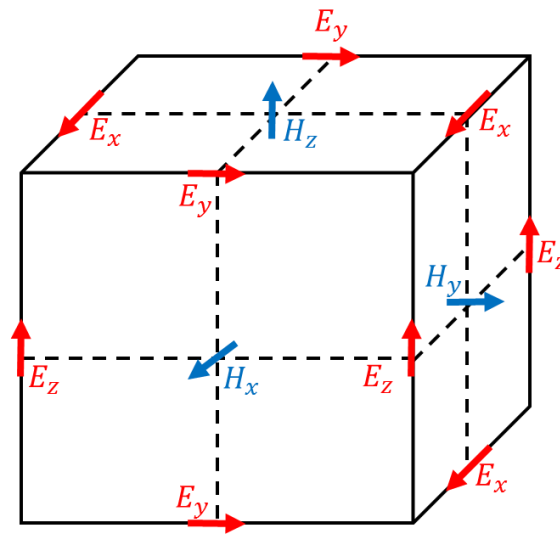


Figure 2.35: Yee cell schematic. Yee cell stores H -field information in the centre of each face and corresponding E -field on the centre of each edge.

An approach treating 3D curved thin conductive sheets (TC) based on their physical properties has been reported by Schild et al (110). In this method, the discretized form of the TC sheet is matched to the unaltered FDTD equations by defining special requirements for the conductivity and permittivity of the TC sheet (110). This way, the 3D TC sheets are efficiently treated without the need to resolve the thickness of the TC sheet (110). Since the EM field created by an RF coil radiates infinitely into the space, suitable boundary conditions limiting the space, such as perfectly matched layers, have to be defined (111). This way, a considerable amount of computational time and memory can be saved.

2.6.3 Combining FDTD and Circuit Co-Simulation

Tuning and matching of the RF coil using lumped element circuits in 3D EMS yield to a numerous time consuming repetitions of the simulations especially when a human body model is included in the simulation. It has been shown that for a linear RF network at a specified frequency, 3D EM fields are equal in the two following conditions (112):

- 3D EM fields are obtained from EM simulation associated with the necessary networks for tuning, matching and decoupling.
- 3D EM fields are obtained in several steps: first, necessary networks for tuning, matching and decoupling are replaced by 50 Ω ports in EM simulation. Second, the S-parameter matrix associated with the previous step is processed by co-circuit simulation and the necessary coefficients are obtained. Finally, the obtained coefficients in the second step are used to scale 3D EM fields which were obtained in the first step.

In this technique, all of the lumped components (e.g. tuning, matching, decoupling capacitors) are replaced by 50 Ω ports in the 3D EMS which is performed, with only one port activated during each run while all the other ports are terminated by a 50 Ω load. 3D EMS provides the electric and magnetic fields as well as the scattering matrix (S-parameters) i.e. the reflection and transmission scattering parameters of all ports within the system under simulation. The full S-parameter matrix is then used in the circuit co-simulation where a block is defined containing the simulated S-parameter matrix. Each port of the defined block is then connected to the appropriate lumped element network. Optimization algorithms in the circuit co-simulation are used to obtain suitable values for lumped elements e.g. tuning and matching capacitors. The electrical properties of each circuit node i.e. current (I) and voltage (V) are calculated to determine the electromotive force (ξ) across each port j

$$\xi_j = I_j(\omega) \cdot Z_0 - V_j(\omega) \quad (2.124)$$

Based on the calculated emf for each port (ξ_j) the power (P_j) and phase (φ_j) can be calculated for each port using the following formulas

$$P_j(\omega) = \frac{|(\xi_j - \xi_j^*)|}{|2Z_0|P_j^0} \quad (2.125)$$

$$\varphi_j = \text{phase}(\xi_j) - \varphi_j^0 \quad (2.126)$$

where P_j^0 and φ_j^0 denote prototype initial port power and phase, respectively, which are usually set to 0.01 W (power delivered from 1 A current when the coil is matched to 50 Ω) and 0°. The E -field and B_1 field of the coil accounting for the lumped elements can be calculated by linear superposition of the initially calculated EM data for each port (\vec{B}_{1j}, \vec{E}_j) weighted by the corresponding port power and phase

$$\vec{B}_1 = \sum_{j=1}^N \vec{B}_{1j} \cdot \sqrt{P_j(\omega)} e^{i\varphi_j(\omega)} \quad (2.127)$$

$$\vec{E} = \sum_{j=1}^N \vec{E}_j \cdot \sqrt{P_j(\omega)} e^{i\varphi_j(\omega)} \quad (2.128)$$

This way, the calculated fields are exactly the same as the fields that would have been obtained in the 3D EMS including the lumped element components (112). Therefore using circuit co-simulation enables fast calculation of the B_1 field and other RF coil characteristics (e.g. SAR, transmit efficiency and SNR) for various tuning and matching conditions based on one run of 3D EMS data.

2.6.4 3D EM Simulation of TLRs

Since the resonance frequency depends on the geometry of TLR, designing a TLR for a specific Larmor frequency is difficult and relies on the redoing of the full-wave 3D EMS model. This is particularly time consuming and cannot be done by circuit-co simulation. The FDTD simulation which is a time-domain method, for resonant structures with relatively high Q -factors (e.g. TLRs) may take a very long time to converge to the steady state (113). In contrast, for conventional loops, replacing lumped elements by 50 Ω feed ports prevents the structure

from resonating, thus it takes shorter to reach the steady state in comparison with TLRs. Furthermore, due to the thin substrate (typically 50 - 510 μm) in TLR designs, a very fine mesh resolution has to be chosen in the substrate. This rule should be also applied in the conductor planes on both sides of the TLR where the conductor thickness is also in the order of μm (typically 35 μm). Increasing the mesh resolution increases the time for 3D EMS, and therefore adjusting the design to obtain the desired frequency is time consuming. This demands for a complementary tool to make 3D EMS more efficient, such as using analytical modelling to predict TLR resonance frequency in combination with 3D EMS. Then by a few fine adjustments, the desired design with an appropriate mesh resolution can be obtained.

2.7 Current State of Cardiac MRI

Nowadays cardiac MRI (CMRI) is widely used in clinical routine (e.g. at 1.5 T and 3 T) for cardiac function assessment and acquiring anatomical and morphological images of the heart. As an organ lying in a deep region in the thorax (roughly 2 - 5 cm from the chest surface depending on the patient body) various sequences together with RF coils tailored for CMRI are needed to acquire clinically relevant images. In this chapter, an overview over the clinically used sequences for cardiac imaging is discussed and the challenges for moving towards UHF (e.g. 7 T application) are presented. The discussed background for clinical CMRI is based on the book given in (114) and most of the figures are re-produced from the same book.

The general sequence diagram for CMRI is shown in Figure 2.36.

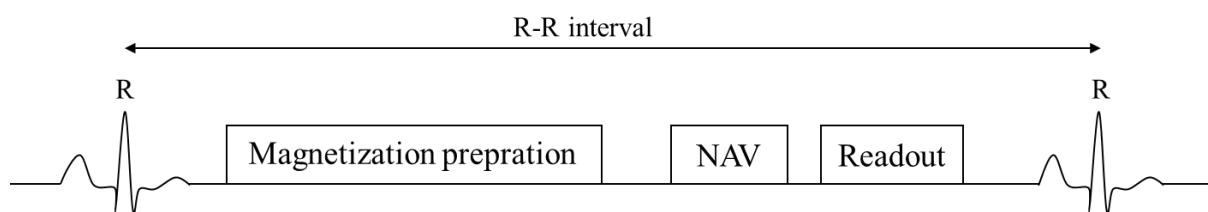


Figure 2.36: *general structure of a CMRI sequence. The key components are magnetization preparation, respiratory navigation (NV) and data acquisition (readout).*

Typically CMRI acquisition is relative to an electrocardiogram (ECG) signal within the period between two R-waves referred to as R-R interval. This allows data acquisition to occur in one specific time frame within the cardiac cycle to capture phase-dependent features in an image which allows to minimize imaging artefact such as blurring and flow artefacts due to the cardiac motion. Breath-holding is usually done in CMR application to account for the respiratory motion.

Magnetization preparation in Figure 2.36 is different excitation forms leading to various imaging contrast such as T_1 weighted, T_2 weighted and black-blood imaging.

Black blood preparation is one of the commonly magnetization preparation used in CMRI to visualize blood vessel walls (including coronary arteries), cardiac chambers and myocardium without any blood contribution. In this technique, a non-selective 180° inversion pulse is immediately followed by a slice-selective 180° pulse referred to as “double inversion recovery (IR)” method (see Figure 2.37).

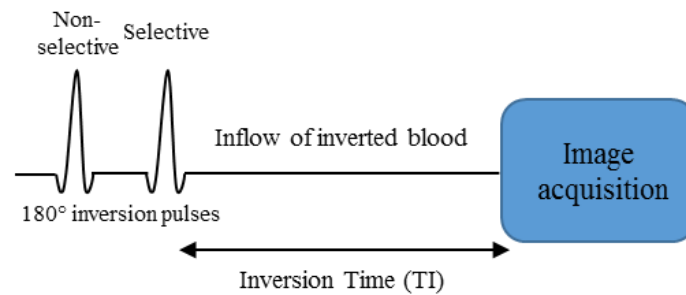


Figure 2.37: double inversion recovery technique used for black-blood magnetization preparation.

In the black-blood strategy, the first 180° pulse inverts all of the spins within the coil FOV. The second 180° pulse affects only those spins within the selected slice (e.g. myocardium) and rotate them backup to the equilibrium ($+M_0$) and leaving all of the magnetization outside of the selected slice inverted at $-M_0$. After the time TI (inversion time), inverted blood outside of the selected slice undergoes T_1 -decay and passes through zero as it attempts to realign with \vec{B}_0 . When the inverted blood passes zero, data acquisition is done. This way the signal of the inflow blood is zero and results in the moving blood in the selected slice to appear “black”. Figure 1 shows a black-blood prepared image of the heart in short-axis view.



Figure 2.38: short axis image of the heart acquired with black-blood prepared gradient echo acquisition (114).

Fast blood flow may cause the inverted blood to move into the selected slice before starting data acquisition. Similar effect can be due to the myocardium movement which can result in the inverted myocardium entering the selected slice, causing an artefactual reduction in myocardium signal. In addition, low blood flow has high signal intensity which may artificially appear as an extension of anatomical structures.

CMRI is usually performed with breath-holding (typically 10-15 s) to eliminate respiratory motion. In cases where the patient cannot suspend breathing during the data acquisition period, other motion compensation approaches are applied, such as navigator gating. In this approach, a quick excitation is applied perpendicular to the diaphragm, and an echo is acquired. The acquired echo is analyzed to determine its position to estimate respiratory motion. During data acquisition, only those data points which fall within the pre-defined window of diaphragm motion (~ 5 mm) are collected and used for image reconstruction. However, this technique reduces the time efficiency of acquisition, particularly for patients with variable breathing patterns, since sufficient data points should be collected to reconstruct an artefact-free image.

Readout in the diagram shown in figure 1, refers to various sequences which are used for data acquisition. GRE sequences (see section 2.3.2) are very fast as they use a small TR and TE and a low flip angle. This causes the transversal magnetization to not have time to fully dephase. Therefore, a residual transversal magnetization remains. The residual transversal magnetization can be spoiled using Spoiled GRE sequences or can be refocused, leading to a steady state of longitudinal and transversal magnetizations.

One of the commonly used sequences for data acquisition in CMRI clinical routine is the balanced Steady-State Free Precession (bSSFP). The sequence diagram for bSSFP is shown in Figure 2.39.

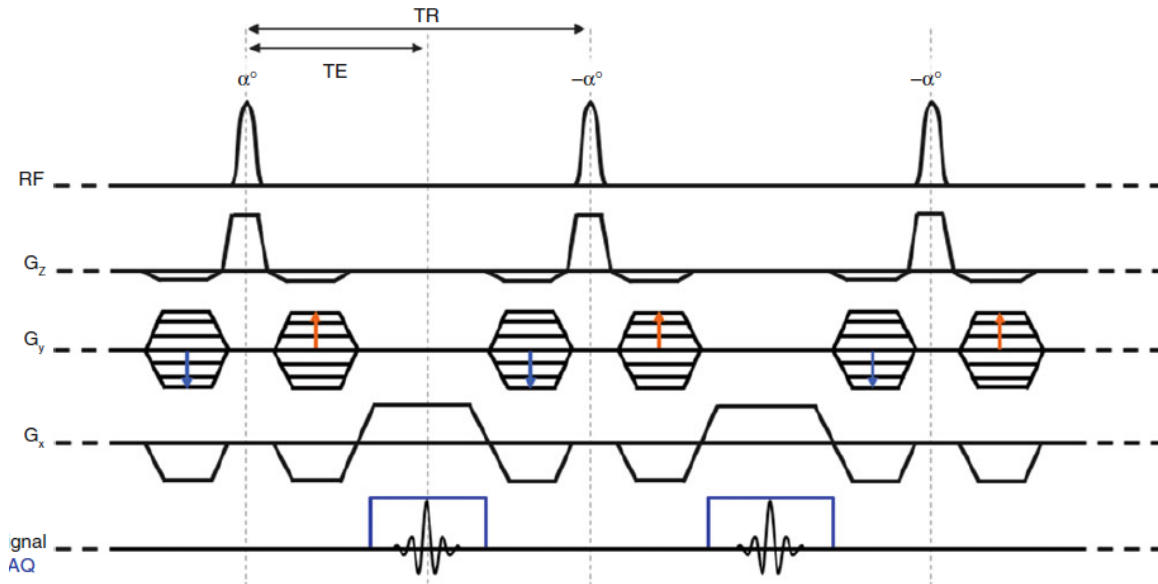


Figure 2.39: sequence diagram for bSSFP. The RF pulses are applied every TR and gradients are reversed before the next excitation. The same for excitation flip angle (α to $-\alpha$).

In this sequence, a train of RF pulses is used to reach a dynamic range between excitation and relaxation. The time between RF pulses (i.e. repetition time TR) is minimized in a way so that both longitudinal and transversal magnetisation are relatively small ($TR \ll T_2^*$). When TR is shorter than T_2 , transversal magnetization does not have enough time to decay completely before the next RF pulse. Therefore, there will be some residual transversal magnetization left over which is fed back to the longitudinal magnetization in the next excitation. Increasing the flip angle results in larger amount of the residual transversal magnetization to fed back to the longitudinal magnetization. The residual magnetization is significantly lower than M_0 and its magnitude can be determined with relaxation times T_1 , T_2 and the flip angle α . In bSSFP sequence, all the gradient dephasing from one repetition to the next are fully compensated. In the other words, when a gradient is applied with a certain polarity, at the end of the sequence its effects are reversed by applying the same gradient with a reverse polarity. This holds for the excitation pulse as well (see Figure 2.39). In case of no compensation for the applied gradient in each excitation, the spins in that direction obtain different phases resulting in a reduction of the signal intensity.

The bSSFP images are T_2/T_1 weighted which is particularly important for CMRI application as the T_2/T_1 ratio of blood is approximately factor of 3 times higher than that of myocardium causing the blood to appear brighter. Such a high contrast enables description of endocardial border between myocardium and blood.

Although bSSFP is known as an accurate and fast method for cardiac function assessment, it is very sensitive to the magnetic field inhomogeneities which are the source of the so called image banding artefact. The banding artefacts occur at regions with strong field inhomogeneities (off-resonance frequencies) where the bSSFP gives zero signal resulting in dark bands (signal null in the image). The range of the field inhomogeneities causing banding artefacts is inversely dependent to the TR. The banding artefacts can be eliminated by careful B_0 shimming around the heart region and shortening TR as much as possible, e.g. by increasing the sampling bandwidth. On one hand, increasing TR increases the sensitivity to the field inhomogeneity and on the other hand by shortening TR one can run into SAR issues (see section 2.7.1.4). The bSSFP is important for myocardial viability due to its high contrast to noise ratio in comparison with spoiled GRE which is a very fast sequence but gives a very weak contrast between the myocardium and blood ($< 40\%$).

Cine imaging is usually done in CMRI application to acquire multiple images of the heart at a single slice during the cardiac cycle. The bSSFP with single-breath holding during acquisition is the gold standard for CINE imaging in CMRI clinical routine (e.g. at 1.5 T) allowing for very short TR and TE values. Hence multiple k-space lines can be acquired during a single heartbeat. Electrocardiography (ECG) gating is performed to assign appropriate phase to each imaging data.

2.7.1 UHF CMR

Studies have shown that UHF can be beneficial for CMR due to the inherent increase in SNR. The base line SNR gain at UHF enables $1 \times 1 \times 4 \text{ mm}^3$ resolution which is a factor of 6 superior to that of clinical practice at 1.5 T (27,31). However CMR at UHF is still challenging due to the following reasons:

- Magnetic field inhomogeneities associated with the shortened wavelength (see section 2.4.1.2)
- Dielectric effects
- Localized heating and RF power deposition (see section 2.5)

2.7.1.1 Multi-Channel RF Coil Arrays

Multi-channel transceiver RF coil arrays (see section 2.4.2.3) tailored for UHF CMR play an important role to tackle the above mentioned constraints. Existing coil arrays for UHF CMR take advantage of various coil technologies such as strip lines (28), loop elements (29,31,32) and radiative elements (33). Also it has been demonstrated that 2D array coils with larger number of elements gives more freedom for perfecting B_1^+ uniformity and improving the parallel imaging (see section 2.3.7) performance (30). Optimizing the coil elements for CMRI at UHF is challenging and various requirements are needed to improve the transmit efficiency and boost the SNR for cardiac imaging. In general array coils tailored for UHF CMRI are required to have the following features (27):

- Light weight coils
- Mechanical flexibility
- Capability to accommodate multiple patient bodies
- A large enough sensitive region to cover cardiovascular region

Among the various type of cardiac coils for UHF, radiative elements (e.g. dipole antenna) are interesting because the Poynting vector (i.e. the direction of the EM field passing through a plane) is perpendicular to the main axis of the structure (115). This make such a design suitable for imaging of deep region with efficient propagation such as heart. In addition, it was demonstrated that the local SAR of the dipole and loop coils is substantially less than that of strip line elements (115).

2.7.1.2 B_1^+ Mapping

To manage the transmission field inhomogeneity a knowledge of B_1^+ distribution is needed. This can be done by flip angle mapping methods described in section 2.4.4.2. However, B_1^+ mapping for CMRI at 7 T is still challenging and previous studies have reported that phase-based techniques are found to be more accurate than magnitude-based methods in the low-flip angle regime as they are not affected by TR/T_1 variations (27,116). Also using a slice selective RF pulse (e.g. sinc pulse) as a preconditioning RF pulse instead of non-selective preconditioning RF pulse together with a fast turbo FLASH readout can mitigate the TR constraints in previous B_1^+ mapping taking such as DAM (see section 2.4.4.2).

2.7.1.3 Using pTx in UHF CMRI

Using pTx (see section 2.3.8) has the mean and freedom to shape the transmit field at UHF CMRI resulting in an improved transmit efficiency and boost SNR of myocardium and blood. This is an advantage versus the single transmit shimming which efficiency relies on the pre-defined voxel-models used for the static B_1^+ optimization (see section). In a recent study the use of pTx with simultaneous multi slice (SMS) imaging under a breath-hold has been demonstrated to mitigate contrast heterogeneity in UHF CMRI (117).

2.7.1.4 SAR Constraints

Another constraint in UHF CMRI is the assessment of the power deposition which ensures the MR safety of the patient. Sufficiently low wavelength in the upper torso at 7 T may offset SAR prediction by (27),

$$SAR \propto \frac{B_1^2 B_0^2 \tau_{RF}}{mTR}$$

where τ_{RF} is the duration of the RF pulse, TR is the repetition time and m is the sample mass. Performed studies in UHF CMRI underline that local SAR is highly dependent to the coil geometry, transmit field uniformity, position of the coil with respect to the torso, number of elements (27). In addition, RF driving condition is highly affecting the local SAR (see section 3.4.4). This effects is particularly important when using pTx techniques with individual amplitude and phase for each elements, thus care must be taken in SAR assessment prior to the in-vivo experiments. 3D numerical simulations (see section 2.6) are widely used to evaluate SAR based on the pre-defined human voxel models.

2.7.1.5 ECG Gating

As mentioned in section 2.7, ECG triggering is often used in CMRI for accurate synchronization to the cardiac cycle. However a UHF, the flowing blood induces a voltage in the ECG leads which is superimposed with the ECG signal and causes problems with recognition of R-waves (118). Alternative solution is an MR stethoscope which detects the heart first tone and transform it into a trigger signal (119). This device is not affected by the EM fields.

2.7.1.6 Cardiac Morphology Assessment

Performed studies in UHF CMRI to quantify cardiac chamber, demonstrated that 2D Cine Flash GRE correlates closely with the parameters acquired with 2D CINE SSFP at 1.5 T (119). The SSFP-based sequences are elusive in UHF CMRI due to their sensitivity to the magnetic field inhomogeneities (see section 2.7) and shortened TR which is limited by SAR constraints. Prepared black-blood sequences (see section 2.7) can be used for CMRI application that demand the highest resolution such as plaque imaging, arterial and carotid wall imaging demonstrating spatial resolutions below than 0.6 mm (119).

2.7.1.7 Cardiac Quantitative Parametric Mapping

The prolonged T_1 at 7 T can enhance the contrast between blood and myocardium which is superior to that of GRE at 1.5 T. This improvement can be used to identify subtle anatomic structures of the heart such as pericardium, mitral, tricuspid valves and their associated papillary and trabeculae (119). Furthermore, parametric mapping-based sequences such T_2^* mapping is beneficial due to linear increase of microscopic susceptibility effects with magnetic field strength leading in myocardial tissue characterization (119,120).

2.7.1.8 Conclusion

In conclusion, UHF CMRI is still under development and highly challenging mainly regarding safety reasons. The use of multi-dimensional coil array tailored for UHF CMRI together with pTx and parallel imaging techniques is necessary to overcome the constraints associated with the UHF. Various applications and future horizon of UHF CMRI are discussed in detail in a review given by Niendorf et al (119).

3 Development of a 12-Element Flexible TLR Array for ^1H 7T Cardiac MRI

In this chapter, we will first present general tools used to evaluate the performance of the investigated designs in this study and then the development procedure of the single element and the array will be presented with the corresponding results. This chapter is finalized by a brief conclusion over the performed studies.

3.1 Tools and Materials

All the designs presented in this work were investigated by 3D EMS, bench, and MR experiments. Bench and MR experimental tools were already presented in section 2.4.4. The 3D EMS setup used for all of the investigated designs is presented in section 3.1.1. The phantoms used for bench and MR measurement are described in section 3.1.2.

3.1.1 EM Simulation

In this study, full wave 3D EMS (XFDTD 7.4 Remcom, State College, PA) was used in combination with circuit co-simulation (ADS, Keysight Technologies, USA). For all of the simulations performed, a basic mesh resolution of $3 \times 3 \times 3 \text{ mm}^3$ was used for free space regions. The mesh resolution was increased to 0.5 mm in the coil planes to simulate S-parameters and transmit efficiency. The mesh size inside the substrate along the coil axis was set to half of substrate thickness as suggested by Kriegl et al. (17). This yields 2 mesh cells in the axis perpendicular to the substrate as shown in Figure 3.1.

With the simulation setup as used in this thesis, 3D EMS of TLRs in bent configuration is not possible due to the required mesh resolution in the substrate demanding long calculation times and large amounts of memory.

To demonstrate this, we assume a single, flat TLR, which is tilted by 45° with respect to the mesh. This corresponds to a simplified representation of the situation when the array is bent over a torso. In that case, elements positioned centrally above the body will remain relatively horizontal, but side elements would be tilted. The bending of the TLR itself is neglected for this thought experiment, but its incorporation in the calculation would increase the computational demand even more.

To achieve a minimum mesh requirement of 2 cells placed in the axis perpendicular to the substrate, as stated above, 4 cells are required in the horizontal direction as shown in Figure 3.1. This increases the required mesh resolution to approximately $53 \text{ }\mu\text{m}$ for a $150 \text{ }\mu\text{m}$ thick substrate. For a 45° tilted TLR of 10 cm diameter, the number of mesh cells per transversal

slice increases to approximately 4.3 million which is 43 times larger than that of the flat configuration resulting in a total calculation time of approximately 3 months and required memory of approximately 197 GB for simulation of a 12-element TLR array in the (simplified) bent configuration – as compared to 2 days for the flat TLR array. Therefore, such requirements currently prevented the 3D EMS of developed TLR array in the bent configuration with FDTD which is required for static B_1^+ shimming and SAR evaluation.

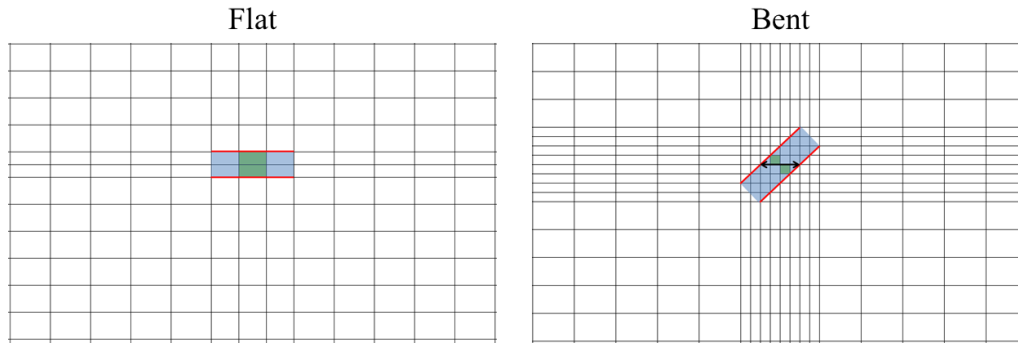


Figure 3.1: Mesh configuration for TLR in flat (left) and bent (right) configurations.

Since sample losses are expected to be dominant for the investigated coil size at 297.2 MHz (121), conductors were modelled as perfect electric conductors (PEC) and losses from the lumped elements and the substrate were neglected.

To simulate the coil in flat configuration, a 20 cm thick rectangular-shaped phantom with electromagnetic properties of muscle tissue (0.71 S/m conductivity, 63.86 relative permittivity) positioned 10 mm under the coil was used as load. The lateral dimensions of the phantom were chosen so that the phantom exceeds the outer diameter of the TLR by around 10 cm. The mesh resolution inside the phantom was set to 2 mm. In order to improve the meshing accuracy, the XACT-mesh technology (122,123) embedded in the simulation software was enabled. To speed up simulations, the lumped elements of the tuning/matching network were replaced by 50 Ω ports in 3D EMS and the resulting S-parameters were further analyzed in the circuit co-simulation (112) to determine the lumped element values for which coils are tuned and matched (see section 2.6.3). Simulated B_1^+ maps were post-processed using MATLAB (Mathworks, Natick, MA) with a dedicated toolbox (SimOpTx, Research Studio Austria, Medical University of Vienna, Austria).

3.1.2 Phantoms

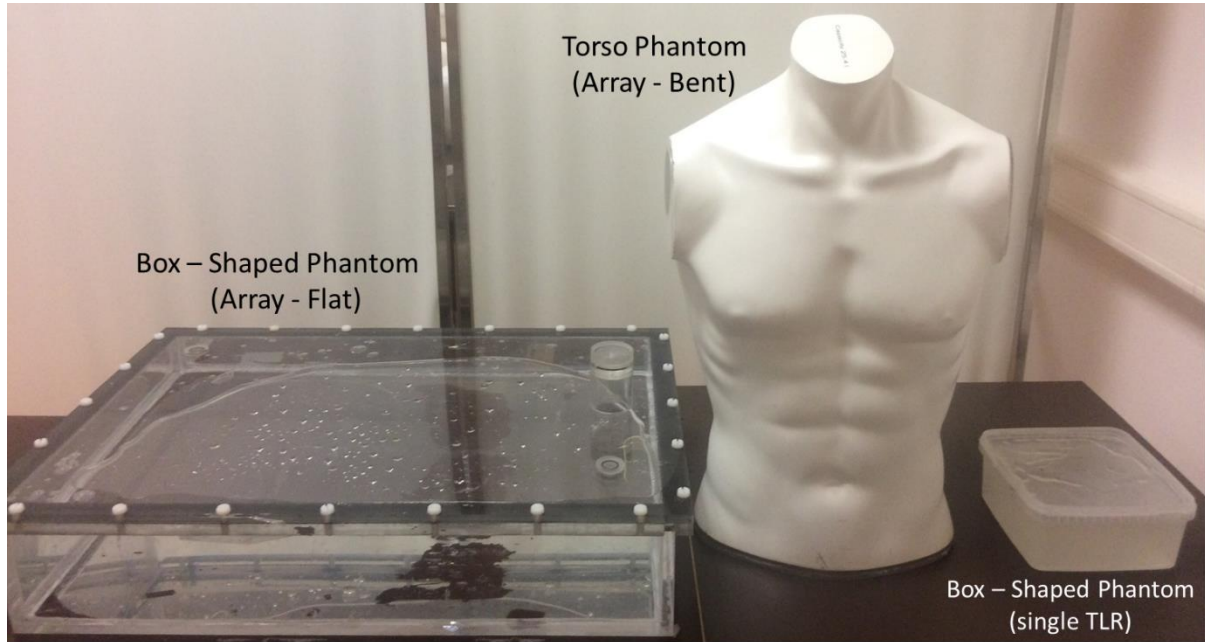


Figure 3.2: Phantoms used for bench and MR measurements.

3.1.2.1 Flat Phantom for Single Element Measurements

For bench measurements and MRI experiments of single TLR designs, a rectangular-shaped phantom ($16 \times 16 \times 7 \text{ cm}^3$) filled with polyacrylic acid gel with human tissue-like dielectric properties ($\sigma = 0.61 \text{ S/m}$, $\epsilon = 76$) was used as load (Figure 3.2, right).

3.1.2.2 Flat Phantom for Array Measurements

A rectangular-shaped phantom ($64.5 \times 44.7 \times 11.6 \text{ cm}^3$) filled with NaCl solution ($\sigma = 0.53 \text{ S/m}$) was used as a load for the 12-element array in the flat configuration (Figure 3.2, left). The coil to sample distance was set to 10 mm for both the single element and the 12-element array.

3.1.2.3 Torso Phantom for Array Measurements

To evaluate the performance of the 12-element flexible TLR array on bench and by MR measurements in bent configuration, a torso phantom filled with tissue-like gel ($\sigma = 0.60 \text{ S/m}$, $\epsilon = 62$) was developed in house (Figure 3.2, middle). The torso casing was a mannequin made of glass-reinforced plastic (GRP) originally intended for clothing display. It was modified by removing all metallic parts and making a hole in the bottom part to fill it with muscle tissue-like gel. A general concept of producing MR compatible gel phantoms can be found in (124).

Agarose is one of the main ingredients for developing MR gel phantoms (). However, agarose is very expensive and it is not cost efficient when developing large phantoms such as the torso phantom in this thesis. We used agar-agar which is from the same family as agarose, however, no publication could be found that investigated agar-agar for MRI gel phantoms particularly for 7 T application. Thus, we found the concentrations of the ingredients used in this study based on the experiments using small portions of the gel with varied ingredient concentrations. To lower the permittivity ethylene glycol was added.

The recipe for the final gel used in the phantom are presented in Table 3.1.

Table 3.1: The ingredients and their corresponding amounts used to produce 15 kg of tissue-equivalent gel.

Ingredients for 15 kg of gel	Amount
Distilled Water	7500 g
Ethylene Glycol	7500 g
Agar-Agar Powder	150 g
Magnevist (Contrast Agent)	2.4 ml
Salt	135 g
Sodium Acid (NaN_3)	7.5 g

The gel preparation was done as follows:

1. Mixing deionized water with ethylene glycol.
2. Taking a small sample from the cold mixture to mix in the agar-agar powder.
3. Heat up the rest to 80°C while stirring, put a lid on the pot to minimize evaporation.
4. Start pouring in the agar-agar mixture from step 2 at 80°, heat further, keep the temperature under 100°C to avoid burning the ethylene glycol.
5. Adding Sodium Acid (NaN_3) and Magnevist solution any time during heat-up.
6. Pouring the solution in another container and adding NaCl and stir with a glass rod, minimizing air bubbles.
7. Pouring the phantom with gel and let it to cool down with the cap on.

The abovementioned procedure was performed in two batches of 15 kg of gel each to fill the torso mannequin with a capacity of about 25 l. Sodium acid (NaN_3) was added to the mixture to preserve the gel for a longer time due to its anti-bacterial properties.

The achieved conductivity and permittivity was measured using a dielectric probe following the method detailed in (125,126).

3.2 Individual Array Elements

In this section, the workflow used to design and characterize the individual elements of the array is presented. In the following, individual element refers to a single TLR surrounded by a decoupling ring together with the corresponding capacitive tuning and matching network.

3.2.1 Single TLR Design

Figure 3.3 shows the basic geometry of the single TLR. The initial diameter of the TLR was chosen with respect to the desired FOV, penetration depth, and loss mechanisms targeting cardiac MRI at 7 T (121). Taking into account the initial TLR diameter, the number of turns, gaps, and conductor width were determined using the analytical calculation of the resonance frequency (see equation (2.95)). Each side of the TLR contains four gaps as shown in Figure 3.3.

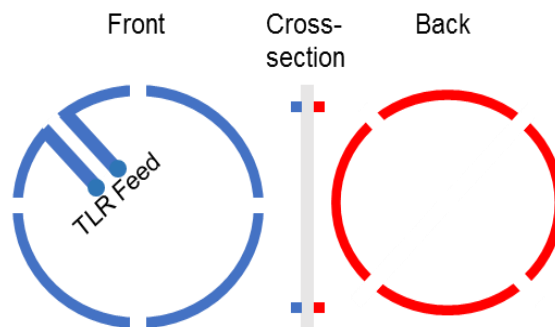


Figure 3.3: Basic geometry of the single TLR.

In this thesis, an LC network for tuning and matching was used as shown in Figure 3.4. The capacitive tuning and matching network is composed of four fixed capacitors and a shunt inductor connected in symmetric configuration between the capacitors.

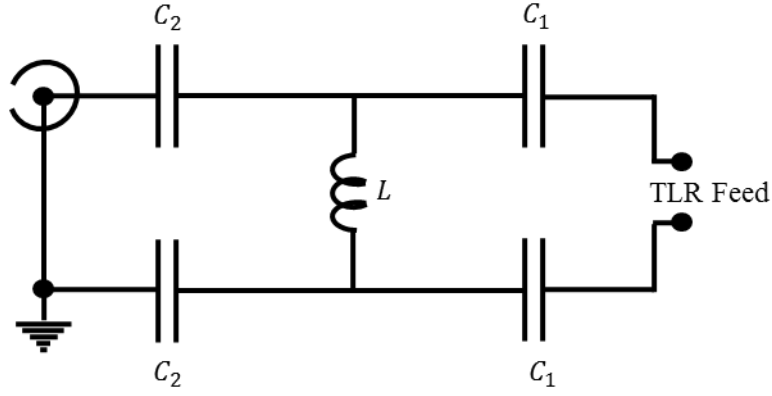


Figure 3.4: LC tuning and matching network.

Initially, the capacitive tuning and matching network shown in Figure 2.26 was simulated, however, the resulting values for the tuning capacitors were too small (< 0.5 pF) in comparison to the parasitic capacitance formed by the feed legs and consequently the target frequency could not be reached. From the smith chart analysis of the single element TLR measured on the bench, an LC network was designed so as to allow for the required impedance transformation achieving the target frequency and matching level. The LC network configuration shown in Figure 3.4 was obtained experimentally and was simulated by circuit-co simulation. The LC components values were further finely optimized on the bench. The resulting values for LC components are given in Table 3.2.

The position of the feed ports in the TLR was chosen in the middle of a conductor section in order to prevent disturbing the intrinsic current density of the TLR and achieve the highest current flowing in the LC network, as pointed out in previous work (82). Figure 3.5 shows the simulated current density distribution of the single element TLR when fed capacitively through the feeding ports. Using 3D EMS and circuit co-simulation and starting with the initial diameter value and the values of the other geometrical parameters obtained from the analytical calculation, the TLR geometry was finely adjusted together with a capacitive matching network to resonate at the Larmor frequency of 297.2 MHz (^1H at 7 T). The final TLR design is composed of a single turn TLR with 4 gaps, an external diameter of 84 mm, and a conductor thickness of 2 mm deposited on a 100 μm thick substrate made of polyamide.

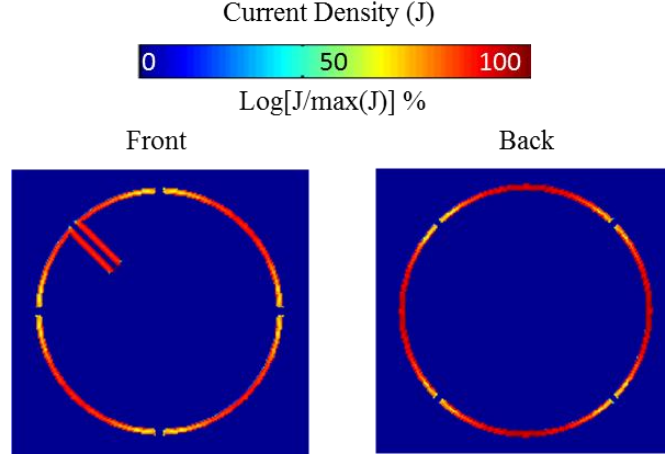


Figure 3.5: Current density distribution of the single TLR.

3.2.2 Inter-TLR Decoupling

The decoupling ring considered in this study results from the intersection of a circle with a square forming a closed square-shaped loop with curved corners as represented in Figure 3.6a. The overlap distance between two decoupling rings can be optimized by modifying the size of the square only while the diameter of the circle can be kept constant. In comparison with a circular decoupling ring, a square-shaped decoupling ring with curved corners enables a wider range of overlap distance without significantly increasing the overall size of the decoupling ring. Decoupling efficiency using circular decoupling rings is limited when the maximum overlap distance is not sufficient to cancel the shared magnetic flux between two TLRs. Therefore, the size of the circular decoupling ring has to be increased in order to increase the compensation flux. However, at the same time, it results in an increase of the coupling flux and therefore limits the decoupling efficiency.

The decoupling efficiency was firstly optimized by analytically calculating the shared magnetic flux between the nearest elements as a function of the decoupling ring overlap distance using the analytical model presented in A.2 (90). This technique was studied for a 4-element TLR array with decoupling rings as shown in Figure 3.6b.

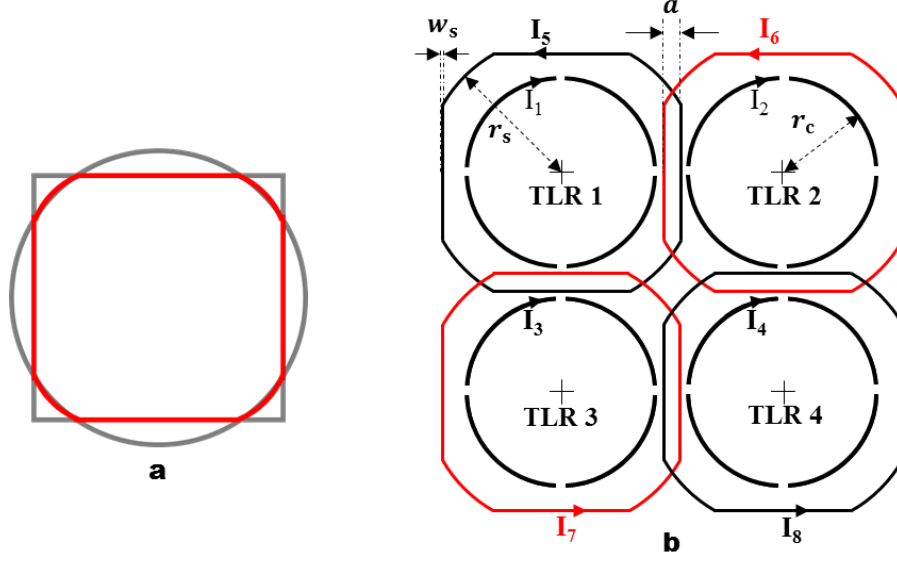


Figure 3.6: (a) Decoupling element: decoupling ring was made of an intersection of a circle with radius r_s and a square, (b) 4-element TLR array with overlapped decoupling rings: decoupling rings of opposite sides (shown in red) were deposited on both sides of the substrate for overlapping with overlap distance a , decoupling ring conductor thickness w_s and r_c is the TLR outer radius.

For the optimization process, current I_1 in TLR 1 was considered as the source current and the other currents were induced in the other TLRs. The corresponding decoupling rings are shown in Figure 3.6b. Using the total magnetic flux theory, the following linear system of equations can be obtained

$$\begin{pmatrix} L_2 I_2 \\ L_3 I_3 \\ L_4 I_4 \\ L_5 I_5 \\ L_6 I_6 \\ L_7 I_7 \\ L_8 I_8 \end{pmatrix} = \begin{pmatrix} |M_{21}| & 0 & |M_{23}| & |M_{24}| & -|M_{25}| & |M_{26}| & -|M_{27}| & -|M_{28}| \\ |M_{31}| & |M_{32}| & 0 & |M_{34}| & -|M_{35}| & -|M_{36}| & |M_{37}| & -|M_{38}| \\ |M_{41}| & |M_{42}| & |M_{43}| & 0 & -|M_{45}| & -|M_{46}| & -|M_{47}| & |M_{48}| \\ |M_{51}| & -|M_{52}| & -|M_{53}| & -|M_{54}| & 0 & |M_{56}| & |M_{57}| & |M_{58}| \\ -|M_{61}| & |M_{62}| & -|M_{63}| & -|M_{64}| & |M_{65}| & 0 & |M_{67}| & |M_{68}| \\ -|M_{71}| & -|M_{72}| & |M_{73}| & -|M_{74}| & |M_{75}| & |M_{76}| & 0 & |M_{78}| \\ -|M_{81}| & -|M_{82}| & -|M_{83}| & |M_{84}| & |M_{85}| & |M_{86}| & |M_{87}| & 0 \end{pmatrix} \begin{pmatrix} I_1 \\ I_2 \\ I_3 \\ I_4 \\ I_5 \\ I_6 \\ I_7 \\ I_8 \end{pmatrix} \quad (3.1)$$

where L_i is the self-inductance of structure i , I_i is the current flowing in structure i and M_{ij} is the mutual inductance between structures i and j , respectively.

Because of the symmetry of the 4-element design, currents $I_2 = I_3$ and $I_6 = I_7$, assuming a constant current $I_1 = 1$, the linear system of equations (3.1) can be solved. More detailed formulas to solve the linear system of equations (3.1) are given in appendix section A.2. Due to the complex geometry of the decoupling ring, the software FastHenry (127) was used in order to calculate the self and mutual inductances within the 4-element array more accurately.

The net magnetic flux induced by current I_1 in TLRs 2, 3 and 4 can be decomposed into a coupling flux and a compensation flux as follows:

$$\Phi_{\text{netTLR2}} = \underbrace{|M_{21}|I_1 + |M_{23}|I_3 + |M_{24}|I_4 + |M_{26}|I_6}_{\text{Coupling Flux}} - \underbrace{|M_{25}|I_5 - |M_{27}|I_7 - |M_{28}|I_8}_{\text{Compensation Flux}} \quad (3.2)$$

$$\Phi_{\text{netTLR3}} = \underbrace{|M_{31}|I_1 + |M_{32}|I_2 + |M_{34}|I_4 + |M_{37}|I_7}_{\text{Coupling Flux}} - \underbrace{|M_{35}|I_5 - |M_{36}|I_6 - |M_{38}|I_8}_{\text{Compensation Flux}} \quad (3.3)$$

$$\Phi_{\text{netTLR4}} = \underbrace{|M_{41}|I_1 + |M_{42}|I_2 + |M_{43}|I_3 + |M_{48}|I_8}_{\text{Coupling Flux}} - \underbrace{|M_{45}|I_5 - |M_{46}|I_6 - |M_{47}|I_7}_{\text{Compensation Flux}} \quad (3.4)$$

In Figure 3.7, the calculated coupling and compensating fluxes as well as the net magnetic flux through TLR 3 in the 4-element design are plotted as a function of the decoupling ring overlap distance a (as defined in Figure 3.6b).

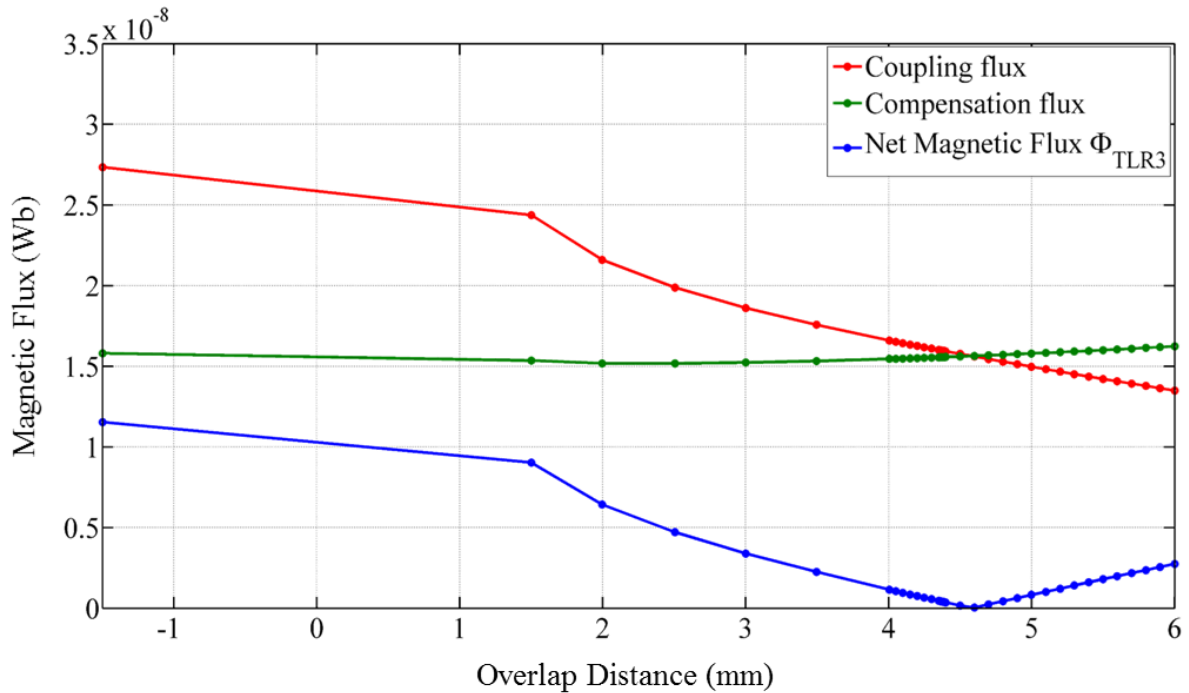


Figure 3.7: Decoupling ring overlap optimization: analytically calculated coupling, compensation and net magnetic fluxes through TLR 3 in the 4-element TLR array when TLR 1 is driven by a current of 1 A.

Due to the symmetric configuration of the 4-element array, results for TLR 2 are equal to those of TLR 3 and are thus not shown. Figure 3.7 demonstrates that the intersection of coupling and compensation magnetic flux curves occurs for an overlap distance of 4.6 mm. This overlap corresponds to the minimum value of the net magnetic flux (1.6054×10^{-10} Wb). The decoupling efficiency between diagonal TLRs of the array cannot be optimized since the decoupling rings of the diagonal elements are deposited on the same side of the substrate and therefore cannot be overlapped. The non-minimized net magnetic flux through TLR 4 is 4.8871×10^{-9} Wb for the overlap distance of 4.6 mm.

The decoupling efficiency achieved with the 4-element array was also investigated by 3D EMS of the transmission scattering parameters (S_{ij}) for an overlap distance ranging from 4.1 mm to 5.1 mm with a 0.1 mm step. The S_{21} values were recorded once each TLR element was tuned to ^1H Larmor frequency at 7 T, i.e 297.2 MHz, and matched to 50 Ω .

The simulated transmission scattering parameters of the 4-element array (Figure 3.6b) as a function of the overlap distance of the decoupling rings are shown in Figure 3.8. The simulated transmission scattering parameters between TLR1 and its neighbors, i.e. TLRs 2 and 3 (S_{21} and S_{31}) show minimum values of -28.9 (dB) and -29.3 (dB), respectively, for an overlap distance of 4.7 mm, i.e. about 2 % higher than the value obtained using the analytical calculation. In addition, the simulated S_{41} representing the diagonal decoupling efficiency between TLR 1 and TLR 4 is -23.5 dB. To consider the contributions of all elements in the decoupling efficiency optimization, the averaged value of the whole transmission scattering parameter matrix (S_{ij}) is also plotted as a function of the overlap distance. This curve shows a minimum of -27 (dB) for an overlap distance of 4.5 mm, which is very close to the value found by the analytical modelling in the previous step (see Figure 3.8). Therefore, 4.5 mm was chosen as the final overlap distance to design the 12-element TLR array. It represents a compromise between decoupling levels of nearest neighbour (-29 dB) and decoupling levels between diagonal elements (-24 dB). By increasing the overlap distance, the size of the decoupling ring increases and it gets closer to the diagonal neighbors increasing mutual flux. Since it is not overlapping with the diagonal decoupling ring, the increased flux cannot be compensated and coupling is increased. This is well observed as an increase in simulated S-parameters between diagonal elements (S_{41} and S_{32}) for overlap distances larger than 4.4 mm in Figure 3.8. The final geometry of the decoupling ring after optimization by analytical model and 3D EMS consists of intersection of a circle with diameter of 120 mm and a square with sides of 100 mm.

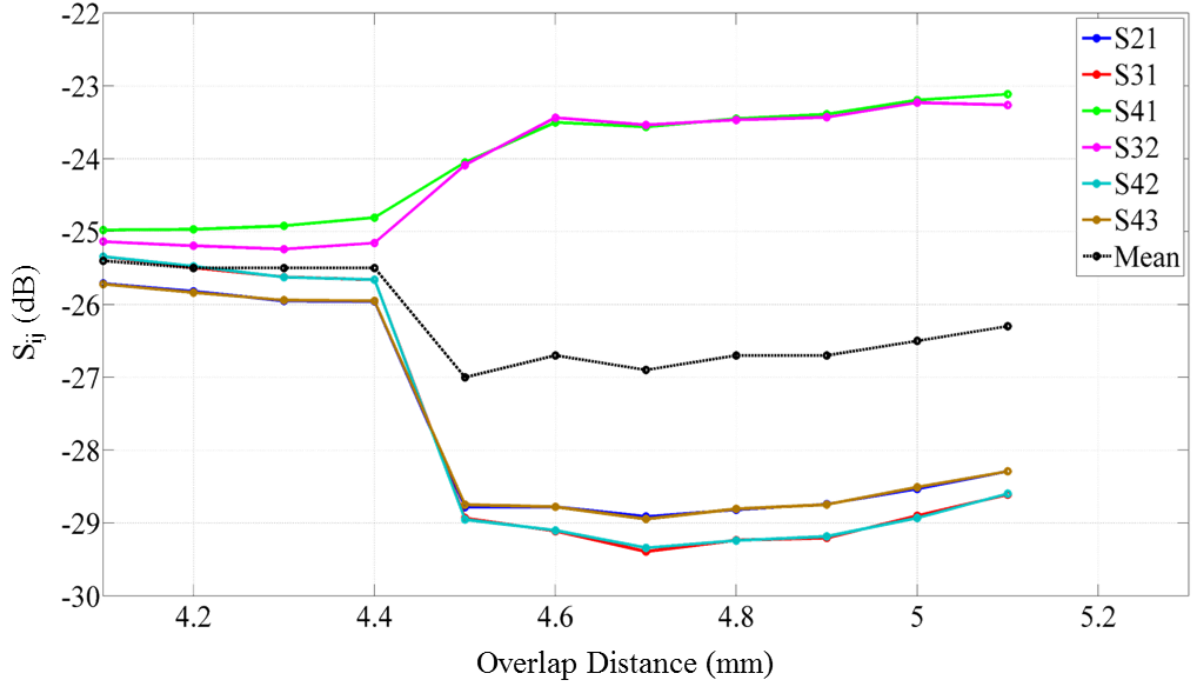


Figure 3.8: Decoupling ring overlap optimization: Simulated transmission scattering parameters (S_{ij}) as a function of overlap distance.

3.2.3 Decoupling Ring Effects on TLR Performance

The final geometry of the single TLR with the decoupling ring obtained in the previous sections is represented in Figure 3.9b. The decoupling ring effects on the performance of the single TLR were investigated by 3D EMS for single TLR with and without decoupling ring. Furthermore, the effects of the decoupling ring were evaluated on the bench and by MR measurements using fabricated single element TLRs without and with the decoupling ring (Figure 3.9c and d, respectively). The details of coil fabrication are given in section 3.3.1. The performance of the decoupling ring was evaluated by determining the following effects:

- the induced shift in the resonance frequency of the TLR
- Q -factor
- transmit efficiency
- SAR
- image quality

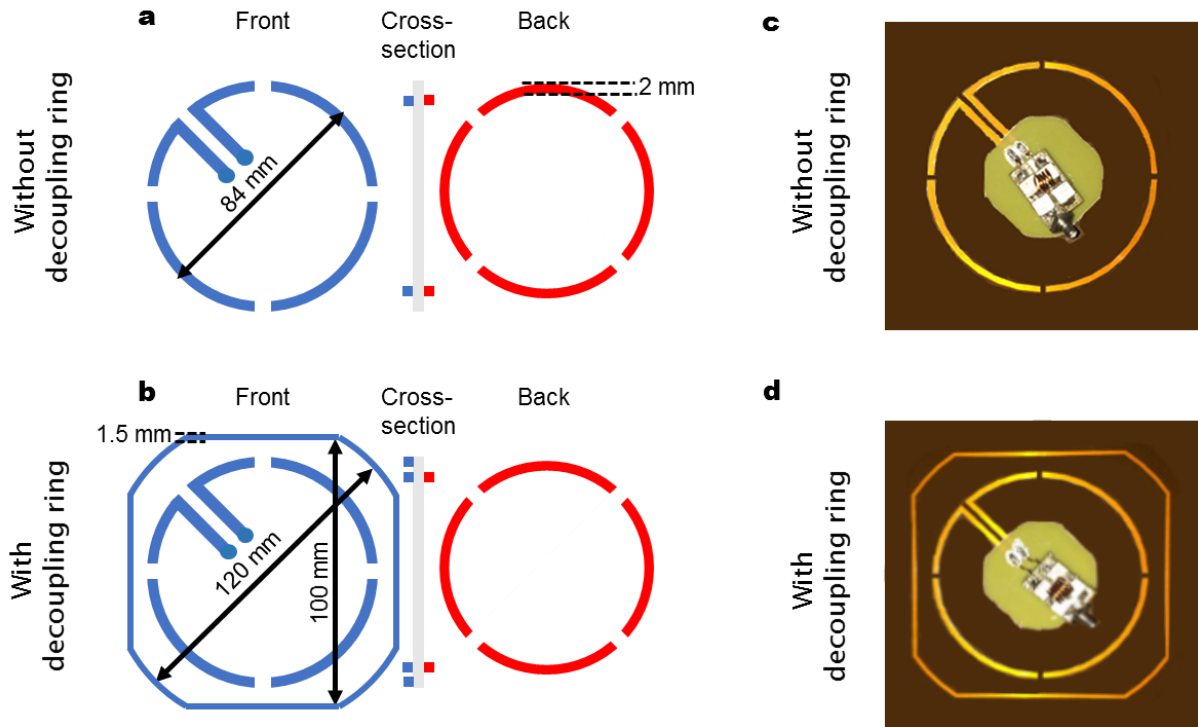


Figure 3.9: Single element TLR design without (a) and with (b) the decoupling ring. Fabricated single element TLR without (c) and with (d) the decoupling ring.

3.2.3.1 Frequency Shift Determination by 3D EMS

The shift in resonance frequency induced by the decoupling for TLR with and without the decoupling ring was evaluated by 3D EMS. It was found that the presence of the decoupling ring increases the resonance frequency by about 8 MHz and can be compensated by the tuning and matching circuitry.

3.2.3.2 Measured Q-factor on Bench

Table 3.2 presents the loaded and unloaded Q -factor measured on bench together with obtained values for capacitive tuning and matching circuitry for the TLR with and without the decoupling ring.

Table 3.2: Unloaded and loaded Q -factor measured on bench for single TLR with and without decoupling ring.

Single TLR	C_1 (pF)	L (nH)	C_2 (pF)	Q unloaded	Q loaded
Without Decoupling Ring	1.5	57	8.2	127	14.2
With Decoupling Ring	2.7	150	15	148.4	29.6

Table 3.2 demonstrates that the unloaded Q -factor is reduced by 89 % and 80 % when loaded for TLR without and with the decoupling ring, respectively. This shows that sample noise is clearly the dominant noise mechanism.

3.2.3.3 Simulated and Measured Transmit Efficiency $B_1^+ / \sqrt{P_{\text{input}}}$

The B_1^+ field was determined by 3D EMS and MR measurement for single TLR with and without the decoupling ring. For MR measurements, flip angle maps were acquired using the saturated Turbo FLASH (satTFL) method (104) employing a rectangular slice-selective saturation pulse with a 2 ms pulse duration and a 20 V amplitude. The experimental setup used for MR measurements with single element TLR is shown in Figure 3.10c. The loss of the acquisition chain including the transmit/receive switch was -1.5 dB which was measured on bench (see Figure 3.10a). Simulated B_1^+ maps were scaled, taking into account the acquisition chain losses, as described later in section 3.4.2.

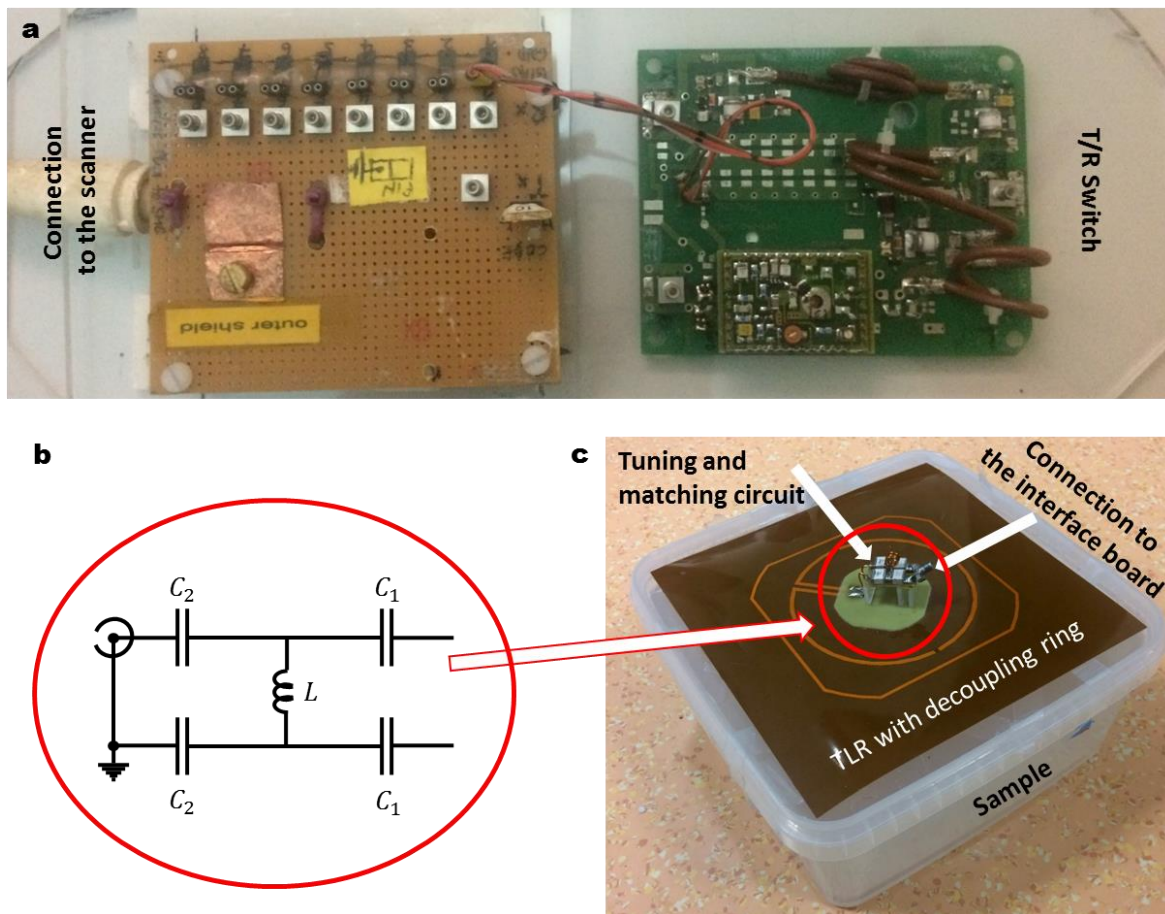


Figure 3.10: (a) Interface board including the T/R switch and the connection board to the scanner. (b) The capacitive tuning and matching network. (c) Experimental setup for MR measurement using single element TLR.

Figure 3.11 shows simulated and measured B_1^+ maps normalized to the corresponding input power. It can be observed that for both simulated and measured $B_1^+ / \sqrt{P_{input}}$ profiles, the decoupling ring slightly increases the transmit efficiency on the central axis of the TLR close to the coil. However, at larger distances the profile is comparable for both TLRs with and without the decoupling ring.

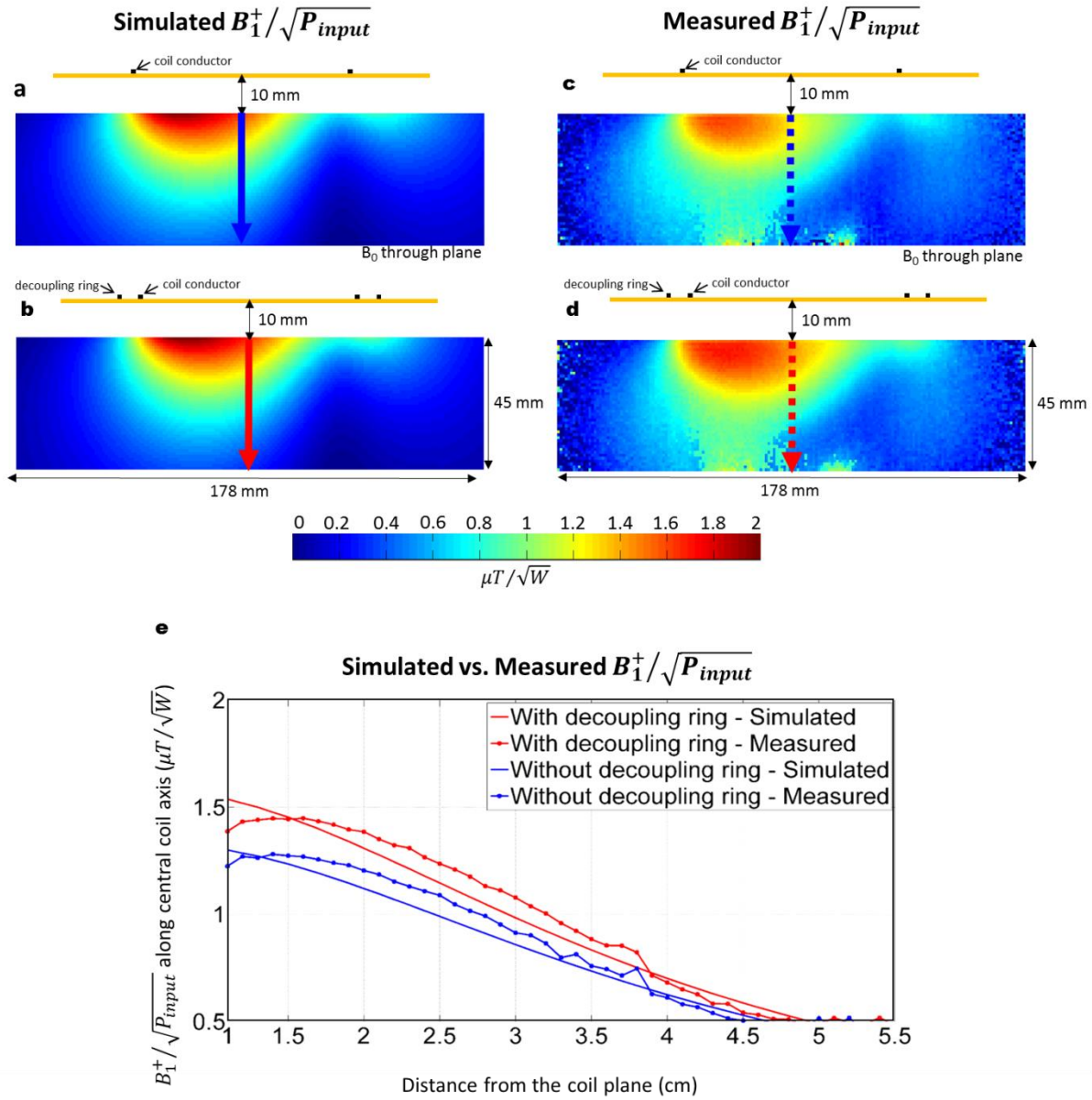


Figure 3.11: Simulated transversal transmit efficiency ($B_1^+ / \sqrt{P_{input}}$) for TLR without (a) and with (b) decoupling ring. Measured transversal transmit efficiency for TLR without (c) and with (d) decoupling ring. (e) Simulated and measured 1D profiles of transmit efficiency for TLR with and without decoupling ring along TLR central axis.

3.2.3.4 SAR Performance of TLR with Decoupling Ring

To evaluate the influence of adding a decoupling ring on the performance of TLR in terms of SAR, 10 g averaged SAR distributions were derived from the 3D EMS data. Post-processing was done using the SimOpTx toolbox (see section 2.6.3) based on the power correlation matrices (128). Figure 3.12 shows the maximum intensity projection of the simulated 10 g averaged SAR distributions for TLR with and without the decoupling ring.

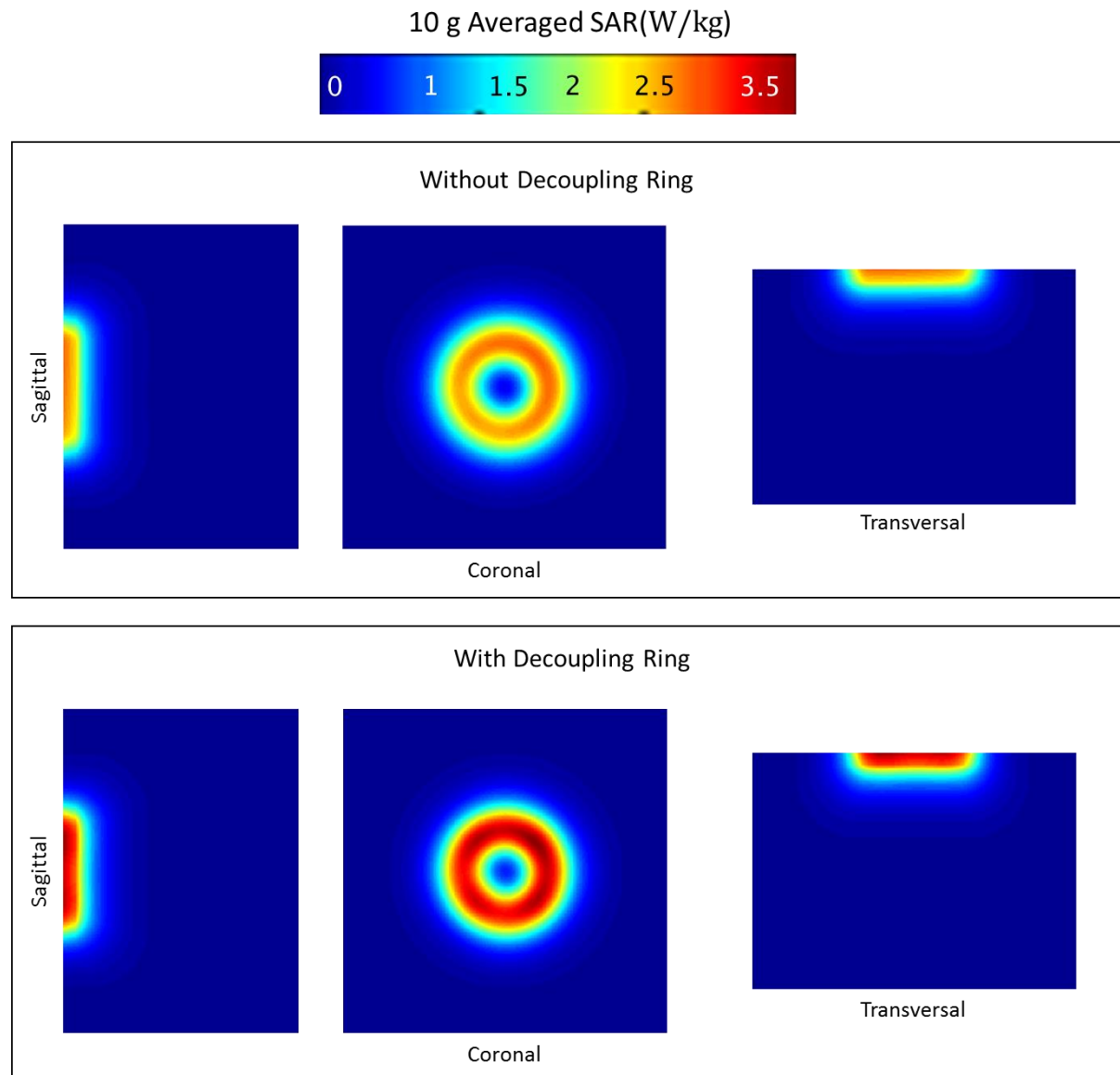


Figure 3.12: Maximum intensity projection of the simulated 10 g averaged SAR distribution for the single element TLR with and without decoupling ring.

Figure 3.12 demonstrates that the maximum intensity of the 10 g averaged SAR is increased by adding the decoupling ring. The maximum 10 g averaged SAR for TLR without and with the decoupling ring are 2.69 W/kg and 3.42 W/kg, respectively.

3.2.3.5 Imaging Performance of TLR with Decoupling Ring

3D gradient echo sequence ($TR/TE = 14/6.75$ ms, $T_{acq} = 2:25$ min, $1 \times 1 \times 1$ mm³ nominal resolution, $96 \times 192 \times 192$ mm³ FOV) was used to acquire MR images using single TLR with and without the decoupling ring in order to investigate the impact of the decoupling ring on the image quality.

3D gradient echo images are shown in Figure 3.13. For the TLR with the decoupling ring, no significant artifacts can be observed.

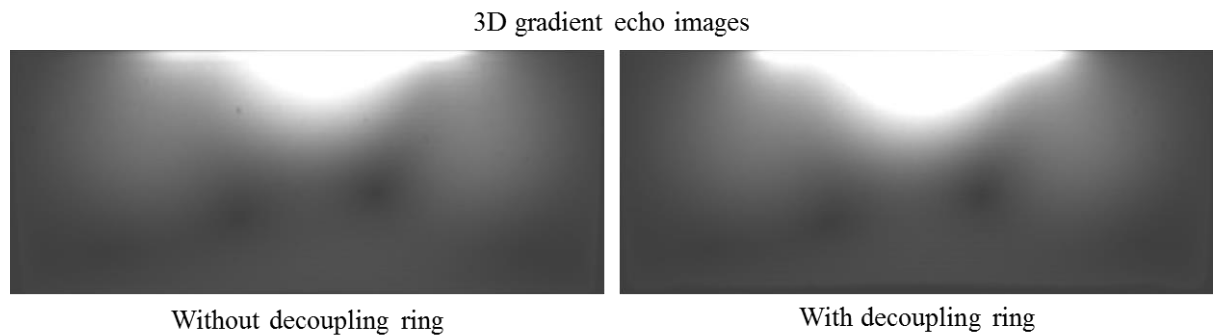


Figure 3.13: Transversal 3D gradient echo images ($TR/TE = 14/6.75$ ms, $T_{acq} = 2:25$ min, $1 \times 1 \times 1$ mm³ nominal resolution, $96 \times 192 \times 192$ mm³ FOV) of the phantom.

The SNR maps of the acquired 3D gradient echo images were calculated using the following formula (129)

$$SNR = 0.655 \frac{I}{SD_{air}} \quad (3.5)$$

where I is the mean signal intensity of the ROI and SD_{air} is the standard deviation of an ROI placed in the air surrounding the phantom.

Figure 3.14a shows the 2D SNR maps of the single TLR with and without the decoupling ring. The SNR profile along the central axis of the TLR with and without the decoupling ring is plotted for different depths along the sample as shown in Figure 3.14b. For TLR with the

decoupling ring, the SNR is slightly increased for depth values below 4 cm, and above which the profile is comparable for both TLR with and without the decoupling ring.

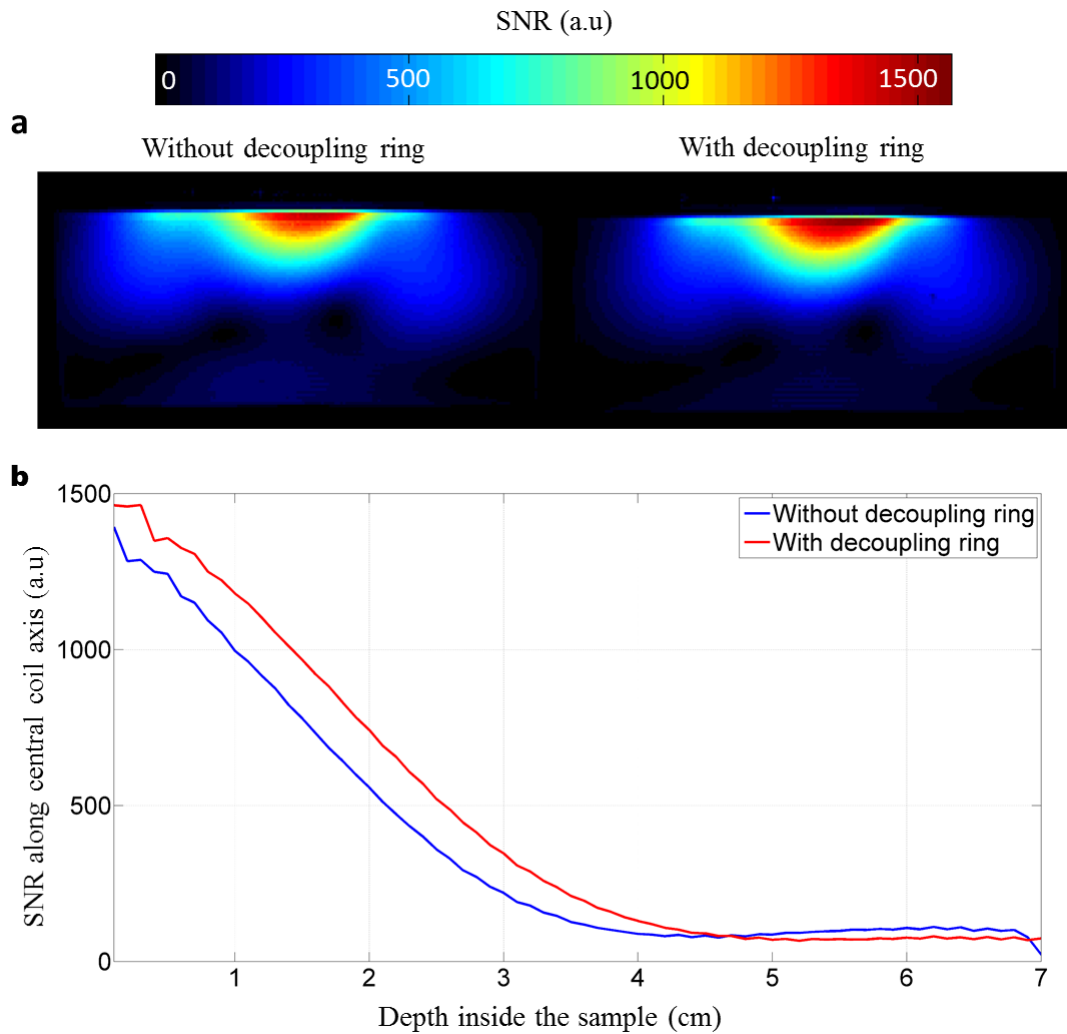


Figure 3.14: Calculated SNR maps: (a) 2D SNR maps calculated from the acquired 3D GRE images. (b) 1D profile of the calculated SNR along the coil central axis.

3.2.4 Single Element TLR vs. Conventional loop

In order to validate the choice of TLR in this study, 3D EMS was used to compare the designed single element TLR with a conventional loop of the same size. Since the TLR designed in this study has 4 gaps on each size, the designed conventional loop was segmented by 8 capacitors as shown in Figure 3.15.

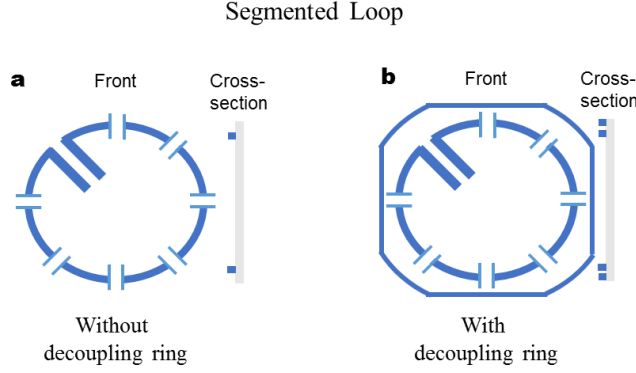


Figure 3.15: Segmented conventional loop without (a) and with (b) decoupling ring. The segmented loop has the same geometry as the single TLR design. In addition, the geometry of the decoupling ring was kept constant.

Both coils were tuned at 297.2 MHz and matched to $50\ \Omega$. Designed TLR and segmented loop were simulated individually with and without the decoupling ring. Simulated B_1^+ maps for TLR and segmented loop with and without decoupling ring are shown in Figure 3.16.

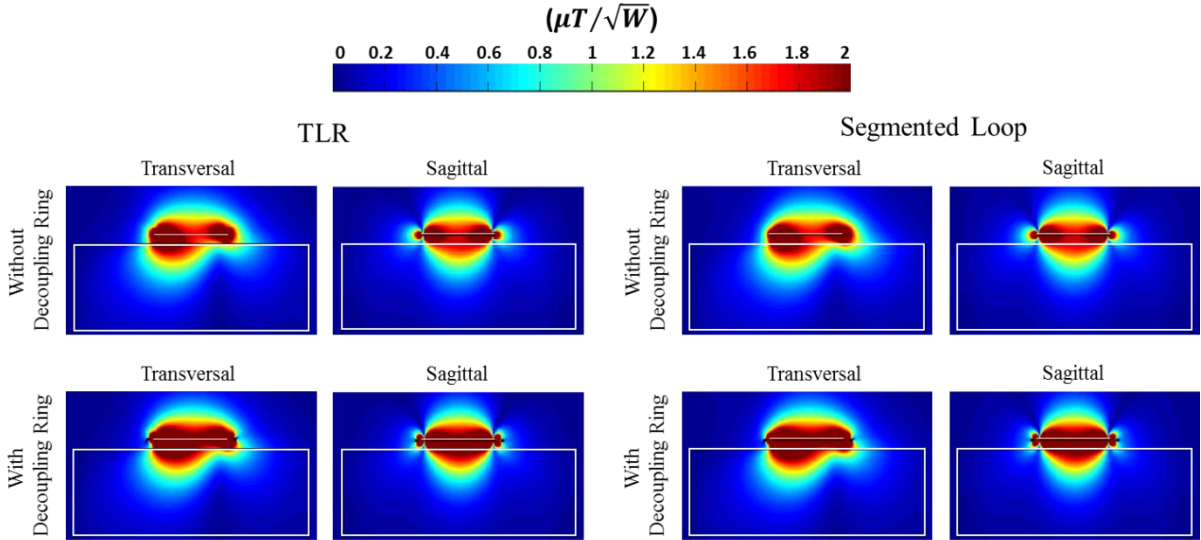


Figure 3.16: Simulated B_1^+ profiles normalized to the input power ($B_1^+/\sqrt{P_{\text{input}}}$) for the single element TLR and the segmented loop. The white line shows the coil plane and the white rectangle shows the phantom which has size of $27.6\text{ cm} \times 10\text{ cm}$.

Based on the results demonstrated in Figure 3.16, it can be observed that the $B_1^+/\sqrt{P_{\text{input}}}$ profiles of TLR are similar to those of conventional loop with discrete capacitors.

Figure 3.17 shows the E -field vector magnitude profiles for TLR and the segmented loop with and without the decoupling ring.

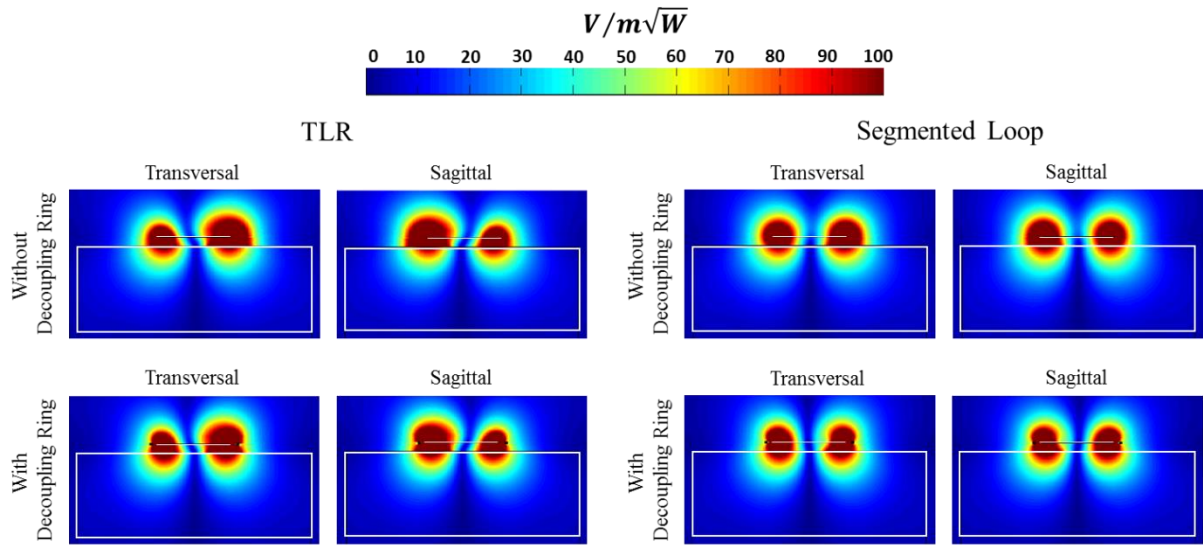


Figure 3.17 Simulated E -field vector magnitude profiles normalized to the input power for the single element TLR and segmented loop with and without decoupling ring. The white line shows the coil plane and the white rectangle shows the phantom which has size of $27.6 \text{ cm} \times 10 \text{ cm}$.

Figure 3.17 demonstrates no significant difference in E -field of the TLR and segmented loop.

In addition, the 10 g averaged SAR values for the TLR and the segmented loop with and without decoupling ring are presented in Table 3.3.

Table 3.3: 10 g averaged SAR values for single element TLR and segmented loop, with and without decoupling ring.

Max 10 g Averaged SAR	Without Decoupling Ring (W/kg)	With Decoupling Ring (W/kg)	Relative Change (%)
TLR	2.69	3.42	27.01 %
Segmented Loop	2.68	3.38	26.21 %

Table 1.2 demonstrates that the difference in the maximum 10 g averaged SAR for the TLR and segmented loop without and with the decoupling ring is 0.4 % and 1.2 %, respectively.

In conclusion, the single element TLR and a conventional segmented loop of the same size demonstrated no significant differences in terms of transmit field (B_1^+/P_{input}), E -field and maximum 10 g averaged SAR.

3.3 Array Development and Implementation

The obtained geometry for single TLR with decoupling ring was used to design a 12-element (4 columns, 3 rows) TLR array with overlapped decoupling rings as shown in Figure 3.18.

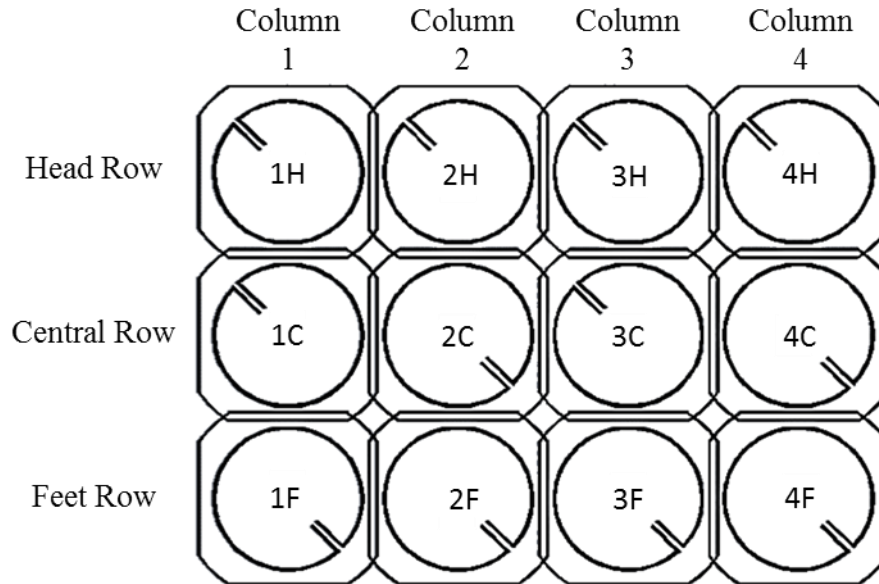


Figure 3.18: Schematic of the 12-element TLR array.

3.3.1 Coil Fabrication on Flexible PCB

The single TLR with and without the decoupling ring (see Figure 3.9cd), as well as the 12-element TLR array (Figure 3.19) were fabricated using standard photolithographic techniques (db electronic Daniel Boeck GmbH, Bregenz, Austria). A double sided copper layer of 35 μm in thickness was used on a 100 μm thick polyamide substrate ($\epsilon = 3.5$). In all of the fabricated coils, two insulator layers made from Polyamide with thicknesses of 75 μm and 100 μm were placed on top and bottom of each coil design for copper protection and coil insulation, respectively. A square-shaped rigid layer with curved corners made of FR4 with thickness of 1 mm was mount on top-centre of each coil element to place interface components while preserving the flexibility of the array. After fabrication, 1mm Teflon[®] (PTFE) layers are deposited on both sides of the array for mechanical stability and patient to coil insulation. All 12-elements of the array were used in transmit/receive mode.

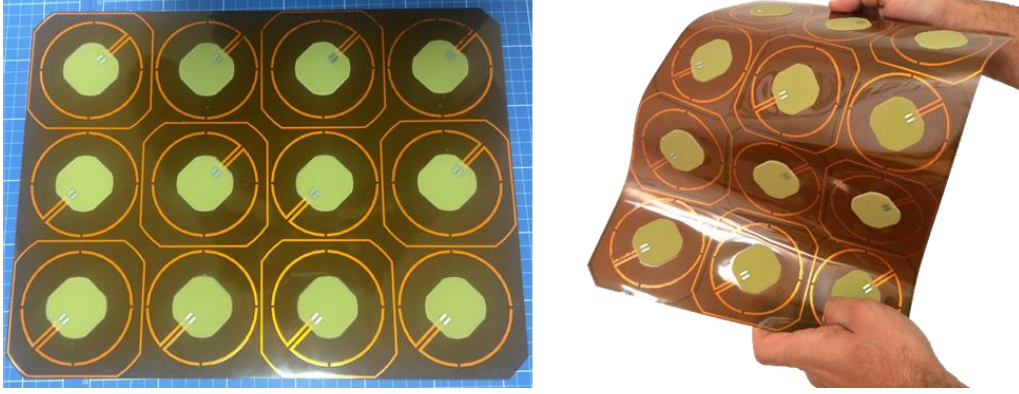


Figure 3.19: Fabricated 12-element flexible TLR array.

3.3.2 Static B_1^+ Shimming

Before cabling the array, a 3D EMS was performed to determine the optimal phase setting, i.e. the phase shift between columns which gives the highest B_1^+ homogeneity. Targeting cardiac MRI, the static B_1^+ shimming for a heart voxel model should be done to determine the phase setting for the individual elements of the array. However, 3D simulation of the TLR array in bent configuration was not possible in this study due to the complexity of meshing (see section 3.1.1). Therefore, to obtain the phase setting for static B_1^+ shimming, a cubic-shaped ROI ($12 \times 8 \times 6 \text{ cm}^3$) comparable to the size of human heart was defined in the cubic phantom used in array simulation. The relative phase shift between the columns of elements was varied equally from 0° to 350° in steps of 10° with one column being fixed to the phase of 0° . The phases between the elements in each column were kept equal since the columns are in the same direction as B_0 field. Therefore, the induced phase shift between elements within one column could be neglected. This led to 36 phase combinations, thus 36 excitation vectors with a constant amplitude for the 12-element array. The simulated B_1^+ field for each phase subset was used to calculate the transmit efficiency SE, in terms of deposited power using the following formula (88)

$$SE = \frac{\overline{B_1^+}}{\sqrt{\max(\text{SAR}_{10g})}} \quad (3.6)$$

where $\overline{B_1^+}$ is the mean value of B_1^+ and $\max(\text{SAR}_{10g})$ denotes the maximum value of the 10 g averaged SAR.

Furthermore, the relative inhomogeneity RI, is calculated using the following equation (88)

$$RI = \frac{\text{std}(B_1^+)}{B_1^+} \quad (3.7)$$

where $\text{std}(B_1^+)$ denotes the standard deviation of B_1^+ .

The figure of merit, f, for optimal phase setting was defined as follows (88)

$$f = \frac{SE}{\max(SE)} \cdot \left(1 - \frac{RI}{\max(RI)}\right) \quad (3.8)$$

Equation (3.8) combines B_1^+ homogeneity with the transmit efficiency including the maximum 10 g averaged SAR to evaluate safety and efficiency of the developed array for future use, e.g. in vivo.

Figure 3.20 shows the transmit efficiency in terms of the absorbed power (SE), the relative inhomogeneity (RI) of B_1^+ and the figure of merit (f), determined from the simulated B_1^+ maps and 10 g averaged SAR as a function of phase shift between columns of the array.

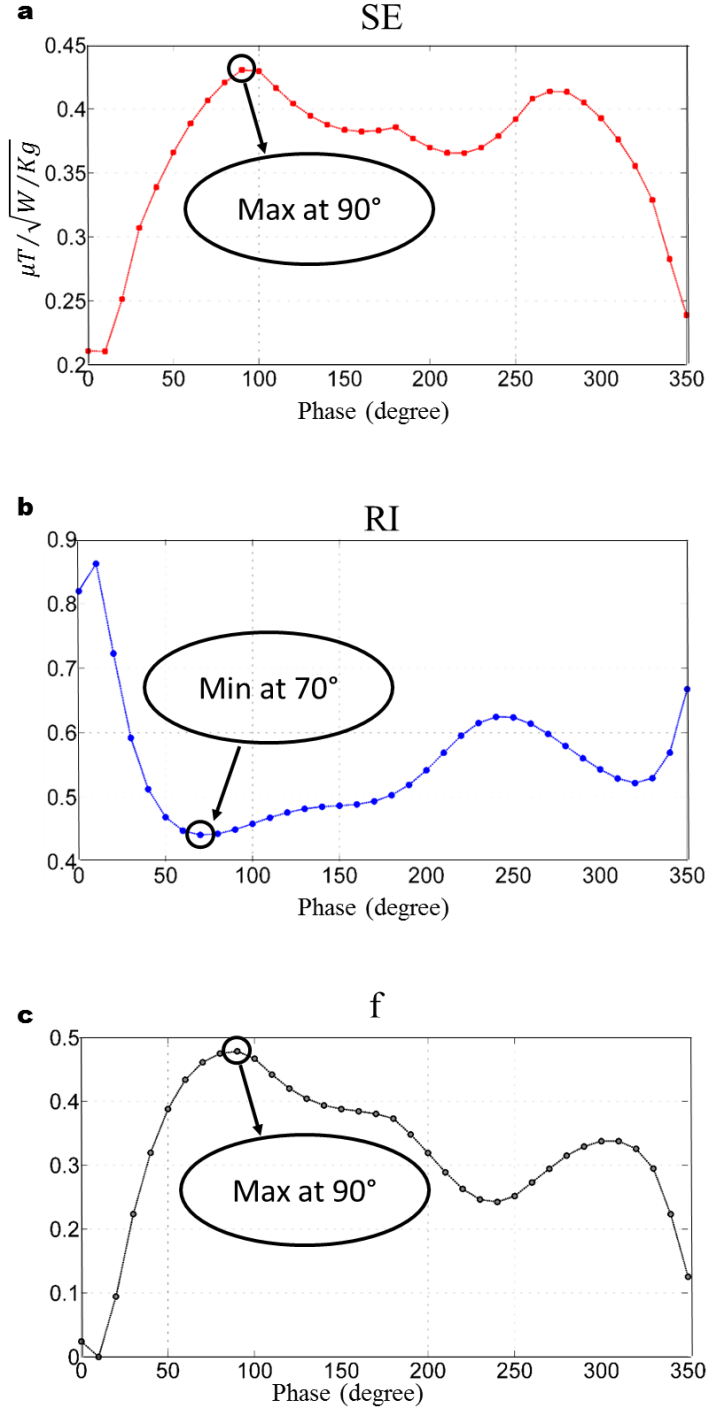


Figure 3.20: Static B_1^+ phase shimming: (a) simulated transmit efficiency in terms of SAR (SE), (b) simulated relative inhomogeneity, (c) simulated figure of merit function f for fixed phase variations between each column within the array (d).

Figure 3.20 shows that the SE profile reaches its maximum at 90° phase shift while RI is minimum for a 70° phase shift. The figure of merit, f , that combines the transmit efficiency and the B_1^+ homogeneity is maximum for a 90° phase shift. Therefore, 90° was chosen as the optimal phase difference between each column of the array.

3.3.3 Cabling, Interfacing, and Housing

3.3.3.1 Cabling

Since the MR scanner (see section 2.4.4.2) used in this study is equipped with only one ^1H transmit channel, the total power delivered by the scanner was initially split into four parts (using a 1:4 power splitter) to feed the four elements in the central row. Interface boards of the central row elements contained 1:3 power splitters to split the power between three elements in each column.

The cables were passed through cylindrical floating cable traps (Figure 2.29d) placed on the interface of each element in order to eliminate common mode currents. This cable trap geometry and cable arrangement is an essential part of the mechanical design of the array, as the cables passing through them can slide back and forth without imposing limits on the mechanical flexibility of the array. Further, floating cable traps can accommodate several cables and, therefore, occupy less space. In that way, the traps can be integrated on the interface boards inside each coil housing, as shown in Figure 3.22.

The determined transmit phase configuration in section 3.3.2 was implemented using cables with different lengths. To determine on which side of the patient the cable outlet should be positioned, the length of the required phase shifter cables for both cases were calculated, as shown in Table 3.4. Placing the cable outlet in the left side of the patient resulted in ca. 70 cm shorter overall cable length, yielding approximately 0.2 dB lower cable loss using the indicated cable loss of -0.48 dB/m from the data sheet. Therefore, the cable outlet was placed on the left side of the patient as shown in Figure 3.21.

Table 3.4: Calculated length of the phase shifter cables based on the cable outlet position in the left or right side of the patient.

Patient side of cable outlet	Cable length (cm)				Total cable length (cm)	Total loss (dB)
	0°	90°	180°	270°		
Left	45.8	63.2	80.6	98	287.7	-1.39
Right	74	91.4	108.8	56.6	330.8	-1.59

The 12 receive cables were equally distributed between two plugs; each containing 6 receive cables (see Figure 3.21). These two strands of cables were routed along the head and foot row of the array.

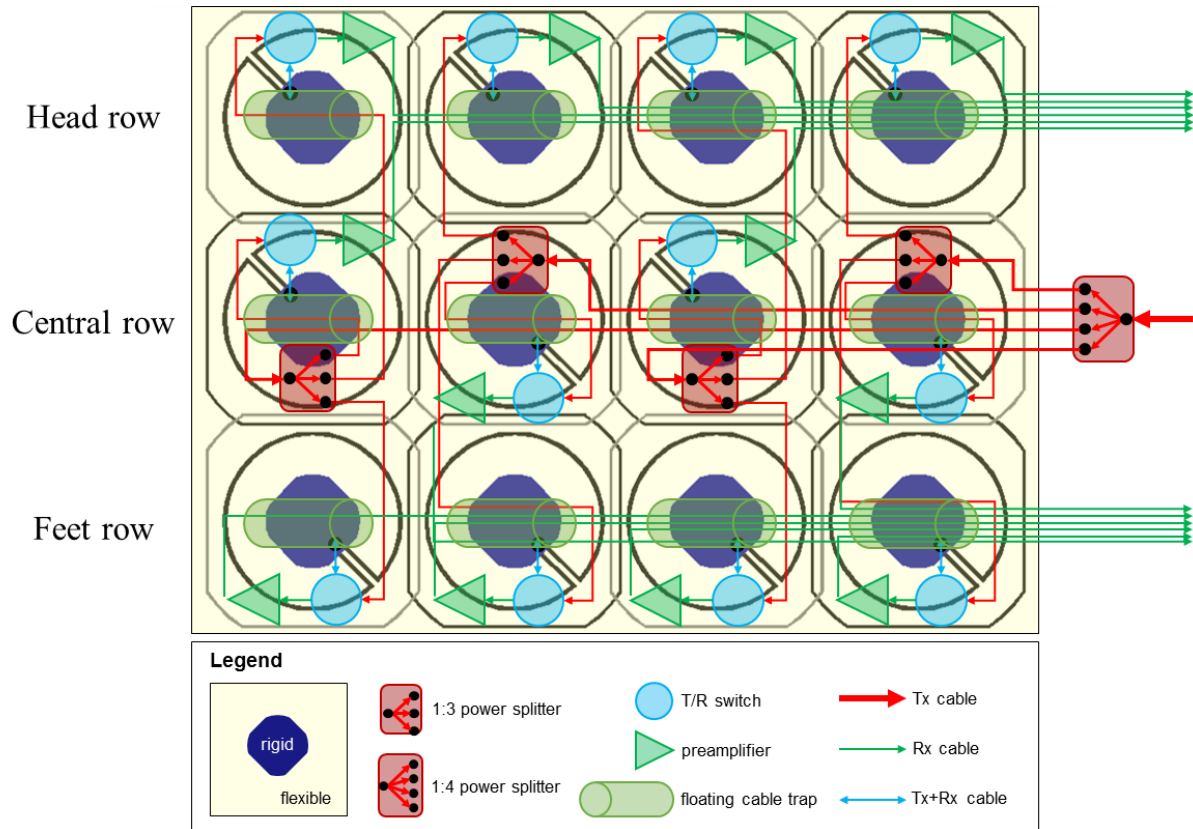


Figure 3.21: 12-channel array cabling and interfacing scheme.

3.3.3.2 Interfacing

Interface boards including self-made T/R switch (see section 2.4.3.6), Wilkinson power splitters (see section 2.4.3.7), and low noise preamplifier (0.5 dB noise figure, 27.2 ± 0.2 dB gain, Siemens Healthineers, Erlangen, Germany) were fabricated as shown in Figure 3.22.

A photograph of the complete cabling and interfacing of the array is shown in Figure 3.23.

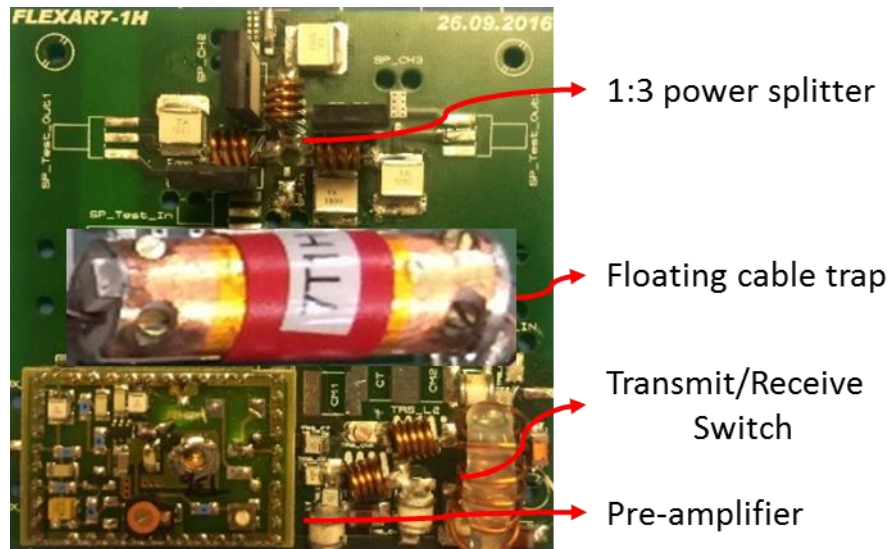


Figure 3.22: Interface board containing power splitter, floating cable trap, transmit/receive switch, and preamplifier.

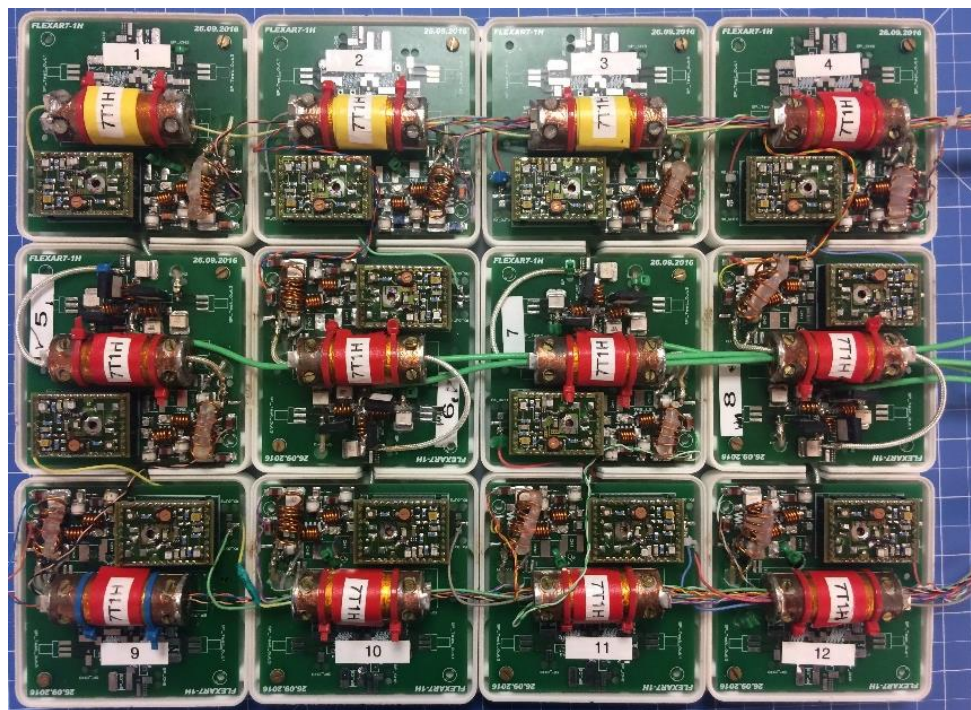


Figure 3.23: Developed 12-element flexible TLR array.

3.3.3.3 Housing

Figure 3.24 a and b show the designed housing for each interface board. They are cuboid boxes of $93 \times 93 \times 43 \text{ mm}^3$ with rounded edges, split into a bottom and a top part. The bottom part of the housing was attached to the rigid part with the capacitive tune and match circuit attached (Figure 3.24b). The interface boards were screwed onto the bottom part of the housing and the

whole box was closed by the top part. Slits on the sides of the top housing parts are used to route the cables from one housing to the neighbouring one.

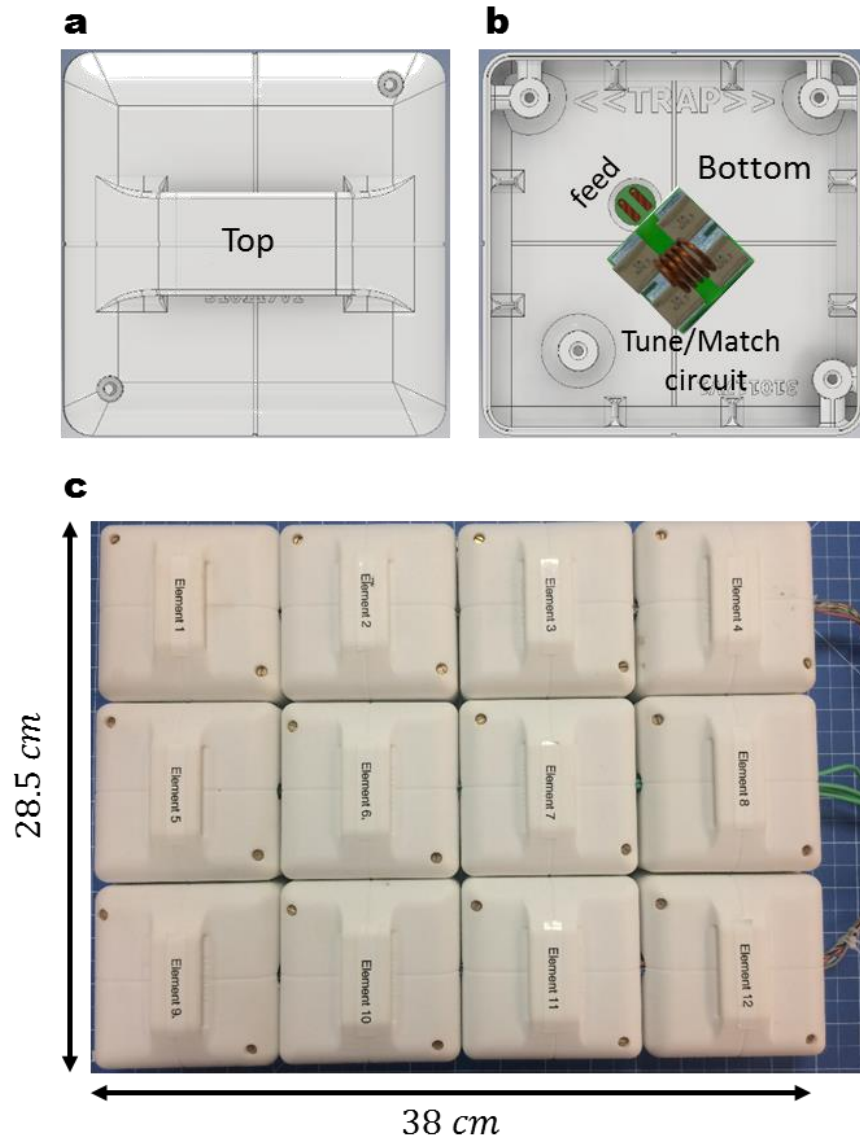


Figure 3.24: Designed housing top (a) and bottom (b) parts with the capacitive tune and match circuit attached to the bottom part. (c) Final array housing.

On top of the top housing parts, there is a slit to accommodate straps that to attach and bend the array around the subject. There is one strap for each row of the array, which allows for adjustment of the shape to each section of the body individually, improving the form fitting of the array. Figure 3.25 shows the developed 12-element TLR array bent on a human torso. The total weight of the array is about 2.4 kg.



Figure 3.25: The flexible array bent on a human torso.

3.4 Performance Evaluation of the Array

Following the fabrication of the array, its performance was evaluated by 3D EMS, bench and MR measurements.

3.4.1 Decoupling Performance

The decoupling efficiency of the 12-element array was evaluated by 3D EMS and on bench by measuring the transmission scattering parameters (S_{ij}). On bench, the S-parameter matrix was recorded for three experimental configurations: when the array was positioned flat onto the rectangular-shaped phantom, when it was bent onto a torso phantom and when it was bent on the torso of a volunteer (male, 30 years old, body mass index = 28.4 kg/m²). Figure 3.26 shows the simulated and measured scattering parameters of the developed array in flat configuration (box-shaped phantom) demonstrating decoupling values (S_{ij}) below -19 dB and matching values (S_{ii}) of at least -8 dB.

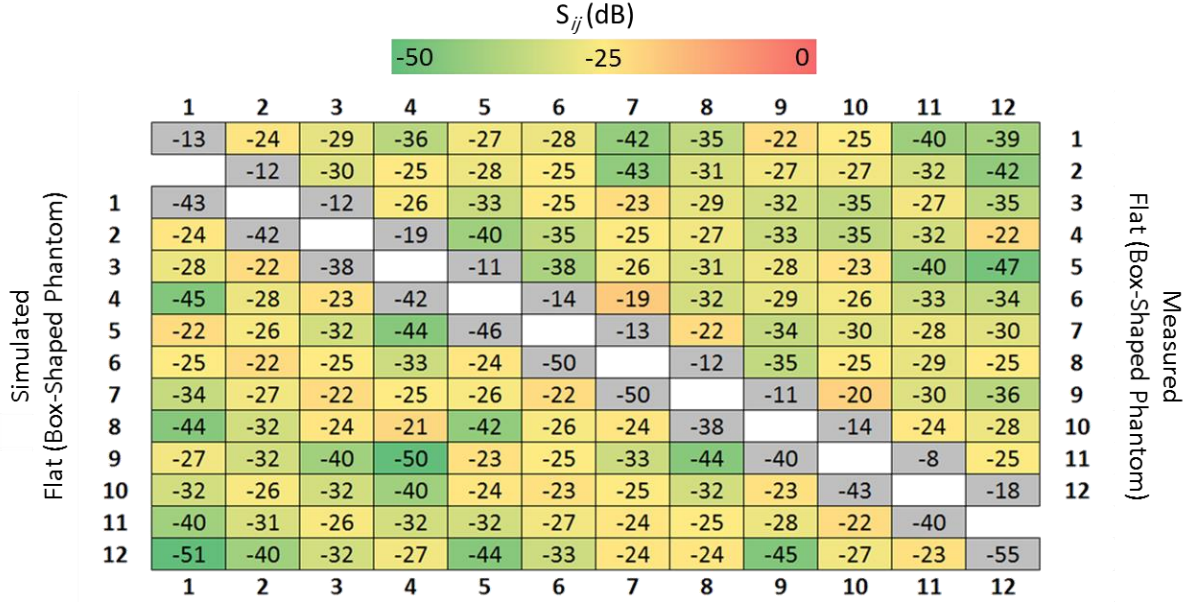


Figure 3.26: Simulated and measured scattering parameters of the 12-element TLR array in flat configuration for the box-shaped phantom.

Figure 3.27 represents the S-parameters values of the developed array measured on the bench when the array was bent on the torso phantom and the torso of the volunteer.

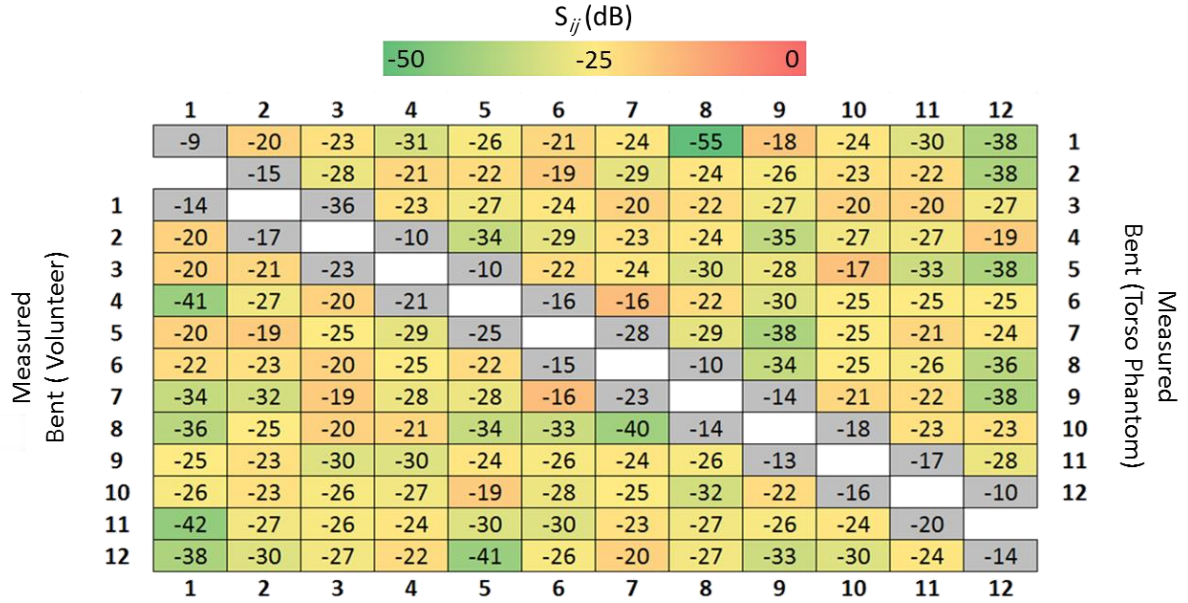


Figure 3.27: Measured S-parameters on bench when the 12-element TLR array in bent configuration for the torso phantom and torso of the volunteer.

In the bent configuration, decoupling level (S_{ij}) below -16 dB and matching level (S_{ii}) of at least -9 dB were obtained.

3.4.2 Power Loss Evaluation

As for the single element investigation, the losses of the measurement chain of the 12-element array were evaluated. To do so, cables and the corresponding interface including, power splitters, T/R switch and transmit cables as well as the respective phase shift between each column were calculated using reflection and transmission measurements performed on bench. Furthermore, since the array was intentionally tuned and matched for an average human torso, reflections due to the imperfect matching for the box-shaped and torso phantoms were also considered in the total loss evaluation. The obtained amplitude and phase of the power delivered to each element port were used to scale the simulation results for comparison with the measured ones. Figure 3.28 presents the measured data on bench which were considered in total loss evaluation.

Element	Name	measurement data									
		cable length Tx cable from 1:4 splitter to 1:3 splitter, calculated from measured phase (cm)	cable length connection cables (cm)	total Tx cable length from 1:4 splitter (cm)	measured phases [°]	measured insertion loss from testrig to 1:3 splitter (dB)	measured S11 at T/R	50 Ohm load (dB)	flat phantom (dB)	torso phantom (dB)	in vivo with 1cm foam padding (dB)
1	T1H	97.1	17	114				-19	-13	-9	-14
2	T2H	80.0	17	97				-17	-12	-15	-17
3	T3H	62.6	17	80				-18	-12	-36	-23
4	T4H	45.8	17	63				-18	-19	-10	-21
5	T1C	97.1	17	114	20.5	-8.04		-19	-11	-10	-25
6	T2C	80.0	17	97	-67.9	-8.11		-17	-14	-16	-15
7	T3C	62.6	17	80	-158.0	-7.92		-20	-13	-28	-23
8	T4C	45.8	17	63	115.2	-7.85		-20	-12	-10	-14
9	T1F	97.1	17	114				-17	-11	-14	-13
10	T2F	80.0	17	97				-22	-14	-18	-16
11	T3F	62.6	17	80				-28	-8	-17	-30
12	T4F	45.8	17	63				-24	-18	-10	-14

Tx cable data	
-0.48 dB/m cable loss	
282.49 max. CW power	
0.19 cm/° phase shift	

max. MR scanner Tx power at coil socket	
4400 W	

Figure 3.28: Measured data on bench for total loss evaluation.

Obtained contributions for losses in the measurement chain are provided in Figure 3.29.

Element	Name	loss contributions (dB)									
		Testrig, guess (~same as Siemens plug+cables)	Plug+Siemens cable, calculated from total losses minus known losses	1:4 splitter	phase shifter cables, from datasheet and length	1:3 splitter insertion loss	connection cables, from data sheet and length	T/R insertion loss, without reflection	flat phantom	torso phantom	in vivo
1	T1H	-0.70	-0.56	-0.31	-0.47	-0.40	-0.08	-0.21	-0.25	-0.58	-0.18
2	T2H	-0.70	-0.72	-0.30	-0.39	-0.40	-0.08	-0.13	-0.26	-0.14	-0.09
3	T3H	-0.70	-0.63	-0.29	-0.30	-0.40	-0.08	-0.13	-0.30	0.00	-0.02
4	T4H	-0.70	-0.68	-0.25	-0.22	-0.40	-0.08	-0.15	-0.06	-0.46	-0.03
5	T1C	-0.70	-0.56	-0.31	-0.47	-0.40	-0.08	-0.18	-0.33	-0.46	-0.01
6	T2C	-0.70	-0.72	-0.30	-0.39	-0.40	-0.08	-0.14	-0.18	-0.11	-0.14
7	T3C	-0.70	-0.63	-0.29	-0.30	-0.40	-0.08	-0.15	-0.20	-0.01	-0.02
8	T4C	-0.70	-0.68	-0.25	-0.22	-0.40	-0.08	-0.13	-0.29	-0.46	-0.18
9	T1F	-0.70	-0.56	-0.31	-0.47	-0.40	-0.08	-0.17	-0.41	-0.18	-0.22
10	T2F	-0.70	-0.72	-0.30	-0.39	-0.40	-0.08	-0.24	-0.18	-0.07	-0.11
11	T3F	-0.70	-0.63	-0.29	-0.30	-0.40	-0.08	-0.13	-0.71	-0.09	0.00
12	T4F	-0.70	-0.68	-0.25	-0.22	-0.40	-0.08	-0.19	-0.07	-0.46	-0.18

Figure 3.29: Various loss contributions considered in the measurement chain for total loss evaluation.

Total losses attributed to each element together with the calculated amplitude and phase of the maximum available power delivered to each element feed for different loading situations (i.e. box-shaped and torso phantom and an average human torso) are demonstrated in Figure 3.30.

Element	Name	results									
		total losses [dB]			Tx power			max. power [W]			Phase [°]
		flat phantom	torso phantom	in vivo	flat phantom	torso phantom	in vivo	flat phantom	torso phantom	in vivo	
1	T1H	-2.28	-2.62	-2.21	59%	55%	60%	217	201	220	265.3
2	T2H	-2.28	-2.16	-2.11	59%	61%	62%	217	223	226	177.0
3	T3H	-2.13	-1.84	-1.86	61%	66%	65%	224	240	239	86.8
4	T4H	-1.84	-2.24	-1.82	65%	60%	66%	240	219	241	0.0
5	T1C	-2.33	-2.46	-2.01	58%	57%	63%	214	208	231	265.3
6	T2C	-2.21	-2.14	-2.17	60%	61%	61%	221	224	223	177.0
7	T3C	-2.06	-1.86	-1.88	62%	65%	65%	228	239	238	86.8
8	T4C	-2.05	-2.22	-1.94	62%	60%	64%	229	220	235	0.0
9	T1F	-2.39	-2.16	-2.21	58%	61%	60%	211	223	220	265.3
10	T2F	-2.32	-2.20	-2.25	59%	60%	60%	215	221	219	177.0
11	T3F	-2.55	-1.92	-1.84	56%	64%	66%	204	236	240	86.8
12	T4F	-1.89	-2.28	-1.99	65%	59%	63%	237	217	232	0.0

Figure 3.30: Total loss evaluation of the measurement chain Individual element loss contributions together with calculated amplitude and phase of the delivered power to each element feed for flat phantom (box-shaped), torso phantom and an average torso of a volunteer. The values for Tx amplitude are shown as the percentage of the total power available at coil socket of the scanner.

The transmit power delivered at each coil port is shown graphically in Figure 3.31 for various loading cases.

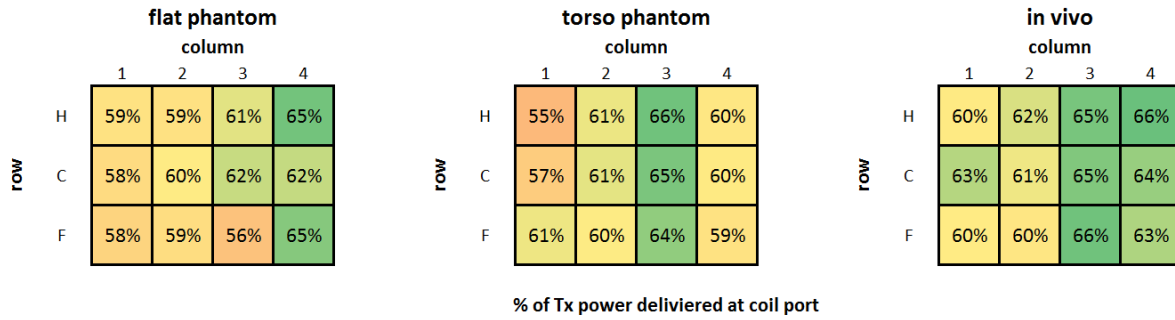


Figure 3.31: Calculated transmit power delivered to each element port.

Figure 3.31 demonstrates that on average, 60.3 %, 60.7 % and 62.9 % of the available power at the coil socket of the scanner are expected to be delivered to each coil port when the array is loaded with the flat phantom, the torso phantom and the torso of the volunteer, respectively.

The loss contributions of various sources in the transmit chain are demonstrated in Figure 3.32.

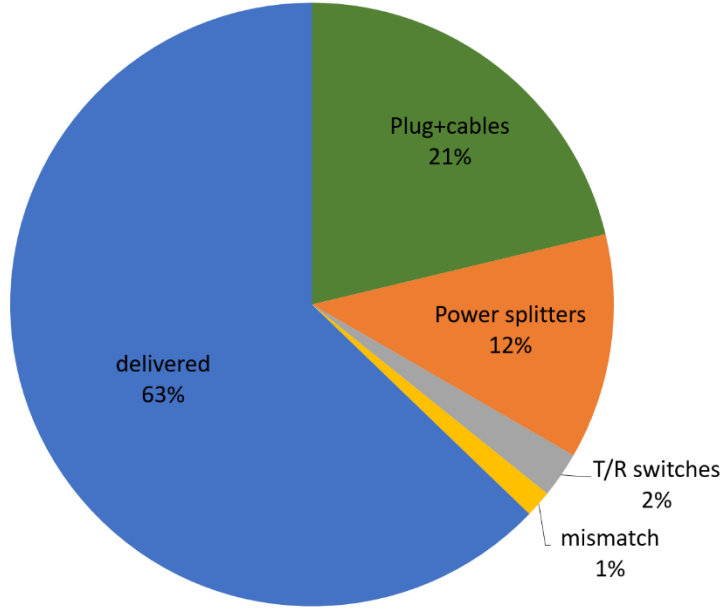


Figure 3.32: chart of the loss contributions in the transmit chain.

3.4.3 Transmit Efficiency ($B_1^+/\sqrt{P_{\text{input}}}$) Profiles

The transmit efficiency ($B_1^+/\sqrt{P_{\text{input}}}$) of the developed array was evaluated by 3D EMS (for box-shaped phantom) and MR measurement (for box-shaped and torso phantoms). To determine B_1^+ profiles, flip angle maps were acquired using the saturated Turbo FLASH (satTFL) method (104) employing a rectangular saturation pulse with a 2 ms pulse duration and 75 V (flat, box-shaped phantom) pulse amplitude. For the bent configuration (torso phantom) a rectangular saturation pulse with the duration of 0.35 ms and 429 V amplitude was used. The obtained B_1^+ maps were normalized to the input power at the coil port. For the box-shaped phantom, simulated $B_1^+/\sqrt{P_{\text{input}}}$ maps were scaled using the losses measured on the bench in section 3.4.2. For the array in flat configuration, initially, each column of the array was excited (bridging the 1:4 power splitter, see Figure 3.10) to investigate the transmit efficiency of each element. The simulated and measured $B_1^+/\sqrt{P_{\text{input}}}$ profiles obtained with column – wise excitation are presented in the Figure 3.33.

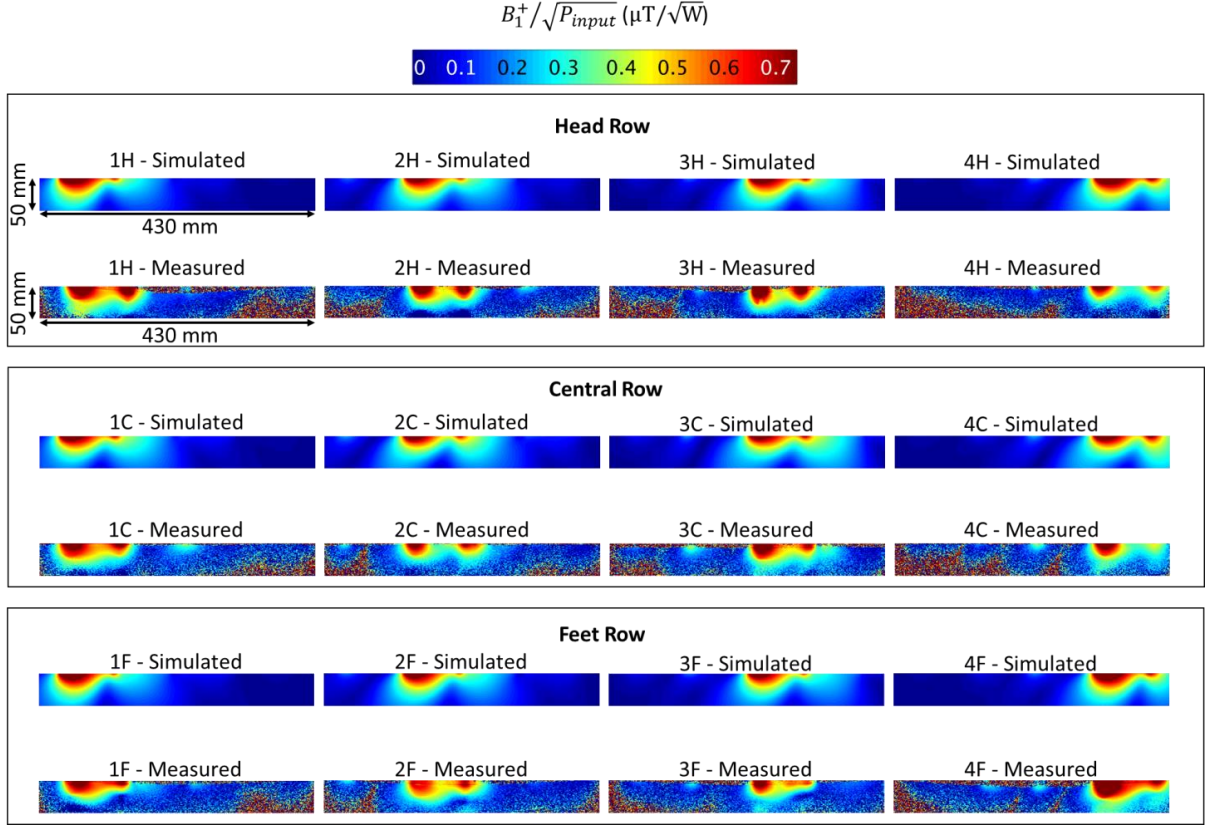


Figure 3.33: Column-wise excitation: transversal simulated and measured $B_1^+ / \sqrt{P_{input}}$ maps for each element of the array.

The measured $B_1^+ / \sqrt{P_{input}}$ profiles in Figure 3.33 demonstrate that each element produces its own transmit profile which is similar to that of the single element TLR with the decoupling ring (see Figure 3.11).

The simulated and measured $B_1^+ / \sqrt{P_{input}}$ maps of the developed array in flat configuration (box-shaped phantom) when all elements were excited simultaneously are shown in Figure 3.34.

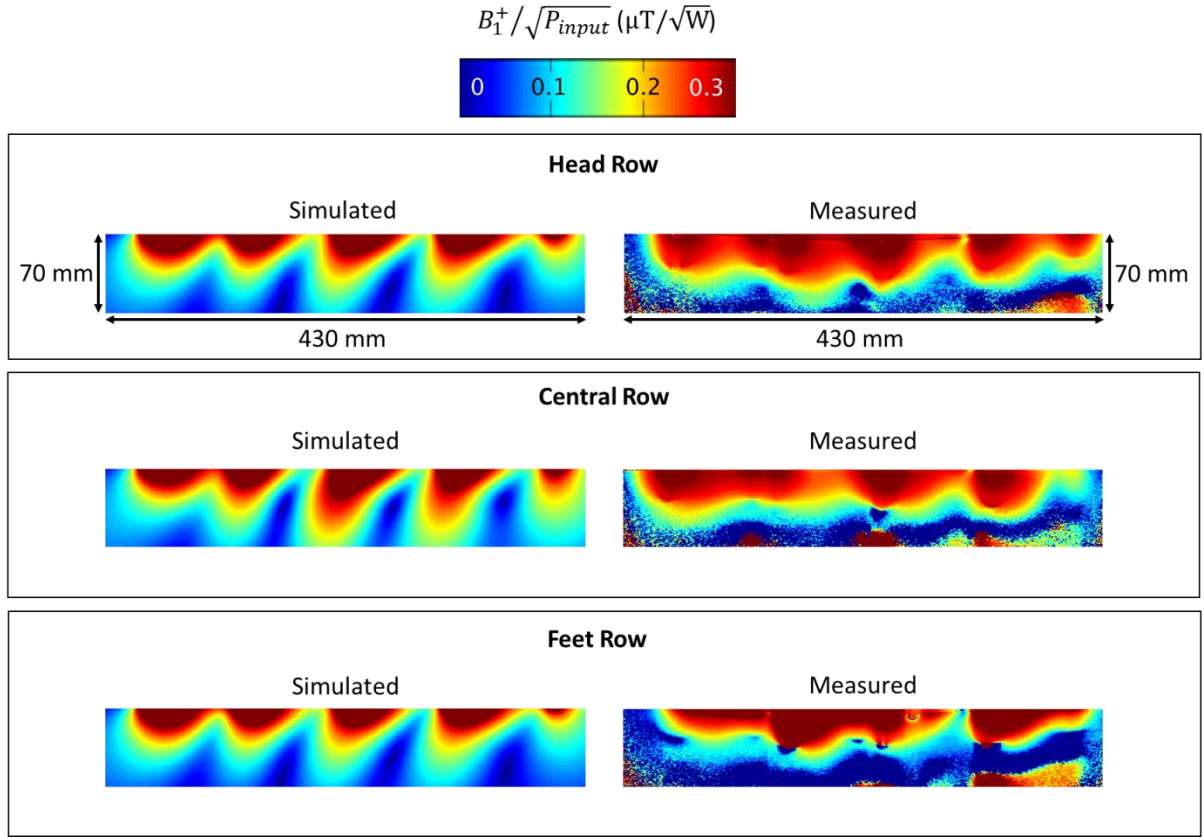


Figure 3.34: Transversal simulated and measured $B_1^+ / \sqrt{P_{input}}$ maps of each row of the developed array in flat configuration (box-shaped phantom).

Figure 3.35 shows the measured $B_1^+ / \sqrt{P_{input}}$ profiles of the developed array in bent configuration for the torso phantom when all of the elements were excited simultaneously. Table 3.5 provides the sequence parameters used for B_1^+ mapping of the array in bent configuration.

Table 3.5: Sequence parameters of B_1^+ mapping for the array in bent configuration (torso phantom).

Saturation flip angle	90°
Pulse Duration	0.35 ms
Pulse amplitude	429 V
Readout Flip Angle	2°
TR	10 s
Band Width	400 Hz/pixel
Field of View	384 × 264 mm ²
Acquisition Matrix	128 × 88 mm ²
Resolution	3 × 3 × 5 mm ³

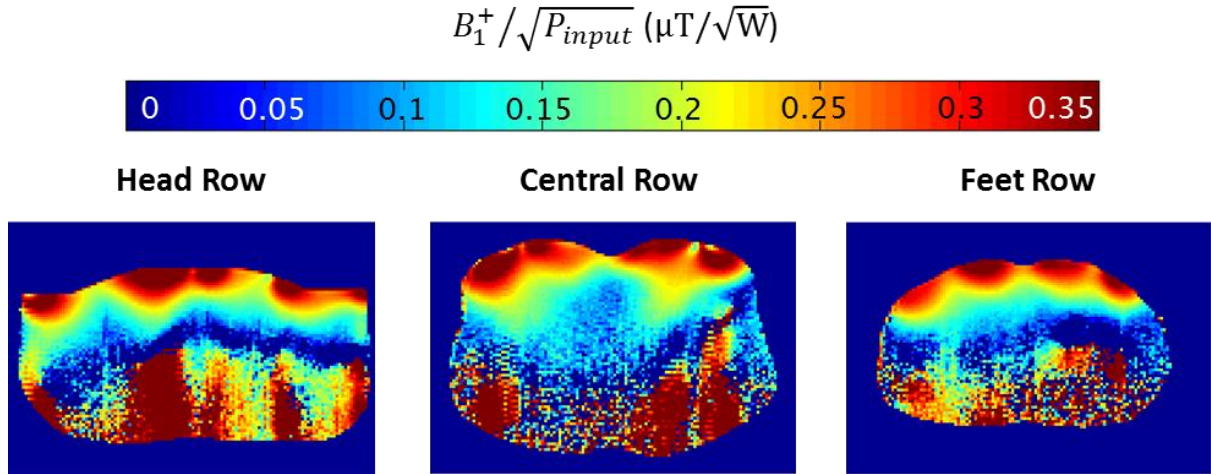


Figure 3.35: Measured $B_1^+ / \sqrt{P_{input}}$ of each row of the developed array in bent configuration for the torso phantom.

Obtained $B_1^+ / \sqrt{P_{input}}$ profiles of each row of the array in bent configuration are comparable to each other, although the bending of each row is slightly different according to the underlying anatomy. At the position of the heart in the central row of the array, rather low transmit efficiency is observed. This is attributed to a suboptimal phase setting for the bent

configuration, since the phases for static B_1^+ shimming could only be determined for the flat geometry, as described in section 3.3.2.

3.4.4 Array Performance in Terms of SAR

To evaluate the performance of the developed array in terms of SAR, 10 g averaged SAR patterns were derived from 3D EMS and calculated by SimOpTx toolbox (see section 2.6.3) for the array in flat configuration (box-shaped phantom, see section 3.1.1). Since SAR distribution is strongly dependent on the power amplitude and the phase of the individual elements, the evaluation was done for the three following different excitation case:

- As a starting point, all channels were driven with the same amplitude and phase as this is the simplest approach to excite an array.
- All channels were driven with the same amplitude but 90° phase difference between each column. This excitation vector corresponds to the optimal phase setting found for static B_1^+ shimming (see section 3.3.2).
- After the implementation of the phase setting obtained with static B_1^+ shimming and total loss evaluation of the measurement chain (see section 3.4.2), the real amplitude and phase of the delivered power to each element port was calculated.

Figure 3.36 provides the calculated 10 g averaged SAR distributions of the developed array in flat configuration for three different excitation modes. The maximum 10 g averaged SAR values for excitation with equal amplitude/phase, equal amplitude/ 90° phase difference between each column and calculated individual amplitude/phase based on the loss calculation are, 0.25 W/kg, 0.43 W/kg and 0.16 W/kg, respectively. The maximum 10 g averaged SAR value for the optimum excitation vector found by static B_1^+ shimming is reduced by 62 % when applying the calculated amplitude and phase of the delivered power to each element port due to the losses of the measurement chain (see section 3.4.2). Of course, this does not change the SAR per square root of power, if the power actually arriving at coil ports is considered.

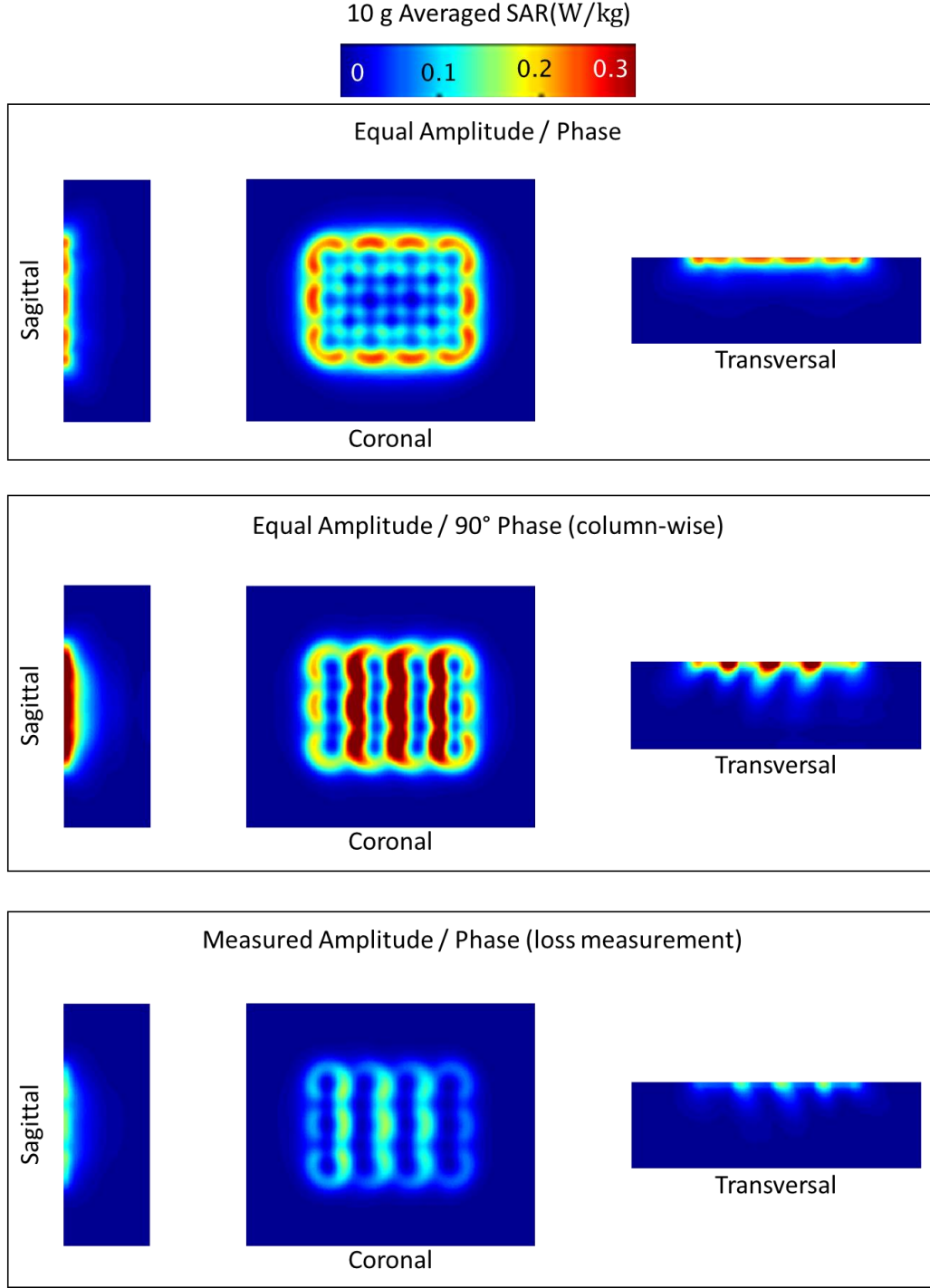


Figure 3.36: Calculated 10 g averaged SAR distributions of the 12-element TLR array in flat configuration (box-shaped phantom) for three different excitation cases. SAR values were normalized to 1 W input of power.

3.4.5 Noise Correlation and Parallel Imaging Performance

The parallel imaging (PI) performance of the developed array was evaluated in flat and bent configuration using pseudo-multiple replica technique (130) and off-line grappa reconstruction

method (131). To calculate the noise correlation matrix, noise-only data were acquired using an FID sequence without excitation. For the box-shaped (flat configuration) and torso (bent configuration) phantoms, fully-encoded 2D GRE images ($TR/TE = 427 \text{ ms}/3.76$, nominal flip angle of 10° , $1.16 \times 1.16 \text{ mm}^2$ nominal resolution and 5 mm slice thickness) were acquired by positioning three transversal slices in each row of the array (see Figure 3.18). In addition, for the box-shaped phantom coronal slices placed at distances of 2 and 4 cm from the coil plane were acquired. Reconstructed 2D images, SNR and g-factor maps were calculated for acceleration factors of $R = 1$ (no acceleration), $R = 2$, $R = 3$ and $R = 4$. Acceleration factors were mimicked during reconstruction by eliminating the phase encoding lines referred to as under sampling (see section 2.3.7). Based on equation (2.67), g-factor maps were calculated using SNR maps of a fully-encoded image and reconstructed images with different acceleration factors.

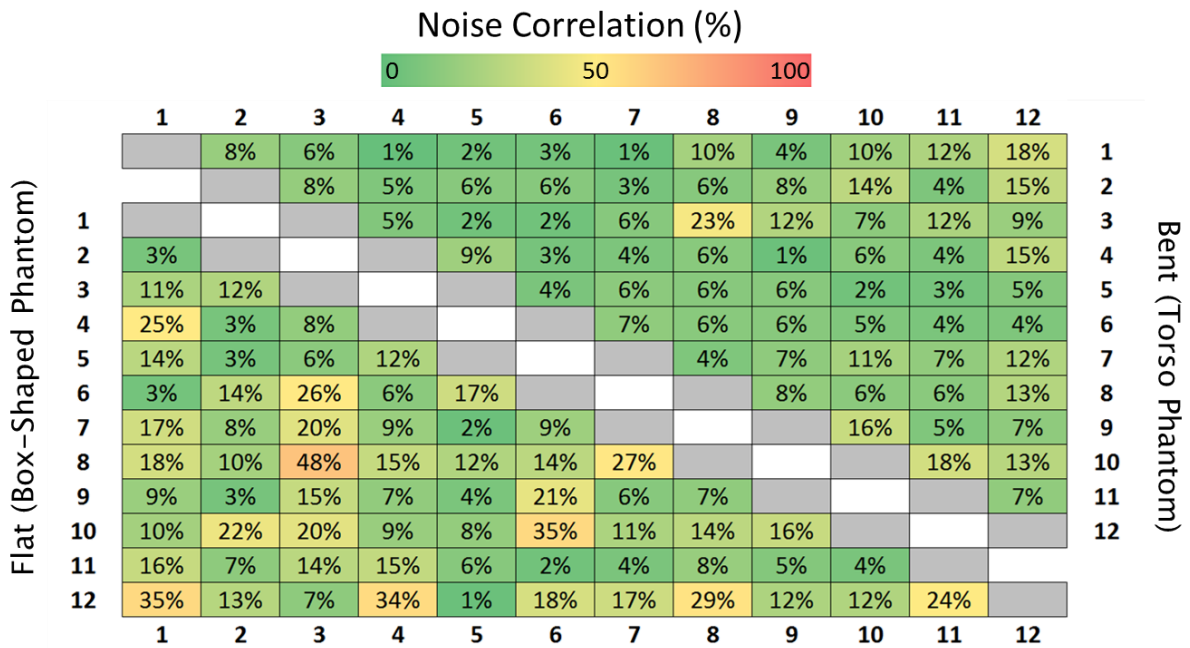


Figure 3.37: Noise correlation matrix for the developed array in flat (box-shaped phantom) and bent (torso phantom) configurations.

Figure 3.37 shows the calculated noise correlation matrix for the array in flat and bent configurations. It can be observed that for the array in flat configuration, noise correlation has a minimum of 1 % and a maximum of 48 %. The calculated noise correlation of the array in bent configuration, has a minimum of 1 % and a maximum of 23 %. It was observed that the noise correlation between elements 3 and 8 was significantly higher than all other values for

both flat and bent configuration. The reason for these outlier values is not known, but the noise correlation values are still in an acceptable range, as reported in many other studies in literature.

It was observed that the noise correlation is significantly decreased in bent configuration, which is counter-intuitive, because random charge movements within a conductive sample yield fluctuating magnetic dipoles which induce noise voltage in the coil elements which can be correlated (132) when the coil sensitivity profiles overlap. In bent configuration, an increase in noise correlation values would, therefore, be expected, since the coil profiles are expected to be more overlapped in comparison with the flat configuration. One explanation for the observed decrease in noise correlation for the bent array might be the rigid surface of the torso phantom onto which the array could not be perfectly conformed. This led to a larger coil-to-sample distance for some elements, resulting in a reduced noise correlation pathway, which might explain the generally lower noise correlation coefficients in the bent measurement.

The reconstructed MR images obtained by the developed array in flat (box-shaped phantom) and bent (torso phantom) configurations for different acceleration factors are provided in Figure 3.38. It can be observed that the image gets noisier by increasing the acceleration factor. The red square ($8\text{ cm} \times 6\text{ cm}$) assumed at depth of 2 cm from the phantom surface in the central row represents the heart assuming to be at the center of the array (see Figure 3.38).

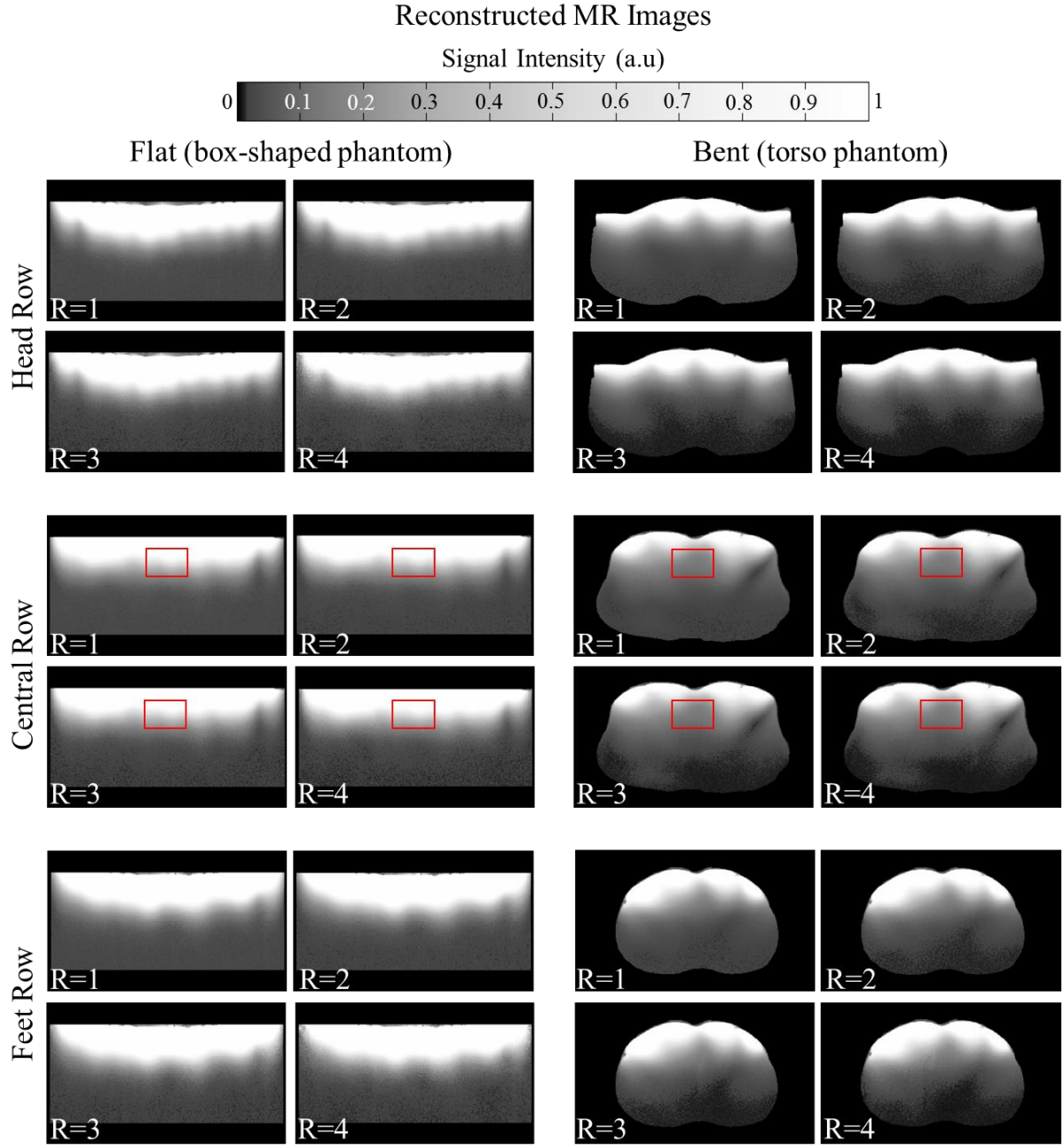


Figure 3.38: 2D transversal slices of the reconstructed MR images acquired with the developed array in flat (box-shaped phantom) and bent (torso phantom) configuration for different acceleration factors.

Figure 3.39 shows transversal reconstructed SNR maps for different acceleration factors obtained by the 12-element TLR array in flat and bent configurations. SNR reduction when increasing the acceleration factor can be observed (see equation (2.67)), the white box mimics the heart in central row slice. The mean values and the standard deviations of the calculated SNR for the defined ROI in the central row slice are 4000 ± 3000 ($R = 1$), 2400 ± 1700 ($R = 2$), 1700 ± 1100 ($R = 3$), 1100 ± 700 ($R = 4$) for the flat configuration and 1600 ± 800 ($R =$

1), 1100 ± 500 ($R = 2$), 800 ± 400 ($R = 3$), 700 ± 300 ($R = 4$) for the bent configuration, respectively.

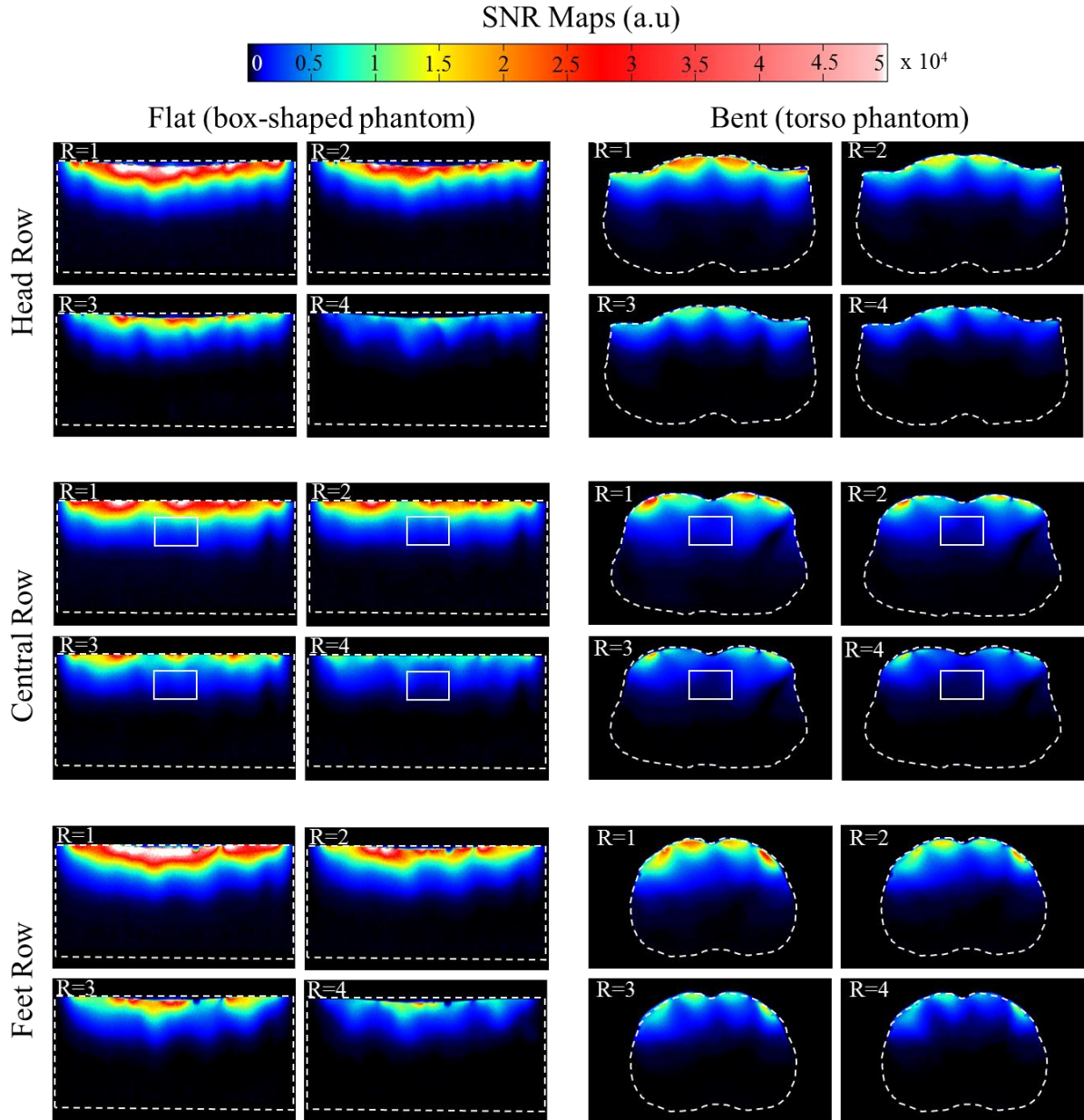


Figure 3.39: Reconstructed transversal SNR maps of the developed array in flat (box-shaped phantom) and bent (torso phantom) configurations for different acceleration factors.

In the bent configuration, acceleration factors up to 3 in left-right direction were possible without significant degradation in SNR, as could be expected from the geometry of the array with four elements in that orientation. SNR is expected to improve in case a solution for simulation of the optimal transmit phase setting in bent configuration can be found.

The calculated g-factor maps in flat and bent configurations for acceleration factors $R = 2$, $R = 3$ and $R = 4$ are presented in Figure 3.40. Mean values of the calculated g-factors for the defined ROI in the central row slice are 1.1 ± 0.1 ($R = 2$), 1.3 ± 0.2 ($R = 3$) and 1.6 ± 0.5 ($R = 4$) for the flat configuration and 1.0 ± 0.1 ($R = 2$), 1.1 ± 0.1 ($R = 3$) and 1.2 ± 0.2 ($R = 4$) for the bent configuration, respectively.

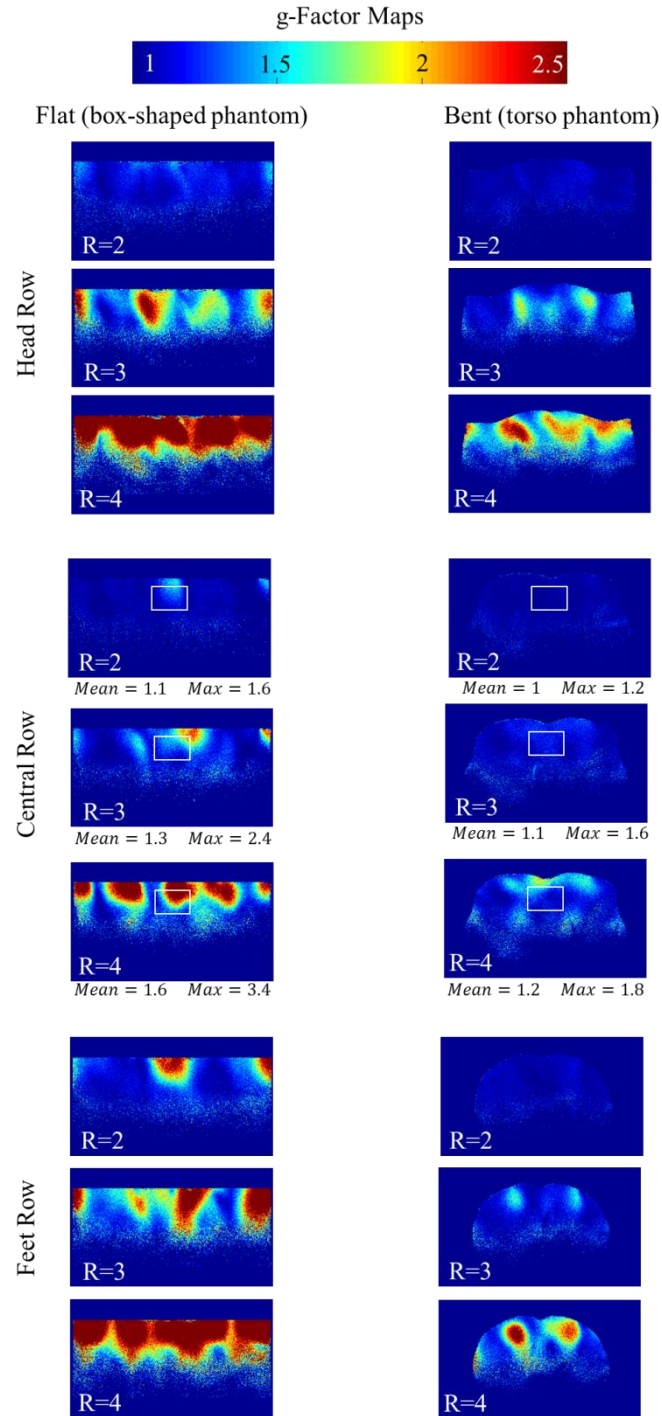


Figure 3.40: Calculated g-factor maps for the developed array in flat (box-shaped phantom) and bent (torso phantom) configurations for different acceleration factors.

In addition to the transversal slices, reconstructed GRE images and corresponding SNR and g-factor maps for coronal slices placed 2 and 4 cm from the coil plane in flat configuration (box-shaped phantom) were acquired and shown in Figure 3.41.

Mean values of the calculated g-factors for the defined ROI (12 cm \times 8 cm box, mimicking the heart) in the coronal slices (Figure 3.41) are 1.4 ± 0.2 (R = 2), 1.5 ± 0.3 (R = 3) and 2.5 ± 0.7 (R = 4) for the depicted slice placed 2 cm below the coil plane and 1.2 ± 0.1 (R = 2), 1.4 ± 0.2 (R = 3) and 1.8 ± 0.4 (R = 4) for the slice placed 4 cm below the coil plane.

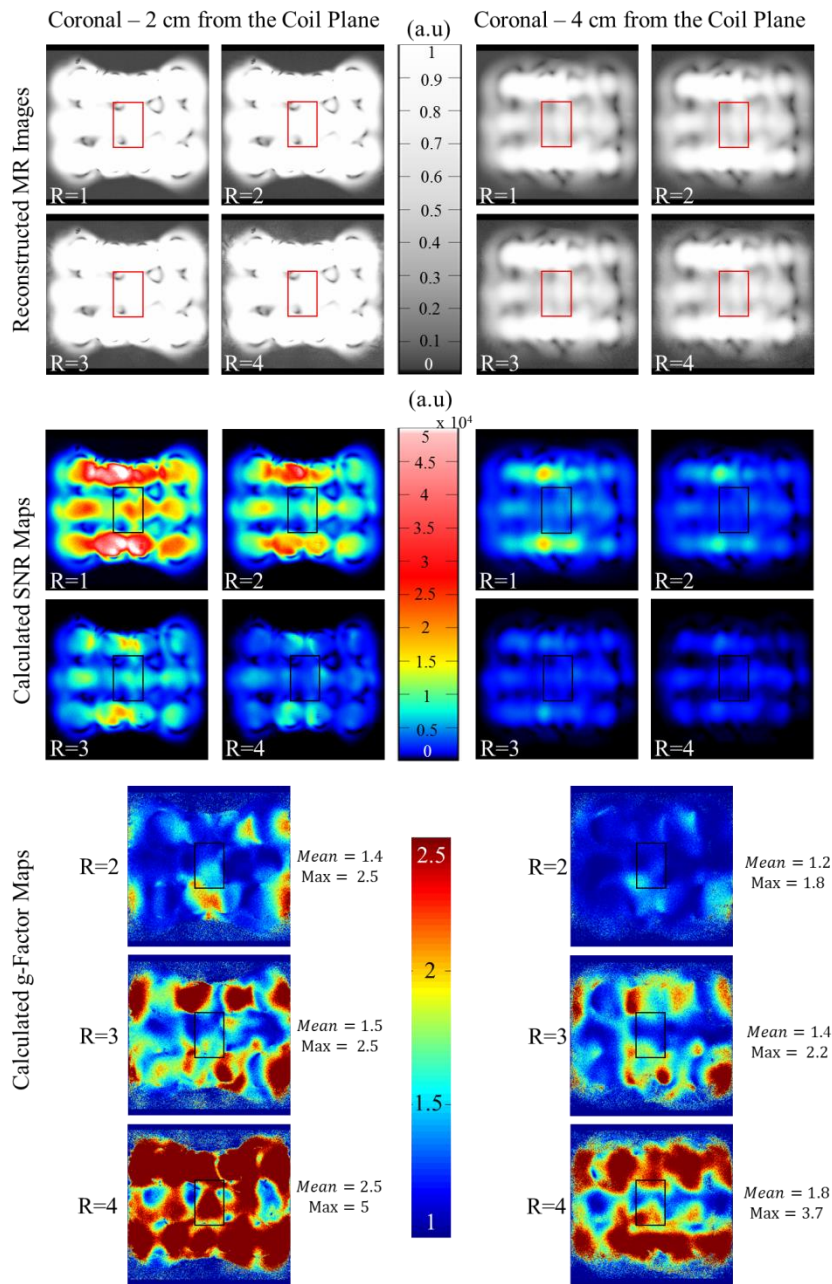


Figure 3.41: Reconstructed coronal GRE images and corresponding calculated SNR and g-factor maps acquired with the developed array in flat configuration using the box-shaped phantom. The presented slices are positioned 2 cm and 4 cm below the coil plane, respectively.

3.5 Conclusion and Summary

In this chapter, the development, implementation and testing a flexible 12-element TLR array for cardiac MRI at 7 T were presented.

An individual element of the array consists of a TLR surrounded by a decoupling ring with tuning and matching circuitry. The initial geometry of the TLR was optimized with respect to the penetration depth, FOV and loss mechanisms targeting cardiac MRI at 7 T. TLR geometry was finely adjusted together with capacitive matching network for Larmor frequency of 297.2 MHz (^1H at 7 T) using 3D EMS and circuit co-simulation resulting in a single turn TLR of 84 mm diameter (2 mm line width) with 4 gaps. In the next step, the size of the decoupling ring was optimized first by analytical modelling and then validated by 3D EMS by studying a 4-element TLR array. The obtained overlap level was 4.5 mm. The effects of the optimized decoupling ring on the performance of the TLR was studied by 3D EMS, bench and MR measurements. Induced shift (about 8 MHz) in the resonance frequency of the TLR due to the added decoupling ring can be accounted by the capacitive tuning and matching network. A slight increase in the $B_1^+/\sqrt{P_{\text{input}}}$ map close to the coil for the TLR with decoupling ring was observed, however, this effect became negligible at larger distances and $B_1^+/\sqrt{P_{\text{input}}}$ profile for both TLR with and without the decoupling ring were comparable. This can be attributed to the field-concentration effect of the decoupling ring. Due to the same effect, the maximum 10 g averaged SAR was increased (27 %) for TLR with the decoupling ring. No significant artefact was observed in the image quality of the TLR with decoupling ring, however the SNR was slightly increased (depth < 4 cm) due to the field-concentration effect of the decoupling ring.

A 3D EMS study was performed to compare the single element TLR optimized in this study with a conventional segmented loop of the same size. In this study, transmit efficiency ($B_1^+/\sqrt{P_{\text{input}}}$), E -field vector magnitudes and 10 g averaged SAR were evaluated for both the TLR and the segmented loop. Results demonstrated no significant difference in the performance of the TLR and the segmented loop.

The optimized individual element was used to fabricate a 12-element array. The array was fabricated on a flexible PCB (Polyamide) with rigid PCBs attached on the center of each element to place the interface component, i.e. transmit/receive switch, power splitter, pre-amplifier and capacitive tuning/matching circuitry. The power available at the coil sockets of the scanner was distributed to the individual elements of the array using power splitters. Before

cabling the array, a static B_1^+ shimming algorithm was used to determine the necessary phase shift between each column of the array in order to maximize the B_1^+ homogeneity. The performance of the array was evaluated by 3D EMS, bench and MR measurements in flat and bent configurations. Efficient decoupling was demonstrated for the developed array elements in flat ($S_{ij} < -19$ dB) and bent ($S_{ij} < -16$ dB) configurations. The amplitude and phase of the power delivered to each element port were calculated considering the total losses of the measurement chain. The simulation results were scaled using the calculated power amplitude and phase of the individual elements. The simulated and measured $B_1^+ / \sqrt{P_{\text{input}}}$ maps of the developed array in flat configuration were comparable. The performance of the array in terms of SAR was evaluated using 3D EMS by comparing three different excitation cases, i.e. equal amplitude/equal phase, equal amplitude/ 90° phase difference (between each column of the array) and the calculated amplitude and phase of the delivered power to each element port. Due to the losses within the measurement chain, the power amplitude for each element was reduced and the phase values measured on bench deviated slightly from those found by static B_1^+ shimming. Therefore, the maximum 10 g averaged SAR was the lowest (0.16 W/kg) when the array was excited using the calculated power amplitude and phase considering losses of the measurement chain. The parallel imaging performance of the developed array was investigated in flat and bent configurations. No significant degradation in parallel imaging performance of the array was observed due to the bending of the array. Furthermore, in bent configuration, acceleration factors of up to 3 was possible without significant degradation in SNR.

4 Discussion, Conclusions and Perspectives

4.1 Discussion

A flexible 12-element transceiver array for 7 T MRI based on TLRs was developed, implemented and tested using 3D EMS and experimental methods, i.e bench and MR measurements.

A single TLR and a conventional segmented loop of the same size were compared in this work, with no significant differences in B_1^+ , E-field, or SAR. However, the results of this comparison are only valid for the TLR geometry used in this thesis and may vary for different cases. Therefore, a dedicated study is needed to fully investigate and compare the performances of a TLR with a conventional loop of the same size.

An inter-element decoupling technique employing overlapped decoupling rings was investigated. For a single element with such a decoupling ring, a slight increase in quality factor, transmit efficiency, and SAR close to the coil was observed, as compared to a TLR without the decoupling ring. This can be interpreted as a field concentration effect caused by the decoupling ring. The decoupling ring may induce extra noise in the coil, however it was demonstrated that sample noise is still clearly the dominant noise mechanism, even with the decoupling ring.

In the investigated decoupling technique, diagonal elements cannot be overlapped for decoupling. Previously (90), decoupling between diagonal elements was not accounted for explicitly in the optimization of decoupling ring size. In this work, both nearest-neighbor and diagonal coupling were taken into account, resulting in sufficient and more uniform decoupling levels. The method was found to be robust against bending of the array. The decoupling ring-based technique can be optimized for any coil size and geometry using an analytical model (24). Furthermore, the use of overlapped decoupling rings retains the larger FOV of non-overlapped coils with distinct individual sensitivities that can potentially improve the parallel imaging performance (2,3). In addition, the decoupling ring-based technique is especially beneficial for TLR arrays allowing for scalability of such a design.

The performance of the developed flexible array was evaluated on bench and by MR experiments while the array was wrapped around a torso phantom. Measured scattering parameters, noise correlations, as well as SNR- and g-factor maps proved the robustness of the array versus bending. Parallel imaging performance matched the expected behavior with respect to the array geometry. In addition, acceleration could be done in two directions as the

developed array is two-dimensional, this can offer even more speed and reduce the noise amplification in parallel imaging in comparison with 1D cardiac arrays (27,30).

A good compromise between mechanical stability and flexibility could be achieved. With the introduced shape of the rigid parts of the substrate, bending is not limited to one bending axis only. This is especially beneficial for the two lateral elements in the most inferior row of the array, giving more degrees of freedom for coil to patient conformity. The good conformity to the patient ensures low variation in load and thus releaves the need for subject-specific tuning and matching, which may be necessary for CMR arrays with rigid housings and a low number of elements (29,133). The total weight of the coil array is 2.4 kg and is therefore light-weight enough for the use in patients.

A main limitation in this work is that 3D EMS of the array in bent configuration could not be performed due to the complexity of meshing and extremely long computation time with the simulation techniques as performed in this work (see section 3.1.1). This prevents the array from being used on humans for the moment, since SAR evaluation is an integral part of the required certification and testing process (see section 4.3.6). It also implies that an optimized static B_1^+ shim could only be calculated for the flat configuration. This means, that B_1^+ performance with the bent array is very likely suboptimal.

In comparison with existing CMR UHF arrays, the presented array potentially suffers from a limited coverage and penetration depth due to the lack of a posterior array (see section 4.3.3).

For now, the developed array was used with only one transmit channel and therefore only static B_1^+ shimming techniques could be applied. The potential of the developed array to be modified for use with parallel transmission systems is discussed in section 4.3.2.

The array in its current form can only be used for ^1H measurements. However, additional information could be gained from ^{31}P spectroscopy. With sufficient measurement sensitivity, it can provide the most direct and non-invasive measure of the heart's energy metabolism (134,135) highly related to cardiac dysfunction (136–138). The possibility of the integration of a ^{31}P array is discussed in section 4.3.1.

A well-known issue with conformal cardiac coils is the conformity to the female body due to the presence of the breasts. Even more flexible coil designs would be required to adapt to the variance in the population.

Induced eddy currents in the decoupling ring by the gradient coils were not investigated in this thesis. A potential solution to eliminate these currents could be to insert low-frequency-blocking capacitors in the decoupling rings. This way, the RF current could pass, while low frequency induced eddy currents would be blocked. However, this technique may impose limitations on the flexibility of the design due to the rigid solder joints.

4.2 Conclusions

In this thesis, TLR technology, decoupling rings, flexible-rigid PCBs, and innovative mechanical solutions were combined for the development of a mechanically flexible cardiac array for 7 T MRI with all interfacing circuitry positioned directly on the coils.

The flexibility enables coil conformity to patients with various sizes, increasing detection sensitivity in MR experiments. The properties of the coil have been shown to be robust against bending. The fabricated array is compatible with parallel imaging and pTx techniques yielding accelerated imaging and dynamic B_1^+ shimming.

4.3 Future Work

4.3.1 Integration of an additional ^{31}P array

The low inherent sensitivity of ^{31}P MRS prevents this method from being widely used in clinical routine, although it could provide direct quantitative measurement of tissue health and biomarkers. The following technologies can considerably improve the sensitivity of ^{31}P :

- Working at UHF intrinsically increases magnetization and, thus, the achievable SNR.
- Simultaneous proton MRI and ^{31}P MRS allowing for accurate localization and efficient sampling, resulting in an increase in spectral quality, SNR and tissue selection accuracy.
- The use of flexible coil arrays giving access to parallel imaging and parallel transmission methods, resulting in reduced acquisition times and improved SNR.

Therefore, a combined flexible $^1\text{H}/^{31}\text{P}$ array would be desirable to improve sensitivity, image quality and utility of ^{31}P MRs for clinical research as well as diagnostics.

Future work aims at integrating a ^{31}P array inside the housing of the ^1H array developed in this thesis. Decoupling of the ^{31}P array, avoiding cross-talk between the two arrays and preserving

the flexibility of the ^1H array while implementing ^{31}P , are the most important challenges for such a combined design.

^{31}P array elements could be fabricated using copper wires and the mutual flux between individual elements could be minimized using conventional decoupling techniques as presented in section 2.4.2.3.1. By making slits in the bottom part of the housings (see Figure 3.22), flexible wire segments of the ^{31}P array could connect the coil from one housing to the other. The necessary interfaces for ^{31}P elements, such as tune and match circuitry, transmit/receive switches, and preamplifiers can be placed in the bottom part of the housings and also on the interface boards of the head and feet row of the ^1H array, as there is some space left due to the absence of 1:3 power splitters.

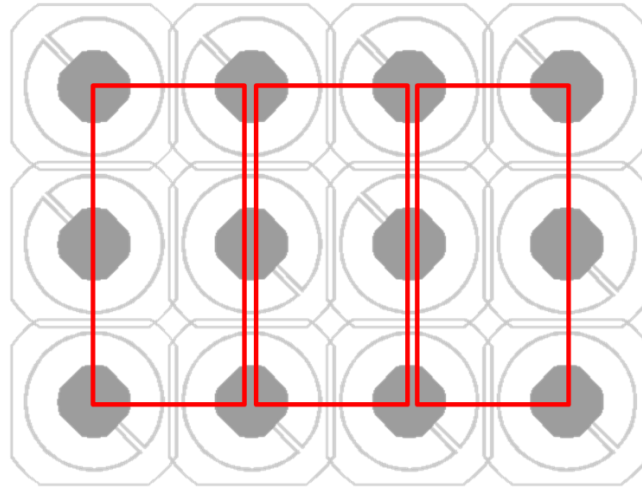


Figure 4.1: Schematic of the suggested combined ^1H / ^{31}P array. The red rectangular elements represent the ^{31}P individual elements.

To avoid interactions (139) between ^1H and ^{31}P arrays, LC (95) and/or LCC traps (135) could be inserted into the ^{31}P elements to block the current at ^1H frequency (i.e. 300 MHz) while allowing the ^{31}P elements to resonate at the corresponding resonance frequency (i.e. 120 MHz).

4.3.2 Compatibility with parallel transmission systems

pTx systems enable dynamic B_1^+ shimming, allowing for exciting array elements with time-dependent individual RF pulse amplitude and phase to, for example, achieve a uniform B_1^+ field. In view of using the array with a pTx system, the design of the developed array can be adapted with slight modifications of its interface and cabling. One possibility would be to modify the array for use with 4 pTx channels as follows: the 1:4 power splitter (see Figure 3.21)

would be removed and the central elements would be connected to the 4 channels of a pTx system, which gives the possibility of driving them with individual pulse amplitudes and phases. The power delivered from the central elements would be distributed to the elements within each column using the currently implemented 1:3 power splitters in the interface boards of the central row elements (see Figure 3.23).

To use the array for parallel transmission (140), the individual RF pulse amplitude and phase should be pre-calculated based on the target profile, knowledge of the transmit profile of each coil and knowledge of the gradient trajectory (58). In parallel transmission, individual RF pulses affect the SAR distribution as the *E*-field (which governs SAR distribution) is superimposed among array elements (58). This can result in changing the SAR hot spot location and intensity when changing the RF pulse amplitude and phase of the individual elements. Therefore, the SAR information should be included in the RF pulse calculation in order to avoid exceeding the local SAR limits. The local SAR can be estimated with the knowledge of the *E*-field which can be provided by 3D EMS of body models.

4.3.3 Improvement of coverage

Another envisioned perspective is to increase the number of channels, by developing another ^1H array that will be placed on the back of the human torso. This would allow to extend the coverage of the array with improved transmit efficiency and receive sensitivity in depth resulting in a high SNR image of the whole torso. However, one has to take into account that the total available power in this case would be divided between the anterior and posterior array which may result in too long pulses for a given flip angle, restricted by the available power from the RF power amplifier(s).

Using different types of coil elements such as radiative elements, e.g. dipole antennas could be beneficial to improve penetration depth as the Poynting vector for such structures is perpendicular to the coil axis. Instead of designing a posterior array, one could design another anterior array with dipole elements to benefit from the penetration depth of dipole antennas and high SNR of the loop coils simultaneously. This way the transmit efficiency in the heart might be improved from the anterior side and the risk of wasting available transmit power without significant improvement (by a posterior array could be reduced).

4.3.4 EM Simulation Methods for bent TLRs

The 3D EMS of TLRs in bent configuration was not possible due to complexity of meshing structure and subsequently significantly large computation time (see section 3.1.1). This is mandatory to optimize the phases for static B_1^+ shimming and accurate SAR evaluation for pre-defined human voxel models.

4.3.4.1 Simulation in parts

A possible strategy is to bend only the side columns of the array and simulate these two and the central two columns separately. The tilted columns should be rotated back together with the torso voxel model so that the setup would be in the initial (horizontal) grid plane as shown in Figure 4.2. This way the array elements can be mimicked in bent configuration without changing the grid plane and increasing the number of mesh cells. The results can be rotated and regridded in post-processing combine the three performed simulations (see Figure 4.2). The following 3 simulations should be performed:

1. Separate simulation of the 1st column with clock-wise rotated torso phantom and coil.
2. Simulation of the two central columns, in this case the body is not rotated assuming the position of these elements remains the same for both and flat configurations (see Figure 4.2).
3. Separate simulations of the 4th column with counter clock-wise rotated torso phantom and coil.

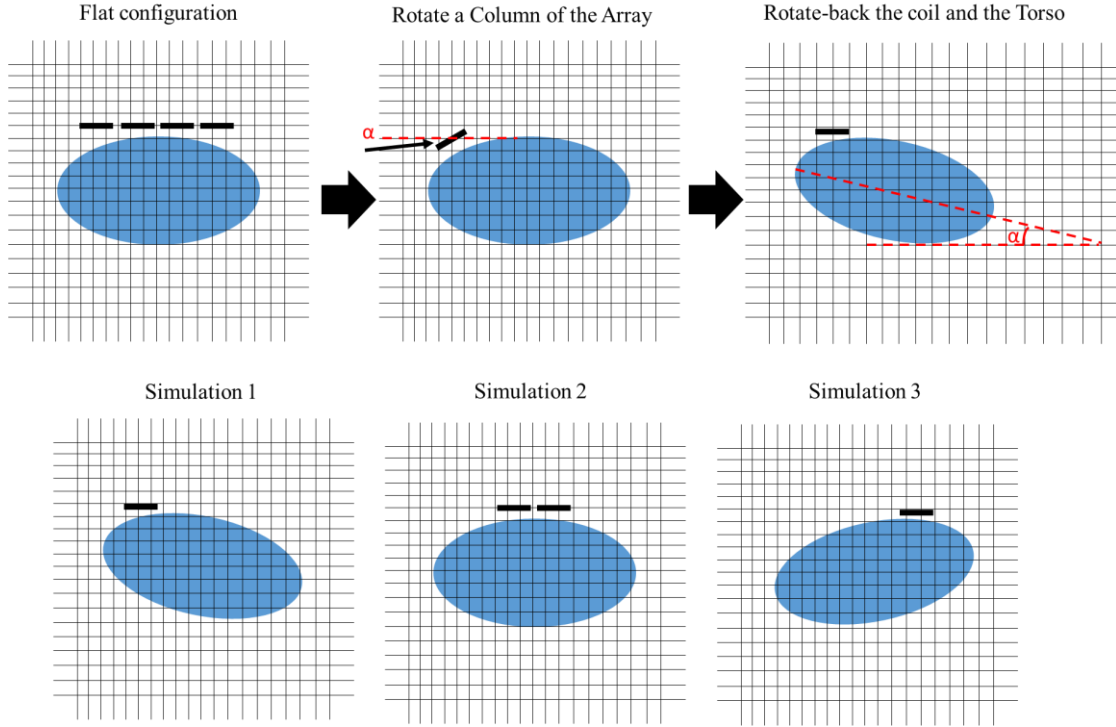


Figure 4.2: Proposed solution for simulation of the TLR array in bent configuration.

The limitation of this technique is that coupling between the elements in the three simulation runs are neglected. However, the decoupling technique used in this thesis is robust against bending (see section 3.4.1).

4.3.4.2 Advanced gridding techniques

Another approach could be to use other software packages such as the multilevel subgridding scheme (MSS) in CST (141) software package as shown in figure. This meshing algorithm ensures a very dense mesh in the critical regions of the simulation space, e.g. the regions where the conductor is bent. Using MSS can reduce the total number of mesh cells, however this approach is efficient only when the number of mesh cells is decreased by a factor of 3-5 (141).

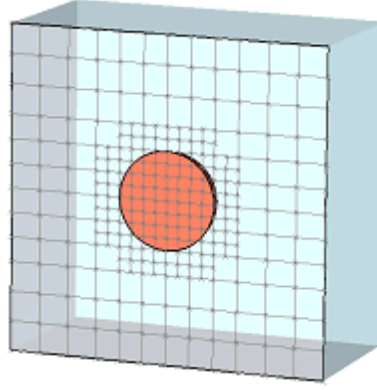


Figure 4.3: multilevel subgridding mesh (MSS) (141).

4.3.5 MR Thermometry

In case the suggested solutions for simulation of bent TLRs mentioned in the previous section can not be applied, one can derive the SAR map directly from the temperature mapping. As long as heat conduction is negligible, the relationship between SAR and temperature change in the sample is given by (142)

$$c \frac{\Delta T}{\Delta t} = \text{SAR} \quad (4.1)$$

where c is the heat capacity constant of the sample, ΔT denotes the temperature change in K and Δt is the time interval. The absolute temperature inside the sample can be measured by inserting non-magnetic fiber optic probes (100). The limitation of this approach is that it can only be used for phantoms. Among the available techniques for temperature mapping, proton resonance frequency (PRF) method is widely used for many application at mid or high field (≥ 1 T) due to its linearity and near-independence with respect to the tissue type (143,144). In this method changes in phase due to the temperature-dependent variations in resonance frequency are measured using the spoiled GRE imaging.

4.3.6 Certification for In Vivo Usage

The final aim for developing the array is to provide an improved tool for clinical or pre-clinical CMRI i.e. to be used on patients or volunteers. RF coils with a transmit part are medical electrical devices of class IIa, according to the EU directive 92/42/EG. To fulfil the criteria set forth in this directive, one has to meet the requirements of the following harmonized standards:

- IEC 60601-1 (Medical electrical equipment - Part 1: General requirements for basic safety and essential performance) (145).
- ISO 14971 (Medical devices - Application of risk management to medical devices) (146).

An additional standard that applies is

- IEC 60601-2-33 (Medical electrical equipment - Part 2-33: Particular requirements for the basic safety and essential performance of magnetic resonance equipment for medical diagnosis) (105).

To fulfil the requirements of these standards, a variety of tests is necessary, in addition to SAR evaluation mentioned previously, so as to ensure patient safety and full functionality of the device during MRI experiments.

Performing the above tests is beyond the scope of this thesis but it is scheduled for following up projects.

A. Appendix

A.1 Analytical model of TLRs

Step by step derivation of the resonance condition for TLRs (see equation (2.95)) is explained in the following sections (19,147).

A.1.1 Description of the Resonator

The basic geometry of the TLR is composed of two conductor deposited on both sides of a dielectric substrate that can be considered as circularly shaped transmission lines. Each conductor is intersected with one or more gaps which the number of gaps is equal for both conductor on bottom and top side of the substrate. The gaps are positioned alternately along both conductors in a way that the gap on one side is positioned in the middle of the conductor section on the other side. This way, the TLR can be represented as sequence of segments shown in Figure A.1.

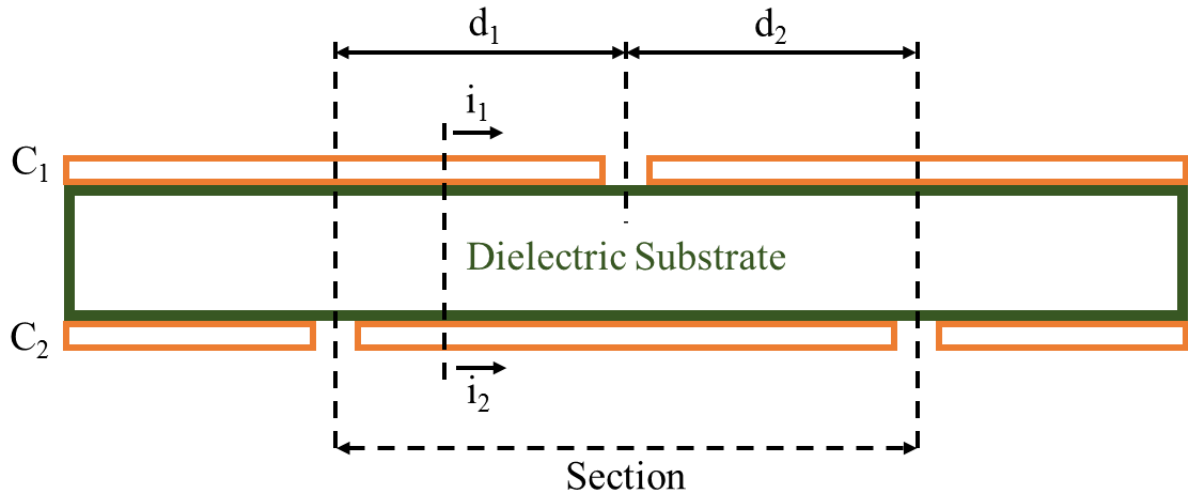


Figure A.1: TLR segmentation.

Considering currents i_1 and i_2 at a given position in the two conductors C_1 and C_2 , the differential current i_D and common mode current i_C can be defined as

$$i_D = \frac{i_1 - i_2}{2} \text{ and } i_C = \frac{i_1 + i_2}{2} \quad (\text{A.1})$$

$$i_1 = i_D + i_C \text{ and } i_2 = i_C - i_D \quad (\text{A.2})$$

The differential mode current does not create a magnetic field outside the transmission line and depends on the properties of the transmission line such as inductance, capacitance and propagation constant β . Also differential mode current depends on the position along the transmission line. In contrast, common mode current is responsible for creation of the magnetic field like the current flowing in a conventional loop. This current is intrinsically constant even if the size of rings is comparable to the wavelength (18,19).

The boundary conditions for the differential and common mode currents at conductor intersections (see Figure A.1) are

$$\text{for } C_1: i_1 = 0 \text{ and therefore } i_C = -i_D \quad (\text{A.3})$$

$$\text{for } C_2: i_2 = 0 \text{ and therefore } i_C = i_D \quad (\text{A.4})$$

A.1.2 Differential mode

$v(x)$ is the voltage across the line, i.e. between bottom and top conductors at position x and V_p denotes the voltage across a certain plan e.g. 4n (see Figure A.2), accordingly, the differential current is denoted by $i_D(x)$ and i_{Dp} . The symbol j is the imaginary unit.

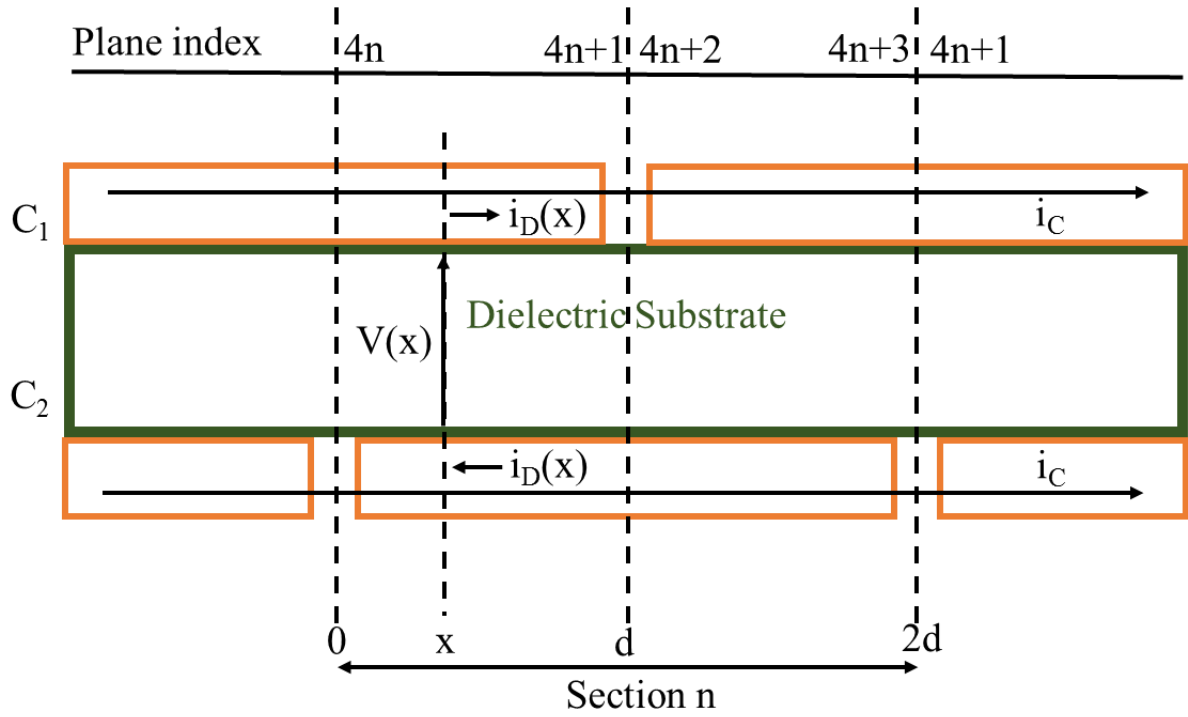


Figure A.2: Plane sections along the transmission line.

To simplify the equations, following equivalent parameters are used

$$\varsigma_D = Z_0 i_D \text{ and } \varsigma_C = Z_C i_C \quad (\text{A.5})$$

The telegrapher's equations for the voltage and current along the transmission lines are given by (19)

$$v(x) = v(0) \cos(\beta x) - j \varsigma(0) \sin(\beta x) \quad (\text{A.6})$$

$$\varsigma(x) = \varsigma(0) \cos(\beta x) - j v(0) \sin(\beta x) \quad (\text{A.7})$$

where propagation constant is given by

$$\beta = \frac{2\pi}{\lambda} = \frac{2\pi f \sqrt{\epsilon}}{c} \quad (\text{A.8})$$

with the boundary condition

$$i_2 = 0 \text{ at } x = 0 \xrightarrow{\text{yields}} \varsigma_{D4n} = \varsigma_C \quad (\text{A.9})$$

$$i_1 = 0 \text{ at } x = d \xrightarrow{\text{yields}} \varsigma_{D4n+1} = -\varsigma_C \quad (\text{A.10})$$

which at $x = d$

$$\varsigma_{D4n+1} = \varsigma_C \cos(\beta d) - jv_{4n} \sin(\beta d) \quad (\text{A.11})$$

Combining equations (A.10) and (A.11), the following expression for the voltage along the plane $4n$ at $x = 0$ can be obtained

$$v_{4n} = -j\varsigma_C \frac{1 + \cos(\beta d)}{\sin(\beta d)} = -j\varsigma_C \cot\left(\frac{\beta d}{2}\right) = U \quad (\text{A.12})$$

Substituting equation (A.12) in the equations (A.9) and (A.10), we have

$$v_{4n+3} = v_{4n+2} = -v_{4n} = -v_{4n+1} = j\varsigma_C \cot\left(\frac{\beta d}{2}\right) \quad (\text{A.13})$$

$$\varsigma_{D4n+3} = -\varsigma_{D4n+2} = -\varsigma_{D4n+1} = -\varsigma_{D4n} = \varsigma_C \quad (\text{A.14})$$

Figure A.3 demonstrates voltages and currents in the transmission line according to this derivation. This way the voltage across the gap is given by $u_g = 2U$.

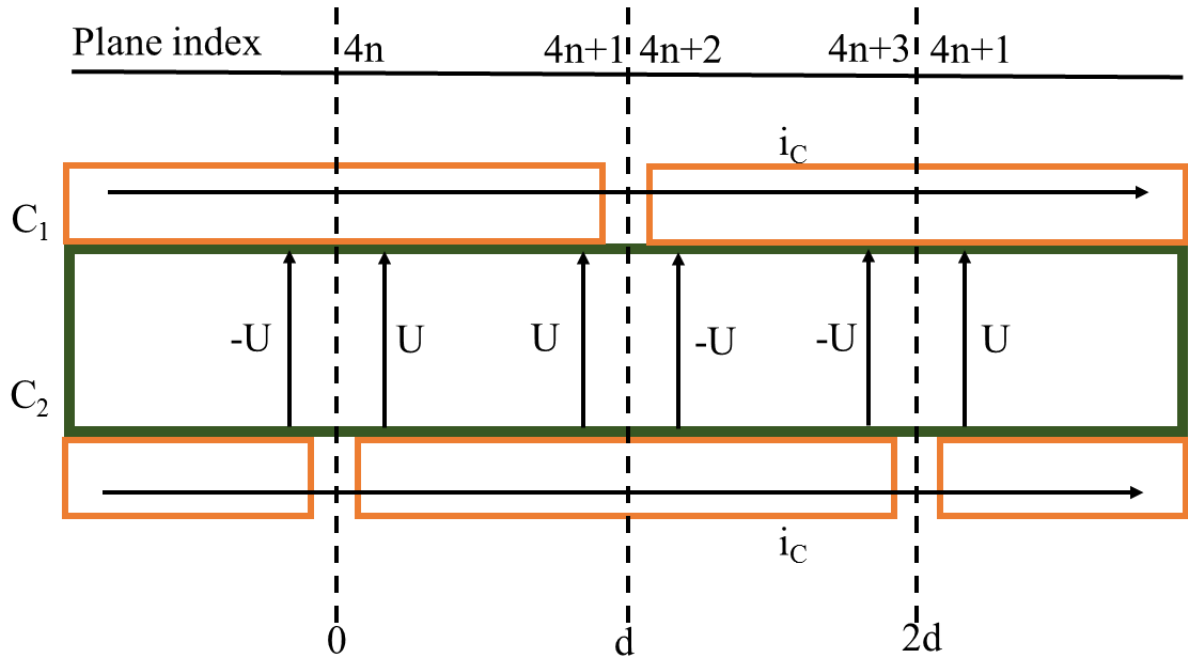


Figure A.3: Voltages and currents along the transmission line.

A.1.3 Common mode

Figure A.4 shows a single turn TLR with two gaps. The magnetic field is created by the common mode current while the differential mode current does not interact with the surrounding of the resonator.

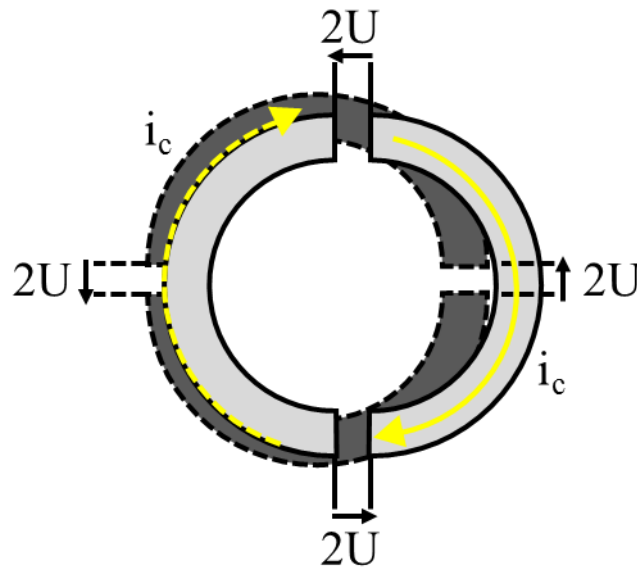


Figure A.4: Single turn TLR with two gaps seen from an external point of view.

The corresponding equivalent electrical circuit based on the Kirchhoff's laws is represented in Figure A.5. This way TLR can be seen as two circular loop coupled to each other where L_1 and L_2 are inductances of the conductors C_1 and C_2 and M is their mutual inductance.

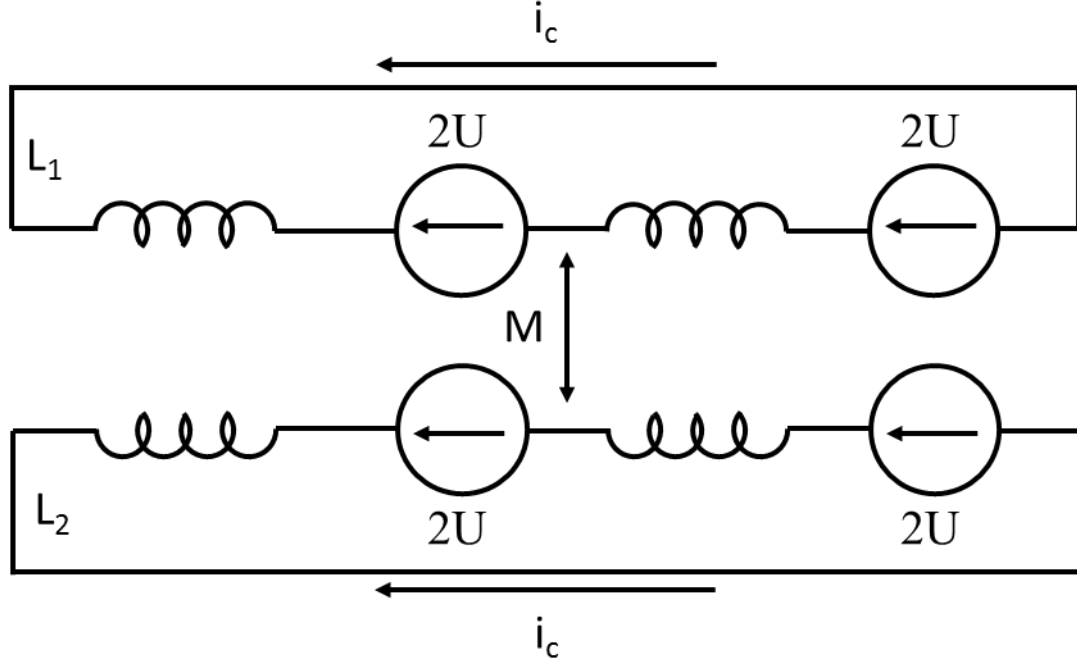


Figure A.5: Equivalent circuit for TLR based on the quasi-static approximation.

In order to have the same common mode current i_c , the two conductors should be in series with each other. For this, it is necessary to calculate the total inductance L_{tot} of the resonator.

$$L_{tot} = L_1 + L_2 + 2M \quad (A.15)$$

where the equation for self and mutual inductances are given in the section A.1.5.

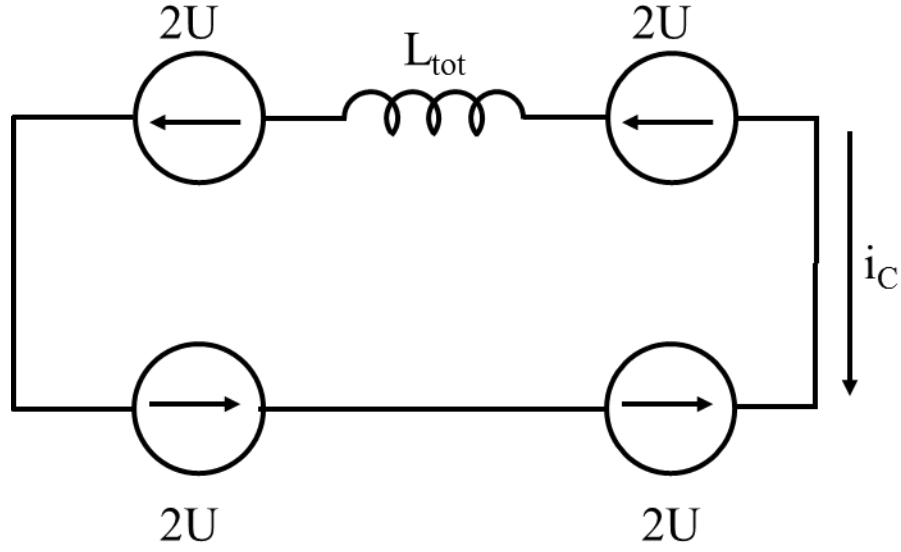


Figure A.6: TLR equivalent electrical circuit with total inductance L_{tot} .

Figure A.6 shows the closed equivalent circuit of single turn TLR with two gaps (Figure A.4). Based on the Kirchhoff's voltage law, for a closed circuit composed of N_g section (N_g number of gaps) with angular frequency ω_0

$$jL_{tot}\omega_0 i_C + 4N_g U = 0 \quad (\text{A.16})$$

A.1.4 Resonance Condition

By combining equations (A.13) and (A.16), the implicit expression for the resonance condition can be obtained,

$$jL_{\text{tot}}\omega_0 i_C - j4N_g Z_0 i_C \cot\left(\frac{\beta d}{2}\right) = 0 \quad (\text{A.17})$$

$$L_{\text{tot}}\omega_0 - 4N_g Z_0 \cot\left(\frac{\beta d}{2}\right) = 0, \text{ for } i_C \neq 0 \quad (\text{A.18})$$

$$\frac{L_{\text{tot}}\omega_0}{4N_g Z_0} \tan\left(\frac{\beta d}{2}\right) = 1 \quad (\text{A.19})$$

With the total length of the transmission line $l_f = 2dN_g$ equation (A.19) becomes,

$$\frac{L_{\text{tot}}\omega_0}{4N_g Z_0} \tan\left(\frac{\beta l_f}{4N_g}\right) = 1 \quad (\text{A.20})$$

Combining equations (A.20) and (A.8) give the final form of the resonance condition for TLRs.

$$\frac{L_{\text{tot}}\omega_0}{4N_g Z_0} \tan\left(\frac{\omega_0 \sqrt{\epsilon} l_f}{4N_g c}\right) = 1 \quad (\text{A.21})$$

A.1.5 Inductance equations

The self inductance of a circular loop with mean radius r and width w can be calculated using the following expression (81)

$$L_i = \frac{4r_i}{\mu_0} \left[\ln\left(\frac{8r_i}{w}\right) - \frac{1}{2} + \frac{w^2}{96r_i^2} \left(\ln\left(\frac{8r_i}{w}\right) + \frac{43}{12} \right) \right] \quad (\text{A.22})$$

The mutual inductance M between two circular loops with both lateral and angular misalignments can be calculated by a method based on the filaments which has been proposed by Grover et al (148). In this method, coils are replaced by infinitesimal filaments. For the

special condition of no angular misalignment, the initial equation can be simplified to the following equations

$$M_{ij} = \frac{2\mu_0}{\pi} \sqrt{r_i r_j} \int_0^\pi \frac{\left(1 - \frac{d}{r_j} \cos \varphi\right) \Psi(k)}{k\sqrt{V^3}} d\varphi \quad (\text{A.23})$$

$$V = \sqrt{1 + \frac{d^2}{r_i^2} - 2\frac{d}{r_j} \cos \varphi} \quad (\text{A.24})$$

$$k^2 = \frac{4V \frac{r_j}{r_i}}{\left(1 + V \frac{r_j}{r_i}\right)^2 + \frac{a^2}{r_i^2}} \quad (\text{A.25})$$

$$\Psi(k) = \left(1 - \frac{k^2}{2}\right) K[k] - E[k] \quad (\text{A.26})$$

$K[k]$ and $E[k]$ are the complete elliptic integrals of first and second kind

$$K[k] = \int_0^\pi \frac{1}{\sqrt{1 - k^2 \sin^2 \theta}} d\theta \quad \text{and} \quad E[k] = \int_0^\pi \sqrt{1 - k^2 \sin^2 \theta} d\theta \quad (\text{A.27})$$

where r_i and r_j are coil radiuses, a and d are vertical and horizontal displacement between coil centres, respectively. For a single TLR, the horizontal distance displacement d can be set to zero since conductors on both sides of the substrate are coaxially aligned.

A.1.6 Characteristic Impedance

The characteristic impedance for a parallel plate transmission line (see Figure A.7) can be calculated based on the semi-empirical models using the following equations

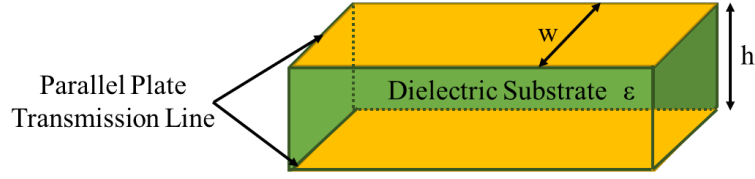


Figure A.7: Parallel plate transmission line.

with band approximation ($w > h$):

$$Z_0 = \frac{120\pi}{\sqrt{\epsilon}} \left[\frac{w}{h} + 0.441 + \frac{\epsilon + 1}{2\pi\epsilon} \left(\ln \left(\frac{w}{h} + 0.94 \right) + 1.452 \right) + 0.082 \frac{\epsilon - 1}{\epsilon^2} \right]^{-1} \quad (\text{A.28})$$

With narrow band approximation ($w < h$):

$$Z_0 = 120\pi \sqrt{\frac{2}{\epsilon + 1}} \left[\ln \left(\frac{4w}{h} \right) + \frac{1}{8} \left(\frac{w}{h} \right)^2 - \frac{\epsilon - 1}{2(\epsilon + 1)} \left(0.451 + \frac{0.241}{\epsilon} \right) \right] \quad (\text{A.29})$$

where w is the width of the conductor, h and ϵ are the thickness and permittivity of the substrate, respectively.

A.2 Analytical Model for Decoupling Optimization of Decoupling Rings

The following analytical model for decoupling optimization is based on the original model available in the PhD thesis of Zhoujian Li (24).

Figure A.8 shows a 4-element TLR array where decoupling rings of the nearest neighbours are deposited on both sides of the substrate for overlapping.

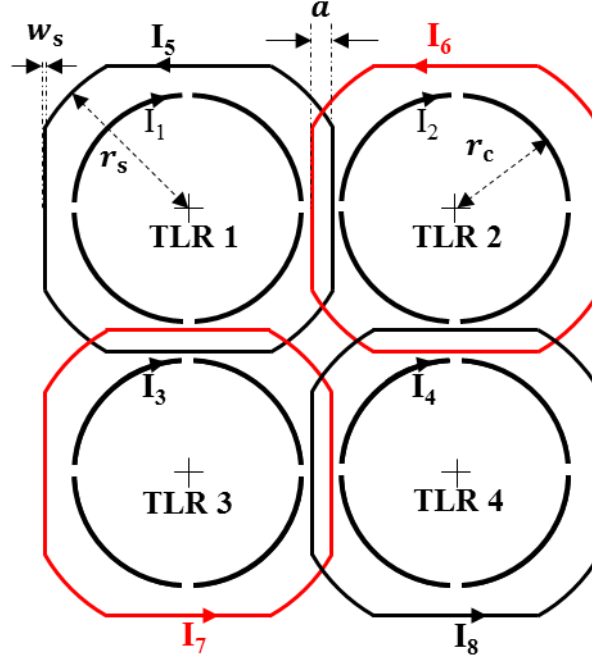


Figure A.8: 4-element array of TLRs with overlapped decoupling rings.

Let I_1 be the source current in the TLR 1 (the source current can be assigned to each of the 4 elements within the array shown in Figure A.8). This way, I_2 , I_3 and I_4 are the induced currents in the TLR 2, TLR 3 and TLR 4, respectively. Accordingly, I_5 , I_6 , I_7 and I_8 represent the induced currents in the decoupling rings as shown in Figure A.8.

Using the total magnetic flux theory for each element, the following system of equations are obtained,

$$\begin{cases} L_2 I_2 = |M_{21}|I_1 + |M_{23}|I_3 + |M_{24}|I_4 - |M_{25}|I_5 + |M_{26}|I_6 - |M_{27}|I_7 - |M_{28}|I_8 \\ L_3 I_3 = |M_{31}|I_1 + |M_{32}|I_2 + |M_{34}|I_4 - |M_{35}|I_5 - |M_{36}|I_6 + |M_{37}|I_7 - |M_{38}|I_8 \\ L_4 I_4 = |M_{41}|I_1 + |M_{42}|I_2 + |M_{43}|I_3 - |M_{45}|I_5 - |M_{46}|I_6 - |M_{47}|I_7 + |M_{48}|I_8 \\ L_5 I_5 = |M_{51}|I_1 - |M_{52}|I_2 - |M_{53}|I_3 - |M_{54}|I_4 + |M_{56}|I_6 + |M_{57}|I_7 + |M_{58}|I_8 \\ L_6 I_6 = -|M_{61}|I_1 + |M_{62}|I_2 - |M_{63}|I_3 - |M_{64}|I_4 + |M_{65}|I_5 + |M_{67}|I_7 + |M_{68}|I_8 \\ L_7 I_7 = -|M_{71}|I_1 - |M_{72}|I_2 + |M_{73}|I_3 - |M_{74}|I_4 + |M_{75}|I_5 + |M_{76}|I_6 + |M_{78}|I_8 \\ L_8 I_8 = -|M_{81}|I_1 - |M_{82}|I_2 - |M_{83}|I_3 + |M_{84}|I_4 + |M_{85}|I_5 + |M_{86}|I_6 + |M_{87}|I_7 \end{cases} \quad (\text{A.30})$$

By assigning a constant value to the I_1 and using equation (A.30), all of the unknown currents can be calculated as

$$\left\{ \begin{array}{l} I_1 = I_1 \\ I_2 = I_3 = -\frac{J_1 L_2 - J_2 L_1}{K_1 L_2 - K_2 L_1} I_1 \\ I_4 = -\frac{J_1 K_2 - J_2 K_1}{L_1 K_2 - L_2 K_1} I_1 \\ I_5 = -\frac{P_1}{S_1} I_1 - \frac{Q_1}{S_1} I_2 - \frac{R_1}{S_1} I_4 \\ I_6 = I_7 = -\frac{A_1}{E_1} I_1 - \frac{B_1}{E_1} I_2 - \frac{C_1}{E_1} I_4 - \frac{D_1}{E_1} I_5 \\ I_8 = \frac{|M_{21}|}{|M_{28}|} I_1 - \frac{L_2 - |M_{23}|}{|M_{28}|} I_2 + \frac{|M_{24}|}{|M_{28}|} I_4 - \frac{|M_{25}|}{|M_{28}|} I_5 + \frac{|M_{26}| - |M_{27}|}{|M_{28}|} I_6 \end{array} \right. \quad (\text{A.31})$$

with

$$J_1 = P_1 S_2 - P_2 S_1; J_2 = P_2 S_3 - P_3 S_2$$

$$K_1 = Q_1 S_2 - Q_2 S_1; K_2 = Q_2 S_3 - Q_3 S_2$$

$$L_1 = R_1 S_2 - R_2 S_1; L_2 = R_2 S_3 - R_3 S_2$$

$$P_1 = A_1 E_2 - A_2 E_1; P_2 = A_2 E_3 - A_3 E_2; P_3 = A_3 E_4 - A_4 E_3$$

$$Q_1 = B_1 E_2 - B_2 E_1; Q_2 = B_2 E_3 - B_3 E_2; Q_3 = B_3 E_4 - B_4 E_3$$

$$R_1 = C_1 E_2 - C_2 E_1; R_2 = C_2 E_3 - C_3 E_2; R_3 = C_3 E_4 - C_4 E_3$$

$$S_1 = D_1 E_2 - D_2 E_1; S_2 = D_2 E_3 - D_3 E_2; S_3 = D_3 E_4 - D_4 E_3$$

$$A_1 = \frac{|M_{21}|}{|M_{28}|} + \frac{|M_{41}|}{|M_{48}|}; A_2 = \frac{|M_{51}|}{|M_{58}|} - \frac{|M_{41}|}{|M_{48}|}; A_3 = -\frac{|M_{51}|}{|M_{58}|} - \frac{|M_{61}|}{|M_{68}|}; A_4 = \frac{|M_{61}|}{|M_{68}|} + \frac{|M_{81}|}{L_8}$$

$$\begin{aligned} B_1 &= \frac{|M_{42}| + |M_{43}|}{|M_{48}|} - \frac{L_2 - |M_{23}|}{|M_{28}|}; B_2 = -\frac{|M_{42}| + |M_{43}|}{|M_{48}|} - \frac{|M_{52}| + |M_{53}|}{|M_{58}|}; B_3 \\ &= \frac{|M_{52}| + |M_{53}|}{|M_{58}|} + \frac{|M_{62}| - |M_{63}|}{|M_{68}|}; B_4 = \frac{|M_{82}| + |M_{83}|}{L_8} - \frac{|M_{62}| - |M_{63}|}{|M_{68}|} \end{aligned}$$

$$\begin{aligned}
C_1 &= \frac{|M_{24}|}{|M_{28}|} - \frac{L_4}{|M_{48}|}; C_2 = \frac{L_4}{|M_{48}|} - \frac{|M_{54}|}{|M_{58}|}; C_3 = \frac{|M_{54}|}{|M_{58}|} - \frac{|M_{64}|}{|M_{68}|}; C_4 = \frac{|M_{64}|}{|M_{68}|} - \frac{|M_{84}|}{L_8} \\
D_1 &= -\frac{|M_{25}|}{|M_{28}|} - \frac{|M_{45}|}{|M_{48}|}; D_2 = \frac{|M_{45}|}{|M_{48}|} - \frac{L_5}{|M_{58}|}; D_3 = \frac{L_5}{|M_{58}|} + \frac{|M_{65}|}{|M_{68}|}; D_4 = -\frac{|M_{65}|}{|M_{68}|} - \frac{|M_{85}|}{L_8} \\
E_1 &= \frac{|M_{26}| - |M_{27}|}{|M_{28}|} - \frac{|M_{46}| + |M_{47}|}{|M_{48}|}; E_2 = \frac{|M_{46}| + |M_{47}|}{|M_{48}|} + \frac{|M_{56}| + |M_{57}|}{|M_{58}|}; E_3 \\
&= -\frac{|M_{56}| + |M_{57}|}{|M_{58}|} - \frac{L_6 - |M_{67}|}{|M_{68}|}; E_4 = \frac{L_6 - |M_{67}|}{|M_{68}|} - \frac{|M_{86}| + |M_{87}|}{L_8}
\end{aligned}$$

The net flux passing through TLR 2 and TLR 3 (next nearest neighbours with respect to TLR 1) can be written as

$$\begin{aligned}
\Phi_{\text{net_TLR 2}} &= |M_{21}|I_1 + |M_{23}|I_3 + |M_{24}|I_4 - |M_{25}|I_5 + |M_{26}|I_6 \\
&\quad - |M_{27}|I_7 - |M_{28}|I_8
\end{aligned} \tag{A.32}$$

$$\begin{aligned}
\Phi_{\text{net_TLR3}} &= |M_{31}|I_1 + |M_{32}|I_2 + |M_{34}|I_4 - |M_{35}|I_5 - |M_{36}|I_6 \\
&\quad + |M_{37}|I_7 - |M_{38}|I_8
\end{aligned} \tag{A.33}$$

The net flux passing through TLR 4 (diagonal with respect to the TLR 1) can be determined as

$$\begin{aligned}
\Phi_{\text{net_TLR4}} &= |M_{41}|I_1 + |M_{42}|I_2 + |M_{43}|I_3 - |M_{45}|I_5 - |M_{46}|I_6 \\
&\quad - |M_{47}|I_7 + |M_{48}|I_8
\end{aligned} \tag{A.34}$$

This model can be extended to an array with n elements with I_1 being the source current, we obtain the following system of equations described by the following matrices of equations

$$\begin{bmatrix} L_2 & \cdots & M_{22n} \\ \vdots & \ddots & \vdots \\ M_{2n2} & \cdots & L_{2n} \end{bmatrix} \times \begin{bmatrix} I_2 \\ I_3 \\ I_4 \\ I_5 \\ I_6 \\ \vdots \\ I_{2n} \end{bmatrix} = \begin{bmatrix} M_{21} \\ M_{31} \\ M_{41} \\ M_{51} \\ M_{61} \\ \vdots \\ M_{2n1} \end{bmatrix} * (-I_1) \quad (\text{A.35})$$

Thereby:

$$AI = B \quad (\text{A.36})$$

The solution for the induced currents can be expressed as,

$$I = A^{-1}B \quad (\text{A.37})$$

List of Figures

Figure 2.1: Proton magnetic moment and spin.	11
Figure 2.2: Energy difference between proton spin states as a function of the external magnetic field B_0	13
Figure 2.3: Spin precession movement of spin around the external magnetic field B_0	16
Figure 2.4: T_1 relaxation	19
Figure 2.5: T_2 relaxation	20
Figure 2.6: Free Induction Decay (FID).	22
Figure 2.7: Parasitic capacitors between RF coil and conductive sample due to the potential differences.....	26
Figure 2.8: Spin echo sequence : Formation of an echo by a 180° pulse after excitation pulse (90°) shown by spins (top) and sequence diagram (bottom).	28
Figure 2.9: Multi-spin echo sequence.....	29
Figure 2.10 Gradient echo sequence diagram.....	29
Figure 2.11: (a) Fourier Transform of a sinc shaped RF pulse results in rectangular slice profile and vice versa. (b) Slice selection in z-direction.....	32
Figure 2.12: Frequency-encoding applied in x direction resulting in shift in Larmor frequency of spins within each column.	33
Figure 2.13: Phase-encoding gradient is applied in y direction resulting in phase difference between spins with in each row.	34
Figure 2.14: Spin-wrap sequence. Sequence diagram (a) and corresponding k-space trajectory (b).....	35
Figure 2.15: (a) Simple conductor loop and its equivalent circuit. (b) Basic geometry of an RF coil with series RLC configuration. (c) Basic geometry of an RF coil with parallel RLC configuration.	39
Figure 2.16: A linearly polarized B_1 field (a) and its corresponding circularly polarized components.	42
Figure 2.17: Common volume coils: Solenoid design (a), Saddle coil design (b) and birdcage coil (c). The yellow arrows depict the orientation of the produced B_1 field.....	47
Figure 2.18: Basic design of Transmission Line Resonators (TLRs). (a) Single turn with four gaps on each side. The gaps on each side, are placed at the center of a conductor segment on the opposite side of the substrate. (b) two turn TLR with three gaps.	49
Figure 2.19: Two resonators placed in close vicinity to each other (top) and their corresponding electrical circuit coupled to each other via mutual coupling between them. ...	52

Figure 2.20: Peak splitting in resonance frequency response due to the mutual coupling of two adjacent RF coils.....	52
Figure 2.21: Overlap distance necessary for mutual decoupling of circular (left) and square (right) loops.....	54
Figure 2.22: Capacitive decoupling scheme for $M > 0$ and its equivalent two-port circuit model (top). Inductive decoupling scheme for $M < 0$ and its equivalent two-port circuit model (bottom.).....	54
Figure 2.23: Preamplifier decoupling: Minimizing the induced current I_2 by transforming a high impedance using the preamplifier.....	56
Figure 2.24: single turn TLR with 4 gaps: Single element TLR with decoupling annexes (top), each conductor side contains two annexes. 2-element TLR array with overlapped annexes (bottom), two annex from opposite conductor sides are overlapped.	57
Figure 2.25: single turn TLR with 4 gaps: Single element TLR with the decoupling ring (top). 2-element TLR array with overlapped decoupling rings (bottom): decoupling rings of the two elements are deposited on both sides of the substrate for overlapping.....	58
Figure 2.26: Basic tuning and capacitive circuitry: unbalanced (left) and balanced (right) network.	60
Figure 2.27: Experimental setup used to demonstrate radiation loss effect: non segmented (a) and segmented (b) loops with unbalanced tune and match network. Non segmented (c) and segmented (d) loops with balanced tune and match network.	61
Figure 2.28: Inductively matched circuit diagram (top) and its equivalent T-circuit (bottom). The ohmic losses in the pick-up loops are considered to be negligible.....	62
Figure 2.29: Typical baluns and cable traps designed to eliminate common mode currents. .	64
Figure 2.30: Transmit and Receive (T/R) switch based on quarter-wavelength transmission line.....	65
Figure 2.31: three-way Wilkinson power splitter.	66
Figure 2.32: lumped element model of the quarter wavelength transmission line.	66
Figure 2.33: A two-port network S-parameters analysis.	67
Figure 2.34: Sniffer loop designs: single loop (a) and double-loop design (b) which the two loops are decoupled via overlapping.....	68
Figure 2.35: Yee cell schematic. Yee cell stores H-field information in the centre of each face and corresponding E-field on the centre of each edge.	74
Figure 2.36: general structure of a CMRI sequence. The key components are magnetization preparation, respiratory navigation (NV) and data acquisition (readout).	77

Figure 2.37: double inversion recovery technique used for black-blood magnetization preparation.	78
Figure 2.38: short axis image of the heart acquired with black-blood prepared gradient echo acquisition (114).	79
Figure 2.39: sequence diagram for bSSFP. The RF pulses are applied every TR and gradients are reversed before the next excitation. The same for excitation flip angle (α to $-\alpha$).	80
Figure 3.1: Mesh configuration for TLR in flat (left) and bent (right) configurations.	88
Figure 3.2: Phantoms used for bench and MR measurements.	89
Figure 3.3: Basic geometry of the single TLR.	91
Figure 3.4: LC tuning and matching network.	92
Figure 3.5: Current density distribution of the single TLR.	93
Figure 3.6: (a) Decoupling element: decoupling ring was made of an intersection of a circle with radius r_s and a square, (b) 4-element TLR array with overlapped decoupling rings: decoupling rings of opposite sides (shown in red) were deposited on both sides of the substrate for overlapping with overlap distance a , decoupling ring conductor thickness w_s and r_c is the TLR outer radius.	94
Figure 3.7: Decoupling ring overlap optimization: analytically calculated coupling, compensation and net magnetic fluxes through TLR 3 in the 4-element TLR array when TLR 1 is driven by a current of 1 A.	95
Figure 3.8: Decoupling ring overlap optimization: Simulated transmission scattering parameters (S_{ij}) as a function of overlap distance.	97
Figure 3.9: Single element TLR design without (a) and with (b) the decoupling ring. Fabricated single element TLR without (c) and with (d) the decoupling ring.	98
Figure 3.10: (a) Interface board including the T/R switch and the connection board to the scanner. (b) The capacitive tuning and matching network. (c) Experimental setup for MR measurement using single element TLR.	99
Figure 3.11: Simulated transversal transmit efficiency ($B_1^+ / \sqrt{P_{input}}$) for TLR without (a) and with (b) decoupling ring. Measured transversal transmit efficiency for TLR without (c) and with (d) decoupling ring. (e) Simulated and measured 1D profiles of transmit efficiency for TLR with and without decoupling ring along TLR central axis.	100
Figure 3.12: Maximum intensity projection of the simulated 10 g averaged SAR distribution for the single element TLR with and without decoupling ring.	101

Figure 3.13: Transversal 3D gradient echo images (TR/TE = 14/6.75 ms, $T_{acq} = 2:25$ min, $1 \times 1 \times 1$ mm ³ nominal resolution, $96 \times 192 \times 192$ mm ³ FOV) of the phantom.	102
Figure 3.14: Calculated SNR maps: (a) 2D SNR maps calculated from the acquired 3D GRE images. (b) 1D profile of the calculated SNR along the coil central axis.....	103
Figure 3.15: Segmented conventional loop without (a) and with (b) decoupling ring. The segmented loop has the same geometry as the single TLR design. In addition, the geometry of the decoupling ring was kept constant.	104
Figure 3.16: Simulated B_1^+ profiles normalized to the input power ($B_1^+ / \sqrt{P_{input}}$) for the single element TLR and the segmented loop. The white line shows the coil plane and the white rectangle shows the phantom which has size of 27.6 cm \times 10 cm.	104
Figure 3.17 Simulated E-field vector magnitude profiles normalized to the input power for the single element TLR and segmented loop with and without decoupling ring. The white line shows the coil plane and the white rectangle shows the phantom which has size of 27.6 cm \times 10 cm.....	105
Figure 3.18: Schematic of the 12-element TLR array.	106
Figure 3.19: Fabricated 12-element flexible TLR array.	107
Figure 3.20: Static B_1^+ phase shimming: (a) simulated transmit efficiency in terms of SAR (SE), (b) simulated relative inhomogeneity, (c) simulated figure of merit function f for fixed phase variations between each column within the array (d).	109
Figure 3.21: 12-channel array cabling and interfacing scheme.	111
Figure 3.22: Interface board containing power splitter, floating cable trap, transmit/receive switch, and preamplifier.....	112
Figure 3.23: Developed 12-element flexible TLR array.....	112
Figure 3.24: Designed housing top (a) and bottom (b) parts with the capacitive tune and match circuit attached to the bottom part. (c) Final array housing.	113
Figure 3.25: The flexible array bent on a human torso.....	114
Figure 3.26: Simulated and measured scattering parameters of the 12-element TLR array in flat configuration for the box-shaped phantom.....	115
Figure 3.27: Measured S-parameters on bench when the 12-element TLR array in bent configuration for the torso phantom and torso of the volunteer.	115
Figure 3.28: Measured data on bench for total loss evaluation.	116
Figure 3.29: Various loss contributions considered in the measurement chain for total loss evaluation.....	117

Figure 3.30: Total loss evaluation of the measurement chain Individual element loss contributions together with calculated amplitude and phase of the delivered power to each element feed for flat phantom (box-shaped), torso phantom and an average torso of a volunteer. The values for Tx amplitude are shown as the percentage of the total power available at coil socket of the scanner.....	118
Figure 3.31: Calculated transmit power delivered to each element port.	118
Figure 3.32: chart of the loss contributions in the transmit chain.....	119
Figure 3.33: Column-wise excitation: transversal simulated and measured $B_1^+/\sqrt{P_{\text{input}}}$ maps for each element of the array.	120
Figure 3.34: Transversal simulated and measured $B_1^+/\sqrt{P_{\text{input}}}$ maps of each row of the developed array in flat configuration (box-shaped phantom).....	121
Figure 3.35: Measured $B_1^+/\sqrt{P_{\text{input}}}$ of each row of the developed array in bent configuration for the torso phantom.	122
Figure 3.36: Calculated 10 g averaged SAR distributions of the 12-element TLR array in flat configuration (box-shaped phantom) for three different excitation cases. SAR values were normalized to 1 W input of power.	124
Figure 3.37: Noise correlation matrix for the developed array in flat (box-shaped phantom) and bent (torso phantom) configurations.	125
Figure 3.38: 2D transversal slices of the reconstructed MR images acquired with the developed array in flat (box-shaped phantom) and bent (torso phantom) configuration for different acceleration factors.....	127
Figure 3.39: Reconstructed transversal SNR maps of the developed array in flat (box-shaped phantom) and bent (torso phantom) configurations for different acceleration factors.	128
Figure 3.40: Calculated g-factor maps for the developed array in flat (box-shaped phantom) and bent (torso phantom) configurations for different acceleration factors.	129
Figure 3.41: Reconstructed coronal GRE images and corresponding calculated SNR and g-factor maps acquired with the developed array in flat configuration using the box-shaped phantom. The presented slices are positioned 2 cm and 4 cm below the coil plane, respectively.	130
Figure 4.1: Schematic of the suggested combined $^1\text{H} / ^{31}\text{P}$ array. The red rectangular elements represent the ^{31}P individual elements.....	138
Figure 4.2: Proposed solution for simulation of the TLR array in bent configuration.	141
Figure 4.3: multilevel subgridding mesh (MSS) (141).....	142

List of Tables

Table 2.1: T_1 and T_2 values of various tissues at 1.5 T (34)	20
Table 2.2: Measured Q-factor at 200 MHz for the loop coil designs demonstrated in Figure 2.27(16).	61
Table 3.1: The ingredients and their corresponding amounts used to produce 15 kg of tissue- equivalent gel.	90
Table 3.2: Unloaded and loaded Q-factor measured on bench for single TLR with and without decoupling ring.	98
Table 3.3: 10 g averaged SAR values for single element TLR and segmented loop, with and without decoupling ring.	105
Table 3.4: Calculated length of the phase shifter cables based on the cable outlet position in the left or right side of the patient.	110
Table 3.5: Sequence parameters of B_1^+ mapping for the array in bent configuration (torso phantom).	122

Bibliography

1. Roemer PB, Edelstein WA, Hayes CE, Souza SP, Mueller OM. The NMR Phased Array. *Magn Reson Med* 1990;16:192–225.
2. Sodickson DK, Manning WJ. Simultaneous Acquisition of Spatial Harmonics (SMASH): Fast Imaging with Radiofrequency Coil Arrays. *Magn Reson Med* 1997;38:591–603.
3. Pruessmann KP, Weiger M, Scheidegger MB, Boesiger P. SENSE: Sensitivity encoding for fast MRI. *Magn Reson Med* 1999;42:952–962. doi: 10.1002/(SICI)1522-2594(199911)42:5<952::AID-MRM16>3.0.CO;2-S.
4. Moser E. Ultra-high-field magnetic resonance: Why and when? *World J Radiol [Internet]* 2010;2:37–40. doi: 10.4329/wjr.v2.i1.37.
5. Moser E, Stahlberg F, Ladd ME, Trattnig S. 7-T MR-from research to clinical applications? *NMR Biomed* 2012;25:695–716. doi: 10.1002/nbm.1794.
6. Clare S, Alecci M, Jezzard P. Compensating for B₁ inhomogeneity using active transmit power modulation. *Magn Reson Imaging* 2001;19:1349–1352.
7. Van Den Bergen B, Van Den Berg CAT, Klomp DWJ, Lagendijk JJW. SAR and power implications of different RF shimming strategies in the pelvis for 7T MRI. *J Magn Reson Imaging* 2009;30:194–202. doi: 10.1002/jmri.21806.
8. Tang L, Hue Y, Ibrahim T. Studies of RF Shimming Techniques with Minimization of RF Power Deposition and Their Associated Temperature Changes. *Concepts Magn Reson Part B Magn Reson Eng* 2011;39B:11–25. doi: 10.1002/cmr.b.20185.Studies.
9. Hardy CJ, Giaquinto RO, Piel JE, Rohling KW, Marinelli L, Blezek DJ, Fiveland EW, Darrow RD, Foo TKF. 128-Channel body MRI with a flexible high-density receiver-coil array. *J Magn Reson Imaging* 2008;28:1219–1225. doi: 10.1002/jmri.21463.
10. Adrian G, Van De Moortele PF, Ritter J, Moeller S, Auerbach EJ, Akgün C, Snyder CJ, Vaughan T, Ugurbil K. A geometrically adjustable 16-channel transmit/receive transmission line array for improved RF efficiency and parallel imaging performance at 7 Tesla. *Magn. Reson. Med.* 2008;59:590–597. doi: 10.1002/mrm.21488.
11. Goense J, Logothetis NK, Merkle H. Flexible, phase-matched, linear receive arrays for high-field MRI in monkeys. *Magn Reson Imaging [Internet]* 2010;28:1183–1191. doi: 10.1016/j.mri.2010.03.026.

12. Nordmeyer-Massner JA, De Zanche N, Pruessmann KP. Stretchable coil arrays: Application to knee imaging under varying flexion angles. *Magn Reson Med* 2012;67:872–879. doi: 10.1002/mrm.23240.
13. Wu B, Zhang X, Wang C, Li Y, Pang Y, Lu J, Xu D, Majumdar S, Nelson SJ, Vigneron DB. Flexible transceiver array for ultrahigh field human MR imaging. *Magn Reson Med* 2012;68:1332–1338. doi: 10.1002/mrm.24121.
14. Corea JR, Flynn AM, Lechêne B, Scott G, Reed GD, Shin PJ, Lustig M, Arias AC. Screen-printed flexible MRI receive coils. *Nat. Commun.* [Internet] 2016;7:10839. doi: 10.1038/ncomms10839.
15. Robitaille P-M, Berliner LJ. Ultra high-field magnetic resonance imaging. Springer; 2006.
16. Mispelter J, Lupu M, Briguet A. NMR Probeheads for Biophysical and Biomedical Experiments. Imperial College Press; 2006.
17. Kriegl R, Ginefri JC, Poirier-Quinot M, Darrasse L, Goluch S, Kuehne A, Moser E, Laistler E. Novel inductive decoupling technique for flexible transceiver arrays of monolithic transmission line resonators. *Magn Reson Med* 2015;73:1669–1681. doi: 10.1002/mrm.25260.
18. Gonord P, Kan S, Leroy-Willig A. Parallel-plate split-conductor surface coil: Analysis and design. *Magn Reson Med* 1988;6:353–358. doi: 10.1002/mrm.1910060313.
19. Gonord P, Kan S, Leroy-Willig A, Wary C. Multigap parallel-plate bracelet resonator frequency determination and applications. *Rev Sci Instrum* 1994;65:3363–3366. doi: 10.1063/1.1144573.
20. Serfaty S, Haziza N, Darrasse L, Kan S. Multi-Turn Split-Conductor Transmission-Line Resonators. *Magn Reson Med* 1997;38:687–689.
21. Poirier-Quinot M, Ginefri JC, Darrasse L, Coutrot A, Dufour-Gergam E, Grand. Evaluation of Multi-Turn Transmission Line Resonator for Localized MR Spectroscopy at 1.5 T. In: *Proc. Intl. Soc. Mag. Res. Med.* Vol. 11. ; 2003. p. 2389.
22. Frass-Kriegl R, Laistler E, Hosseinnzhadian S, Schmid AI, Moser E, Poirier-Quinot M, Darrasse L, Ginefri JC. Multi-turn multi-gap transmission line resonators – Concept, design and first implementation at 4.7 T and 7 T. *J Magn Reson Imaging* [Internet] 2016;273:65–72.

doi: 10.1016/j.jmr.2016.10.008.

23. Kuhns PL, Lizak MJ, Lee SH, Conradi MS. Inductive coupling and tuning in NMR probes; Applications. *J Magn Reson* 1988;78:69–76. doi: 10.1016/0022-2364(88)90157-6.
24. Zhoujian L. Développement de réseaux d'antennes supraconductrices pour l'Imagerie par Résonance Magnétique haute résolution à champ intermédiaire. PhD Thesis, L'UNIVERSITE PARIS-SACLAY, préparée à l'Université Paris-Sud; 2016.
25. WU B, QU P, WANG C, YUAN J, SHEN G. Interconnecting L/C Components for Decoupling and Its Application to Low-Field Open MRI Array. *Concepts Magn Reson Part B Magn Reson Eng* 2007;31B:116–126. doi: 10.1002/cmr.b.
26. Lanz T, Griswold MA. Concentrically Shielded Surface Coils - A New Method for Decoupling Phased Array Elements. In: *Proce Intl Soc Mag Reson Med*. Vol. 14. ; 2006. p. 217.
27. Niendorf T, Graessl A, Thalhammer C, et al. Progress and promises of human cardiac magnetic resonance at ultrahigh fields: A physics perspective. *J Magn Reson [Internet]* 2013;229:208–222. doi: 10.1016/j.jmr.2012.11.015.
28. Snyder CJ, DelaBarre L, Metzger GJ, Van De Moortele PF, Akgun C, Ugurbil K, Vaughan JT. Initial results of cardiac imaging at 7 Tesla. *Magn Reson Med* 2009;61:517–524. doi: 10.1002/mrm.21895.
29. Dieringer MA, Renz W, Lindel T, et al. Design and application of a four-channel transmit/receive surface coil for functional cardiac imaging at 7T. *J Magn Reson Imaging* 2011;33:736–741. doi: 10.1002/jmri.22451.
30. Winte L, Kellman P, Renz W, Gräl A, Hezel F, Thalhammer C, Von Knobelsdorff-Brenkenhoff F, Tkachenko V, Schulz-Menger J, Niendorf T. Comparison of three multichannel transmit/receive radiofrequency coil configurations for anatomic and functional cardiac MRI at 7.0T: Implications for clinical imaging. *Eur. Radiol.* 2012;22:2211–2220. doi: 10.1007/s00330-012-2487-1.
31. Thalhammer C, Renz W, Winter L, Seifert F, Hoffmann W, Knobelsdorff- F Von. A Two-dimensional Sixteen Channel Transmit/Receive Coil Array for Cardiac MRI at 7.0 Tesla: Design, Evaluation and Application. *J Magn Reson Imaging* 2012;36:847–857. doi: 10.1002/jmri.23724.A.

32. Graessl A, Renz W, Hezel F, et al. Modular 32-channel transceiver coil array for cardiac MRI at 7.0T. *Magn Reson Med* 2014;72:276–290. doi: 10.1002/mrm.24903.
33. Oezerdem C, Winter L, Graessl A, et al. 16-channel bow tie antenna transceiver array for cardiac MR at 7.0 tesla. *Magn Reson Med* 2016;75:2553–2565. doi: 10.1002/mrm.25840.
34. Haacke E, Brown RW, Thompson MR, Venkatesan R. *Magnetic Resonance Imaging: Physical Principles and Sequence Design*. A JOHN WILEY & SONS; INC.; PUBLICATION; 1999.
35. Bloch F. Nuclear Induction. *Phys rev* 1946;70:460–474.
36. Hoult DI. The Principle of Reciprocity in Signal Strength Calculations- A Mathematical Guide. *Concepts Magn Reson* 2000;12:173–187. doi: 10.1002/1099-0534(2000)12:4<173::AID-CMR1>3.0.CO;2-Q.
37. Hoult DI, Richards R. The signal-to-noise ratio of the nuclear magnetic resonance experiment. *J Magn Reson* 1976;24:71–85. doi: 10.1016/0022-2364(76)90233-X.
38. Nyquist H. Thermal agitation of electric charge in conductors. *Phys Rev* 1928;32:110.
39. Gabriel C, Gabriel S, Corthout E. The dielectric properties of biological tissues: I. Literature survey. *Phys Med Biol [Internet]* 1996;41:2231–2249. doi: 10.1088/0031-9155/41/11/001.
40. Hoult DI, Lauterbur PC. The sensitivity of the zeugmatographic experiment involving human samples. *J Magn Reson* 1979;34:425–433. doi: 10.1016/0022-2364(79)90019-2.
41. Decorps M, Blondet P, Reutenauer H, Albrand JP, Remy C. An Inductively Coupled , Series-Tuned NMR Probe. *J Magn Reson* 1985;65:100–109.
42. Hoult DI, Ginsberg NS. The quantum origins of the free induction decay signal and spin noise. *J Magn Reson* 2001;148:182–199. doi: 10.1006/jmre.2000.2229.
43. Darrasse L, Ginefri JC. Perspectives with cryogenic RF probes in biomedical MRI. *Biochimie* 2003;85:915–937. doi: 10.1016/j.biochi.2003.09.016.
44. Hahn EL. Spin Echoes. *Phys Rev [Internet]* 1950;80:580–594. doi: 10.1103/PhysRev.80.580.
45. Carr H, Purcell E. Effects of Diffusion on Free Precession in Nuclear Magnetic Resonance Experiments. *Phys. Rev. [Internet]* 1954;94:630–638. doi:

10.1103/PhysRev.94.630.

46. Edelstein W a, Hutchison JM, Johnson G, Redpath T. Spin warp NMR imaging and applications to human whole-body imaging. *Phys Med Biol* 1980;25:751–756. doi: 10.1088/0031-9155/25/4/017.

47. Garroway AN, Grannell PK, Mansfield P. Image formation in NMR by a selective irradiative process. *J. Phys. C Solid State Phys.* [Internet] 1974;7:L457–L462. doi: 10.1088/0022-3719/7/24/006.

48. Kumar A, Welte D, Ernst RR. NMR Fourier zeugmatography. *J Magn Reson* 1975;18:69–83. doi: 10.1016/0022-2364(75)90224-3.

49. Twieg DB. The k-trajectory formulation of the NMR imaging process with applications in analysis and synthesis of imaging methods. *Med Phys* [Internet] 1983;10:610–621. doi: 10.1118/1.595331.

50. Ljunggren S. A simple graphical representation of fourier-based imaging methods. *J Magn Reson Imaging* 1983;54:338–343. doi: 10.1016/0022-2364(83)90060-4.

51. Glockner JF, Hu HH, Stanley DW, Angelos L, King K. Parallel MR Imaging : A User ' s Guide 1. *RadioGraphics* 2005;25:1279–1297.

52. Larkman DJ, Nunes RG. Parallel magnetic resonance imaging. *Phys Med Biol* [Internet] 2007;52:R15–R55. doi: 10.1088/0031-9155/52/7/R01.

53. Blaimer M, Breuer F, Mueller M, Heidemann RM, Griswold MA, Jakob PM. Smash, sense, pils, grappa. *Top Magn Reson Imaging* 2004;15:223–236.

54. Deshmene A, Gulani V, Griswold M, Seiberlich N. Parallel MR Imaging. *J Magn Reson Imaging* 2012;36:55–72. doi: 10.1038/nature13478.The.

55. Griswold MA, Jakob PM, Heidemann RM, Nittka M, Jellus V, Wang J, Kiefer B, Haase A. Generalized Autocalibrating Partially Parallel Acquisitions (GRAPPA). *Magn Reson Med* 2002;47:1202–1210. doi: 10.1002/mrm.10171.

56. Katscher U, Börner P, Leussler C, Van den Brink JS. Transmit SENSE. *Magn Reson Med* 2003;49:144–150. doi: 10.1002/mrm.10353.

57. Padormo F, Beqiri A, Hajnal J V., Malik SJ. Parallel transmission for ultrahigh-field imaging. *NMR Biomed* 2016;29:1145–1161. doi: 10.1002/nbm.3313.

58. Wald L, Adalsteinsson E. Parallel-Excitation Techniques for Ultra-High-Field MRI. In: Parallel Imaging in Clinical MR Applications SE - 45. ; 2007. pp. 511–521. doi: 10.1007/978-3-540-68879-2_45.
59. Agarwal A, Lang JH. Foundations of Analog and Digital Electronic Circuits. 2005.
60. Avdievich N, Hetherington HP, Kuznetsov AM, Pan JW. 7 T Head Volume Coils: Improvements for Rostral Brain Imaging. J Magn Reson Imaging 2009;29:461–465. doi: 10.1002/jmri.21660.7.
61. Sohn S, Delabarre L, Vaughan JT, Gopinath A. RF Multi-Channel Head Coil Design with Improved B₁ Fields Uniformity for High Field MRI Systems. In: Microwave Symposium Digest (MTT), IEEE MTT-S International. ; 2012. doi: 10.1109/MWSYM.2012.6259669.
62. Connel I. Design of Radio-Frequency Arrays for Ultra-High. PhD Thesis, The University of Western Ontario; 2017.
63. Sengupta S, Fritz FJ, Harms RL, Hildebrand S, Tse DHY, Poser BA, Goebel R, Roebroek A. NeuroImage High resolution anatomical and quantitative MRI of the entire human occipital lobe ex vivo at 9.4 T. Neuroimage [Internet] 2017. doi: 10.1016/j.neuroimage.2017.03.039.
64. Chen G, Collins CM, Sodickson DK, Wiggins GC. A Method to Assess the Loss of a Dipole Antenna for Ultra-High-Field MRI. Magn Reson Med 2017. doi: 10.1002/mrm.26777.
65. Vaidya M, Collins CM, Sodickson DK, Brown R, Wiggins C, Lattanzi R. Dependence of B₁₊ and B₁₋ Field Patterns of Surface Coils on the Electrical Properties of the Sample and the MR Operating Frequency. Concepts Magn Reson Part B Magn Reson Eng 2016;46:25–40. doi: 10.1001/jamainternmed.2014.5466.Association.
66. Collins CM, Wang Z. Calculation of Radiofrequency Electromagnetic Fields and Their Effects in MRI of Human Subjects. Magn Reson Med 2011;65:1470–1482. doi: 10.1002/mrm.22845.Calculation.
67. Haase A, Odoj F, Kienlin M Von, et al. NMR Probeheads for In Vivo Applications. Concept Magn Reson 2000;12:361–388. doi: 10.1002/1099-0534(2000)12:6<361::AID-CMR1>3.0.CO;2-L.
68. Ginsberg DM, Melchner MJ. Optimum geometry of saddle shaped coils for generating a uniform magnetic field. Rev. Sci. Instrum. 1970;41:122–123. doi: 10.1063/1.1684235.

69. Laistler E, Dymerska B, Sieg J, Goluch S, Frass-Kriegl R, Kuehne A, Moser E. In vivo MRI of the human finger at 7 T. *Magn Reson Med* 2017;0:1–5. doi: 10.1002/mrm.26645.
70. Hayes CE, Edelstein WA, Schenck JF, Mueller OM, Eash M. An efficient, highly homogeneous radiofrequency coil for whole-body NMR imaging at 1.5 T. *J Magn Reson* 1985;63:622–628. doi: 10.1016/0022-2364(85)90257-4.
71. Hayes CE. The development of the birdcage resonator: A historical perspective. *NMR Biomed* 2009;22:908–918. doi: 10.1002/nbm.1431.
72. Ackerman JJH et al. Mapping of metabolites in whole animals by ³¹P NMR using surface coils. *Nature* 1980;283:167–170. doi: 10.1038/283167a0.
73. Elabyad IA, Kalayciyan R, Shanbhag NC, Schad LR. First in vivo potassium-39 (³⁹K) MRI at 9.4 T using conventional copper radio frequency surface coil cooled to 77 K. *IEEE Trans. Biomed. Eng.* 2014;61:334–345. doi: 10.1109/TBME.2013.2294277.
74. Hu B, Varma G, Randell C, Keevil SF, Schaeffter T, Glover P. A novel receive-only liquid nitrogen (LN₂)-Cooled RF coil for high-resolution in vivo imaging on a 3-tesla whole-body scanner. *IEEE Trans. Instrum. Meas.* 2012;61:129–139. doi: 10.1109/TIM.2011.2157575.
75. Junge S. Cryogenic and Superconducting Coils for MRI. *eMagRes [Internet]* 2012;1:505–514. doi: 10.1002/9780470034590.emrstm1162.
76. Laistler E, Poirier-Quinot M, Lambert SA, Dubuisson R-M, Girard OM, Moser E, Darrasse L, Ginefri J-C. In vivo MR imaging of the human skin at subnanoliter resolution using a superconducting surface coil at 1.5 tesla. *J Magn Reson Imaging [Internet]* 2015;41:496–504. doi: 10.1002/jmri.24549.
77. Neuberger T, Webb A. Radiofrequency coils for magnetic resonance microscopy. *NMR Biomed* 2009;22:975–981. doi: 10.1002/nbm.1246.
78. Webb AG. Radiofrequency microcoils for magnetic resonance imaging and spectroscopy. *J Magn Reson [Internet]* 2013;229:55–66. doi: 10.1016/j.jmr.2012.10.004.
79. Film P. DupontTM kapton®. 2017.
80. Zhoujian L, Willoquet G, Guillot G, Hosseinnzhadian S, Jourdain L, Poirier-Quinot M, Darrasse L, Ginefri JC. Study of two contact-less tuning principles for small monolithic

- radiofrequency MRI coils and development of an automated system based on piezoelectric motor. *Sensors Actuators, A Phys.* [Internet] 2016;241:176–189. doi: 10.1016/j.sna.2016.02.008.
81. Serfaty S, Haziza N, Darrasse L, Kan S. Multi-turn split-conductor transmission-line resonators. *Magn Reson Med* [Internet] 1997;38:687–689.
 82. Kriegl R. A flexible coil array for high resolution magnetic resonance imaging at 7 Tesla. PhD Thesis, Medical University of Vienna- Université Paris-Sud; 2014.
 83. Malko JA, McClees EC, Braun IF, Davis PC, Hoffman JC. A flexible mercury-filled surface coil for MR imaging. *Am. J. Neuroradiol.* 1986;7:246–247.
 84. Rousseau J, Lecouffe P, Marchandise X. A NEW; FULLY VERSATILE SURFACE COIL FOR MRI. *Magn Reson Imaging* 1990;8:517–523.
 85. Woytasik M, Ginefri JC, Raynaud JS, et al. Characterization of flexible RF microcoils dedicated to local MRI. *Microsyst Technol* 2007;13:1575–1580. doi: 10.1007/s00542-006-0277-x.
 86. Adriany G, Van De Moortele PF, Wiesinger F, et al. Transmit and receive transmission line arrays for 7 tesla parallel imaging. *Magn Reson Med* 2005;53:434–445. doi: 10.1002/mrm.20321.
 87. Nordmeyer-Massner JA, De Zanche N, Pruessmann KP. Mechanically adjustable coil array for wrist MRI. *Magn Reson Med* 2009;61:429–438. doi: 10.1002/mrm.21868.
 88. Goluch S, Kuehne A, Meyerspeer M, et al. A form-fitted three channel 31P, two channel 1H transceiver coil array for calf muscle studies at 7 T. *Magn Reson Med* 2015;73:2376–2389. doi: 10.1002/mrm.25339.
 89. Fujita H, Zheng T, Yang X, Finnerty MJ, Handa S. RF surface receive array coils: The art of an LC circuit. *J Magn Reson Imaging* 2013;38:12–25. doi: 10.1002/jmri.24159.
 90. Li Z, Kriegl R, Hosseinneshadian S, Poirier-Quinot M, Laistler E, DARRASSE L, Ginefri JC. Design of a Four-Element Array of Small Monolithic RF Coils with Shielding-Rings Decoupling. In: *ESMRMB.* ; 2015. p. 55. doi: 10.1007/s10334-015-0487-2.
 91. Nordmeyer-Massner JA, De Zanche N, Pruessmann KP. Noise figure characterization of preamplifiers at NMR frequencies. *J. Magn. Reson.* [Internet] 2011;210:7–15. doi:

10.1016/j.jmr.2011.01.025.

92. Hoult DI, Tomanek B. Use of mutually inductive coupling in probe design. *Concepts Magn Reson Part B Magn Reson Eng* 2002;15:262–285. doi: 10.1002/cmr.10047.

93. Seeber DA, Jevtic J, Menon A. Floating shield current suppression trap. *Concepts Magn Reson Part B Magn Reson Eng* 2004;21:26–31. doi: 10.1002/cmr.b.20008.

94. Boskamp B. Coil Imaging of the Excitation in MR : Decoupling and Receiver Coils. *Radiology* 1985;157:449–452.

95. Dabirzadeh A, McDougall MP. Trap design for insertable second-nuclei radiofrequency coils for magnetic resonance imaging and spectroscopy. *Concepts Magn. Reson. Part B Magn. Reson. Eng.* 2009;35:121–132. doi: 10.1002/cmr.b.

96. Wilkinson EJ. An N-Way Hybrid Power Divider. *IEEE Trans. Microw. Theory Tech.* 1960;8:116–118. doi: 10.1109/TMTT.1960.1124668.

97. Darrasse L, Kassab G. Quick measurement of NMR-coil sensitivity with a dual-loop probe. *Rev Sci Instrum* 1993;64:1841–1844. doi: 10.1063/1.1144020.

98. Ginefri JC, Durand E, Darrasse L. Quick measurement of nuclear magnetic resonance coil sensitivity with a single-loop probe. *Rev Sci Instrum* 1999;70:4730–4731. doi: 10.1063/1.1150142.

99. Ibrahim TS, Abduljalil a M, Baertlein B a, Lee R, Robitail PM. Analysis of B1 field profiles and SAR values for multi-strut transverse electromagnetic RF coils in high field MRI applications. *Phys Med Biol [Internet]* 2001;46:254525–55. doi: 10.1088/0031-9155/46/10/303.

100. Goluch S. A design and development procedure for transceive radio frequency coils in ultra-high field magnetic resonance. PhD Thesis, Medical University of Vienna; 2015.

101. Pohmann R, Scheffler K. A theoretical and experimental comparison of different techniques for B1 mapping at very high fields. *NMR Biomed* 2013;26:265–275. doi: 10.1002/nbm.2844.

102. Insko EK, Bolinger L. Mapping of the Radiofrequency Field. *J Magn Reson. Ser. A [Internet]* 1993;103:82–85. doi: 10.1006/jmra.1993.1133.

103. Morrell GR, Schabel MC. An analysis of the accuracy of magnetic resonance flip angle

measurement methods. *Phys Med Biol* [Internet] 2010;55:6157–74. doi: 10.1088/0031-9155/55/20/008.

104. Chung S, Kim D, Breton E, Axel L. Rapid B1+ mapping using a preconditioning RF pulse with turboFLASH readout. *Magn Reson Med* 2010;64:439–446. doi: 10.1002/mrm.22423.

105. Anon. IEC 60601-2-33 (Medical electrical equipment - Part 2-33: Particular requirements for the basic safety and essential performance of magnetic resonance equipment for medical diagnosis).

106. Balanis CA. *Advanced Engineering Electromagnetics*. second edi. WILEY; 2012.

107. Lemdiasov RA, Obi AA, Ludwig RL. A Numerical Postprocessing Procedure for Analyzing Radio Frequency MRI Coils. *Concepts Magn Reson Part A* 2011;38A:133–147. doi: 10.1002/cmr.a.

108. Hand JW. Modelling the interaction of electromagnetic fields (10 MHz–10 GHz) with the human body: methods and applications. *Phys Med Biol* [Internet] 2008;53:243–286. doi: 10.1088/0031-9155/53/16/R01.

109. Yee K. Numerical solution of initial boundary value problems involving Maxwell's equations in isotropic media. *Antennas Propagation, IEEE Trans.* [Internet] 1966;14:302–307. doi: 10.1109/TAP.1966.1138693.

110. Schild S, Chavannes N, Kuster N. A robust method to accurately treat arbitrarily curved 3-D thin conductive sheets in FDTD. *IEEE Trans. Antennas Propag.* 2007;55:3587–3594. doi: 10.1109/TAP.2007.910321.

111. Berenger J-P. A perfectly matched layer for the absorption of electromagnetic waves. *J. Comput. Phys.* [Internet] 1994;114:185–200. doi: 10.1006/jcph.1994.1159.

112. Kozlov M, Turner R. Fast MRI coil analysis based on 3-D electromagnetic and RF circuit co-simulation. *J Magn Reson* [Internet] 2009;200:147–152. doi: 10.1016/j.jmr.2009.06.005.

113. Gedney SD. *Introduction to the Finite-Difference Time-Domain (FDTD) Method for Electromagnetics*. 2011. doi: 10.2200/S00316ED1V01Y201012CEM027.

114. Syed MA, Raman S V., Simonetti OP. *Basic Principles of cardiovascular MRI*.

Springer; 2015. doi: 10.1007/978-3-319-22141-0.

115. Raaijmakers AJE, Ipek O, Klomp DWJ, Possanzini C, Harvey PR, Lagendijk JJW, Van Den Berg CAT. Design of a radiative surface coil array element at 7 T: The single-side adapted dipole antenna. *Magn Reson Med* 2011;66:1488–1497. doi: 10.1002/mrm.22886.

116. Carinci F, von Samson-Himmelstjerna F, Santoro D, Lindel T, Dieringer M, Seifert F, Sobesky J, Niendorf T. Comparison of four phase based Methods for the B1+ Mapping at 7T. In: *Proc. Intl. Soc. Mag. Res. Med.* Vol. 19. ; 2011. p. 4418. doi: 10.1002/mrm.22683.

117. Schmitter S, Moeller S, Wu X, Auerbach EJ, Metzger GJ, Van de Moortele PF, Uğurbil K. Simultaneous multislice imaging in dynamic cardiac MRI at 7T using parallel transmission. *Magn Reson Med* 2017;77:1010–1020. doi: 10.1002/mrm.26180.

118. Staeb D, Roessler J, O'Brien K, Hamilton-Craig C, Barth M. ECG Triggering in Ultra-High Field Cardiovascular MRI. *Tomography* 2016;2:167–174. doi: 10.18383/j.tom.2016.00193.

119. Niendorf T, Schulz-Menger J, Paul K, Huelnhagen T, Ferrari VA, Hodge R. High Field Cardiac Magnetic Resonance Imaging: A Case for Ultrahigh Field Cardiac Magnetic Resonance. *Circ. Cardiovasc. Imaging* 2017;10. doi: 10.1161/CIRCIMAGING.116.005460.

120. Rodgers CT. Ultrahigh Field Cardiovascular MRI at 7T: Towards Clinical Applications: Parametric Mapping at 7.0T. *Proc. Intl. Soc. Mag. Res. Med* 2012;20:7–9.

121. Kumar A, Edelstein WA, Bottomley PA. Noise figure limits for circular loop MR coils. *Magn. Reson. Med.* 2009;61:1201–1209. doi: 10.1002/mrm.21948.

122. Jurgens T, Taflove A, Umashankar K, Moore TG. Finite-difference time-domain modeling of curved surfaces (EM scattering). *IEEE Trans. Antennas Propag.* [Internet] 1992;40:357–366. doi: 10.1109/8.138836.

123. Remcom. XFDTD Reference Manual Release 7.2.2.2. REMCOM; 2011.

124. Larry Wald's group, Martinos Center for Biomedical Imaging MGH. "anthropomorphic MRI phantoms", https://phantoms.martinos.org/Main_Page.

125. Zajíček R, Vrba J, Novotný K. Evaluation of a Reflection Method on an Open-Ended Coaxial Line and its Use in Dielectric Measurements. *Acta Polytech.* 2006;46.

126. Zajíček R, Vrba J. Broadband Complex Permittivity Determination for Biomedical

Applications, Advanced Microwave Circuits and Systems, Vitaliy Zhurbenko (Ed.). In: ; 2010.

127. Kamon M, White JK, Tsuk MJ. FASTHENRY: A Multipole-Accelerated 3-D Inductance Extraction Program. *IEEE Trans. Microw. Theory Tech.* 1994;42:1750–1758. doi: 10.1109/22.310584.

128. Kuehne A, Goluch S, Waxmann P, Seifert F, Ittermann B, Moser E, Laistler E. Power balance and loss mechanism analysis in RF transmit coil arrays. *Magn Reson Med* 2015;74:1165–1176. doi: 10.1002/mrm.25493.

129. Firbank MJ, Harrison RM, Williams ED, Coulthard A. Quality assurance for MRI: practical experience. *Br. J. Radiol.* 2000;73:376–383. doi: 10.1259/bjr.73.868.10844863.

130. Robson PM, Grant AK, Madhuranthakam AJ, Lattanzi R, Sodickson DK, McKenzie CA. Comprehensive quantification of signal-to-noise ratio and g-factor for image-based and k-space-based parallel imaging reconstructions. *Magn Reson Med* 2008;60:895–907. doi: 10.1002/mrm.21728.

131. Breuer FA, Kannengiesser SAR, Blaimer M, Seiberlich N, Jakob PM, Griswold MA. General formulation for quantitative G-factor calculation in GRAPPA reconstructions. *Magn Reson Med* 2009;62:739–746. doi: 10.1002/mrm.22066.

132. Hayes CE, Roemer PB. Noise correlations in data simultaneously acquired from multiple surface coil arrays. *Magn Reson Med* 1990;16:181–191. doi: 10.1002/mrm.1910160202.

133. Keith GA, Rodgers CT, Hess AT, Snyder CJ, Vaughan JT, Robson MD. Automated tuning of an eight-channel cardiac transceive array at 7 Tesla using piezoelectric actuators. *Magn Reson Med* 2015;73:2390–2397. doi: 10.1002/mrm.25356.

134. Bizino MB, Hammer S, Lamb HJ. Metabolic imaging of the human heart: clinical application of magnetic resonance spectroscopy. *Heart [Internet]* 2014;100:881–890. doi: 10.1136/heartjnl-2012-302546.

135. Webb A, Smith N. ³¹P spectroscopy in human calf muscle at 7 tesla using a balanced double-quadrature proton-phosphorus RF coil. *Proce Intl Soc Mag Reson Med* 2010;18:3818.

136. Stefan N. The Failing Heart — An Engine Out of Fuel. *N ENGL J Med* 2007;356:1140–1151.

137. Taegtmeier H. Cardiac metabolism as a target for the treatment of heart failure. *Circulation* 2004;110:894–896. doi: 10.1161/01.CIR.0000139340.88769.D5.
138. Rajagopalan B, Blackledge MJ, McKenna WJ, Bolas N, Radda GK. Measurement of phosphocreatine to ATP ratio in normal and diseased human heart by ³¹P magnetic resonance spectroscopy using the rotating frame-depth selection technique. *Ann NY Acad SCI* 1987;508:321–322.
139. Meyerspeer M, Roig ES, Gruetter R, Magill AW. An improved trap design for decoupling multinuclear RF coils. *Magn. Reson. Med.* 2014;72:584–590. doi: 10.1002/mrm.24931.
140. Baert AL, Knauth M, Sartor K. Parallel Imaging in Clinical MR Applications. (Schoenberg S., Dietrich O, Reiser M., editors.). Springer; 2007.
141. CST. Understanding Time Domain Meshing in CST MICROWAVE STUDIO®. 2010.
142. Rieke V, Pauly KB. MR thermometry. *J. Magn. Reson. Imaging* 2008;27:376–390. doi: 10.1002/jmri.21265.
143. Quesson B, de Zwart JA, Moonen CT. Magnetic resonance temperature imaging for guidance of thermotherapy. *J Magn Reson Imaging* 2000;12:525–533.
144. Wang P. Evaluation of MR thermometry with proton resonance frequency method at 7T. *Quant Imaging Med Surg [Internet]* 2017;7:259–266. doi: 10.21037/qims.2017.03.05.
145. Anon. IEC 6061-1 (Medical electrical equipment - Part 1: General requirements for basic safety and essential performance).
146. Anon. ISO 14971 (Medical devices - Application of risk management to medical devices).
147. Gonord P, Kan S, Leroy-Willig A. Parallel-Plate Split-Conductor Surface Coil: Analysis and Design. *Magn Reson Med* 1988;6:353–358.
148. Grover FW. The Calculation of the Mutual Inductance of Circular Filaments in Any Desired Positions. *Proc IRE* 1944;32:620–629. doi: 10.1109/JRPROC.1944.233364.

Publication List

Journal articles

Roberta Frass-Kriegl, Elmar Laistler, **Sajad Hosseinneshadian**, Albrecht Ingo Schmid, Ewald Moser, Marie Poirier-Quinot, Luc Darrasse, Jean-Christophe Ginefri. *Multi-Turn Multi-Gap Transmission Line Resonators –Concept, Design and First Implementation at 4.7 T and 7 T*. Journal of Magnetic Resonance. S1090-7807(16)30199-9.

Zhoujian Li, Georges Willoquet, **Sajad Hosseinneshadian**, Marie Poirier-Quinot, Luc Darrasse, Jean-Christophe Ginefri. *Study of two contact-less tuning principles for small monolithic radiofrequency MRI coils and development of an automated system based on piezoelectric motor*. Sensors and Actuators A 241 (2016) 176–189.

Conference proceedings

Sajad Hosseinneshadian, Roberta Kriegl, Sigrun Goluch, Michael Pichler, Jürgen Sieg, Marie Poirier-Quinot, Luc Darrasse1, Ewald Moser, Jean-Christophe Ginefri., Elmar Laistler A *Flexible Transceiver Array for 7 T Cardiac MRI: First Imaging Experiments*. ESMRMB, Barcelona, Spain, 2017: vol.30, p.299

Sajad Hosseinneshadian, Roberta Kriegl, Sigrun Goluch, Michael Pichler, Jürgen Sieg, Marie Poirier-Quinot, Luc Darrasse1, Ewald Moser, Jean-Christophe Ginefri., Elmar Laistler *Towards a Flexible Transceiver Array for 7 T Cardiac MRI: Evaluation of Decoupling Ring Effects*. ISMRM, Honolulu, Hawaii, USA, 2017 (Traditional Poster)

Sajad Hosseinneshadian, Roberta Kriegl, Zhoujian Li, Marie Poirier-Quinot, Luc Darrasse1, Ewald Moser, Elmar Laistler, Jean-Christophe Ginefri. *Decoupling an Array of Monolithic Transmission Line Resonators (TLRs) for 7 T MRI using Shielding Rings*. ESMRMB, Vienna, Austria, 2016 : vol.29, p.80

Zhoujian Li, **Sajad Hosseinneshadian**, Geneviève Guillot, Georges Willoquet, Laurène Jourdain, Marie Poirier-Quinot, Luc Darrasse, and Jean-Christophe Ginefri. *Proton Imaging at 4.7 T Using a Piezoelectric-based Automation System for impedance matching of Monolithic Transmission Line Resonators*. ISMRM, Singapore, 2016 (Traditional Poster)

Zhoujian Li, Roberta Kriegl, **Sajad Hosseinneshadian**, Marie Poirier-Quinot, Elmar Laistler, Luc Darrasse, Jean-Christophe Ginefri. *Design of a Four-Element Array of Small Monolithic RF Coils with Shielding-Rings Decoupling*. ESMRMB, Edinburg, UK, 2015: vol.28, p.55

Curriculum Vitae

Sajad Hossein Nezhadian, born 6th September 1990, Ahvaz, IRAN

EDUCATION AND QUALIFICATIONS

2014-2017: IR4M- University of Paris-Sud (Paris-Saclay University)- CMPBE- Medical University of Vienna

- Joint PhD thesis between Univ. Paris-Sud, CNRS, Université Paris-Saclay (1.10.2014 – 31.3.2016) and Medical University of Vienna (1.04.2016 - 31.12.2017): A Flexible Transceiver Array Employing Transmission Line Resonators For Cardiac MRI at 7 T.

2012-2014: Medical Faculty of Mannheim of Heidelberg University

M.Sc. in Biomedical Engineering, specialization: Imaging (Graduated on 30th August 2014)

- Subjects include: Mathematical Modelling, Biophysics, Basic Medical Science, Genetics, Radiation Physics, Magnetic Resonance Imaging, Physics of Imaging Systems, Image Analysis, Biomedical Engineering, Basic Optics, Nuclear Medicine, Radiation Therapy
- Master Thesis: Cooled RF coils at 0.5 Tesla application

2008-2012: Jondi Shapur University of Technology

B.Sc. in Electrical Engineering, specialization: Electronic

- Subjects include: Electronic Engineering, Electrical Circuits, Electrical Machines, Physics of Electronics, Engineering Mathematics, Electromagnetism, Signals and Systems, Communication Circuits
- Overall GPA: 15.64 (fifteen point sixty four out of twenty)
- Bachelor Thesis: Predicting and detecting seizure onset using intracranial EEG sample entropy

2007-2008: Razavi Pre-University Center-Ramhormoz-Iran, Mathematics and Physics

- Overall GPA: 18.71 (eighteen point seventy one out of twenty)

2004-2007: Imam Jafar-Sadegh High School-Ramhormoz-Iran, Mathematics and Physics

- Overall GPA: 19.21 (nineteen point twenty one of twenty)

WORK EXPERIENCE

- May 2013-March 2014: Research Assistant in SNiP Group (Systemische Neurowissenschaften in der Psychiatrie) at Central Institute for Mental Health Mannheim (ZI)
- April 2013-September 2014: Member of "RF Methods and Imaging" group at Computer Assisted Clinical Medicine (CKM) in Medical Faculty of Mannheim of University of Heidelberg (Master student- Project : Quadrature birdcage resonator for Na-23 for animal MRI at 3 Tesla)

RESEARCH INTERESTS

RF resonator development for x-nuclei in MRI	Flexible RF coils
Phased-Array RF coils	Cooled RF coils
Transmission Line Resonators	Biomedical engineering

Titre : Réseau flexible de résonateurs à ligne de transmissions pour l'émission et la réception en IRM cardiaque à 7T

Mots clés : Antennes, Flexible, RLT, IRM Cardiaque

Ce projet doctoral s'est déroulé dans le cadre d'une collaboration entre le laboratoire d'Imagerie par Résonance Magnétique Médicale et Multi-Modalités (IR4M) de l'Université Paris-Sud (France) et le Center for Medical Physics and Biomedical Engineering at Medical (CMPBME) de l'Université Médicale de Vienne (Autriche). L'objectif principal de ce travail était de développer un réseau d'antennes radiofréquence flexible fonctionnant en émission/réception pour l'IRM à 7T. Les réseaux d'antennes permettent de bénéficier du rapport signal sur bruit élevé des antennes de surface de petites tailles tout en accédant à un champ de vue étendu. De plus, les réseaux d'antennes permettent l'utilisation de technique d'imagerie parallèle afin d'accélérer l'acquisition des images ainsi que l'utilisation d'algorithme de transmission parallèle afin de produire un champ radiofréquence homogène, ce qui est crucial en IRM. Ce projet doctoral visait la conception, le développement, l'installation et l'évaluation d'un réseau d'antenne RF flexible basé sur le principe des résonateurs à lignes de transmission (RLT). Ces structures sont intrinsèquement monolithiques et auto-résonantes et ne nécessitent donc pas l'emploi de condensateurs discrets pour accorder l'antenne. Des simulations électromagnétiques 3D, ainsi que des caractérisations expérimentales sur table et en IRM ont été réalisées pour évaluer les performances de ce réseau, en configuration plate et courbée.

Title: A Flexible Transceiver Array Employing Transmission Line Resonators For Cardiac MRI at 7 T

Keywords : Array coils, Flexible, TLR, Transceiver, Cardiac MRI

This PhD thesis was conducted in the frame of a bilateral project between the laboratoire d'Imagerie par Résonance Magnétique Médicale et Multi-Modalités (IR4M) at Université Paris-Sud (Orsay, France) and the Center for Medical Physics and Biomedical Engineering (CMPBME) at the Medical University of Vienna (Vienna, Austria). The main objective of this work was to develop a flexible transceiver RF coil array for 7 T MRI. Coil arrays benefit from the high SNR of small surface coils over an extended field of view (FOV). Furthermore, array coils enable the use of parallel imaging (PI) techniques for accelerated image acquisition and pTx algorithms that can be used to produce a homogeneous transmit field which is of importance in MRI. This project targets the design, development, implementation and evaluation of a flexible RF coil array based on the transmission line resonator (TLR) principle. TLRs are inherently monolithic and self-resonant structures, i.e. there is no need for lumped element capacitors to tune the coil. 3D electromagnetic simulation (EMS) together with bench and MRI experiments were performed to evaluate the performance of the developed array in flat and bent configuration.